Association of the Dawson-type polyoxometalates with photoactive transition metal monomers and polymers.

James J. Walsh, B.Sc.

Dublin City University

September 2011

Thesis submitted for the degree of

Doctor of Philosophy

Supervised by

Prof. Tia E. Keyes

Prof. Robert J. Forster

I hereby certify that this material, which I now submit for assessment on the programme of study leading to the award of Doctor of Philosophy is entirely my own work, that I have exercised reasonable care to ensure that the work is original, and does not to the best of my knowledge breach any law of copyright, and has not been taken from the work of others save and to the extent that such work has been cited and acknowledged within the text of my work.

Signed: ____________
ID No.: ___________
Date: _______

Acknowledgements:

Firstly I would like to thank my parents, Anne and Pete, who instilled within me a love of learning from a very young age. They have always given me sound advice, encouragement and financial assistance and I certainly wouldn't be where I am in life without their continued help. I couldn't have asked for better parents.

My sincere thanks go to Prof Tia Keyes and Prof Robert Forster. Throughout the course of this project they guided me in the right direction but also let me implement my own ideas. They were always full of useful suggestions if I encountered any issues and their enthusiasm for my research never faltered.

The technical staff in DCU have been fantastic throughout the years. My thanks to Damien for the mass spec analyses, John for his assistance with NMR, Vinny for help with the ATR, Barry for his running of Dektak measurements and Úna for help with the IR microscope. Also I would like to thank Dr. Brendan Twamley for the extensive assistance with SEM and EDX and also for hours of interesting scientific discussion; Maurice for all his assistance with the Raman, arc lamp and the transient absorption, and Dr. Chuck Blackledge for his invaluable assistance with all kinds of malfunctioning equipment.

Within the Keyes/Forster research group I thank all members past and present. My thanks go to Ciarán, Lynda, Gavin, Shane, Elena, Qiang, Colm and Damian for lending me samples of various compounds. My thanks also go to Vlado for the help with synthesis; Tib for the help with the IR and Raman and Jie for the many in-depth discussions. In particular I would like to thank Dr. Colm Mallon for all of his assistance, particularly with my electrochemistry, and for putting up with my ceaseless questioning. I would be months behind in my work if it wasn't for his assistance, and I am very grateful. My thanks also go to the rest of the scientific community in DCU, and to SFI for funding me for over three years.

Finally I thank Sharon, who has been by my side for my whole scientific career to date. It is an amazing thing that I have someone to bounce ideas off, ask to correct my work, run MS samples for me, ask theory of and listen to my moaning day-in day-out for all these years. She has shown real strength of character in struggling through a very hard PhD which was full of difficulties, setbacks

and delays. She does it with a big smile and infectious enthusiasm for life, and I respect and love her no end for that.

“Elephants are a lot like people, Mrs. Simpson. Some of them act badly because they've had a hard life, or have been mistreated…but, like people, some of them are just jerks.”

Glossary:

2A5NP – 2-amino-5-nitropyridine

A – geometric electrode surface area (cm^2)

AB – alcian blue

AFM – atomic force microscopy

ATR – attenuated total reflectance

bpy – 2, 2’-bipyridine

biH_2 – 2,2’-biimidazole, doubly protonated

biq – 2,2’-biquinoline

bmte – 1,2-bis(1-methyl-5-mercapto-1,2,3,4-tetrazole)-ethane

bmtp – 1,5-bis(1-methyl-5-mercapto-1,2,3,4-tetrazole)pentane

BnOH – benzyl alcohol

box – bisoxazoline

BPBH – 1, 6 bis-(2-(2-pyridyl)benzimidazoyl)hexane

$[(But)_4N]^+$ – tetrabutylammonium cation

$(But)_4NBF_4$ – tetrabutylammonium tetrafluoroborate

$(But)_4NOH$ – tetrabutylammmonium hydroxide

$(But)_4NPF_6$ – tetrabutylammmonium hexafluorophosphate

^{t}Bubpy – 4, 4’-di-*tert*-butyl-2, 2’-bipyridine

C – concentration of electroactive material in a thin film ($mol.cm^{-3}$)

(caip-COOH) – 2-(4-carboxyphenyl)imidazo[4,5-f][1,10]phenanthroline

(caip-NH_2) – 2-(4-aminophenyl)imidazo[4,5-f][1,10]phenanthroline

(caip-NO_2) – 2-(4-nitrophenyl)imidazo[4,5-f][1,10]phenanthroline

co-poly – co-polymer

CPE – carbon paste electrode

CT – charge transfer

CV – cyclic voltammetry/cyclic voltammogram

d – thin film thickness (cm)

DAB – diaza-di(5-amino-2,2’-bipyridine)

dcbpy – 4,4′-dicarboxy-2,2′-bipyridine

DCM – dichloromethane

D_{CT} – homogeneous charge transfer diffusion coefficient ddbpy – 4,4’-*bis*[3,5-*bis*(dodecyloxy)benzyloxy]-2,2’-bipyridine

DLS – dynamic light scattering

DMF – *N*, *N*-dimethylformamide

DMSO – dimethylsulfoxide

DODA – dimethyldioctadecylammonium

dpb – 4, 4’-diphosphonic-2, 2’-bipyridine acid

dpp – 4, 7-diphenyl (1, 10-phenanthroline)

dppz – dipyrido[3, 2-*a*:2’, 3’-*c*]phenazine

DSSC – dye-sensitized solar cell

$E_{1/2}$ – formal redox potential (Volts)

E_a – activation energy

ECL – electrochemiluminescence

EDX – energy dispersive X-ray

EPR – electron paramagnetic resonance

ESI-MS – electrospray ionization mass spectrometry/ electrospray ionization mass spectrum

Et_2O – diethyl ether

EtOH – ethanol

F – Faraday’s constant (96485 $C.mol^{-1}$)

Fc/Fc^+ – ferrocene/ferrocenium

FDTO – fluorine-doped tin oxide

FeSEM – field emission scanning electron microscopy

FLIM – fluorescence lifetime imaging

FRET – fluorescence resonance energy-transfer

FTIR – Fourier-transform infrared

GC – glassy carbon

$[(Hex)_4N]^+$ – tetrahexylammonium cation

ILCT – interligand charge transfer

ILs – ionic liquids

i_p – peak current (Amps)

ISC – intersystem crossing

ITO – indium tin oxide/indium-doped tin oxide

IVCT – intervalence charge transfer

K_a – association constant

k_q – quenching rate constant

K_{SV} – Stern-Volmer constant

LB – Langmuir-Blodgett

LBL – layer-by-layer

LMCT – ligand to metal charge transfer

LP – long pass

LUMO – lowest unoccupied molecular orbital

m/z – mass to charge ratio (mass spectrometry)

MB – methylene blue

MBL–PPV – poly[5-methoxy-2-(4-sulfobutoxy)-1,4-phenylvinylene]

Mebpy-py – 4-(4’’-pyridinyl ethyl)-4’-methyl-2, 2’-bipyridine

MeCN – acetonitrile

MeOH – methanol

MLCT – metal to ligand charge transfer

n – number of electrons transferred (electrochemistry)

NB – narrow band

Nd:YAG – neodymium-doped yttrium aluminium garnet

NHE – normal hydrogen electrode

NIR – near-infrared

NMR – nuclear magnetic resonance

ORTEP – Oak Ridge Thermal Ellipsoid Plot Program (X-ray diffraction)

oop – out of plane

p0p – 4, 4’-bipyridine

PAH – poly(allylaminehydrochloride)

PDDA – poly(diallyldimethylammonium chloride)

PEC – photoelectrochemistry/ photoelectrochemical

PEG – polyethylene glycol

PEI – poly(ethylenimine)

phen – 1, 10-phenanthroline

pK_a – acid dissociation constant

PMT – photomultiplier tube

$[(Pn)_4N]^+$ – tetrapentylammonium cation

polyazabpy – poly[1-(2, 2’-bipyridine-4-yl)-1, 4- diazabutadiene-4, 4’-diyl]

POM – polyoxomolybdate

POW – polyoxotungstate

ppy-*CN* – phenylpyridinate

PR$^+$ – pararosaniline

PSS – (poly(styrenesulfonate)

Pt$_C$ – colloidal platinum

PVP – poly(4-vinylpyridine)

Q – Faradaic charge passed (Coulombs)

QD – quantum dot

qpy – 2, 2':4, 4'':4', 4''-quarterpyridyl

R – universal gas constant (8.31 J.mol^{-1}.K^{-1})

RR – resonance Raman

R_S – quenching sphere radius

SANS – small-angle neutron scattering

SCE – saturated calomel electrode

SEM – scanning electron microscope/ scanning electron microscopy

SEC - spectroelectrochemistry

SV – Stern-Volmer

SWCNTs – single-wall carbon nanotubes

T – absolute temperature (K)

TCSPC – time-correlated single photon counting

terpy/tpy – 2, 2'; 6', 2''-terpyridine

THABr – tetrahexylammmonium bromide

TM – transition metal

TPA – tripropylamine

TTF – tetrathiafulvalene

UV/Vis – Ultraviolet/visible

UV/Vis/NIR – Ultraviolet/visible/near-infrared

υ – electrochemical scan rate (V.s^{-1})

X^2 – regression coefficient (luminescent lifetime fitting)

X_{POM} – mole fraction of polyoxomolybdate

X_{POW} – mole fraction of polyoxotungstate

XPS – X-ray photoelectron spectroscopy

α – transfer coefficient of the potential energy barrier

ε – molar absorption coefficient (M^{-1}.cm^{-1})

Γ – surface coverage of electroactive material (mol.cm^{-2})

λ_{max} – wavelength of highest absorption/emission intensity

δ – depletion layer thickness

τ – luminescent lifetime (luminescence)

τ – experimental timescale (electrochemistry)

ν – wavenumber (cm^{-1})

Φ – fluorescence quantum yield

η – overpotential

Table of contents:

Chapter 1:

Introduction and literature survey.

1.1 – Introduction to photovoltaics:

1.1.1 - Dye-sensitised solar cells:

The first dye-sensitized solar cell (DSSC) was produced by Michael Grätzel in 1991 and was based on the ruthenium complex $[Ru(dcbpy)_2(NCS)_2)]^{2-}$ (where dcbpy = 4,4′-dicarboxy-2,2′-bipyridine and NCS = isothiocyanate) immobilized on TiO_2 (see Fig 1.1.1).[1] This type of cell was the first "second-generation" functioning material with promising efficiency, and research in this area is extensive (first generation materials are semiconductor based; see section 1.6.1). These cells require the presence of a donating electrolyte typically based on an I^-/I_3^- redox cycle. In 1997 Grätzel's group immobilized $[Ru(4, 4', 4''-(COOH)_3-terpy)(NCS)_3]^{3-}$ on TiO_2 (where terpy = 2, 2', 6', 2''-terpyridine).[2] This so-called "black-dye" absorbs up to 900 nm and had a higher energy conversion efficiency of the previous system. In 2008 a new ruthenium complex, [*cis*-Ru(4,4'-*bis*(5octylthieno[3,2-b]thiophen-2-yl)-2,2'-bpy)(4,4'-dicarboxyl-2,2'bpy)$(NCS)_2$], was employed in a TiO_2 DSSC with an overall reported efficiency of 11 %.[3]

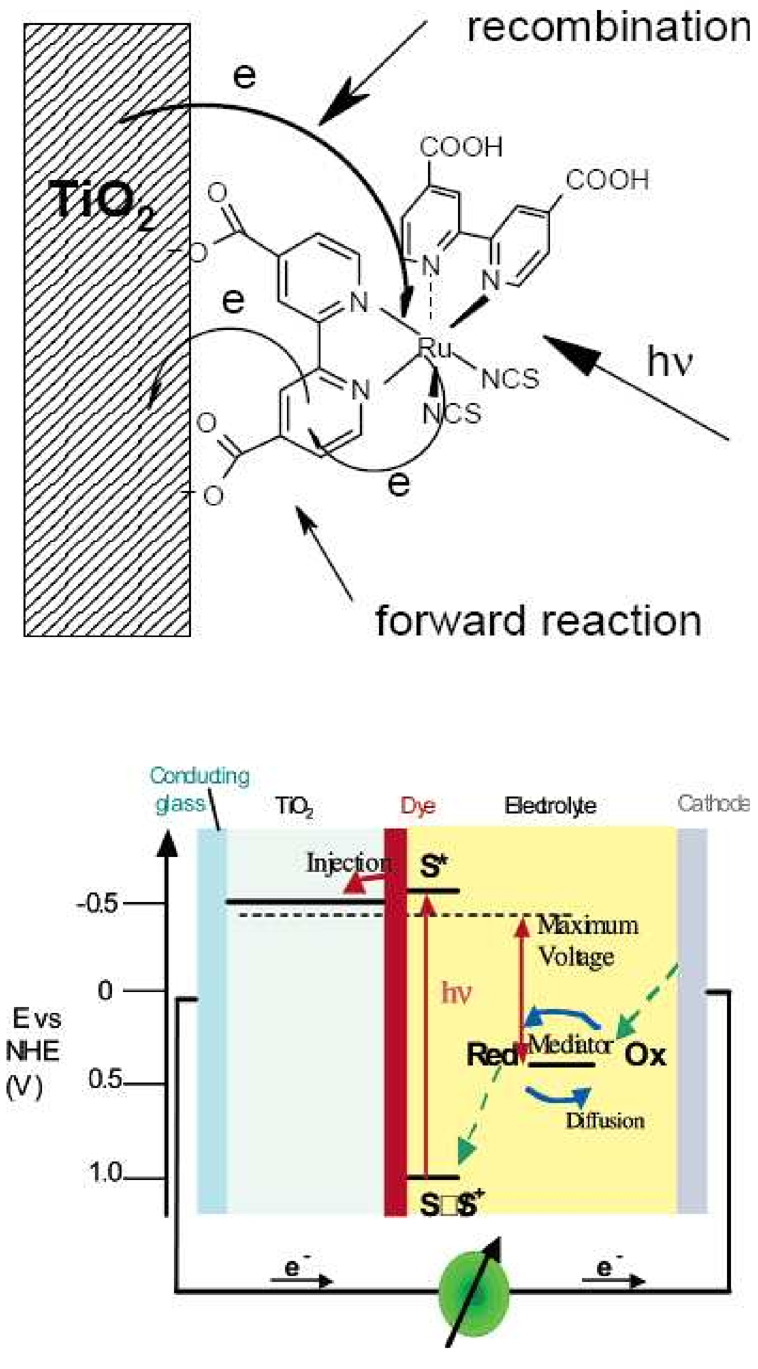

Fig 1.1.1: Schematic diagram of a functioning Grätzel Cell employing the famous “N3” dye as a sensitizer and iodide/tri-iodide as the regenerative redox couple. Reproduced from [4]. Below is an energy level diagram of the system, with potentials referenced to the normal hydrogen electrode (NHE). Reproduced from [5].

The energy level diagram shown in Fig 1.1.1 shows the basic operating principles of DSSCs. The Ru dye is immobilized on the surface of the TiO_2 nanoparticles via strong covalent bonds. Absorption of a photon in the visible region by the dye results in population of the dye singlet excited state S*, from which the excited electron is injected into the conduction band of the TiO_2. The Ru^{3+} center is regenerated to Ru^{2+} via the redox couple mediator, which is itself regenerated at the cathode. The magnitude of the photogenerated voltage is equal to the difference between the Fermi level of the electron in the TiO_2 and the redox potential of the electrolyte. The use of DSSCs in electricity generation is hampered mainly by the necessity of adding the regenerative donor (I^-/I_3^-) to the system. This liquid electrolyte has proven difficult to seal into a closed cell, as it can react with adhesives and the organic solvent can leak through plastic. A recent study by Bai *et al* has investigated the use of a ternary eutectic melt based on alkylimidazolium ionic liquids and the complex [NaRu(4-carboxylic acid-4'-carboxylate)(4, 4'-dinonyl-2, 2'-bipyridine)$(NCS)_2$].[6] Although a decrease in overall conversion efficiency was recorded (a reduction from 11 % to 8.2 %) this could prove to be a significant breakthrough in getting this technology to mass markets as these salts do not permeate plastic. This system has yet to be optimised.

Materials other than transition metal complexes have been investigated as sensitizers for TiO_2. For example the use of porphyrins and phthalocyanines have also been investigated in recent years. Wang *et al* recently reported the use of zinc metalloporphyrins on TiO_2 nanocrystalline films.[7] The use of a range of Ru-phthalocyanines in DSSCs has also been recently reported; however the conversion efficiency obtained was relatively low at 3.5 %.[8] While some of these other systems show promise none have been studied to the same extent as the Ru polypyridyl complexes.

As first generation solar technologies have achieved such high levels of efficiency the key reason for research in dye-sensitised technologies is to address the high production cost of the first generation cells. The dye sensitised titanium dioxide cells are comprised of relatively cheap and abundant components. TiO_2 is available in bulk and although ruthenium ore is rare and expensive to mine, the concentrations required are small (ie: monolayer coverage of the TiO_2 nanoparticles). Certainly the cost of obtaining these materials is a fraction of that for first generation materials. The chemistry of both ruthenium complexes and TiO_2 is also very well defined. The physicochemical properties of the materials, when considered along with their associated economic benefits, indicate that these materials will become commercially very important in medium-term energy generation consideration.

In the context of this thesis it was hoped that a series of photoelectrochemical cells involving interfacial assemblies of Ru polypyridyl complexes and polyoxometalates could be designed and tested. Very little research has been conducted into the photocatalytic properties of polyoxometalates deposited on conducting substrates, and the Keyes group has extensive experience working with Ru complex/polyoxometalate photochemical interactions in solution. It was hoped that by merging the group's expertise in surface electrochemistry and ruthenium based interfacial photochemistry that some of the first dye-sensitized polyoxometalate based photoelectrochemical cells could be produced.

1.2 – Polyoxometalates:

1.2.1 - Introduction:

Polyoxometalates are a broad class of (poly)oxoanions in which the metal atoms are linked via shared oxygen atoms. They have long been the focus of study due to their potential applications in photocatalysis.[9, 10, 11] The metal atoms are known as addenda atoms, typically high oxidation state (d^0 or d^1) transition metals such as Mo, W, V and Nb. In many structures this bridged framework may encapsulate a coordinated heteroatom, such as sulfur in the form of tetrahedral SO_4^{2-}.[12] The different polyoxometalate geometrical structures are typically named after their discoverer and they include the Keggin, Dawson, Lindqvist, Anderson, Tourné and Preyssler structures; although other less well known structures also exist. The synthesis of new sub-varieties of polyoxometalate is constantly being reported in the literature, but in general the Keggin and Dawson structures have been studied to the largest degree.[13]

1.2.2 – Types of polyoxometalate structure:

The first polyoxometalate reported was an ammonium phosphomolybdate of the formula $(NH_4)_3[PMo_{12}O_{40}]$ by Berzelius in 1826.[14] Linus Pauling was one of the first to attempt to describe its structure, in terms of ionic radii.[15] However the structure of the molecule was not determined until the tungstate analogue $[PW_{18}O_{40}]^{3-}$ was discovered in 1934 by Keggin.[16] By the mid twentieth century hundreds of polyoxometalate structures had been isolated and identified, including the Dawson structure, which is the main focus of this work.[17] Some of the more common conventional polyoxometalate structures are given in Fig 1.2.1. Octahedral edges are O atoms, with addenda metal atoms at centre of each octahedron, encapsulated groups are yellow.

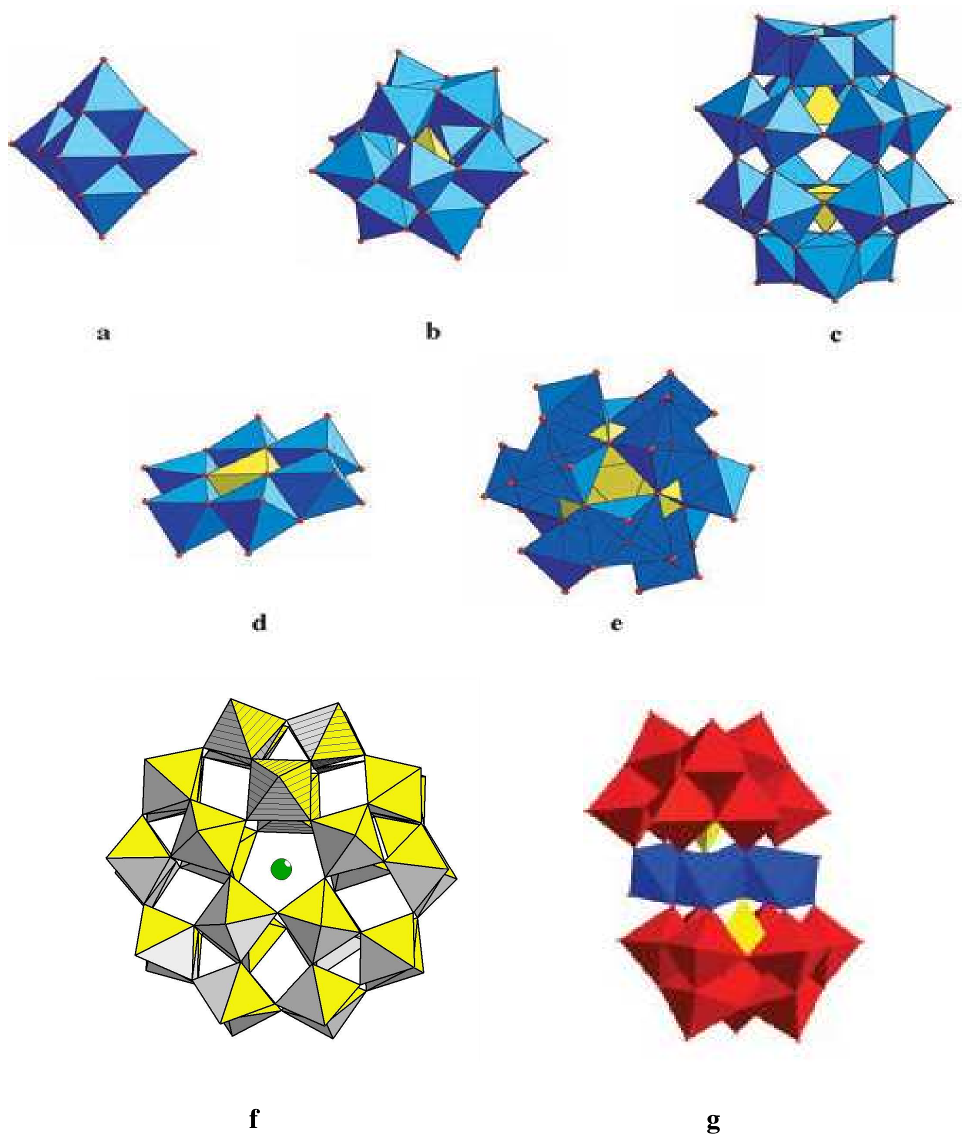

Fig 1.2.1: Diagrams of various polyoxometalate geometrical structures. (a) Lindqvist structure; (b) α-Keggin structure; (c) α-Dawson structure; (d) Anderson structure; (e) Icosahedral structure $[\{XO_{12}\}Mo_{12}O_{30}]^{n-}$ incorporating (X), which is a tetravalent lanthanide or actinide anion (Reproduced from [18]); (f) Preyssler anion $[Na(H_2O)P_5W_{30}O_{110}]^{14-}$ incorporating Na^+ viewed approximately down the molecular C_5 axis (Reproduced from [19]) and (g) the Tourné "sandwich" anion $[Co^{II}_4(PW_9O_{34})_2]^{10-}$, showing Co atoms (blue) sandwiched between two $\{PW_9O_{34}\}^{9-}$ fragments (Reproduced from [20]).

Polyoxometalates are capable of accepting multiple protons and electrons and hence are powerful electrocatalysts for hydrogen and oxygen evolution. As mentioned previously, the Dawson (sometimes denoted Wells-Dawson) polyoxometalates are the primary focus of this investigation. The general structure of these molecules is $[X_2M_{18}O_{62}]^{n-}$, where M = Mo, W and X = P, S. The structure of a Dawson polyoxometalate is shown in Fig 1.2.2.

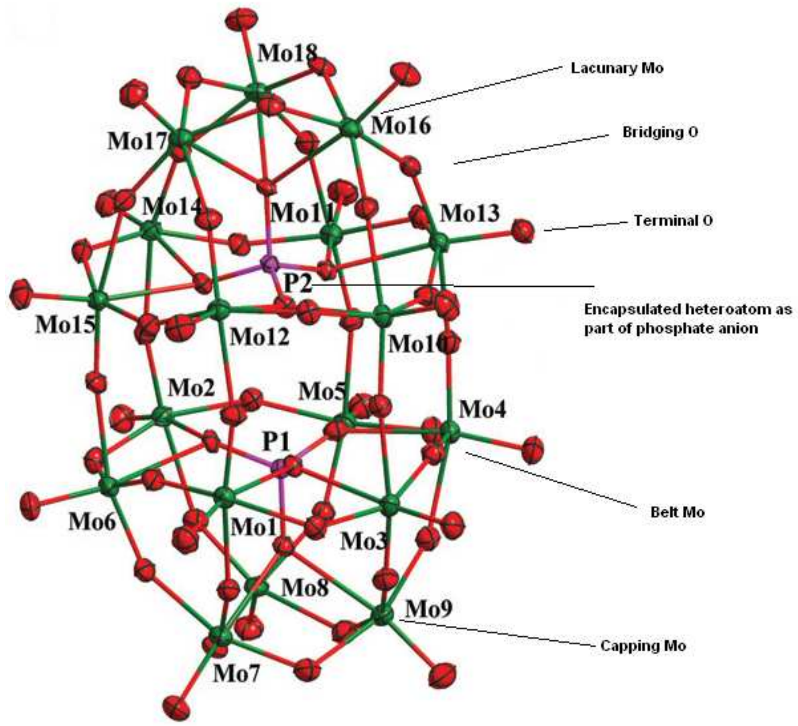

Fig 1.2.2: Structure of the phosphate containing Dawson polyoxomolybdate α-$[Mo_{18}O_{54}(PO_4)_2]^{6-}$ as determined by X-ray crystallography. Red = oxygen, green = molybdenum and purple = phosphorous. Reproduced from [21].

The structure in Fig 1.2.2 shows the general features of the Dawson polyoxometalates. The molecules exhibit a horizontal mirror plane which separates two Mo_9 clusters. The Mo atoms can be subclassified as occupying either the "capping" or "belt" positions and are connected by bridging oxygen ligands. The principle axis of rotation is C_3 and connects the two phosphorus atoms. The structure of α-$[Mo_{18}O_{54}(PO_4)_2]^{6-}$ is a conventional one, as the shape of the metal-oxide framework is not distorted at any location. In the case of the non-conventional sulfite-containing Dawson clusters, such as α-$[W_{18}O_{54}(SO_3)_2]^{4-}$, the structure of the molecule is distorted inwards at the equator. This "peanut" configuration is due to the unusual charge distribution of the encapsulated SO_3^{2-} groups, which are not isostructural with true tetrahedral ions such as PO_4^{3-} and SO_4^{2-}.[22]

A huge variety of derivitised polyoxometalates also exist, with new structures and variants being reported frequently. An important polyoxometalate synthon for making derivitised analogues is the lacunary defect structure. If one or more addenda atoms are removed from the structure a defect site becomes available for functionalization. The space left by the removal of a metal atom is usually filled with a labile ligand such as H_2O, which is easily removed under conventional synthetic conditions. An example of the structure of a lacunary-substituted polyoxometalate dimer is shown below.[23]

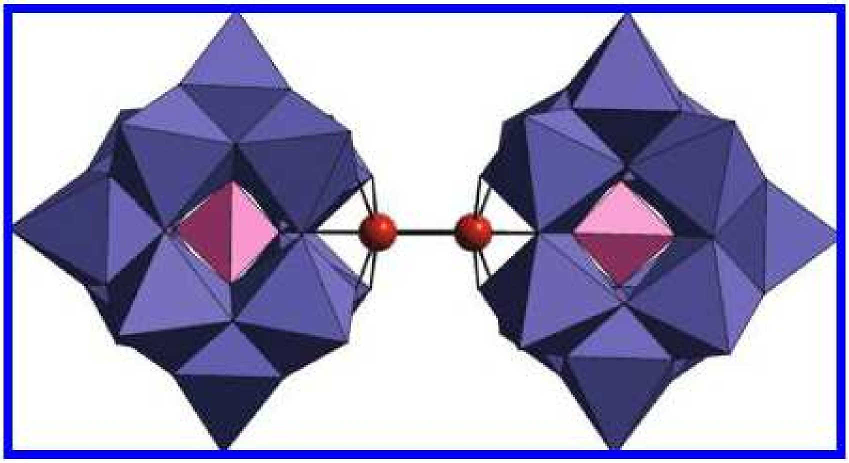

Fig 1.2.3: Polyhedral view of the $[Re_2(PW_{11}O_{39})_2]^{8-}$ anion as obtained from X-ray crystallography. Red = Re atoms, blue = WO_6 octahedra, and pink = PO_4 tetrahedra. Reproduced from [23].

This novel structure, which contains a Re-Re quadruple bond, was synthesized from the lacunary defective polyoxometalate precursor $K_7[PW_{11}O_{39}]$ and $(Bu_4N)_2[Re_2Cl_8]$ at low pH. A great many modified polyoxometalates have been synthesized in more recent years via similar lacunary starting materials. The linking of potentially sensitizing units in such fashion is discussed in sections 1.4.2 – 1.4.4.

1.2.3: Structural isomerism in polyoxometalates:

Structural isomerism in polyoxometalates is subtle and common. Minor differences in the orientations of atoms or groups within the molecule give different isomers. This is usually achieved by rotating one isolated part of the molecule around the C_n axis so that the groups along the axis will be oriented differently relative to each other. The isomers for each structure are differentiated by an α, β, γ, δ, ε, etc prefix. Fig 1.2.4 shows the subtle differences in symmetry between Dawson polyoxometalates.

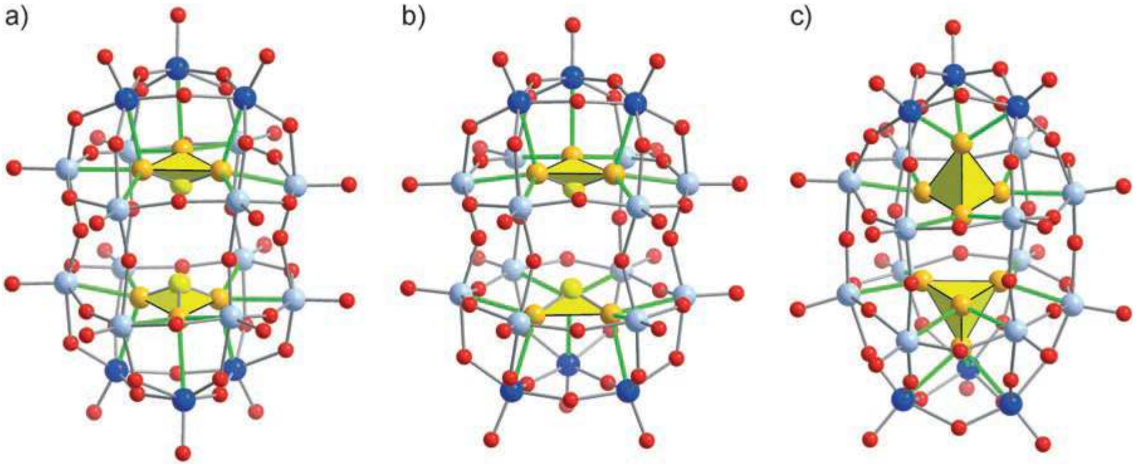

Fig 1.2.4: Geometric isomerism in Dawson polyoxomolybdates. (a) β-$[Mo_{18}O_{54}(SO_3)_2]^{4-}$, (b) α-$[Mo_{18}O_{54}(SO_3)_2]^{4-}$ and (c) α-$[Mo_{18}O_{54}(SO_4)_2]^{4-}$. Red = oxygen, light blue = belt Mo, dark blue = capping Mo, yellow = sulfite or sulfate anions. Reproduced from [24].

The structures of the α/β-$[Mo_{18}O_{54}(SO_3)_2]^{4-}$ vary mainly in the orientation of the encapsulated sulfite moieties relative to each other, as viewed down the principal axis of rotation; in the α case the sulfite groups are eclipsed and in the β case they are staggered. The α isomer is considered the more stable of the two and this difference is considered negligible in the case of the fully oxidized (ie: 4- charge) polyoxometalate ions; however in their reduced forms this energy difference becomes increasingly significant. EPR studies demonstrated that β → α isomerisation occurs in solution over a period of 37 days, both under light and dark conditions. The study concludes that this slow isomerization is due to thermodynamic differences and this indicates that the reduced form of the α isomer is favoured energetically over the reduced form of the β isomer. This renders the α isomer potentially more useful in photocatalytic applications, as the β isomer is potentially unstable under photoelectrochemical conditions.[24]

This difference in stability of isomeric pairs is not restricted to α/β-$[Mo_{18}O_{54}(SO_3)_2]^{4-}$ alone. The Dawson polyoxotungstate $[W_{18}O_{54}(SO_4)_2]^{4-}$ is unusual in that it crystallizes naturally as the γ* isomer.[12] The corresponding α-$[W_{18}O_{54}(SO_4)_2]^{4-}$ isomer could only be synthesized via the one-electron reductive electrosynthesis γ*-$[W_{18}O_{54}(SO_4)_2]^{4-}$ → α-$[W_{18}O_{54}(SO_4)_2]^{5-}$.[25] This reaction demonstrates again how the α form of the Dawson polyoxometalates is generally favoured, but only under photochemically or electrochemically reductive conditions. Under ambient, dark conditions in solution this isomerization is either not favoured or very slow (months or longer). Since the goal of this study is to develop a well-defined and reversible photocatalyst the use of anything other than α-type Dawson anions has been avoided wherever possible.

1.2.4 – General Dawson polyoxometalate properties:

Polyoxometalates generally have the following properties:[26]

(a) They can accept and subsequently release a number of electrons (either photochemically or electrochemically) without any substantial change in their molecular structure. Reduction results in the formation of mixed-valence metal compounds with a blue or green-blue colour. These "heteropoly blues" exhibit broad electronic transitions between 650 and 1100 nm (see Fig 1.3.1).

(b) Reduction is very often accompanied by a pH dependant protonation step. The reduction potentials of each step are therefore pH dependant. The electrochemistry of γ*-$[W_{18}O_{54}(SO_4)_2]^{4-}$ is an excellent example of this kind of behaviour.[12]

(c) Molybdates are easier to reduce than their tungstate analogues. This makes them more efficient oxidants; however their reoxidation requires stronger oxidising agents. Under ambient conditions the only oxidising agent present in any significant amount is molecular oxygen, therefore only tungstates will complete the photocatalytic cycle under aerated (ambient) conditions. Molybdates require the addition of a stronger oxidising agent, such as an acid, to complete the catalytic cycle and hence tungstates are generally better candidates for solution phase photocatalysis.

(d) The addition of electrons beyond a certain number results in distortion of the molecular geometry due to the formation of d^2 metal electronic configuration. For example in the case of the reduction of $[W_{12}O_{40}]^{6-}$ to $[W_{12}O_{40}]^{7-}$.[27]

(e) Molybdates generally absorb at longer wavelengths than their corresponding tungstates, and this is true in the cases of γ^*-$[W_{18}O_{54}(SO_4)_2]^{4-}$ (colourless) and α-$[Mo_{18}O_{54}(SO_4)_2]^{4-}$ (yellow).[12, 28]

Special attention must be paid to the fact that reduced polyoxomolybdates are very difficult to reoxidise, and this makes the photocatalytic potential of molybdates in solution quite poor. Although they are better initial oxidants and they absorb further into the visible these seemingly advantageous points are simply negated by the fact that the back reaction is so difficult to complete. This is because the speed of regeneration of the catalyst is very important in determining the turnover number. A high turnover number is one of the necessary prerequisites of a good photocatalyst, and tungstates are more likely to be able to accommodate this.[10] It is hoped that immobilising the polyoxometalate as a film on an electrode will allow ease of catalyst regeneration, as the rate of interfacial electron transfer at electrode interfaces is usually very fast and the applied potential can be controlled.

1.3 - Photodegradation of organic compounds by polyoxometalates:

1.3.1 – Background:

Both polyoxomolybdates and polyoxotungstates can undergo multiple electron and proton transfer reactions in the presence of a suitable catalytic substrate under UV irradiation, and hence may be employed as photocatalysts to oxidise simple organic compounds such as benzyl alcohol and isopropanol.[29, 30] Examples of polyoxometalate photocatalysis include the use of a homogeneously dispersed powder of $H_3[PW_{12}O_{40}]/TiO_2$, which has been used to decompose a range of organic dyes;[31] the use of $[PW_{12}O_{40}]^{3-}$ in decomposing toxic herbicide atrazine;[32] and more recently the use of the novel iridium-substituted polyoxotungstate $K_{14}[(IrCl_4)KP_2W_{20}O_{72}].23H_2O$ in splitting water.[33]

The quantum yield of a photochemical reaction (i.e.: is the number of molecules of reactant consumed or product formed, per photon absorbed) is dependant on a number of factors including the nature of the polyoxometalate, which reduction step is taking place, the pH, the type of substrate and, importantly, the formation of a preassociation complex. The photodecomposition of organic substrates can be followed easily by electronic spectroscopy, as the reduction of all polyoxometalates results in the formation of new features in the visible/near-IR region of the spectrum. An example of the reduction of $[PMo_{12}O_{40}]^{3-}$ is given below.

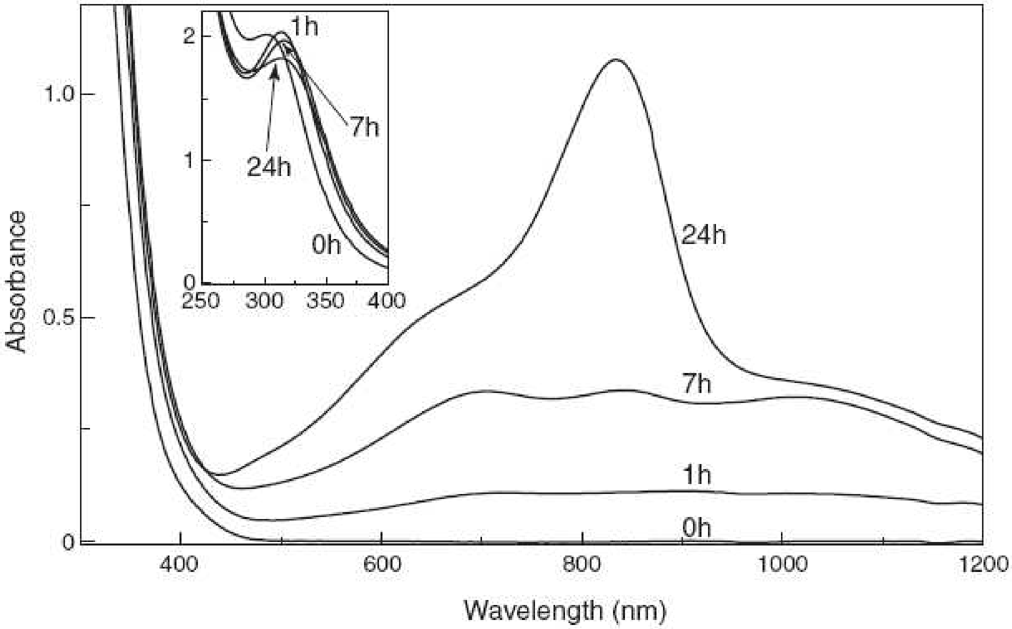

Fig 1.3.1: The electronic absorption change during the steady-state photolysis (λ = 254 nm) of a deaerated aqueous solution containing 1.0 mM $[PMo_{12}O_{40}]^{3-}$ and 5.0 M MeOH at pH = 2.0. Reproduced from [34].

The new features present here are typical of reduced polyoxometalate spectra. In its fully-oxidized form all $[PMo_{12}O_{40}]^{3-}$ Mo atoms are d^0 or d^1, and when the molecule is reduced the extra electron is localized on a single Mo atom. A new type of intervalence metal to metal charge transfer ($Mo^V \rightarrow Mo^{VI}$) is thus observed which exhibits absorption at very high wavelengths. The low wavelength absorption present both before and after photoreduction is a $Mo^{VI} \rightarrow O$ LMCT. This type of band is common to all polyoxometalates but shifts slightly depending on which metallic elements are present.

1.3.2 - The photocatalytic mechanism:

Two mechanisms of substrate photodecomposition by polyoxometalates have been identified previously: (a) the formation of a pre-associated {catalyst---substrate} complex leading to hole transfer and (b) radical hydroxylation.

Polyoxometalate-substrate systems studied to date have typically involved the formation of a preassociated equilibrium complex between catalyst and substrate in solution.

$$\text{POM} + \text{S} \rightarrow (\text{POM---S})$$

This mechanism has been confirmed to take place in reactions involving both polyoxometalates and semiconductor catalysts. In each case an increasing concentration of substrate results in an increased initial rate of photocatalysis under conditions of constant catalyst concentration. An example of one such study is given below.

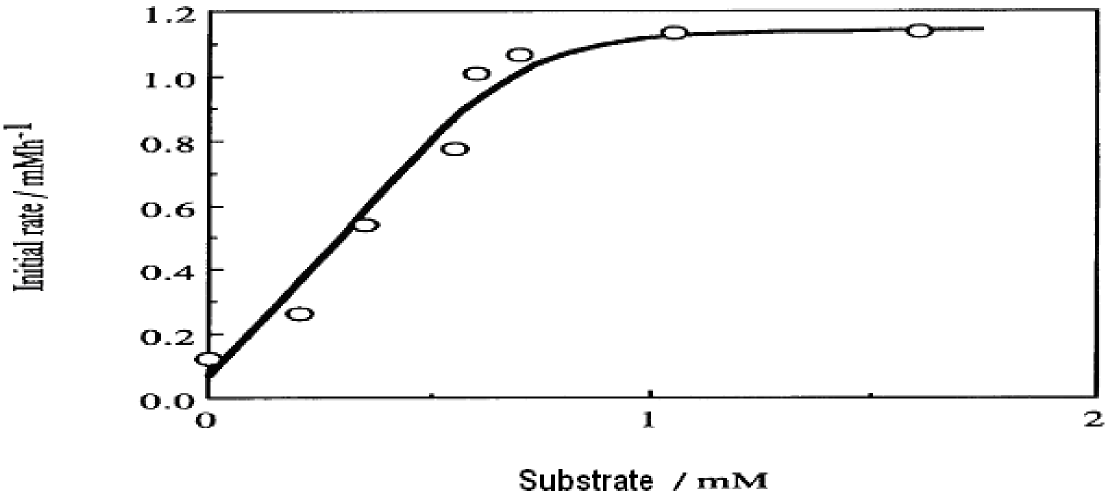

Fig 1.3.2: Study of the affect of increasing 4-chlorophenol (substrate) concentration on the initial rate of photocatalysis ($\lambda < 300$ nm) under conditions of constant $[PW_{12}O_{40}]^{3-}$ (catalyst) concentration in deaerated aqueous media with pH adjusted to 1.[35]

Fig 1.3.2 shows an adherence to the Langmuir-Hinshelwood model, the reciprocal plot of which yields a straight line. This model indicates that at constant $[PW_{12}O_{40}]^{3-}$ concentration and relatively low concentrations of substrate the photochemical reaction is first order, but as the substrate concentration reaches saturation the reaction becomes zero-order in the substrate. This implies that the photochemistry is reliant on the pre-association complex formed between catalyst and substrate. The formation of this preassociated complex is extremely fast, and its value is one of the factors affecting the initial rate of catalysis.[36] For example this rate was measured by single-photon counting to be in the region of 10^{12} $M^{-1}s^{-1}$ for the complexation between the weakly fluorescent $[NaPW_{12}O_{40}]^{3-}$ and *n*-propanol substrate.[36]

Direct photolysis of organic compounds, such as alcohols, via the preassociation complex (i.e.: via hole (h^+) transfer with the substrate) has been demonstrated to be the dominant photocatalytic pathway. Using semiconductor notation

$$\mathrm{POM}\ (h^+ + e^-) + S \rightarrow \mathrm{POM}(e^-) + S(ox)$$

However it is possible that another mechanism of action occurs indirectly by hydroxyl radicals in the presence of water and/or organics

$$\mathrm{POM}\ (h^+ + e^-) + H_2O \rightarrow \mathrm{POM}\ (e^-) + {}^{\bullet}OH + H^+$$

Evidence for the second mechanism is derived from the fact that several hydroxylated products and intermediates have been found after the irradiation of *p*-chlorophenol in the presence of $W_{10}O_{32}^{4-}$, and from spin-trapping experiments involving EPR spectroscopy.[37, 38] However photochemistry also occurs in dry, inert solvents to a substantial degree meaning that the reaction can occur without radicals and must be attributed to electron or hole transfer. This cannot be due to the presence of trace amounts of water as the photochemistry is too extensive. It has been postulated that the dominant mechanism is hole transfer as in some cases specific products only are formed and hydroxyl radicals tend to be highly unselective.[9] For example, primary alcohols have been selectively photooxidised to aldehydes and secondary alcohols to ketones by $[SiW_{12}O_{40}]^{5-}$ under UV irradiation.[28]

1.3.3: The polyoxometalate photocatalytic cycle:

Absorption of a photon by a polyoxometalate in the presence of an oxidizable substrate in the UV region results in the formation of a reduced blue polyoxometalate species and oxidised substrate. Typically a single polyoxometalate catalytic cycle is thought to follow the scheme in Fig 1.3.3:

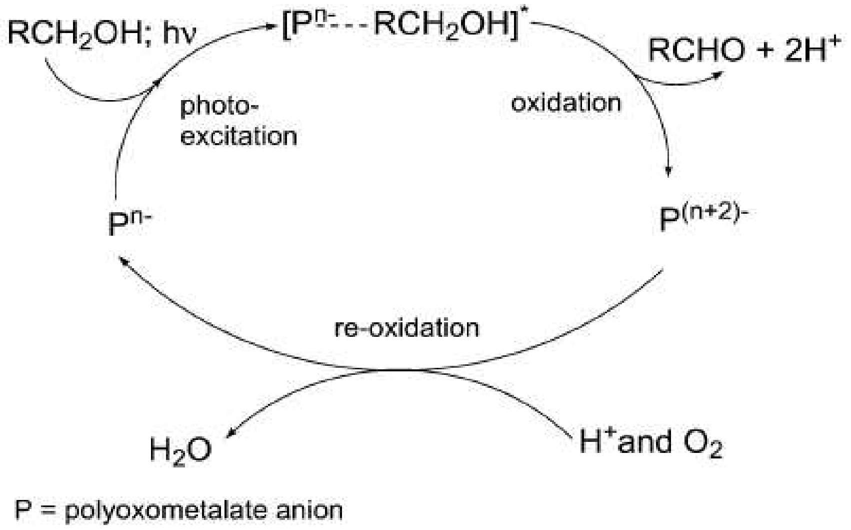

Fig 1.3.3: A complete photocatalytic cycle involving polyoxometalate and an alcoholic substrate. Reproduced from [39].

In Fig 1.3.3 [P^{n-}---RCH_2OH]* is the pre-associated complex containing a polyoxometalate molecule in its excited state which is pre-associated with the substrate, and this is the state responsible for redox chemistry. The re-oxidation of the reduced polyoxometalate is usually the rate-determining step for the catalytic cycle. This can be achieved using an artificially added acid reagent, by applying an electrochemical potential or, in the case of polyoxotungstates, by molecular oxygen. This reaction is generally thermodynamically unfeasible for polyoxomolybdates and polyoxovanadates. Rüther *et al* have demonstrated that for the Dawson polyoxotungstate γ^*-$[S_2W_{18}O_{62}]^{4-}$ the reoxidation step is facile when O_2 is employed, and although oxidation by H^+ is thermodynamically possible it is also a slow process, relative to the corresponding polyoxomolybdate.[40]

As discussed in section 1.3.2 the formation of the pre-associated complex is thought to be a crucial step in determining the initial rate of reaction between the polyoxoanion and the substrate. Other factors include the redox potential of the polyoxometalate; the nature of the substrate (eg: primary alcohols are far easier to oxidise than their corresponding secondary and tertiary analogues); and the pH, which has an effect on reoxidation of polyoxometalate to close the catalytic cycle by dioxygen or other oxidising agents. This is normally the rate determining step for the photocatalytic cycle.

In order for a photocatalyst to be practically useful it must have a high turnover number; that is “the number of events that the overall reaction (the photochemical transformation) includes during a photocatalytic cycle”.[41] Essentially this means that the catalyst must be able to undergo all of the processes highlighted in Fig 1.3.3 (one turnover) many times without any degradation of the pathway or poisoning of the catalyst occurring. It is a measure of the number of moles of substrate that a catalyst can degrade before it becomes deactivated. Most turnover numbers are in the region of 10^1 to 10^4 but some very efficient enzymes have values exceeding several million. The turnover number of polyoxometalates in solution is quite high, and in many cases the reaction simply proceeds until all the substrate has been used up. For example, in the case of the photooxidation of toluene by the metal-substituted $[Ru(II)\text{-}(DMSO)_3Mo_7O_{24}]^{4-}$ the POM was demonstrated to be stable up to 700 turnovers.[133] This is due to the ease of reversibility of the first few redox steps.

1.3.4 – Working example polyoxotungstate photoreactor:

The production of a functioning photoreactor exploiting the Keggin ion $[SiW_{12}O_{40}]^{4-}$ (tungstosilicic acid) has been reported by Muradov and Raissi.[42] This reactor incorporated an array of fused silica tubes 1 m long filled with $H_4[SiW_{12}O_{40}]$. A variety of simple organic species such as sugars, alkanes and alcohols were used as “fuel” and the decomposition measured by the amount of H_2 gas produced. The addition of colloidal platinum (Pt_C, optimum concentration 2-20 μM) was reported to increase the efficiency by one order of magnitude in preliminary experiments. It was found that substrate degradation was more efficient in the presence of trace amounts of Pt than without; and that hydrogen evolution was dependant on the strength of the C-H bonds in each molecule. Therefore alcohols gave higher levels of H_2 generation, while alkanes had low efficiency. The average solar-to-hydrogen conversion efficiency of the system was estimated to be approximately 2%. It is important to note that this system was not electrochemical.

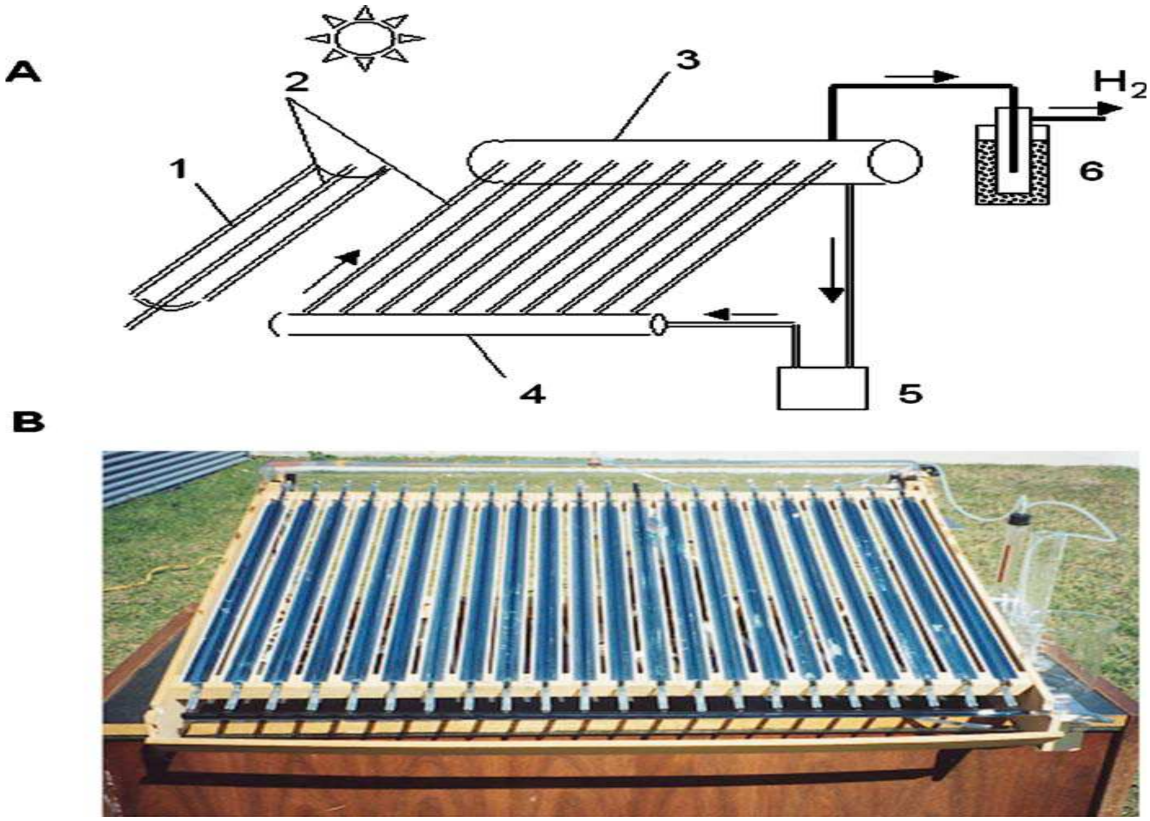

Fig 1.3.4: Functioning $[SiW_{12}O_{40}]^{4-}$ based photoreactor employing organic substrates as 'feedstocks' for H_2 evolution. 1: Trough with reflective surface, 2: Fused silica reactor tubes containing $[SiW_{12}O_{40}]^{4-}/Pt_C$, 3: Gas collection chamber, 4: Distribution manifold, 5: Pump, and 6: Ice trap. Reproduced from [52].

It is one of the primary goals of this project that we harness substrate oxidation and photocurrent production of polyoxometalates in one system; and that the use of a visible sensitizer would increase the overall catalytic efficiency. The main drawback of the above system is that its efficiency is inherently low due to the UV absorption spectrum of the ground state polyoxometalate, particularly in climates without intense sunshine. Only a relatively small percentage of incident solar photons can be absorbed by the polyoxometalate, and only a small percentage of those will be converted to harnessed energy. Hence it is extremely desirable to couple an effective visible sensitizer to the polyoxometalate. It is vital however that the sensitizer itself is stable against photodegradation or else the photocatalytic cycle would be broken. An overview of optically interesting molecules that have been investigated as sensitizers or charge transfer counterions for polyoxometalates is given in section 1.3.2.

1.4: Ru polypyridyl complexes and their supramolecular chemistry:

1.4.1 – Ru polypyridyl complexes and supramolecular chemistry:

Ruthenium is a second row transition metal (TM) which forms complexes of co-ordination number 6 with polypyridyl ligands when in the Ru (II) oxidation state. The prototypical example is Ru (II) tris-2, 2-bipyridine, or $[Ru(bpy)_3](X^-)_2$ for short, where X is an anionic counterion such as Cl^- or PF_6^-. The complex exhibits D_3 symmetry and the two optical isomers of the complex, Δ and Λ, are photophysically and electrochemically identical and are generally omitted when naming the complex. Ru (II) polypyridyl complexes are well known for their ability to absorb in the visible region, their intense and long lived phosphorescence and their reversible electrochemistry. These properties make them ideal candidates for a wide range of optical technologies and the photophysics of $[Ru(bpy)_3]^{2+}$ and related compounds has thus been studied extensively.[43, 44]

The energy of low lying antibonding orbitals on the bipyridine ligands facilitates their direct optical population from the occupied Ru t_{2g} orbitals, which is manifest by the appearance of the characteristic MLCT absorption band in the visible region of the electronic spectrum (centered around 450 nm for $[Ru(bpy)_3]^{2+}$). Photon absorption at 450 nm results in the electronic population of a vibrationally hot S_1 state which, after vibrational relaxation, is succeeded by ultrafast intersystem crossing (ISC) to the T_1 state with $k_{ISC} \approx 300$ fs and a probability of unity.[45] This is the long lived state from which phosphorescence occurs. ISC is a spin forbidden isoenergetic process which is facilitated by the presence of the heavy Ru nucleus. The total amount of time that an complex spends in the excited state before returning to the ground state is its lifetime, denoted τ. Photophysical parameters such as the wavelengths of absorption and phosphorescent emission, the luminescent lifetime, and other excited state processes such as electron transfer, are heavily dependant on a wide range of external factors. These include solvent polarity, temperature and the presence of oxygen.

The excited state of ruthenium complexes is often sufficiently long-lived to facilitate both inter and intramolecular processes such as electron transfer and energy transfer. A well known example of electron transfer from a Ru complex excited state is in a Grätzel cell when the Ru complex absorbs a photon in the visible which is injected into the conduction band of the

TiO_2.[5] Some of the fundamental photophysical processes that $[Ru(bpy)_3]^{2+}$ can undergo are shown in Fig 1.4.1.

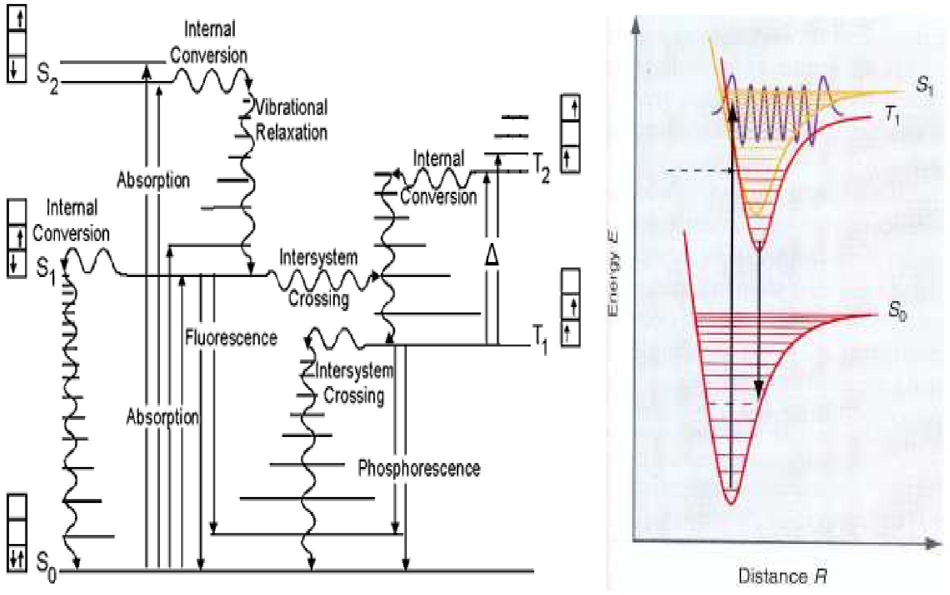

Fig 1.4.1: Jablonski diagram outlining electronic excitation and some of the deactivation pathways for the $[Ru(bpy)_3]^{2+}$ ion (left). The $T_1 \rightarrow T_2$ transition is thermally activated. Potential energy diagram showing the isoenergetic nature of intersystem crossing (right). Reproduced from [46].

The Jablonski diagram in Fig 1.4.1 outlines some of the photophysical pathways open to an excited electron in the $[Ru(bpy)_3]^{2+}$ ion. Initial excitation from the ground S_0 state results in the population of a vibrationally hot S_1 state. From this unstable state the molecule sheds excess energy via vibrational relaxation ie: energy transfer, in the form of heat, by collision with neighboring molecules. This is an equilibrium process by which the molecule relaxes into vibrational equilibrium with its surroundings. The forbidden process of ISC may occur only if the excited electron occupies a vibrationally hot S_1 state which is both isoenergetic and geometrically equivalent to a vibrationally hot T_1 state (see dotted arrow, Fig 1.4.1 right). The probability of ISC depends on a wide range of factors but since it is forbidden its probability is usually inherently low. However ISC is greatly favoured due to the heavy atom effect, and the probability of ISC occurring is dependant on the fourth power of the number of protons in the metal in the system (a Z^4 dependence). This means that ISC and hence phosphorescence is seen much more commonly in molecules containing a metallic or otherwise heavy nucleus; and in $[Ru(bpy)_3]^{2+}$ the probability of ISC occurring is one. From the bottom of the T_1 state many intramolecular processes, such as electron transfer and collisional energy transfer, can occur. This is also the state from which thermal population of a dissociative ^{3}MC state (the T_2 state shown in Fig 1.4.1) can occur, which leads to ligand exchange in solvents such as acetonitrile. Long-lived phosphorescence also occurs from the T_1 state. The Φ of phosphorescence of $[Ru(bpy)_3]^{2+}$ in H_2O at 25ºC is ~ 4.2 %, making thermal deactivation of T_1* to S_0 the dominant process.[47]

1.4.2 – Transition metal polypyridyl complex/polyoxometalate systems:

Investigation into the interaction between Ru (II) complexes and polyoxometalates is a relatively new endeavor, except for one notable exception published over 20 years ago. This first work in this area was conducted by Ballardini *et al*, who investigated the intramolecular electron-transfer rates between the polyoxotungstates $[Mn(OH)PW_{11}O_{39}]^{6-}$ or $[Co(H_2O)SiW_{11}O_{39}]^{6-}$ and $[Ru(bpy)_3]^{2+}$. The authors observed that changing the polyoxotungstate and Ru complex allowed them to tune the electron transfer properties of the system in solution. K_a values for both POW ions with $[Ru(bpy)_3]^{2+}$ were calculated and values of 7.4 x 10^4 for the Mn POW and 5.4 x 10^4 for the Co POW were obtained. These values were calculated from quenching data in the presence of excess Ru, and hence are for the 1:1 associated species only. This study concentrated primarily on fitting quenching data to various models; however the group did not isolate the associated species in the solid state.[48]

Hultgren *et al* have reported the synthesis of solid $[Ru(bpy)_3]_2[S_2Mo_{18}O_{62}]$.[49] It was reported that the redox properties of both the Dawson polyoxomolybdate and $[Ru(bpy)_3]^{2+}$ changed very slightly upon association in a 0.1 M $(Bu_4N)PF_6$ solution of DMF. SEM images showed an amorphous mesoporous structure when adhered to a surface. Inspiration for the synthesis of this compound was based on the multilayer work involving $[Os(bpy)_3]^{2+}$ and $[P_2Mo_{18}O_{62}]^{6-}$ of Anson *et al* (see multilayers section 1.5.2).[50]

The report of the synthesis of $[Ru(bpy)_3]_2[S_2Mo_{18}O_{62}]$ led to investigations of the photophysics of the ion-pair both in solution and in the solid state. Keyes *et al* observed that the associated species displayed a new feature in its electronic difference spectra centered at ~ 480 nm. This new transition was assigned to an inter-complex charge transfer transition by resonance Raman spectroscopy under 488 nm excitation, as polyoxometalate modes were enhanced at this wavelength where the fully-oxidized polyoxometalate anion does not absorb.

The association between the two complexes was electrostatic in nature, as demonstrated by luminescence quenching measurements. The 2:1 adduct exhibited a reasonably high association constant ($K_a = 4 \times 10^5$) but it is worth noting that in the case of the 1:1 complex $\{[Ru(bpy)_3]^{2+}$---$[S_2Mo_{18}O_{62}]^{4-}\}$ this figure was reduced to 3×10^4, which is close to the K_a values of the 1:1 complexes obtained by Ballardini *et al* (*vide supra*).[48] It was observed that $[Ru(bpy)_3]^{2+}$ exhibited remarkable photostability as part of the associated species, relative to free $[Ru(bpy)_3]^{2+}$ in solution. The adducts also displayed weak luminescence which was red-shifted with respect to the parent complex, and excitation spectra confirmed that this new emission arose from the new absorption band seen in the visible spectrum. Transient absorption spectroscopy revealed the existence of a short-lived charge-separated $[Ru(III)\text{-}(bpy)_3]^{3+}$-$[S_2Mo_{18}O_{62}]^{5-}$ state, shown in Fig 1.4.2.[51]

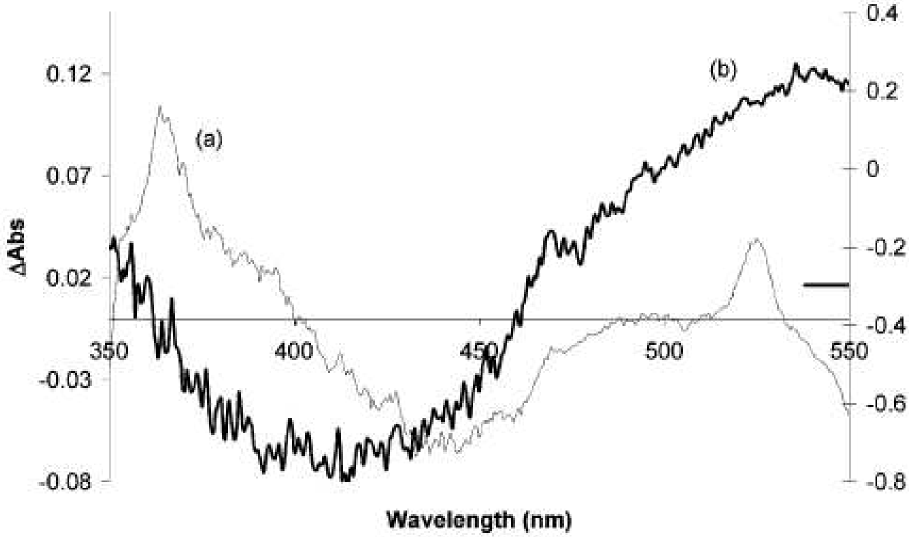

Fig 1.4.2: Transient absorption spectra of (a) $[Ru(bpy)_3](Cl)_2$ and (b) $[Ru(bpy)_3]_2[S_2Mo_{18}O_{62}]$ in MeCN 20 ns after excitation. Excitation wavelength was 355 nm.[51]

The investigation of the corresponding tungstate derivative, $[Ru(bpy)_3]_2[S_2W_{18}O_{62}]$, was later carried out by Seery *et al.* The photophysics proved to be similar to those for $[Ru(bpy)_3]_2[S_2Mo_{18}O_{62}]$ as a statically associated species again was formed, displaying significant $[Ru(bpy)_3]^{2+}$ luminescence quenching. In this case the charge transfer state was not observed in the transient absorption and this was attributed to the lower reduction potential of the tungstate relative to the molybdate (i.e.: the ΔG of intramolecular electron transfer was less negative). Temperature dependant luminescence measurements yielded values of E_a from the Arrhenius equation and demonstrated that the E_a value for $[Ru(bpy)_3]_2[S_2Mo_{18}O_{62}]$ was an order of magnitude lower than that for free $[Ru(bpy)_3]^{2+}$ (where E_a is the energy in cm^{-1} required to populate the ^{3}MC state from the ^{3}MLCT state). The ^{3}MC state is antibonding with respect to the Ru-N bond and leads to photodissociation in solvents that can act as ligands, such as MeCN. The Arrhenius equation relates the combined rate of radiative and non-radiative decay, k_0, to the temperature. The K_a values for the 2:1 and 1:1 associated clusters were 1 x 10^6 and 7.7 x 10^5 respectively, an order of magnitude higher than those observed for the corresponding molybdate (*vide supra*). The study concludes that the presence of $[S_2W_{18}O_{62}]^{4-}$ distorts the $[Ru(bpy)_3]^{2+}$ energy levels and hence the thermally populated ^{3}MC state is inaccessible in the associated species.[52]

A later study by Seery *et al* employing $[Ru(bpy)_3]^{2+}$ and a variety of substituted polyoxotungstates investigated the effects of increasing polyoxometalate charge on $[Ru(bpy)_3]^{2+}$ associations.[53] It was found that $[P_2W_{17}O_{61}(FeOH_2)]^{7-}$, $[P_2W_{17}O_{61}(FeBr)]^{6-}$ and $[P_2W_{17}O_{61}]^{10-}$ all formed fully charge-compensated adduct species with $[Ru(bpy)_3]^{2+}$, as demonstrated by elemental analysis of the solids. Surprisingly, there was no correlation in the size of the association constants and the charge on the POW. In fact $[P_2W_{17}O_{61}]^{10-}$ displayed a much lower K_a value with $[Ru(bpy)_3]^{2+}$ than did $[P_2W_{17}O_{61}(FeOH_2)]^{7-}$ and $[P_2W_{17}O_{61}(FeBr)]^{6-}$ (four to five orders of magnitude smaller), and this huge reduction was attributed to the steric difficulty of forming a complex unit of 5:1 stoichiometry. The Rehm-Weller expression was used to assess if the exoergonicity of a Ru to POW electron transfer was related to the differences in polyoxometalate charge and association constants, but the thermodynamics of all three systems were predicted to be very similar. Interestingly the resonance Raman spectrum of the 5:1 complex $[Ru(bpy)_3]_5[P_2W_{17}O_{61}]$ showed no polyoxotungstate modes under 488 nm excitation, even though the complex showed a new transition at that wavelength in the UV/Vis difference spectra. The other two adducts $[Ru(bpy)_3]_{3.5}[P_2W_{17}O_{61}(FeOH_2)]$ and $[Ru(bpy)_3]_3[P_2W_{17}O_{61}(FeBr)]$ had much higher association constants and showed significant polyoxotungstate participation in the ~ 480 nm transition.

A similar study of the photophysics of clusters between the polyoxotungstates α-$[P_2W_{18}O_{62}]^{6-}$ and α_2-$[P_2W_{17}O_{61}(FeOH_2)]^{7-}$ with $[Ru(bpy)_3]^{2+}$ and $[Ru(bpy)_2(Mebpy\text{-}py)]^{2+}$ revealed that the bulky Mebpy-py ligand had a detrimental effect on quenching. The study also revealed that the formation of an electrostatic adduct between $[Ru(bpy)_2(Mebpy\text{-}py)]^{2+}$ and α_2-$[P_2W_{17}O_{61}(FeOH_2)]^{7-}$ was favoured over the formation of a co-ordination bond between the ligand free pyridyl nitrogen and the POW lacunary Fe atom. This is reflected generally in the exceptionally high K_a values for the electrostatic salts.[54]

In the last few years several more studies of Ru complex-polyoxometalate photophysics have been reported. In a study employing the Keggin polyoxometalate $[PW_{12}O_{40}]^{3-}$ as a quencher to $[Ru(bpy)_3]^{2+}$ it was discovered that the I_0/I Stern-Volmer plot curved upward in MeCN. The authors attributed this to very fast quenching process within the ion-pair, but without kinetic data to measure the effects of $[PW_{12}O_{40}]^{3+}$ concentration on $[Ru(bpy)_3]^{2+}$ τ values this model could not be confirmed. Interestingly, the authors obtained crystal structures of $K_5\{[Ru(bpy)_3][PW_{11}O_{39}]\}$ and $K\{[Ru(bpy)_3][PW_{12}O_{40}]\}$ from the 1:1 reaction between $[Ru(bpy)_3]^{2+}$ and $[PW_{11}O_{39}]^{7-}$ or $[PW_{12}O_{40}]^{3-}$. Crystal structures of polyoxometalate/transition metal complex electrostatic clusters are very rare, and since the high K_a values suggest that formation of electrostatically neutral clusters is favoured it is interesting to see the use of a 1:1 mixture in crystallization in this case.[55] Surprisingly, in a different study where solutions of the ratio 1 $[Ru(bpy)_3]^{2+}$: 2 $[PW_{12}O_{40}]^{3-}$ were employed a solid, non-crystalline precipitate was obtained. This solid was analyzed by EDX spectroscopy and the stoichiometry was demonstrated to be $[Ru(bpy)_3]_{1.5}[PW_{12}O_{40}]$. These two studies together may indicate that obtaining crystal structures of Ru/polyoxometalate clusters is more likely when employing 1:1 ratios only.[56]

The charge-transfer character of the polyoxometalate/Ru adducts has been investigated by Fay *et al.*[57] The photochemistry of the associated species $[Ru(bpy)_3]_2[S_2Mo_{18}O_{62}]$ and $[Ru(bpy)_3]_2[S_2W_{18}O_{62}]$ were compared with the photochemistry of $[S_2Mo_{18}O_{62}]^{4-}$ and $[S_2W_{18}O_{62}]^{4-}$ with optically inactive counterions to observe the sensitization effects. It was found that at 420 nm, where $[S_2Mo_{18}O_{62}]^{4-}$ only very weakly absorbs, the quantum yield of polyoxomolybdate photoreduction of BnOH was increased by a factor of 40. Given this increase in quantum yield it was assumed that an increase in photo-electrochemical current generation would be seen under white light irradiation, but a decrease was actually observed when $[Ru(biq)_2(box)]^+$ was used as a sensitizer. This decrease was attributed to competitive absorption from Ru at low wavelengths. The reduction in photocurrent was more drastic in the tungstate than the molybdate. The use of $[Ru(biq)_2(box)]^+$ as a sensitizer resulted in a larger decrease in current generation despite the fact that it displays absorption bands covering more of the visible spectrum. The photophysics of this ion in the presence of $[S_2Mo_{18}O_{62}]^{4-}$ have not been reported and these two ions may only weakly interact, though why they interact differently is not precisely known. However $[Ru(biq)_2(box)]^+$ has a shorter lifetime than most other Ru (II) polypyridyl complexes and a low quantum yield of phosphorescence so either of these properties may render it a poor candidate for polyoxometalate photosensitization.

In another photochemical study of polyoxometalate/$[Ru(bpy)_3]^{2+}$ hybrid salts both $[Ru(bpy)_3][Mo_6O_{19}]$ and $[Ru(bpy)_3]_2[W_{10}O_{32}]$ were synthesized and isolated by centrifugation.[58] As a general rule, it has proven extremely difficult to obtain single crystals of the hybrid materials for X-ray structure analysis. Methylene blue (MB) was also employed as an organic sensitizer and $[MB]_4[W_{10}O_{32}]$ was also isolated. The ruthenium composites were dissolved in water buffered with carbonate (pH = 10.5) which has not been reported previously, possibly due to the exceptionally low solubility of the adducts in water. Homogeneous photocatalysis of phenol in water was carried out at $\lambda > 375$ nm, and it was shown that the 1:1 associated species $[Ru(bpy)_3][Mo_6O_{19}]$ had a higher catalytic response than $[Ru(bpy)_3]_2[W_{10}O_{32}]$. This may be due to the nature of the 1:1 species, which has not been photophysically analyzed previously or may simply be due to the generally higher catalytic activity of molybdates due to their more positive reduction potentials. However the use of buffer is a cause for concern, as our own studies have demonstrated that addition of electrolyte to Ru/Dawson polyoxometalate electrostatic ion-clusters can result in disruption of electrostatic communication.

Recently, the photophysics of $[Ru(bpy)_3]^{2+}$ in the presence of the Dawson-like sulfite containing polyoxomolybdates α/β-$[Mo_{18}O_{54}(SO_3)_2]^{4-}$ has been reported. It was found that the polyoxomolybdate anions were not sensitized by $[Ru(bpy)_3]^{2+}$ under visible irradiation, and this was attributed to their more negative reduction potentials relative to α-$[Mo_{18}O_{54}(SO_4)_2]^{4-}$. The clusters also exhibited mixed static/dynamic quenching, which has not been observed previously in studies of similar systems.[59] These data are discussed in greater detail in Chapter 3. The voltammetry of $[Ru(bpy)_3]_2\alpha/\beta$-$[Mo_{18}O_{54}(SO_3)_2]$ and $[Ru(bpy)_3]_2\alpha$-$[W_{18}O_{54}(SO_3)_2]$ in both organic solvents and ionic liquids (ILs) has also been reported. It was observed that in the presence of ILs that more polyoxometalate based redox processes were observed and that the redox processes were shifted positive by several hundred mV relative to those processes in organic electrolyte.[60] These two studies have contributed significantly to the understanding of photophysical and voltammetric processes of these types of clusters.

Other studies on Ru complex/polyoxometalate associated species have generally focused on electrochemistry both in solution and in the solid state. The syntheses of $[Ru(bpy)_3]_3[P_2W_{18}O_{62}]$ and $[Os(bpy)_3]_3[P_2W_{18}O_{62}]$ have been reported.[61, 62] The authors used ^{31}P-NMR, UV/Vis and FTIR spectroscopy to characterize the systems. The FTIR spectra demonstrated that the terminal stretching modes of both ions were unchanged upon association. These spectroscopic data revealed that the interactions between $[Ru(bpy)_3]^{2+}$/$[Os(bpy)_3]^{2+}$ and α/β-$[P_2W_{18}O_{62}]^{6-}$ were weak, which is in contrast to FTIR data in other Ru/polyoxometalate electrostatic systems reported.[55, 59] SEM images of $[Ru(bpy)_3]_3[P_2W_{18}O_{62}]$ attached to a glassy carbon electrode were obtained and are shown in Fig. 1.4.3.

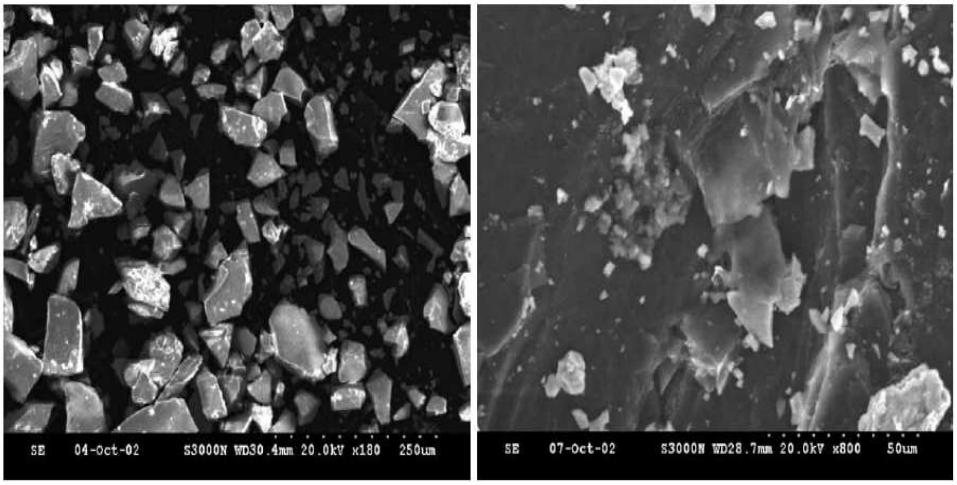

Fig 1.4.3: SEM images of $[Ru(bpy)_3]_3[P_2W_{18}O_{62}]$ before (left) and after (right) voltammetric cycling in 1.0 M $HClO_4$. Electrode area = 0.0707 cm^2, scan rate = 10 $mV.s^{-1}$. Reproduced from [61].

The SEM images show that before cycling in acid the $[Ru(bpy)_3]_3[P_2W_{18}O_{62}]$ material exists as a random array of particles that electrocrystallize upon acidic cycling to form bulk plate-like crystals. Differences in the cyclic voltammetry before and after cycling confirmed that a change in layer structure has occurred. Interestingly this result was not observed in neutral electrolyte. Similar results were seen when $[Os(bpy)_3]_3[P_2W_{18}O_{62}]$ was investigated under the same conditions. Initial EDX spectra of the newly formed crystalline material confirmed the presence of osmium, tungsten, phosphorous, oxygen and carbon; however hydrogen was not detected due to its low atomic number. There was no mention of chlorine detection in the crystal, indicating that the material may still be analytically pure $[Os(bpy)_3]_3[P_2W_{18}O_{62}]$ which does not contain ClO_4^- electrolyte. Future work on the mechanism of electrocrystallization has yet to be reported.

Zhang *et al* have performed electrocatalytic experiments employing the Keggin polyoxomolybdate isomers α-$[SiW_{12}O_{40}]^{4-}$ and β-$[SiW_{12}O_{40}]^{4-}$ and nitrite substrate.[63] A thin film of the reduced form of the α-isomer α-$[SiW_{12}O_{40}]^{5-}$ was found to have greater catalytic activity towards HNO_2 than the β-isomer when immobilized on a glassy carbon electrode. A modified layer of $[Ru(bpy)_3]_2\alpha$-$[SiW_{12}O_{40}]$ was also investigated for catalytic activity (the corresponding β-isomer was not examined at this stage). This layer was formed by dip-coating a GC electrode into a solution of polyoxometalate then cycling it in a solution of $[Ru(bpy)_3]^{2+}$ and Na_2SO_4, which formed a water-insoluble layer of $[Ru(bpy)_3]_2\alpha$-$[SiW_{12}O_{40}]$. Under these conditions the counter-ions precipitated out and were removed. The catalytic behavior of this material was increased at low pH, which was not observed in the parent ion α-$[SiW_{12}O_{40}]^{4-}$. It was observed that a thin film of $[Ru(bpy)_3]_2\alpha$-$[SiW_{12}O_{40}]$ was not formed on the electrode but rather an array of microcrystals. This could affect the voltammetry of the solid due to diffusion through the bulk material.

Although crystal structures of transition metal complex/polyoxometalate adducts are notoriously hard to obtain there have been a few examples of success in this area. As discussed previously, 1:1 electrostatic crystalline adducts between Keggin polyoxometalates and $[Ru(bpy)_3]^{2+}$ have been obtained.[55] The synthesis and crystal structure of $[Ru(bpy)_3]_2[W_{10}O_{32}]$.3DMSO has also been reported by Han *et al*;[64] however their attempts to obtain crystal structures for the related $[Ru(bpy)_3][W_6O_{19}]$ and $[Ru(bpy)_3]_2[Mo_8O_{26}]$ salts were unsuccessful. X-ray structure data indicated that the RuN_6 octahedron is slightly distorted and this was attributed to hydrogen bonding between the bipyridine protons and the terminal oxygen atoms of the anion. A broad feature at 3438 cm^{-1} in the FTIR spectrum of the solid ground in KBr was attributed to intramolecular hydrogen bonding. The X-ray structure of $[Ru(bpy)_3]_2[W_{10}O_{32}]$.3DMSO is shown in Fig. 1.4.4. Knaust *et al* have reported the crystal structure of a molecular host-guest system based on a copper hexamer with "bowl" shaped cavities.[65] Two $[PM_{12}O_{40}]^{3-}$ (M = Mo, W) units were found to occupy the bowl spaces, yielding a molecular entity of the form $[Cu_6(phen)_8(MeCN)_4]_2[PM_{12}O_{40}]$ (M = Mo or W). It was speculated that the orange colour of the crystals was due to some charge transfer character based on a Cu(I) d^{10} – W (VI) d^0 interaction as previously synthesized related composites were yellow.

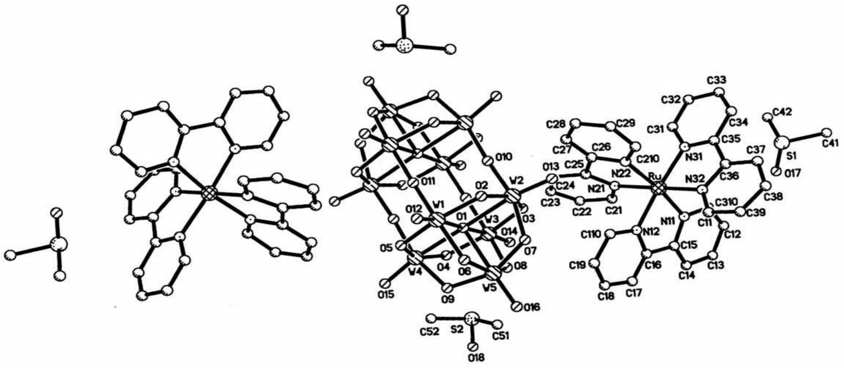

Fig 1.4.4: Crystal structure of $[Ru(bpy)_3]_2[W_{10}O_{32}]$.3DMSO. Reproduced from [64].

Many polyoxometalate/dye composite materials have also been synthesized hydrothermally. This is when very high vapour pressures and temperatures are employed during the synthesis, and it is performed in a sealed pressure vessel. This is a very popular emerging area in synthetic polyoxometalate chemistry. For example $[Zn(bpy)_3]_2[V_4O_{12}].11H_2O$ has been crystallized successfully by reacting at 170 °C for 68 hours in a sealed vessel under autogenous pressure (up to 15 atm).[66] This study also contains a report of the synthesis of the related $[Zn(bpy)_2]_2[V_4O_{12}]$, which formed a covalently bonded single molecule as the Zn atoms simply co-ordinated to two oxygen atoms on either side of the $[V_4O_{12}]^{4-}$ framework. More recently $[Cu_4(bmte)_{3.5}][SiW_{12}O_{40}]$ and $[Cu_4(bmtp)_4][SiW_{12}O_{40}]$ (where bmte = 1,2-bis(1-methyl-5-mercapto-1,2,3,4-tetrazole)-ethane, and bmtp = 1,5-bis(1-methyl-5-mercapto-1,2,3,4-tetrazole)pentane]) have been hydrothermally prepared. It was discovered that the tetrazole N atoms bond strongly to peripheral tungstate oxygen atoms and that the crystal structures can be controlled by altering the ligands.[67] As well as Cu (I) complexes, Ag (I) complexes are also becoming increasingly popular in hydrothermal polyoxometalate composite synthesis. This is mainly due to their versatility under hydrothermal conditions and their ability to form 1D, 2D and 3D chains in the crystal lattice with polyoxometalates. $\{[Ag(bpy)]_2[P_2W_{18}O_{62}]\}\cdot 2[H_2bpy]\cdot 4H_2O$, $\{[Ag(bpy)]_4[P_2W_{18}O_{62}]\}\cdot 2[Hbpy]$ and $K[P_2W_{18}O_{62}]\cdot_{2.5}[H_2bpy]\cdot 2H_2O$ have all been synthesized, with the different ratios controlled by the pH of the hydrothermal syntheses.[68] The authors of this study concluded that the co-ordination geometry and sterics of the TM complex are important in determining the synthetic outcome of hydrothermal syntheses. Very recently the hydrothermal synthesis of $\{[Cu_6(PO_4)_2(H_2O)_4(phen)_6]^{6+}\text{-}[P_2W_{18}O_{62}]^{6-}\}$ has been reported.[69] This composite material had a Cu-polyoxotungstate charge-transfer band at 690 nm, and the system displayed good photocatalytic activity towards methyl orange. The catalyst was also easily recoverable from the reaction solution after use.

In summary, the field of TM complex/polyoxometalate composite synthesis by hydrothermal methods is becoming increasingly popular at present and a broad review of this area would be beyond the scope of this thesis. Although the synthesis of these hybrid materials is interesting in itself, it is not of significant relevance to this project as the LBL multilayer formation approach requires conditions a lot less extreme than those involved in hydrothermal synthesis. A detailed review article of the synthesis of these hybrid materials has been published recently.[70]

1.4.3 - Coupling photoactive organic molecules to polyoxometalates:

Attempts have been made to couple organic ions to polyoxometalates electrostatically in order to exploit their useful optical properties. For example the Lindqvist $[M_6O_{19}]^{2-}$ and Keggin $[SiM_{12}O_{40}]^{4-}$ (M = Mo, W) anions have been co-crystallized with planar arene cations such as pyrenes and anthracenes, modified with cationic side chain groups.[71] This was one of the most extensive cases of polyoxometalate/dye charge-transfer crystallizations reported to date with seven separate species characterized. The crystals obtained were intensely colored, and were characterized by X-ray diffraction. These materials exhibited new bands in the diffuse reflectance UV/Vis spectra that were not present in the parent ion spectra and hence are assigned to be CT transitions. The CT nature of the transitions was confirmed by Mulliken theory as the wavelength of the transition red-shifted with corresponding lowering of polyoxometalate reduction potentials. The location of the bands was also dependant on the CT distance between the two moieties, as shown by X-ray crystallography of two different polymorphs of the same composition. Transient absorption measurements yielded kinetics of back electron transfer and provided further evidence for CT. In another study by Zhang *et al* the intensity of the CT transition between $[SiMo_{12}O_{40}]^{4-}$ and 2,2'-dipyridylamine cations was dependant on the intermolecular distance obtained from X-ray crystal data.[72]

A variety of electrostatic polyoxometalate/organic cation charge-transfer (CT) composites have been synthesized. For example the synthesis of $(2A5NP)_4H_3[PMo_{12}O_{40}]\cdot 2.5H_2O\cdot 0.5C_2H_5OH$ (where 2A5NP = 2-amino-5-nitropyridine) has been reported.[73] The structure was confirmed by X-ray crystallography and elemental analysis. The compound displayed CT character in the visible region, manifested in a new feature > 530 nm which is not present in the parent ion spectra. Protonated 7-methyl quinoline and $[GeMo_{12}O_{40}]^{4-}$ have been used to synthesise the $[C_{10}H_{10}N]_4[GeMo_{12}O_{40}].6DMF$ adduct.[74] Low-temperature EPR spectra demonstrated the existence of a radical electron delocalization over the Mo atoms in the photoreduced sample. This was attributed to a methyl quinoline to POM charge transfer transition. Another example of a polyoxometalate/organic compound CT salt was reported by Xie *et al.*[75] Pararosaniline ($[C_{19}H_{18}N_3]^+$) was used as a cation for the polyoxometalates $[S_2Mo_{18}O_{62}]^{4-}$, β-$[Mo_8O_{26}]^{4-}$, α-$[CoW_{12}O_{40}]^{6-}$ and α-$[ZnW_{12}O_{40}]^{6-}$. The association between the organic fluorophore and anionic polyoxometalate was investigated using luminescence quenching methods. Addition of $[S_2Mo_{18}O_{62}]^{4-}$ to a solution of $[C_{19}H_{18}N_3]^+$ resulted in quenching of the fluorescence at 610 nm. Excitation spectra of solutions of $[(Bu_4N)]_4[S_2Mo_{18}O_{62}]$ and $[C_{19}H_{18}N_3]_4[S_2Mo_{18}O_{62}]$ (Fig 1.4.5, shown below) revealed that different wavelengths were responsible for the two different emission profiles, ie: the electronics of the emitting dye were affected significantly upon association with the polyoxometalates. This indicates that there are two emitting species in solution and that the interaction between the two ions is significant. This is similar to what was observed in studies by our group involving $[Ru(bpy)_3]_2[S_2Mo_{18}O_{62}]$ and $[Ru(bpy)_3]_2[S_2W_{18}O_{62}]$ (*vide supra*).[51, 52]

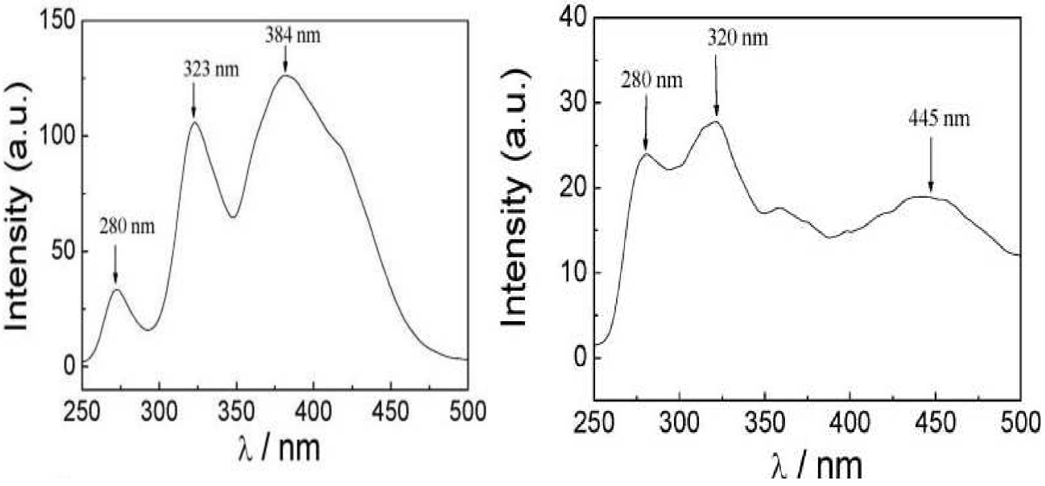

Fig 1.4.5: Excitation spectra of $[C_{19}H_{18}N_3]^+Cl^-$ in DMF (6.0×10^{-4} M) for 610 nm emission (left); and $[C_{19}H_{18}N_3]_4[S_2Mo_{18}O_{62}]$ in DMF (2.5×10^{-5} M) for 590 nm emission (right). Reproduced from [75].

Two recent studies involving organic cationic dyes and polyoxometalates have been reported. Guo *et al* demonstrated that pararosaniline (PR^+) and crystal violet can co-crystallize with the Lindqvist polyoxometalates $[M_6O_{19}]^{2-}$ (where M = Mo, W).[76] These materials displayed similar patterns in their electrochemistry to $[Ru(bpy)_3]_2\alpha/\beta\text{-}[Mo_{18}O_{54}(SO_3)_2]$, where the potential of the polyoxometalate reduction shifts positive by 400 mV in ionic liquid electrolyte. The crystallography of $[PR]_2[Mo_6O_{19}].6DMF$ showed the importance of multiple hydrogen bonds between the terminal polyoxometalate O atoms and the dye NH_2 groups. This extra stability may be the reason that crystal structures were obtained here, and not in our group's studies involving the Dawson polyoxometalates. In another study tetrathiafulvalene (TTF)/polyoxometalate composite materials have been electrocrystallized on a variety of substrates.[77] The film exhibited extremely high conductivity. This is one of the first examples of the formation of polyoxometalate/dye composites by controlled potential electrolysis.

1.4.4 – Coupling cationic organometallics and porphyrins to polyoxometalates:

Research into the synthesis of novel polyoxometalate-organometallic complex ion-clusters has also been carried out; for example ferrocene has been used to this affect as a counter-ion. Juraja *et al* have demonstrated that decamethyl ferrocene crystallizes with $[S_2Mo_{18}O_{62}]^{4-}$ as $[Fe(Cp^*)_2]_5[HS_2Mo_{18}O_{62}].3DMF.2Et_2O$.[78] The species has unusual charge separation characteristics, with a paramagnetic ferrocenyl portion and a diamagnetic POM portion identified by EPR spectroscopy. Magnetic interaction between the two ions is very weak in this case. In a separate study the ferrocene derivative $CpFeCpCH_2N^+(CH_3)_3$ has been isolated as a CT salt with the Lindqvist polyoxometalates $[M_6O_{19}]^{2-}$ where M = Mo, W.[79] Picosecond transient absorption measurements have shown that a short-lived $CpFe^+CpCH_2N^+Me_3$-$[Mo_6O_{39}]^{3-}$ CT state is formed. This state exhibited a new absorbance band centered at ~550 nm in the diffuse reflectance electronic spectrum. This is one of the best literature examples of a time-resolved spectrum confirming the charge separated excited state to date. The spectroscopy is shown in Fig. 1.4.6.

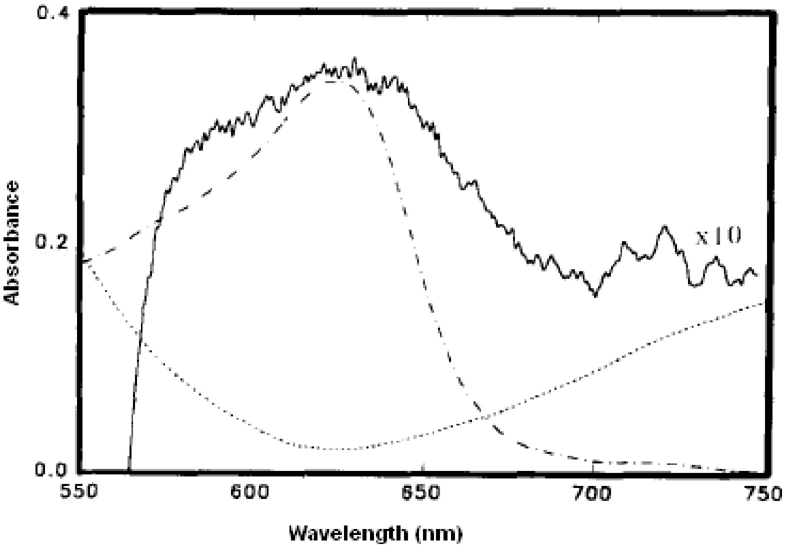

Fig 1.4.6: Transient absorption spectrum taken 25 ps after 532 nm excitation pulse of 10 % $[CpFeCpCH_2NMe_3]_2[Mo_6O_{19}]$ in neutral alumina (solid line, x 10). The reduced polyoxomolybdate acceptor $[Mo_6O_{19}]^{3-}$ (dashed) and oxidized ferrocenyl donor $CpFe^+CpCH_2N^+Me_3$ spectra (dots) are shown for comparison. Reproduced from [79].

In recent years macrocyclic porphyrin-based systems have also been employed as electrostatic sensitizers for polyoxometalates. It has been observed in solution that cationic porphyrins form stable electrostatic adducts with anionic polyoxometalates which display intramolecular charge-transfer characteristics, similar to those involving polyoxometalates and $[Ru(bpy)_3]^{2+}$. Porphyrins are not naturally cationic so substituted macrocycles were synthesized for this purpose by adding quaternary ammonium *N*-methylpyridine groups to each corner of the molecule. For example the tetramethylated Zn porphyrin $[ZnTMePyP]^{4+}$ has been investigated as a sensitizer for the sandwich polyoxometalate $[M_4(H_2O)_2(P_2W_{15}O_{56})_2]^{n-}$ (with n = 16 for M = Zn^{II}, Ni^{II}, and n = 12 for M = Fe^{III}).[80] The complexes exhibited fast intramolecular porphyrin to polyoxometalate quenching and high K_a values. The complex $[ZnTMePyP^{4+}]_3$-$[Fe_4(P_2W_{15}O_{56})_2]$ was also shown to be photoactive towards the reduction of Ag^+ ions in solution under visible irradiation. In another study by the same authors the polyoxotungstate αββα-$Na_{17}[Co_4(H_2O)(OH)(P_2W_{15}O_{56})_2]$ was effectively sensitized by zinc-*meso*-tetrakis(N-pyridinium)-β-octaethylporphyrin $[ZnOETPyP]^{4+}$ in solution to form Ag nanoparticles from dissolved Ag^+ ions.[81] An image of these nanoparticles is given in Fig 1.4.7. The group also studied the possibility of forming a co-ordination complex between 5, 10, 15-tritolyl-20-(3-pyridyl)porphyrin (H_2T_3P-3-Py) and the substituted Keggin polyoxometalates α-$[MSiW_{11}O_{39}]^{3-}$ (M = Co^{II}, Ni^{II}). Surprisingly K_a values of the order of 10^6 were obtained, which is of the same order as most electrostatic Ru complex/polyoxometalate composites reported *vide supra*.[82] In a previous study the interaction between $[Ru(bpy)_2(Mebpy\text{-}py)]^{2+}$ and α_2-$[P_2W_{17}O_{61}(FeOH_2)]^{7-}$ was determined to be purely electrostatic, even though a co-ordination binding mode was possible, it is somewhat surprising to see a co-ordination mode as strong as a typical electrostatic bond in this case.[54]

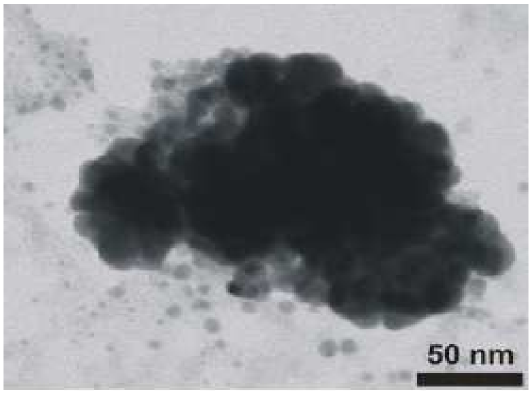

Fig 1.4.7: Ag nanoparticles formed by visible irradiation of 2 x 10^{-6} M $\{[Co_4(H_2O)(OH)(P_2W_{15}O_{56})_2]^{17-}$ - $[ZnOETPyP]^{4+}\}$ aqueous solution in the presence of 8 x 10^{-5} M Ag_2SO_4 (8 hours irradiation). Reproduced from [91].

1.5 – Polyoxometalate photoelectrochemistry and multilayer assemblies:

1.5.1 – Transition metal complex-polyoxometalate multilayer systems:

Multilayers often form as a consequence of physisorption at an interface. However very stable base layers can also be formed by chemisorption. Although the driving force for polyoxometalate multilayer formation is generally purely electrostatic, as the anionic polyoxometalates can be immobilised on any cationic surface, other methods can also be employed. For example, cationic pyridnium dyes have been covalently grafted onto a boron-doped diamond substrate (see Fig 1.5.1). The cationic charge of this initial layer was then used to drive bilayer formation with the anionic polyoxotungstate $[PW_{12}O_{40}]^{3-}$, and these films exhibited promising photoelectrochemistry.[83] Langmuir-Blodgett films of a variety of polyoxometalates and the dimethyldioctadecylammonium cation (DODA) have also been reported.[84] Although polyoxometalate photochemistry has been extensively studied in solution, studies of thin film photochemistry assembled on electrodes are relatively rare. Future solar energy applications would very likely be interfacial in nature so it is our goal to drive research forward in this area.

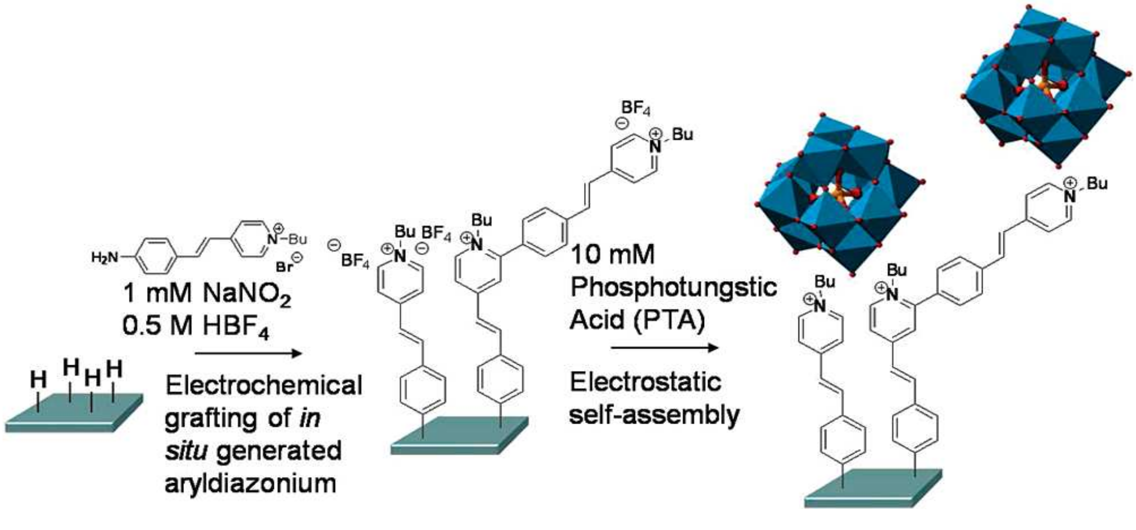

Fig 1.5.1: Electrochemical grafting of the molecular pyridinium dye followed by electrostatic self-assembly of the supramolecular architecture with $H_3[PW_{12}O_{40}]$. Reproduced from [83].

Anionic polyoxometalates can form stable electrostatic multilayers with cationic metal polypyridyl complexes. Anson *et al* have reported the formation of stable multilayers consisting of $[Os(bpy)_3]^{2+}$-$[P_2Mo_{18}O_{62}]^{6-}$ or $[Ru(bpy)_3]^{2+}$-$[P_2Mo_{18}O_{62}]^{6-}$ on various electrode surfaces (ie: glassy carbon, highly ordered pyrolytic graphite, indium tin oxide, and gold-coated quartz electrodes); and assemblies up to 8 bilayers thick were reported.[50] The layers were prepared by dip coating and were stable to multiple redox cycles. Multilayers of $[Fe(bpy)_3]^{2+}$-$[P_2Mo_{18}O_{62}]^{6-}$ have also been reported.[85] These layers were found to have electrocatalytic activity towards the reduction of nitrate, peroxide and bromate ions. The electrochemistry of the polyoxometalate moiety was shown to exhibit pH dependant behavior typical of this polyoxometalate in solution. Based on this work, Zynek *et al* constructed multilayers based on the mixed-metal polyoxotungstate $[P_2W_{17}V^{IV}O_{62}]^{8-}$ and a ruthenium pentaerythritol derivitised terpy metallodendrimer (see Fig 1.5.2) on glassy carbon electrodes.[86] This structure was chosen as it is fully charge-compensated relative to the $[POW]^{8-}$ anion. The multilayers were analyzed by electrochemistry, AFM and XPS. Up to 15 stable bilayers could be formed, as demonstrated by linear growth in cyclic voltammetry measurements. The permeability of ions through the multilayer to the electrode surface was shown to be dependant on the number of layers employed. The group concluded that the charge-compensated nature of the multilayers was responsible for their stability over long periods, which may be a very important observation with implications for future work. In another study a similar metallodendrimer, without any functionalization of the terpy ligands, was built into multilayers with $[P_2W_{18}O_{62}]^{6-}$ on quartz electrodes.[87] They noticed that the film exhibited negligible changes in voltammetry when stored in air for over a month. The films also displayed bifunctional electrocatalysis towards iodate and arsenate ions, so it is likely that POM/Ru metallodendrimer films are good candidates for stable films for electroanalysis. No photochemistry of either metallodendrimer based systems was performed.

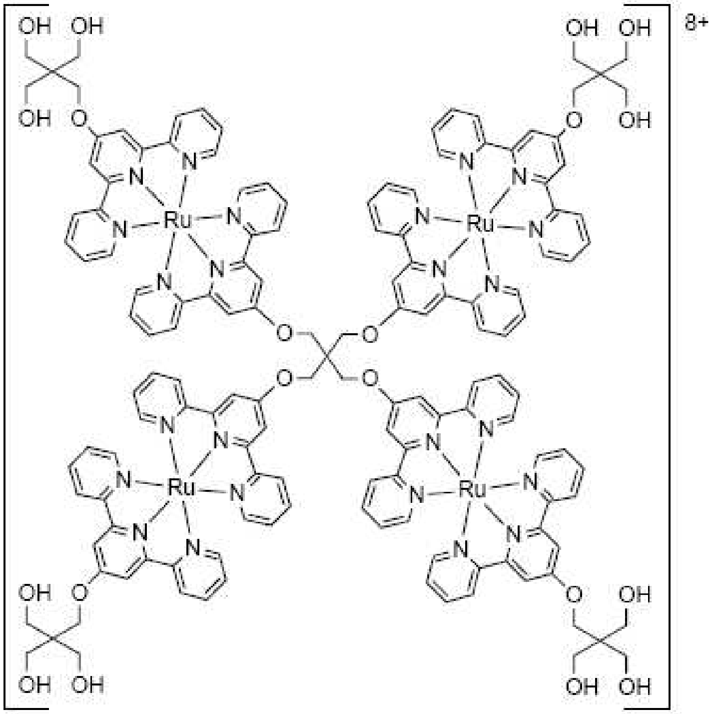

Fig 1.5.2: Structure of the Ru pentaerythritol-derivitised terpyridine metallodendrimers used as the counterion in multilayer formation with $[P_2W_{17}V^{IV}O_{62}]^{8-}$.[88]

The formation of multiply luminescent multilayers of $[Ru(bpy)_3]^{2+}$ and $[Eu(SiMo_9W_2O_{39})_2]^{13-}$ by alternating dip-coating onto poly(ethylenimine) coated quartz has also been described.[89] Interesting catalytic activity towards a variety of substrates was observed for the POW, with separate catalysis of $C_2O_4^{2-}$ ions by the $[Ru(bpy)_3]^{2+}$ also observed. The multilayers thus displayed electrocatalytic behavior of both parent complexes. Up to 50 stable bilayers were produced in this study. A linear growth of discrete layers was confirmed by UV/Vis spectroscopy and cyclic voltammetry. Multilayers of $[Ru(phen)_3]^{2+}$ and $[P_2Mo_{18}O_{62}]^{6-}$ on ITO electrodes have also been reported.[90] The initial POW layer was adhered to the surface by a layer of PEI (poly(ethyleneimine)), a cationic polymer that was deposited onto the quartz substrate. Linear growth was observed with each deposition cycle by UV and CV measurements. Surprisingly, given solution phase quenching experiments, the films retained the luminescent properties of the free $[Ru(phen)_3]^{2+}$; although a blue-shift was observed for the composite film. These films were also used in the electrocatalytic reduction of nitrite. Multilayers of $[Nd(SiW_9Mo_2O_{39})]^{13-}$ and the ruthenium dimer $[Ru(bpy)_2(BPBH)]^{4+}$ (where BPBH = 1,6 bis-(2-(2-pyridyl)benzimidazoyl)hexane) on quartz have also been produced.[91] The same Ru dimer has also been used in films of $[SiW_{12}O_{40}]^{4-}$ and an intramolecular charge-transfer band was seen at 471 nm in the composite film.[92] To our knowledge these are the only reported instance in which a Ru dimer has been employed in a multilayer assembly with a dimeric ruthenium complex.

Several other Ru complex/polyoxometalate multilayer studies have been performed, generally with a view to producing electrocatalytic films. In one instance, the Keggin POM $[PMo_{12}O_{40}]^{3-}$ and $[Ru(bpy)_3]^{2+}$ were fabricated into multilayers on ITO electrodes using PEI and PSS (poly (styrenesulfonate)), which is a commonly used polymer for binding electrostatic multilayers together.[93] In another study these ions were used to coat a carbon paste electrode (CPE). The modified electrode displayed bifunctional electrocatalytic activity towards both the reduction of hydrogen peroxide and bromate and also toward the oxidation of arsenite. The very low solubility of these materials meant the films were exceptionally stable.[94] In a different study the decatungstate anion, $[W_{10}O_{32}]^{4-}$, was used to build films with $[Ru(bpy)_3]^{2+}$ and PDDA (poly(diallyldimethylammonium chloride)). These films showed electrocatalytic activity towards the reduction of iodate and the oxidation of oxalate, which demonstrated the individual properties of the two parent ions. Moreover, the films exhibited electrochemiluminescence (ECL) with TPA (tripropylamine) as the co-reactant and the ECL response was proportional to the number of layers.[95] Recently a multilayer study involving $[Ru(bpy)_3]^{2+}$ and $[P_2Mo_{18}O_{62}]^{6-}$ successfully demonstrated that a thin film of the two ions on ITO undergoes electrochromic changes as a function of applied potential, and that by switching the potential the Ru emission can be switched on and off.[96] The versatility of potential multilayer formation was demonstrated by Salimi *et al*, who formed LBL multilayer assemblies of α-$[SiMo_{12}O_{40}]^{4-}$ and $[Ru(bpy)(terpy)Cl]^{+}$ on single-wall carbon nanotubes (SWCNTs). The layers were stable over a large pH range and displayed catalytic activity towards sulfite ions.[97] Despite the growing interest in the area of Ru complex/polyoxometalate multilayers no reports of the use of Ru metallopolymers in this area have been reported to date and we believe that by integrating both sensitizer and surface binding agent into one metallopolymer we may be able to direct stable multilayer formation on electrode surfaces.

Other TM complexes have also been used in POW multilayer assemblies. Both $[Cu^{II}(phen)_2]^{2+}$ and $[Fe^{II}(phen)_3]^{2+}$ were employed with the lacunary POW α-$[P_2W_{17}O_{61}]^{10-}$ in multilayer LBL assemblies.[98] The films were electrochromically reversible and were very robust; they could be electrochemically cycled reversibly in 0.2 M AcOH/AcONa buffer at pH = 3.5 and were stable up to 150 ºC. Films of α-$[SiMo_{12}O_{40}]^{4-}$ and $[Cu(bpy)_2]^{2+}$ have also been self-assembled on SWCNTs. The films were used for nM detection of bromate ions so may find use as a sensor in future.[99] Langmuir-Blodgett (LB) films of the decatungstoeuropate $[Eu(W_5O_{18})_2]^{9-}$ and the amphiphilic Ir complex $[Ir(ddbpy)(ppy\text{-}CN)_2]^{+}$ have been reported (where (ddbpy) = 4,4’-*bis*[3, 5-*bis*(dodecyloxy)benzyloxy]-2, 2’-bipyridine and (ppy-*CN*) =

phenylpyridinate).[100] The Ir based emission was partially quenched by the proximity to the POW acceptor, but when the surfactant DODA was integrated into the LB films dual emission from the two ions was observed from the film. The colour of the Ir emission also shifts as a function of Ir/DODA ratio. The structure of the ions used and the dual emission of the film are shown in Fig 1.5.3.

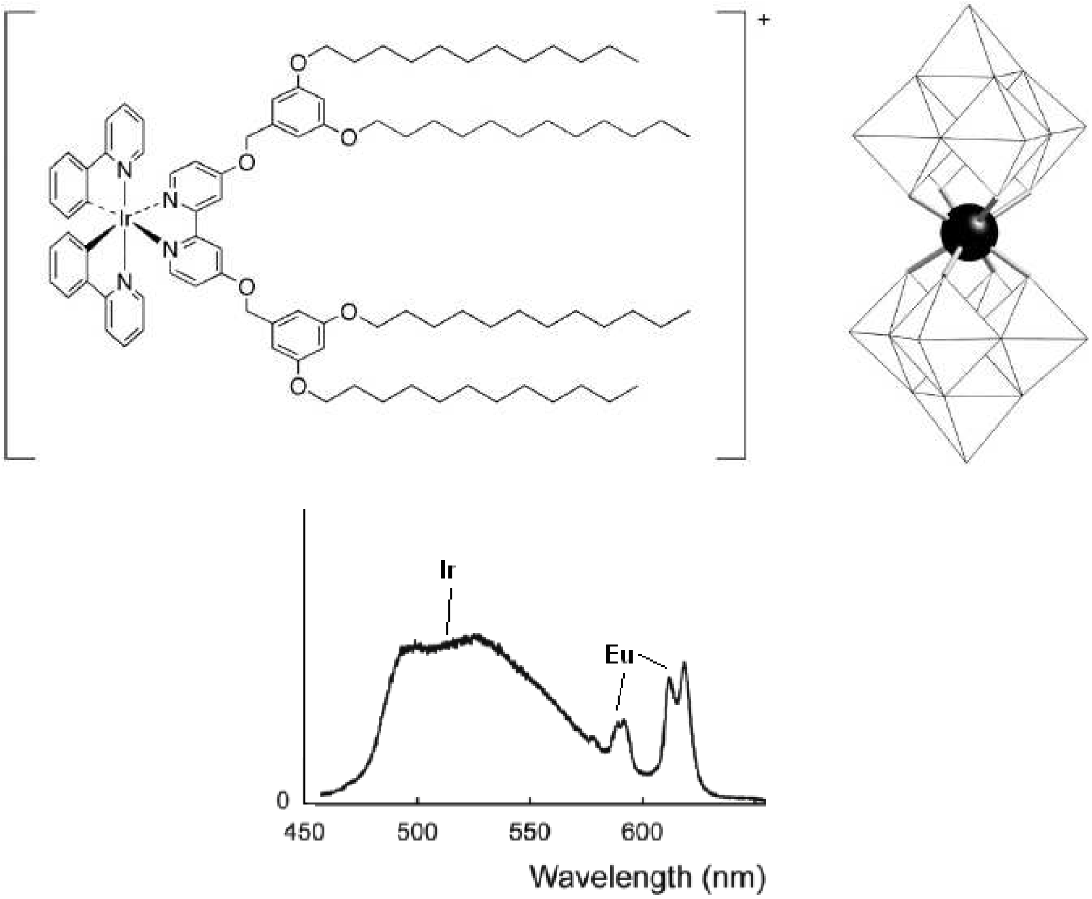

Fig 1.5.3: Above: The structure of $[Eu(W_5O_{18})_2]^{9-}$ and the amphiphilic Ir complex $[Ir(ddbpy)(ppy\text{-}\mathit{CN})_2]^+$ used in building LB films. Below: The dual-emission of the LB film containing above POW and the Ir:DODA in a 20:1 ratio. Reproduced from [100].

1.5.2 – Polyoxometalate multilayers with other photoactive counterions:

Photoactive counterions other than TM polypyridyl complexes have been employed as cations in polyoxometalate multilayer formation. For example a system consisting of $K_6[P_2W_{18}O_{62}]$ and the metalloporphyrin [Tetrakis (*N*-methylpyridyl) porphyrinato] cobalt ($CoTMPyP(ClO_4)_5$) multilayers on 4-aminobenzoic acid functionalized glassy carbon electrodes has been reported.[101] The deposition of homogeneous and stable layers was followed by cyclic voltammetry and UV/Vis spectroscopy. It was observed that as the number of layers increased so did the amount of porphyrin in each layer. The Soret band of the porphyrin red-shifted from 445 nm to approximately 455 nm upon immobilization on the surface, relative to the absorption maximum of the free porphyrin in solution, which was attributed to porphyrin stacking in the film. The multilayers were investigated for photocatalytic activity and it was discovered that $[SiW_{12}O_{40}]^{3-}$ had very different kinetics for the hydrogen evolution reaction than when $[P_2W_{18}O_{62}]^{6-}$ was integrated into this type of multilayer. In a similar report by Jin *et al* multilayers of $[P_2W_{18}O_{62}]^{6-}$ were built up using alcian blue, a cationic copper phthalocyanine.[102] It was shown that a greater amount of both materials was adsorbed onto an ITO electrode when dip-coating into an aqueous solution of 0.01 M PSS than when pure water was used. The multilayers were shown by electrochemistry to be stable when exposed to air for over a month. The multilayers also demonstrated electrocatalytic reduction of nitrite. A simplified schematic of the mutilayers is shown in Fig 1.5.4.

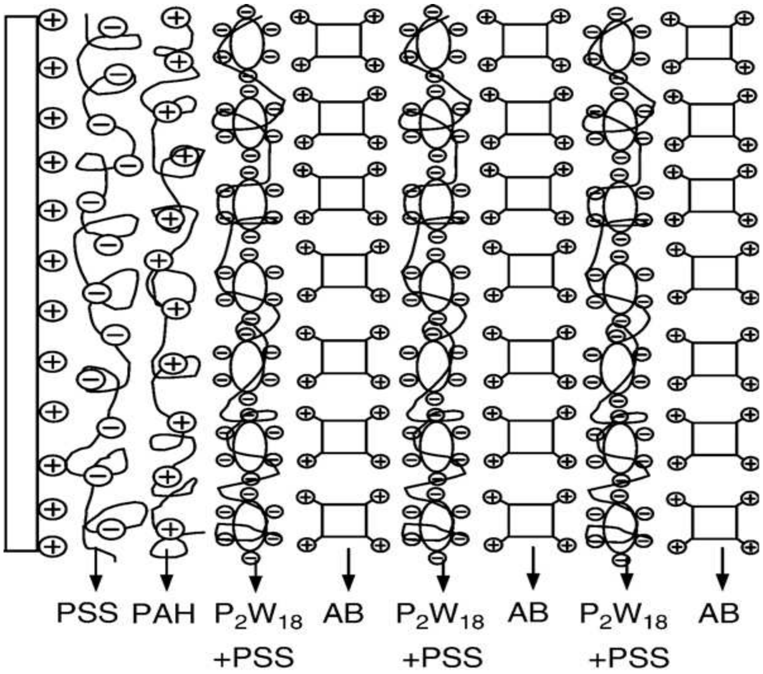

Fig 1.5.4: Schematic representation of the internal layer structure of a $[PSS/PAH(AB–P_2W_{18}O_{62}/PSS)_n]$ multilayer film self-assembled on a substrate. PSS = poly(styrenesulfonate), PAH = poly(allylaminehydrochloride), AB = alcian blue.[102]

This kind of diagram is common in polyoxometalate/cation multilayer publications, but whether such architectures represent reality is highly questionable. Polymers in particular tend to have a lot of interlayer inter-penetration even if true layers do form, and the multilayer films are very likely to exhibit at least some heterogeneity on the nanoscale. Recently reported AFM images show that the structure of a multilayer of cobalt tetraaminophthalocyanine (CoTAPc) and $[P_2Mo_{18}O_{62}]^{6-}$ exhibits granular aggregates with gaps between islands of material.[103] This was attributed to Coulombic repulsion between neighbouring ions. These AFM images are shown in Fig 1.5.5.

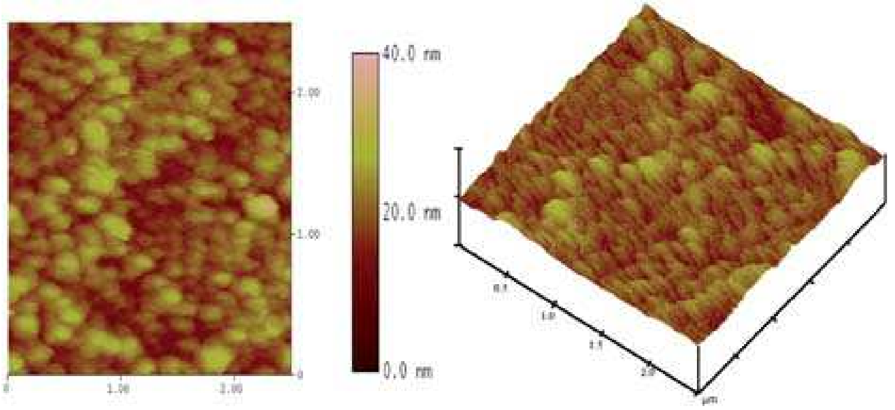

Fig 1.5.5: AFM images of a multilayer film of $(P_2Mo_{18}O_{62}/CoTAPc/PSS/PAH)_3$ showing islands of material on a silicon substrate. Scale 100 nm/div (left) and 500 nm/div (right). Reproduced from [103].

Gao *et al* have investigated the use of various organic dyes as counterions in polyoxoanion multilayers.[104] A variety of related cationic dyes were employed such as methylene blue, thionin and nile blue chloride. When integrated into multilayers with the Keggin ion $[BW_{12}O_{40}]^{5-}$ or the “sandwich” complex $[Co_4(H_2O)_2(PW_9O_{34})_2]^{10-}$ a variety of results were obtained. Some of the dyes did not give a linear growth in absorbance relative to the number of layers deposited, as measure by UV/Vis spectroscopy on a quartz slide. It was therefore postulated that the side groups of the dyes were important in layer formation. A control experiment involving the same dyes and the polyelectrolyte polystyrene sulfonate (PSS) demonstrated that the formation of the layers is dependant on hydrogen bonding between the dye and the polyoxoanion, as well as the relative charges on the ions. Another control experiment showed that some layers are formed between polyoxometalate and uncharged moieties such as polyethylene glycol (PEG), however the formation of more than four layers could not be achieved. This demonstrates that the main driving force for multilayer formation is electrostatics, with hydrogen bonding playing a relatively minor role. The work concluded with photochemical and thermal stability tests of the multilayers. The most stable multilayer system was between the polyoxometalates and the thionin dye, as the NH_2 side groups facilitate H-bonding with the polyoxometalate oxygen atoms which is, as discussed, a secondary factor in multilayer formation.

Significant effort has been invested into making and characterizing multilayers incorporating various polyoxometalates to date. Most of these studies have only focused on the principle of electrostatic LBL multilayer assemblies, as demonstrated by the fact that most have been produced on quartz slides and not on electrodes. The quartz slides do allow for ease of characterization by UV/Vis spectroscopy; however it is difficult to see how such multilayers will have applications. The photocatalytic behavior of these systems has been studied in some cases, but has been neglected in much work. Overall, the potential for photovoltaic devices based on POM/POW multilayers has not been significantly investigated to date. In truth most of the work performed to date represents a newly emerging field that is only beginning to achieve its potential, and studies of polyoxometalate catalysis at electrode interfaces have only become popular in the past four years or so.

1.5.3 – Photocurrent generation/photo-electrochemistry:

Polyoxometalates can be used to generate currents photochemically, and this can be achieved both in solution and when immobilised on the surface of the working electrode. Tungstates generally result in smaller current magnitude than their corresponding molybdates. The lower photocurrent generation of tungstates is generally attributed to the fact that they are harder to reduce than molybdates. In fact, recent quantitative and qualitative study by Bond *et al* showed that under UV/Vis irradiation $[S_2W_{18}O_{62}]^{4-}$ is a significantly less efficient photocatalyst than $[S_2Mo_{18}O_{62}]^{4-}$ due to the more negative redox potential of its excited states.[105] As discussed previously, however, they are also easier to reoxidise and since this is the rate determining step in the catalytic cycle they are more likely to be used in photovoltaics.[9]

The wavelength dependence of photocurrent generation has also been reported for $[S_2W_{18}O_{62}]^{4-}$ as shown in Fig 1.5.6 (b). Strong wavelength dependence is observed for current generation and interestingly as the reduced $[S_2W_{18}O_{62}]^{5-}$ is formed a new absorbance band grows in, similar to that in Fig 1.3.1, which contributes to the photocurrent in the visible region. However a much higher driving force is required to trigger the $[S_2W_{18}O_{62}]^{5-/6-}$ reduction, rendering this process relatively inaccessible.[39] Thus it is critical that a solution or film of reduced polyoxometalate photocatalyst is readily reoxidized in order to complete further catalytic cycles as quickly as possible.

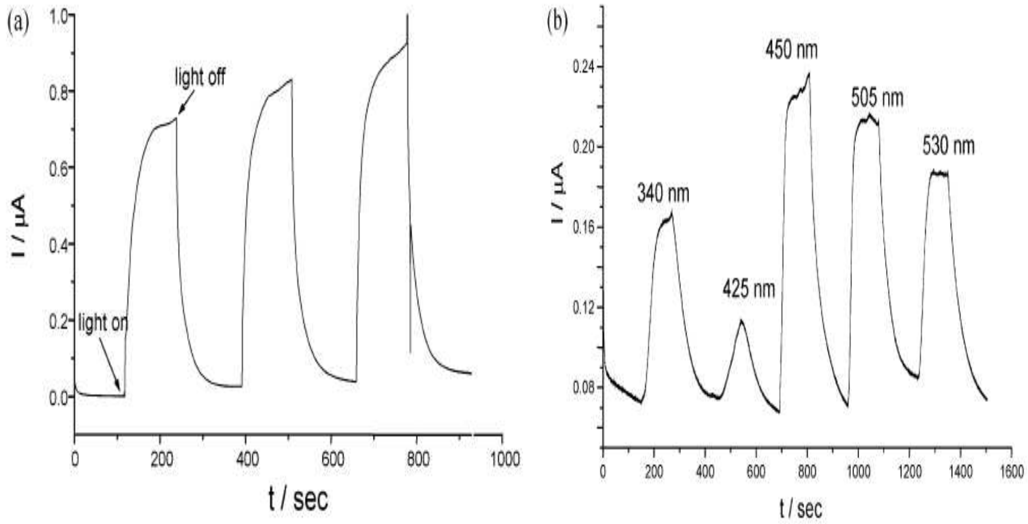

Fig 1.5.6: Photocurrent generation by reduction of $[S_2W_{18}O_{62}]^{4-}$ in the presence of BnOH substrate (a) + 0.2 V, λ = 312 - 700 nm and (b) wavelength dependence at + 0.4 V. 3 mm GC working electrode, potentials vs Ag/Ag^+. Electrolyte: MeCN containing 0.1 M $(Bu_4N)PF_6$. Reproduced from [39].

A significant breakthrough in polyoxometalate photocatalysis came in 2009 with the synthesis of $[\{Ru_4O_4(OH)_2(H_2O)_4\}\text{-}(\gamma\text{-}SiW_{10}O_{36})_2]^{10-}$, a tetraruthenium substituted Keggin POW dimer with excellent photocatalytic activity.[106] The complex was sensitized by $[Ru(bpy)_3]^{2+}$ in aqueous solution and photocatalytic water splitting to form O_2 was observed. Persulfate was used as the sacrificial donor to regenerate the catalyst. This polyoxometalate has also been employed as a water oxidation catalyst in the presence of the tetranuclear Ru tetramer $[Ru(\mu\text{-}dpp)Ru(bpy)_2\}_3]^{8+}$, (where µ-dpp = 2, 3-bis(2'-pyridyl)pyrazine), and displayed a very high quantum yield of O_2 formation of 0.30 at 550 nm, as measured by gas chromatography.[107] This impressive photochemistry has also been exploited as a thin film.[108] A film of the $[Ru(bpy)_3]^{2+}$ derivative, $[Ru(bpy)_2(dpb)]^{2+}$ (dpb = 4, 4'-diphosphonic-2, 2'-bipyridine acid), on a TiO_2 electrode was dipped into a POW solution for 30 minutes to allow self-assembly to occur. The TiO_2-Ru complex-POW films display ultrafast hole scavenging. Fast hole scavenging is a necessary requisite of an efficient photocatalyst as it must be able to scavenge the hole on the photogenerated oxidant in competition with charge recombination. The structure of this interfacial photocatalytic system is shown in Fig 1.5.7. Most recently, our own group published impressive photocurrent results obtained upon visible excitation of a hybrid film of $[S_2Mo_{18}O_{62}]^{4-}$ and $[Ru(bpy)_2(PVP)_{10}]^{2+}$ (where PVP = poly (vinylpyridine)).[109] The current generated by the composite film was approximately 5 times larger than that generated by $[S_2Mo_{18}O_{62}]^{4-}$ alone. The implications of these data will be discussed throughout this thesis.

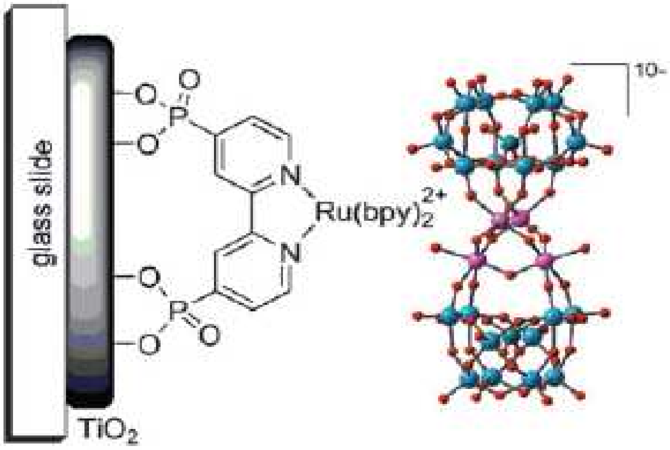

Fig 1.5.7: Interfacial photocatalytic film employed in visible (550 nm) water splitting. Red = oxygen, blue = tungsten and lilac = tetraruthenium core. Reproduced from [108].

1.6 – Scope and future work:

1.6.1 - Photovoltaic devices and their marketability:

At present there are several approaches to building cheap and efficient photovoltaic devices. The first generation of solar cells was based on the use of doped silicon wafers of extremely high quality. These wafers were first used in the 1950's and subsequent developments have produced functioning cells with very high levels of photon to electron conversion efficiency (> 25%). They consist of monocrystalline silica, which is ultra pure and practically homogeneous. Other devices based on semiconductors such as GaAs have been manufactured. These cells have been marketed for a long time but they have not achieved sufficiently high levels of sales due to their cost. At present no novel devices can rival the numerical photon to electron conversion factor of the older silica based systems. However the cost-to-efficiency ratio necessary for mass production of new technologies is coming down annually and solar energy is likely to become one of the main sources of world energy production over the coming years.

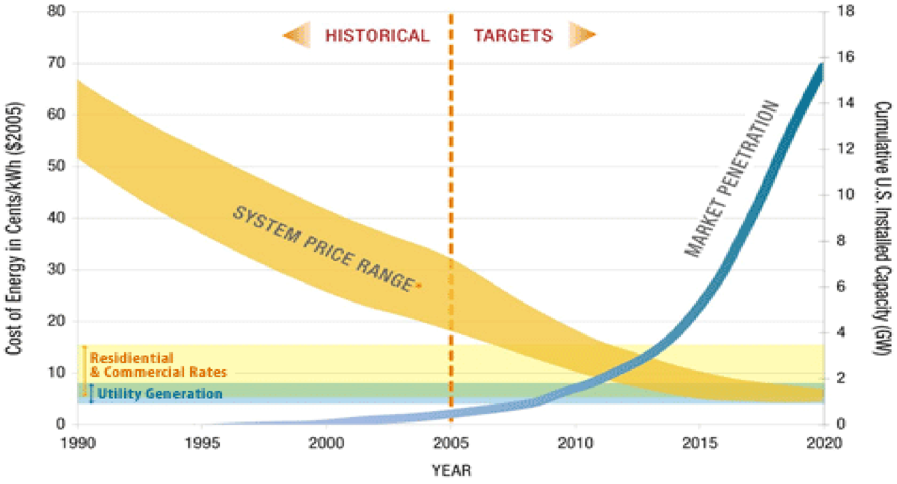

Fig 1.6.1: The projected marketability of solar cells for the US market. As the price falls demand will substantially increase. Assuming fundamental advances, the market should begin to see a significantly increased market share after 2015. Reproduced from U.S. Dept. of Energy [110].

The second generations of solar cells are known as multi-junction devices. They consist of multiply-doped p-n junctions that each have different bandgap energies and hence different absorptivity in the solar spectrum. They are often made from GaAs or InP. The world record for energy generation efficiency as of April 2011 is 43.5 %, generated by Solar Junction Ltd (Watts of electricity generated per incident Watt of solar irradiation).[111] It is beyond reasonable doubt that multijunction semiconductor based photovoltaic technologies are the most efficient of photovoltaics but the cost remains too high for serious commercialisation. Other second generation approaches are therefore invariably based on inherently cheaper technologies.

1.6.2 – Future work:

Much of the work performed on polyoxometalates over the last ten years has been in the synthesis of novel polyoxometalate ions and composites. The real strength in this is that with enough knowledge of these syntheses and a sound theoretical understanding of the systems under study, polyoxometalates can now to a large extent be custom built for a specific purpose. For example polyoxometalates were traditionally considered to generally be non-luminescent. However derivatized polyoxometalates have long ago been synthesized that display luminescence; for example Nd and Eu containing polyoxometalates.[112, 113] These polyoxometalates can thus be directly probed by luminescence spectroscopy when immobilized in multilayer composites.

Some researchers believe that polyoxometalate multilayers look promising as their electrochromic properties may be used to manufacture digital display devices.[114, 115] Another group recently reported the ability of a POW/polymer/quantum dot (QD) composite film to "write" different states.[116] Firstly a film of $[(\mathrm{PEI/Na\text{-}POW})_9\mathrm{/PEI/CdSe@CdS}]_{10}$ (where Na-POW = the Preyssler anion $[\mathrm{Na(H_2O)P_5W_{30}O_{110}}]^{14-}$) was deposited via the LBL method on a silicon substrate, and covered with a square mesh copper grid and irradiated with UV light for 30 seconds. The film exhibited FRET (fluorescence resonance energy-transfer) between the POW and QDs, resulting in a pattern appearing only in the gaps in the grid. When the grid was removed the "information" was stored on the surface. However upon exposure to ambient light at room temperature over a day the film returned to its normal "unwritten" state. It was then covered with a honeycomb copper mesh and the UV irradiation repeated, proving that the film can be reversibly written. This fascinating application is shown in Fig 1.6.2.

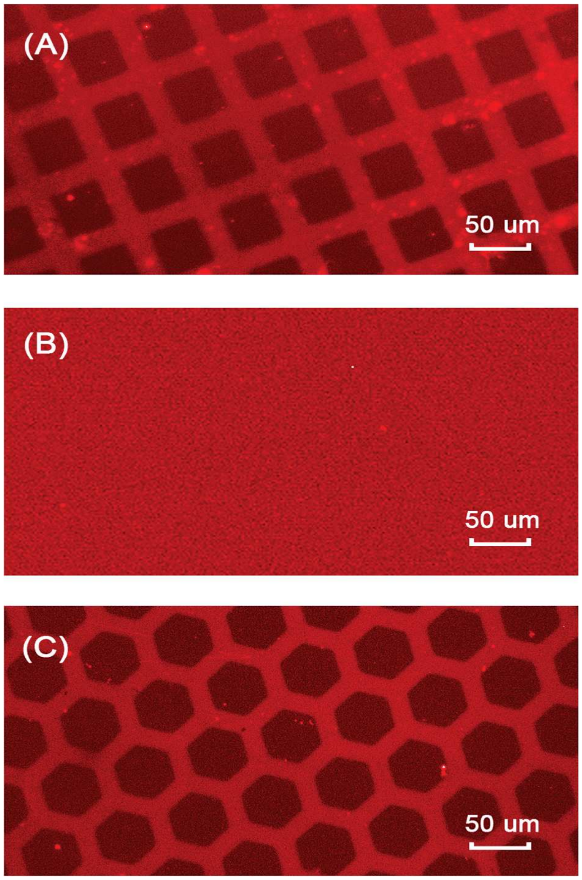

Fig 1.6.2: Confocal fluorescence microscopy of a thin film of $[(\mathrm{PEI/[Na(H_2O)P_5W_{30}O_{110}]^{14-}})_9\mathrm{/PEI/CdSe@CdS}]_{10}$ deposited on a silicon substrate (a) covered with a square mesh copper grid and irradiated with UV light for 30 seconds, (b) after 1 day exposure to ambient light and (b) "rewritten" using a honeycomb mesh and UV light. Reproduced from [116].

Although it is difficult to predict where the field of polyoxometalate chemistry will branch into in future, it is highly likely that both catalysis and thin film applications will play a big role in the coming years. A recent overview of polyoxometalate applications is provided.[117]

1.7 - Techniques:

1.7.1 – Photoluminescence techniques:

1.7.1.1 – Steady state emission measurements and quenching:

Fluorescence is a short-lived process of radiative deactivation that occurs from the vibrational ground state of the S_1 state only (in rare cases, such as that of coronene, it can occur from the S_2 state also).[118] It is generally a short-lived process, usually on the nanosecond or picosecond timescale. Phosphorescence occurs from the T_1 state and is usually much longer lived, often on the micro to millisecond timescale. Note that ISC and emission from $T_1 \rightarrow S_0$ are spin forbidden processes in theory, and this means that the probability of such transitions being observed is in reality quite low and limited to a relatively small number of exceptional cases. As discussed in section 1.4.1, the heavy atom effect is one mechanism by which ISC can occur. Many other important processes such as electron and energy transfer occur when the molecule in the T_1 state interacts with another molecule. For example collisions in solution with other molecules can deactivate the excited state and this is known as collisional (dynamic) quenching. Electron transfer from the T_1 state to an acceptor species can also occur if the donor and acceptor moieties form a ground-state association complex electrostatically, which is known as static quenching. Otherwise, static quenching may arise due to the formation of a non-emissive ground state associated complex. This is the primary mechanism by which Ru (II) polypyridyl complexes studied previously may sensitize polyoxometalates and has been widely reported previously by the Keyes group and by others for electrostatic composites of $[Ru(bpy)_3]^{2+}$ and the Dawson polyoxometalates (see discussion in section 1.4.2).

Studies involving Ru/polyoxometalate donor-acceptor electrostatic clusters frequently investigate the mechanism through which quenching occurs. This is usually achieved by employing the Stern-Volmer model for intramolecular quenching. To apply the Stern-Volmer model to a particular system the quenching of the fluorophore fluorescence intensity must be measured as a function of increasing quencher concentration. In addition either the quenching of the fluorescent lifetime, τ, or quantum yield, Φ, must be recorded. The slopes of the two plots can give much insight into the nature of the quenching process hence the Stern-Volmer model is commonly and widely applied to a huge variety of systems such as proteins and fluorescent polymers.[119, 120]

1.7.1.2 – Time-resolved emission:

The fluorescent lifetime, τ, of a species is "the parameter describing the time evolution of the decay of the fluorescent radiant intensity".[121] The measurement of fluorescence lifetimes is a field which has grown significantly in recent years, in particular with relation to fluorescence lifetime imaging (FLIM) of live cells and in the study of proteins.[122] The current explosion in the use of this technology is likely to continue for some time, as the popularity of the field is still increasing since the study of the Green Fluorescent Protein won the Nobel Prize in Chemistry in 2008.[123, 124]

The decay kinetics of an excited state electron returning radiatively to the ground state can be measured using time-correlated single photon counting (TCSPC) techniques. This technique uses a pulsed laser of short duration (approx 500 ps) to excite the fluorophore and the emitted signal is detected at a PMT. The decay is fitted to an applicable model (ie: monoexponential, biexponential, stretched exponential, etc) using specialized software, in order to extract the lifetime values. The precision and accuracy of the measurement can be improved by collecting large number of counts which is facile because of the way in which the TCSPC method works (counting of individual photons) but can make the acquisition long for long lived species. Fluorescence lifetimes are extremely sensitive to the environment of the fluorophore and are drastically affected by temperature, solvent polarity and the presence of O_2. Measurement of τ of a fluorophore as a function of increasing quencher concentration can give insight into the applicability of the Stern-Volmer model. Both static and dynamic Stern-Volmer behaviour are shown below.

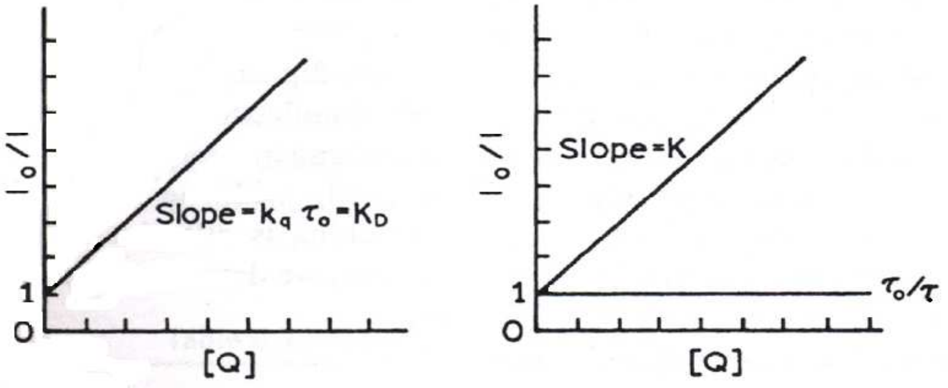

Fig 1.7.1: Stern-Volmer behaviour for dynamic quenching (left) and static quenching (right). Reproduced from [119].

Fig 1.7.1 shows that in the case of dynamic quenching both the fluorescence intensity (I_0/I) and lifetime (τ_0/τ) plots both exhibit a slope, though the slopes are not necessarily coincident as in this idealized case. In the case of purely static quenching the intensity is quenched but the lifetime is not. Therefore luminescence quenching experiments are vital for characterizing the quenching mechanisms in ruthenium complex/polyoxometalate systems.

1.7.2 – Electronic spectroscopy:

1.7.2.1: Difference electronic spectroscopy:

Difference electronic spectroscopy is a technique in which the UV/Vis spectra of two or more components are added together electronically and then subtracted from the spectrum of the corresponding mixture at identical concentrations. This is performed using spreadsheet software such as Microsoft Excel. The reason for generating difference spectra is to clearly see any new spectral features that form as a consequence of ion-pair formation; for instance Ru to polyoxometalate charge-transfer bands. These bands can be difficult to see as they have low extinction coefficients and are usually obscured by intense nearby parent-ion bands. A good example of a set of difference spectra is shown in Fig 1.7.2.

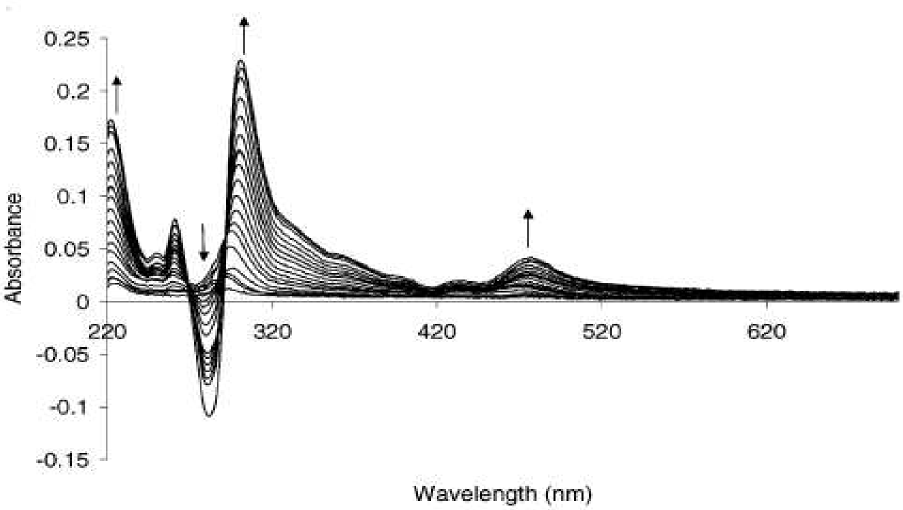

Fig 1.7.2: Difference electronic spectra of a titration of increasing quantities of $[S_2W_{18}O_{62}]^{4-}$ into a solution of $[Ru(bpy)_3]^{2+}$ at constant concentration in acetonitrile showing the grow-in of a new inter-complex charge transfer band at ~ 480 nm. Reproduced from [52].

1.7.2.2 – Transient absorption spectroscopy:

Information about the fate of transient species some time after initial excitation can give valuable information into the kinetics and mechanisms of excited state chemical reactions. Transient absorption is a form of fast time-resolved electronic spectroscopy in which the decay of an excited state signal is measured over a very short period (sometimes as low as femtoseconds). For Ru (II) polypyridyl complexes excited state lifetimes are usually in the region of nanoseconds to microseconds, and it is usually straightforward to elucidate the fate of these states using very short laser pulses. The spectrometer records the absorbance at each wavelength as a function of time, and will hence measure the time-resolved spectrum as the excited state relaxes back to the ground state. Using this technique the movement of electrons to form reactive intermediates can be unambiguously followed. This is of importance in supramolecular systems where several competing excited state processes may possibly occur. Below is the transient spectrum of $[Ru(bpy)_3]^{2+}$.

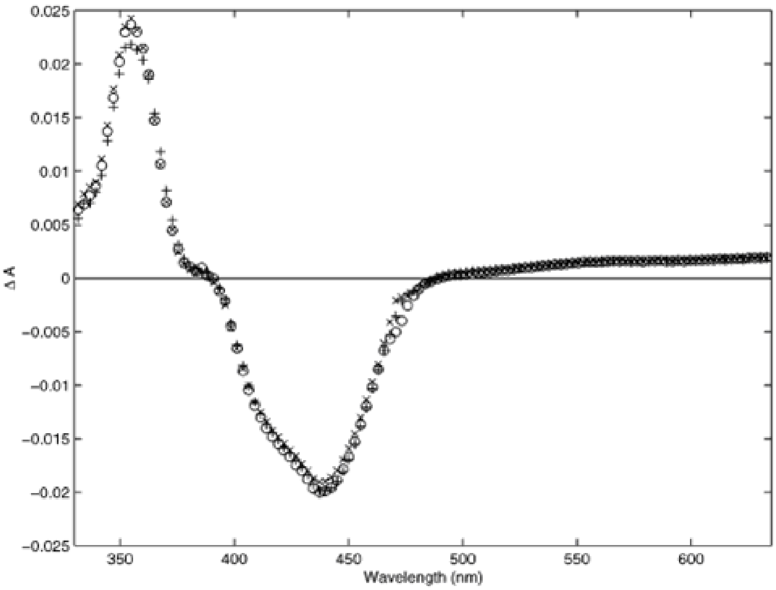

Fig 1.7.3: Transient absorption spectrum of $[Ru(bpy)_3]^{2+}$ at 1 ps (plus signs), 100 ps (circles), and 1 ns (crosses). Reproduced from [125].

Fig 1.7.3 shows that the Ru MLCT absorption decays upon excitation, and that a new peak at 360 nm grows in. This is a $(bpy)^-$ radical peak and reveals the location where the radical electron is localized during the excited state of the molecule. The two peaks then decay back to the baseline after a certain time and the kinetics of the decay give insight into the excited state lifetime of the species. The possibility of studying multilayer films of polyoxometalates and Ru (II) complexes will be investigated using diffuse reflectance. The diffuse reflectance setup is shown in Fig 1.7.4.

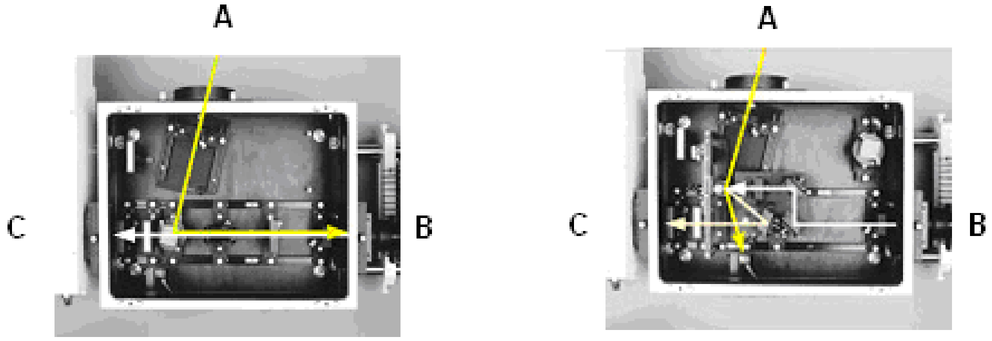

Fig 1.7.4: Sample acquisition using Applied Photophysics LKS.60 transient absorption system. Left: co-linear excitation of liquid sample in a cuvette; right: diffuse reflectance. A: laser source (Nd:YAG, 355 nm), B: white light source (pulsed Xe arc lamp) and C: monochromator and PMT. Reproduced from supplier's website [126].

1.7.3 - Vibrational spectroscopy:

1.7.3.1 – Attenuated total reflectance Fourier-transform infrared spectroscopy:

Attenuated total reflectance (ATR) is an accessory which can be used to acquire FTIR spectra of pure samples without the need for a matrix such as KBr or Nujol. The sample is placed on a reflective surface and a detector tip is screwed down into contact with the sample. The IR beam from the spectrometer is directed onto the sample at an angle, θ, greater than the critical angle, θ_c, so that the infrared light undergoes internal reflection. At each point of internal reflection an evanescent wave is produced, which is absorbed by the sample in direct contact with the reflective surface. ATR measurements have the advantage of being easy to perform, however the ATR accessories tend to be expensive and can be somewhat delicate. Examples of common ATR tips are those made from germanium, ZnSe or diamond. An illustration of an ATR-FTIR measurement is given in Fig 1.7.5.

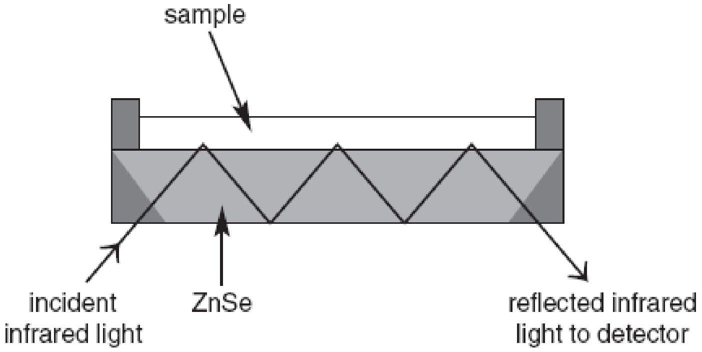

Fig 1.7.5 – Illustration of internal reflections through a high refractive index medium (ZnSe), used as the reflective surface. At each reflection, an evanescent wave is produced that decays exponentially into the tip above. The tip is screwed into contact with the sample from above. Reproduced from [127].

1.7.3.2 – Resonance Raman spectroscopy:

The Raman Effect is an optical phenomenon observed when a small portion (approximately 1 in 10^7 photons) of light incident on a sample surface are scattered inelastically. This light is scattered at a wavelength different to the one incident on the sample and this difference in wavelength is called the Raman Shift. Raman scattering occurs when an incident photon is absorbed by an electron, promoting it to a virtual state. This distorts the electronics of a molecule momentarily, causing the bond to form a temporary dipole. The bond then vibrates back to its ground state, causing the dipole to vanish. The Raman shift results from a change in the wavelength of the emitted light relative to the wavelength of absorption (known as Δv), and a Raman spectrum plots Δv versus emission (scattering) intensity. Only bonds that show a change in polarizabilty are Raman active. In resonance Raman the wavelength of absorbance is coincident with a molecular chromophore and hence excites to vibrationally hot states of the first electronic excited state (see Fig 1.7.6). Different vibrational modes are IR or Raman active (or both), so Raman is often used as a complimentary tool to infrared spectroscopy. For example, water is IR active but has a weak signal in the Raman spectrum; and this useful property makes Raman very useful in biospectroscopy. Raman spectroscopy has inherently low sensitivity and so for years after its discovery (1928) it was difficult to use, usually only for concentrated liquid samples, and hence was only used very rarely. Nowadays it has become popular due to the availability of tuneable lasers and the advent of Resonance Raman spectroscopy.

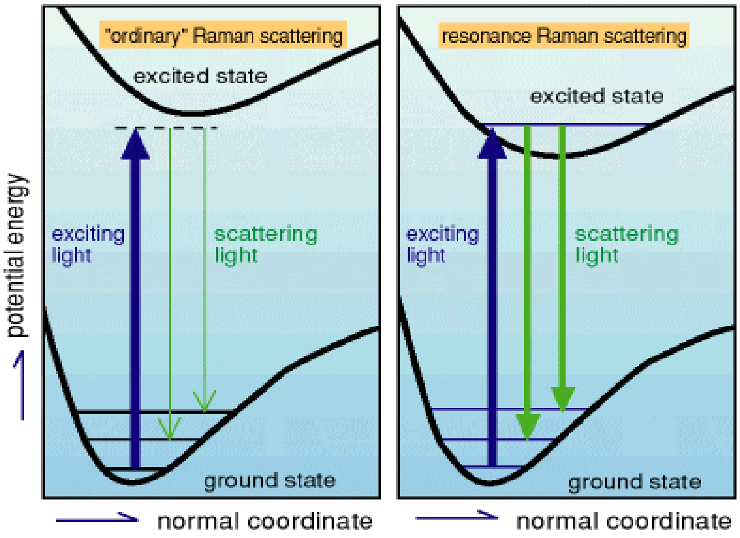

Fig 1.7.6: The origin of Raman signals for non-resonant (left) and resonant Raman spectroscopy. Reproduced from [128].

In resonance Raman (RR) spectroscopy the exciting laser is resonant with an electronic absorbance of the material under study. Any Raman active vibrational modes associated with this electronic transition, i.e. associated with the chromophoric being resonantly probed, will have their signals enhanced greatly; sometimes by as much as seven orders of magnitude.[129] This useful property means that one species can be observed in a mixture by exciting into its chromophore. Even though other molecules in the sample will Raman scatter, the intensity from this conventional Raman scatter is so weak compared with the resonantly enhanced modes that only the resonantly enhanced spectrum is observed. This technique permits study of key transitions in complex materials and has found potential use in biospectroscopy to observe labels entering live cells.[122]

1.7.4 – Electrochemistry:

1.7.4.1 – Photoelectrochemistry:

Photoelectrochemistry is a technique which employs both a conventional three-electrode electrochemical cell and a light source for inducing photochemical reactions. In a photoelectrochemical experiment a molecule either in solution or immobilized on the surface of the working electrode absorbs a photon and undergoes a photochemical reaction. This results in the production of electrons, protons or oxygen which may be captured and stored. The photocatalyst then has to be regenerated in order for it to participate in another catalytic cycle and this can be done by applying the necessary potential at the working electrode. This kind of system obviously doesn't apply to irreversible photochemical reactions or photodegradations but can be used for systems involving polyoxometalates as their electrochemistry is fully reversible. For example, the photoelectrochemistry of the composite material $[Ru(bpy)_3]_2[S_2W_{18}O_{62}]$ and a variety of other Ru (II) polypyridyl complex/Dawson polyoxometalate ion clusters have previously been performed in solution.[57] This data is shown in Fig 1.7.7 and Fig 1.7.8.

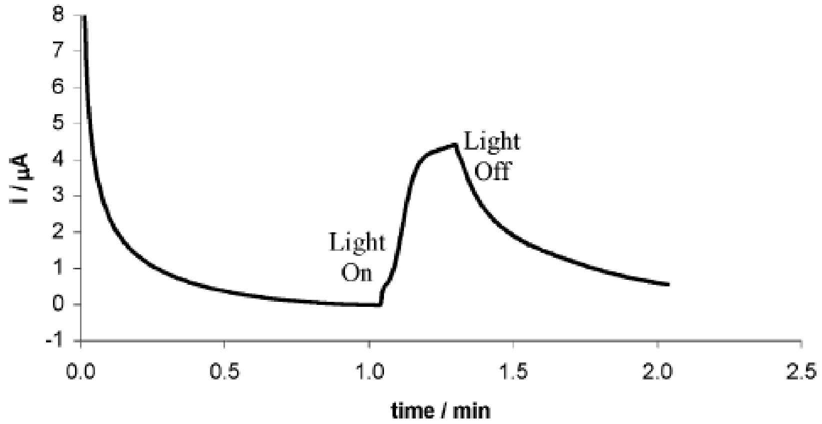

Fig 1.7.7: Photoelectrochemistry of a mixed solution of $[Hex_4N]_4[S_2Mo_{18}O_{62}]$ (0.1 mM) and $[Ru(biq)_2(box)]^+$ (0.4 mM) in DMF (0.1 M Bu_4NPF_6) irradiated by white light. The potential was poised at + 400 mV (vs. Fc/Fc^+). Reproduced from [57].

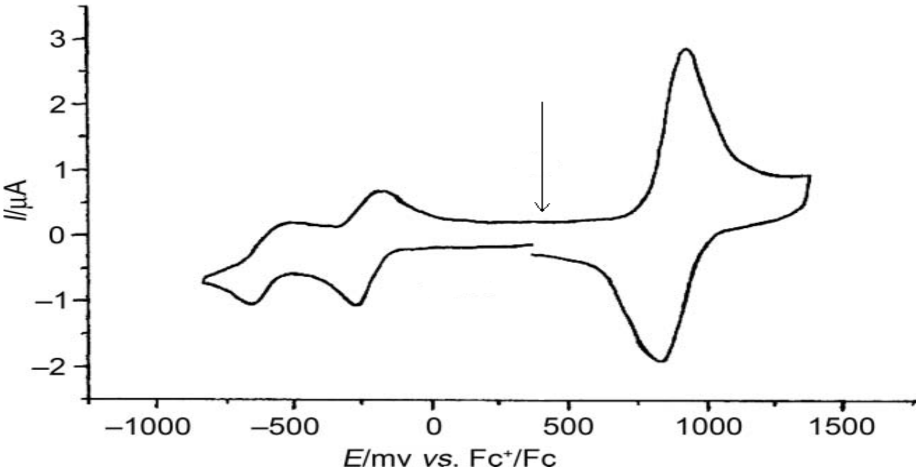

Fig 1.7.8: Cyclic voltammogram of $[Ru(bpy)_3]_2[S_2W_{18}O_{62}]$ in CH_3CN (0.1 M Bu_4NPF_6). Working electrode = glassy carbon (d = 3 mm), scan rate = 100 $mV.s^{-1}$). Reproduced from [57].

Fig 1.7.7 shows the photoelectrochemical response of the hybrid material $[Ru(biq)_2(box)]_4[S_2Mo_{18}O_{62}]$ in the presence of DMF substrate under white light irradiation. The current applied to reoxidise the polyoxotungstate after photoreduction was + 400 mV (see Fig 1.7.8). This potential was chosen as it is more positive than the first reduction of the polyoxoanion and less positive than the oxidation of the Ru cations. Consequently, zero current should be recorded in the absence of light when this potential is applied.

1.7.5.3 – Spectroelectrochemistry:

Spectroelectrochemistry (SEC) is a technique that combines electrochemistry and spectroscopy. In a specially designed electrochemical cell that also acts as a cuvette, a redox active compound is oxidized or reduced. The products of the redox transformation are monitored in situ by the spectrometer. In the case of polyoxometalate reductions new absorption bands appear in the visible and NIR regions as a consequence of electron localization (see Fig 1.3.1). Although these electronic transitions have been well characterized for the Dawson polyoxometalates, the resonance Raman spectroscopy of these chromophores have not been extensively investigated. However, in one literature example the resonance Raman spectroscopy of the "giant" polyoxomolybdate $(NH_4)_{21}[\{V^{IV}(H_2O)O\}_6\{Mo^{V}(\mu\text{-}H_2O)_2(\mu\text{-}OH)Mo^{V}\}_3\{Mo_{15}(MoNO)_2O_{58}(H_2O)_2\}_3].65H_2O$ cluster was studied in solution under 1064 nm irradiation.[130] It was observed that new Raman modes appeared in the spectra of the 6 and 12-electron reduced products and these modes were characterized. The giant polyoxomolybdates commonly undergo multi-electron reductions.[131, 132]

1.8 - References:

---

[1] B. O' Regan and M. Grätzel, *Nature*, 1991, **353**, 737 - 740.

[2] M. K. Nazeeruddin, P. Péchy and M. Grätzel, *Chem. Commun.*, 1997, 1705 - 1706.

[3] F. Gao, Y. Wang, J. Zhang, D. Shi, M. Wang, R. Humphry-Baker, P. Wang, S. M. Zakeeruddin and M. Grätzel, *Chem. Commun.*, 2008, 2635 - 2637.

[4] R.J. Forster, T.E. Keyes and J.G. Vos, *Interfacial Supramolecular Assemblies*, Wiley, UK, 2003, p. 268.

[5] M. Grätzel*, Inorg. Chem.*, 2005, **44**, 6841.

[6] Y. Bai, Y. Cao, J. Zhang, M. Wang, R. Li, P. Wang, S. M. Zakeeruddin and M. Grätzel, *Nature Mater.*, 2008, **7**, 626 - 630.

[7] Q. Wang, W. M. Campbell, E. E. Bonfantani, K. W. Jolley, D. L. Officer, P. J. Walsh, K. Gordon, R. Humphry-Baker, M. K. Nazeeruddin, and M. Grätzel, *J. Phys. Chem. B*, 2005, **109**, 15397 - 15409.

[8] A. Morandeira, I. Lopez-Duarte, B. O' Regan, M. V. Martinez-Diaz, A. Forneli, E. Palomares, T. Torres and J. R. Durrant, *J. Mater. Chem.*, 2009, **19**, 5016 - 5026.

[9] E. Papaconstantinou, A. Hiskia and A. Troupis, *Front. Biosci.*, 2003, **8**, s813 - 825.

[10] A. Hiskia, A. Troupis, S. Antonaraki, E. Gkika, P. Kormali and E. Papaconstantinou, *Int. J. Environ. An. Ch.*, 2006, **86,** 233 - 242.

[11] M. D. Tzirakis, I. N. Lykakis and M. Orfanopoulos, *Chem. Soc. Rev.*, 2009, **38**, 2609 - 2621.

[12] P. J. S. Richardt, R. W. Gable, A. M. Bond and A. G. Wedd, *Inorg. Chem.*, 2001, **40**, 703 - 709.

[13] D-L. Long, E. Burkholder and L. Cronin, *Chem. Soc. Rev.*, 2007, **36**, 105 - 121.

[14] J. J. Berzelius, *Poggend. Ann. Phys. Chem.*, 1826, **6**, 369.

[15] L. Pauling, *J. Am. Chem. Soc.*, 1929, **51,** 2868 - 2880.

[16] J. F. Keggin, *Nature*, 1933, **131**, 908.

[17] B. Dawson, *Acta Cryst.*, 1953, **6**, 113 - 126.

---

[18] P. Gouzerh and M. Che, *L'Actualité Chimique*, 2006, **298**, 1 - 14.

[19] M. H. Alizadeh, S. P. Harmalker, Y. Jeannin, J. Martin and M. T. Pope, *J. Am. Chem. Soc.*, 1985, **107**, 2662 - 2669.

[20] M. T. Ma, T. Waters, K. Beyer, R. Palamarczuk, P. J. S. Richardt, R. A. J. O'Hair and A. G. Wedd, *Inorg. Chem.*, 2009, **48**, 598 - 606.

[21] H. An, T. Xu, X. Liu and C. Jia, *J. Coord. Chem.*, 2010, **63**, 3028 - 3041.

[22] N. Fay, A. M. Bond, C. Baffert, J. F. Boas, J. R. Pilbrow, D-L. Long and L. Cronin, *Inorg. Chem.*, 2007, **46**, 3502 - 3510.

[23] M. N. Sokolov, V. S. Korenev, N. V. Izarova, E. V. Peresypkina, C. Vicent and V. P. Fedin, *Inorg. Chem.* 2009, **48**, 1805 - 1807.

[24] C. Baffert, J. F. Boas, A. M. Bond, P. Kögerler, D. L. Long, J. R. Pilbrow, and L. Cronin, *Chem. Eur. J.,* 2006, **12**, 8472 - 8483.

[25] P. J.S. Richardt, J. M. White, P. A. Tregloan, A. M. Bond and A. G. Wedd**,** *Can. J. Chem.,* 2001, **79**, 613 - 620.

[26] E. Papaconstantinou, *Chem. Soc. Rev.*, 1989, **18**, 1-31.

[27] J. P. Launay, *J. Inorg. Nucl. Chem.*, 1976, **38**, 807 - 816.

[28] J. B. Cooper, D. M. Way, A. M. Bond and A. G. Wedd, *Inorg. Chem.,* 1993, **32**, 2416 - 2420.

[29] N. Fay, V. M. Hultgren, A. G. Wedd, T. E. Keyes, R. J. Forster, D. Leane and A. M. Bond, *Dalton Trans.*, 2006, 4218 - 4227.

[30] E. Papaconstantinou, D. Dimotikali, and A. Politou, *Inorg. Chim. Acta*, 1980, **46**, 155.

[31] Y. Yang, Q. Wu, Y. Guo, C. Hu and E. Wang, *J. Mol. Catal. A - Chem.*, 2005, **225**, 203 - 212.

[32] A. Hiskia , M. Ecke , A. Troupis, A. Kokorakis, H. Hennig and E. Papaconstantinou, *Environ. Sci. Technol.*, 2001, **35**, 2358 - 2364.

[33] R. Cao, H. Ma, Y. V. Geletii, K. I. Hardcastle, and C. L. Hill, *Inorg. Chem.* 2009, **48**, 5596 - 5598.

[34] T. Yamase, *Cat. Surveys Asia*, 2003, **7**, 203 - 217.

---

[35] H. Einaga and M. Misono, *Bull. Chem. Soc. Jpn.*, 1996, **69**, 3435.

[36] M. A. Fox, R. Cardona and E. Gaillard, *J. Am. Chem. Soc.*, 1987, **109**, 6347 - 6354.

[37] A. Mylonas and E. Papaconstantinou, *J. Photoch. Photobio. A*, 1996, **94**, 77 - 82.

[38] T. Yamase, *Chem. Rev.*, 1998, **98**, 307 - 325.

[39] T. Rüther, A. M. Bond and W. R. Jackson, *Green Chem.*, 2003, **5**, 364 - 366.

[40] T. Rüther, V. M. Hultgren, B. P. Timko, A. M. Bond, W. R. Jackson and A. G. Wedd, *J. Am. Chem. Soc.,* 2003, **125**, 10133 - 10143.

[41] http://www.iupac.org/projects/posters01/parmon01.pdf

[42] N. Muradov and A.T. Raissi, *J. Sol. Energy Eng.*, 2006, **128**, 326 - 330.

[43] T. J. Meyer, *Pure & Appl. Chem.*, 1986, **58**, 1193 - 1206.

[44] V. Balzani, A. Juris and M. Venturi, *Chem. Rev.,* 1996, **96**, 759 - 833.

[45] N. H. Damrauer, G. Cerullo, A. Yeh, T. R. Boussie, C. V. Shank and J. K. McCusker, *Science*, 1997, **235**, 54 - 57.

[46] T. Engel, *Quantum Chemistry and Spectroscopy*, Prentice Hall, USA, First Ed, p. 313.

[47] J. Van Houten and R. J. Watts, *J. Am. Chem. Soc.*, 1976, **98**, 4853 - 4858.

[48] R. Ballardini, M. T. Gandolfi and V. Balzani, *Inorg. Chem.*, 1987, **26**, 862 - 867.

[49] V. M. Hultgren, A. M. Bond and A. G. Wedd, *J. Chem. Soc., Dalton Trans.*, 2001, 1076 - 1082.

[50] A. Kuhn and F. C. Anson, *Langmuir*, 1996, **12**, 5481 - 5488.

[51] T. E. Keyes, E. Gicquel, L. Guerin, R. J. Forster, V. M. Hultgren, A. M. Bond, and A. G. Wedd, *Inorg. Chem.*, 2003, **42**, 7897.

[52] M. K. Seery, L. Guerin, R. J. Forster, E. Gicquel, V. M. Hultgren, A. M. Bond, A. G. Wedd, and T. E. Keyes, *J. Phys. Chem. A*, 2004, **108**, 7399 - 7405.

[53] M. K. Seery, N. Fay, T. McCormac, E. Dempsey, R. J. Forster and T. E. Keyes, *Phys. Chem. Chem. Phys.*, 2005, **7** , 3426 - 3433.

---

[54] L. Ruhlmann, C. Costa-Coquelard, J. Hao, S. Jiang, C. He, L. Sun and I. Lampre, *Can. J. Chem.*, 2008, **86**, 1034 - 1043.

[55] J. Song, Z. Luo, H. Zhu, Z. Huang, T. Lian, A. L. Kaledin, D. G. Musaev, S. Lense, K. I. Hardcastle and C. L. Hill, *Inorg. Chim. Acta*, 2010, **363**, 4381 - 4386.

[56] Y. Li, H. Zhu and X. Yang, *Talanta*, 2009, **80**, 870 - 874.

[57] N. Fay, V. M. Hultgren, A. G. Wedd, T. E. Keyes, R. J. Forster, D. Leane and A. M. Bond, *Dalton Trans.*, 2006, 4218 - 4227.

[58] M. Bonchio, M. Carraro, G. Scorrano, A. Bagno, *Adv. Synth. Catal*. 2004, **346**, 648 - 654.

[59] J. J. Walsh, D-L. Long, L. Cronin, A. M. Bond, R. J. Forster and T. E. Keyes, *Dalton Trans.*, 2011, **40**, 2038 - 2045.

[60] M. Góral, T. McCormac, E. Dempsey, D-L. Long, L. Cronin and A. M. Bond, *Dalton Trans.*, 2009, 6727 - 6735.

[61] N. Fay, E. Dempsey, A. Kennedy and T. McCormac, *J. Electroanal. Chem*., 2003, **556**, 63 - 74.

[62] N. Fay, E. Dempsey, A. Kennedy and T. McCormac, *Electrochim. Acta*, 2005, **51**, 281 - 288.

[63] J. Zhang, J. K. Goh, W. T. Tan and A. M. Bond, *Inorg. Chem*., 2006, **45**, 3732 - 3740.

[64] Z. Han, E. Wang, G. Luan, Y. Li, C. Hu, P. Wang, N. Hu, and H. Jia, *Inorg. Chem. Commun*., 2001, **4**, 427 - 429.

[65] J. M. Knaust, C. Inman and S. W. Keller, *Chem. Commun*., 2004, 492 - 493.

[66] Y. Zhang, P. J. Zapf, L. M. Meyer, R. C. Haushalter and J. Zubieta, *Inorg. Chem*., 1997, **36**, 2159 - 2165.

[67] X. Wang, H. Hu, A. Tian, H. Lin, and J. Li, *Inorg. Chem*., 2010, **49**, 10299 - 10306.

[68] J. Sha, J. Peng, Y. Lan, Z. Su, H. Pang, A. Tian, P. Zhang and M. Zhu, *Inorg. Chem.,* 2008, **47**, 5145 - 5153.

[69] H. Yang, T. Liu, M. Cao, H. Li, S. Gao and R. Cao, *Chem. Commun*., 2010, **46**, 2429 - 2431.

[70] R. Yu, X-F. Kuang, X.-Y. Wu, C-Z. Lu and, J. P. Donahue, *Coord. Chem. Rev.*, 2009, **253**, 2872 - 2890.

---

[71] P. Le Maguere, S. M. Hubig, S. V. Lindeman, P. Veya, and J. K. Kochi, *J. Am. Chem. Soc.*, 2000, **122**, 10073 - 10082.

[72] L. J. Zhang, Y. S. Zhou, Z. Yu, G. S. Fang, and X. Z. You, *J. Mol. Struct.*, 2001, **570**, 83 - 90.

[73] J. A. F. Gamelas, F. M. Santos, V. Felix, A. M. V. Cavaleiro, E. de Matos Gomes, M. Belsley and M. G. B. Drew, *Dalton Trans.*, 2006, 1197 - 1203.

[74] J. Y. Nu, J. P. Wang, W. Chen, C. H. L. Kennard and K. A. Byriel, *J. Coord. Chem.*, 2001, **53**, 153 - 162.

[75] J. Xie, B. F. Abrahams and A. G. Wedd, *Chem. Commun.*, 2008, 576 - 578.

[76] S-X. Guo, J. Xie, R. Gilbert-Wilson, S. L. Birkett, A. M. Bond and A. G. Wedd, *Dalton Trans.*, 2011, **40**, 356 - 366.

[77] Q. Li, C. Zhao, A. M. Bond, J. F. Boas, A. G. Wedd, B. Moubarakia and K. S. Murray, *J. Mater. Chem.*, 2011, **21**, 5398 - 5407.

[78] S. Juraja, T. Vu, P. J. S. Richardt, A. M. Bond, T. J. Cardwell, J. D. Cashion, G. D. Fallon, G. Lazarev, B. Moubaraki, K. S. Murray and A. G. Wedd, *Inorg. Chem.,* 2002, **41**, 1072 - 1078.

[79] P.L. Veya and J.K. Kochi, *J. Organomet. Chem.*, 1995, **488**, 4 - 8.

[80] C. Costa-Coquelard, S. Sorgues and L. Ruhlmann, *J. Phys. Chem. A,* 2010**, 114***,* 6394 - 6400.

[81] D. Schaming, C. Costa-Coquelard, S. Sorgues, L. Ruhlmann and I. Lampre, *Appl. Catal. A - Gen.*, 2010, **373**, 160 - 167.

[82] D. Schaming, C. Costa-Coquelard, I. Lampre, S. Sorgues, M. Erard, X. Liu, J. Liu, L. Sun, J. Canny, R. Thouvenot and L. Ruhlmann, *Inorg. Chim. Acta,* 2010, **363**, 2185 - 2192.

[83] Y. L. Zhong, W. Ng, J-X. Yang and K. P. Loh, J. *Am. Chem. Soc.*, 2009, **131**, 18293 - 18298.

[84] M. Clemente-León, E. Coronado, C. J. Gómez-García, C. Mingotaud, S. Ravaine, G. Romualdo-Torres and P. Delhaès, *Chem. Eur. J.*, 2005, **11**, 3979 - 3987.

[85] N. Fay, E. Dempsey, T. McCormac*, J. Electroanal. Chem.,* 2005, **574**, 359 - 366.

[86] M. Zynek, M. Serantoni, S. Beloshapkin, E. Dempsey and T. McCormac, *Electroanal.*, 2007, **19**, 681 - 689.

[87] L. Cheng and J. A. Cox, *Chem. Mater.,* 2002**, 14***,* 6 - 8.

---

[88] E. C. Constable, C. E. Housecroft, M. Cattalini and D. Phillips, *New J. Chem.*, 1998, 193 - 200.

[89] T. Dong, H. Ma, W. Zhang, L. Gong, F. Wang and C. Li, *J. Colloid Interf. Sci.,* 2007, **311**, 523 - 529.

[90] H. Ma, T. Dong, F. Wang, W. Zhang and B. Zhou, *Electrochim. Acta*, 2006, **51**, 4965 - 4970.

[91] Y-Q. Zhang, K-Z. Wang and L-H. Gao, *Colloid Surface A.,* 2005, **257**, 391 - 394.

[92] Y-Q. Zhang, L-H. Gao, K-Z. Wang, H-J. Gao and Y-L. Wang, *J. Nanosci. Nanotech.*, 2008, **8**, 1248 - 1253.

[93] H. Ma, J. Peng, Y. Chen, Y. Feng and E. Wang, *J. Solid State Chem.*, 2004, **177**, 3333 - 3338.

[94] X-L. Wang, Z-B. Han, E. Wang, H. Zhang and C-W. Hu, *Electroanalysis*, 2003, **15**, 1460 - 1464.

[95] L. Bi, H. Wang, Y. Shen, E. Wang and S. Dong, *Electrochem. Commun.*, 2003, **5**, 913 - 918.

[96] B. Wang, L-H. Bi and L-X. Wu, *J. Mater. Chem.*, 2011, **21**, 69 - 71.

[97] A. Salimi, A. Korani, R. Hallaj, S. Soltanian and H. Hadadzadeh, *Thin Solid Films*, 2010, **518**, 5304 - 5310.

[98] G. Gao, L. Xu, W. Wang, W. An, Y. Qiu, Z. Wang and E. Wang, *J. Phys. Chem. B,* 2005**,** **109***,* 8948 - 8953.

[99] A. Salimi, A. Korani, R. Hallaj, R. Khoshnavazi and H. Hadadzadeh, *Anal. Chim. Acta*, 2009, **635**, 63 - 70.

[100] M. Clemente-Léon, E. Coronado, Á. López-Muñoz, D. Repetto, T. Ito, T. Konya, T. Yamase, E. C. Constable, C. E. Housecroft, K. Doyle, and S. Graber, *Langmuir* 2010, **26**, 1316 - 1324.

[101] Y. Shen, J. Liu, J. Jiang, B. Liu, and S. Dong, *J. Phys. Chem. B*, 2003, **107**, 9744 - 9748.

[102] Y. Jin, L. Xu, L. Zhu, W. An and G. Gao, *Thin Solid Films*, 2007, **515**, 5490 - 5497.

[103] Y. Yang, L. Xu, F. Li, X. Du and Z. Sun, *J. Mater. Chem.*, 2010, **20**, 10835 - 10840.

[104] S. Gao, R. Cao and C. Yang, *J. Colloid Interface Sci*, 2008, **324**, 156 - 166.

---

[105] A. M. Bond, J. C. Eklund, N. Fay, P. J.S. Richardt and A. G. Wedd, *Inorg. Chim. Acta*, 2008, **361**, 1779 - 1783.

[106] Y. V. Geletii, Z. Huang, Y. Hou, D. G. Musaev, T. Lian and C. L. Hill, *J. Am. Chem. Soc.,* 2009, **131**, 7522 - 7523.

[107] F. Puntoriero, G. La Ganga, A. Sartorel, M. Carraro, G. Scorrano, M. Bonchio and S. Campagna, *Chem. Commun.,* 2010, **46**, 4725 - 4727.

[108] M. Orlandi, R. Argazzi, A. Sartorel, M. Carraro, G. Scorrano, M. Bonchio and F. Scandola, *Chem. Commun.,* 2010, **46**, 3152 - 3154.

[109] J. Zhu, Q. Zeng, S. O'Carroll, T. E. Keyes and R. J. Forster, *Electrochem. Commun.,* 2011, **13**, 899 - 902.

[110] http://www.energyandcapital.com/articles/solar-energy-stocks/542

[111] (a) http://www.sj-solar.com/

(b) http://cleantechnica.com/2011/04/19/solar-junction-breaks-concentrated-solar-world-record-with-43-5-efficiency/

[112] S. But, S. Lis, R. Van Deun, T. N. Parac-Vogt, C. Gorller-Walrand and K. Binnemans, *Spectrochim. Acta A*, 2005, **62**, 478 - 482.

[113] L. Xu, H. Zhang, E. Wang, D. G. Kurth and Z. Li, *J. Mater. Chem*., 2002, **12**, 654 - 657.

[114] J. Chen, L. M. Ai, W. Feng, D. Q. Xiong, Y. Liu, W. M. Cai, *Mater. Lett*., 2007, **61**, 5247 - 5249.

[115] Y. Wang, X. Wang, C. Hu and C. Shi, *J. Mater. Chem*., 2002, **12**, 703 - 707.

[116] B. Qin, H. Chen, H. Liang, L. Fu, X. Liu, X. Qiu, S. Liu, R. Song and Z. Tang, *J. Am. Chem. Soc*. 2010, **132**, 2886 - 2888.

[117] S. Liu and Z. Tang, *Nano Today*, 2010, **5**, 267 - 281.

[118] C-J. Ho, R. J. Babbitt and M. R. Topp, *J. Phys. Chem.,* 1987, **91***,* 5599 - 5607.

[119] J. R. Lakowicz, *Principles of fluorescence spectroscopy*, Springer, Volume 1, 3rd ed, 2006, Chapter 8, pages 277 - 330.

---

[120] P. C. Innis, F. Masdarolomoor, L. A. P. Kane-Maguire, R. J. Forster, T. E. Keyes and G. G. Wallace, *J. Phys. Chem. B,* 2007**, 111***,* 12738 - 12747.

[121] http://goldbook.iupac.org/FT07377.html

[122] L. Cosgrave, M. Devocelle, R. J. Forster and T. E. Keyes, *Chem. Commun.*, 2010, **46**, 103 - 105.

[123] K. Suhling, J. Siegel, D. Phillips, P. M. W. French, Sandrine Lévêque-Fort, S. E. D. Webb and D. M. Davis, *Biophys. J.*, 2002, **83**, 3589 - 3595.

[124] http://nobelprize.org/nobel_prizes/chemistry/laureates/2008/

[125] S. Wallin, J. Davidsson, J. Modin and L. Hammarstrom, *J. Phys. Chem. A,* 2005, **109***,* 4697 - 4704.

[126] http://www.photophysics.com/lks60options.php

[127] J. D. Schuttlefield and V. H. Grassian, *J. Chem. Educ.*, 2008, **85**, 279 - 281

[128] http://jolisfukyu.tokai-sc.jaea.go.jp/fukyu/tayu/ACT97E/07/0701.htm

[129] J. R. Ferraro, *Introduction to Raman Spectroscopy*, Academic Press, New York, 1994.

[130] A. Nicoara, A. Patrut, D. Margineanu and A. Müller, *Electrochem. Commun.*, 2003, **5**, 511 - 518.

[131] A. Müller, S. Qaiser Nazir Shah, H. Bögge, M. Schmidtmann, P. Kögerler, B. Hauptfleisch, S. Leiding and K. Wittler, *Angew. Chem. Int. Ed.*, 2000, **39**, 1614 - 1616.

[132] T. Yamase, S. Kumagai, P. V. Prokop, E. Ishikawa and A-R. Tomsa, *Inorg. Chem.*, 2010, **49**, 9426 - 9437.

[133] A. M. Khenkin, L. J. W. Shimon and R. Neumann, *Inorg. Chem.*, 2003, **42**, 3331 - 3339.

Chapter 2:

Experimental

2.1 – Materials:

Solution phase studies were carried out in aerated spectroscopic grade acetonitrile, benzyl alcohol, ethanol and dimethylsulfoxide (Sigma-Aldrich, spectrophotometric grade). The solvents were dried over molecular sieves (3 Å) prior to use. Diethyl ether (bench grade) was dried over molecular sieves (3 Å) before use. All aqueous solutions were prepared using deionised water. Concentrated sulfuric acid (VWR) was diluted to 0.5 M with deionised water. Perchloric acid 60% was diluted to 1.0 M with deionised water prior to use. d^6-dimethylsulfoxide and d^3-acetonitrile (Euriso-top) were used as purchased. D_2O (Apollo Scientific) was used as purchased. 1.0 M tetrabutylammmonium hydroxide solution (Fluka) was used as purchased. Ludox AM-30 colloidal silica solution was used as purchased (Aldrich).

Potassium bromide (Riedel de Haën) was heated to 100°C to remove residual water content prior to use. Potassium hexafluorophosphate and lithium perchlorate (Aldrich) were used as purchased. Potassium chloride, tetrabutylammonium tetrafluoroborate, tetrabutylammonium bromide and tetrahexylammonium bromide (Fluka) were used as purchased.

2.2 – Syntheses:

$[Ru(bpy)_3](PF_6)_2$ was synthesised according to literature methods.[1] $[(Pn)_4N]_4\alpha/\beta$-$[Mo_{18}O_{54}(SO_3)_2]$ and $[Ru(bpy)_3]_2\alpha/\beta$-$[Mo_{18}O_{54}(SO_3)_2]$ were provided by Prof. Leroy Cronin, University of Glasgow and were synthesized according to the literature.[2, 3] The polyoxomolybdate $[(Hex)_4N]_4[Mo_{18}O_{54}(SO_4)_2]$ was synthesized according to the procedure of Cooper *et al*.[4] It was characterized by UV/Vis, FTIR and Raman spectroscopies; and also by cyclic voltammetry and ESI-MS. The parent ion peak at m/z = 696 was clearly visible. $[Ru(bpy)_2(PVP)_{10}](NO_3)_2$ was synthesized according to the literature by Mr. Shane O' Carroll.[5] The metallopolymer was characterized by UV/Vis and emission spectroscopy, and the absence of appreciable amounts of the undesired N_5 coordinated monochloride complex was confirmed by cyclic voltammetry. $[Ru(bpy)_2(PVP)_{10}](PF_6)_2$ was synthesized by dissolving $[Ru(bpy)_2(PVP)_{10}](NO_3)_2$ in deionised water with extensive sonication, followed by addition of a saturated aqueous solution of KPF_6. The mixture was sonicated for 30 minutes and then centrifuged, the supernatant was removed and fresh deionised water was added. This was repeated in triplicate and afterwards the solid was dried under N_2. It was then redissolved in spec grade MeCN and any insoluble (nitrate) material was removed by centrifugation. The final concentration of the $[Ru(bpy)_2(PVP)_{10}](PF_6)_2$ solution was measured by UV/Vis spectrophotometry using an ε value of 10233 $M^{-1}.cm^{-1}$ at 455 nm.[5]

$[Ru(bpy)_2(caip\ co\text{-}poly)_n](ClO_4)_2$ (n = 5, 7, 9) were synthesized by Dr. Qiang Zeng according to the following procedure: As illustrated in Scheme 1, the synthesis of the copolymers involved free radical polymerization of styrene with 4-vinylpyridine chloride at ratios of 8:1, 6:1, and 4:1 in order to achieve co-polymer ratios of the same values. The molar mass, obtained by gel permeation chromatography (GPC), revealed that the copolymer-CH_2Cl backbones contain 3, 5, and 7 repeat units, respectively. ^{1}H-NMR spectra indicated that there were no significant changes in the chemical shifts of the backbone and aromatic protons with differing monomer ratio. However, the methylene protons shifted downfield by 0.23 to 4.76 ppm on replacement of chloride by phthalimide and then shifted upfield by 0.77 to 3.79 ppm upon changing from a phthalimide to a primary amine. The chemical shift of these methylene protons was observed at 4.47 ppm in their metallopolymers. This observation is in agreement with a previous report on the characterisation of a similarly structured copolymer and its metallopolymers, and suggests that the alkyl chlorides within the copolymers were first transformed into primary amines, and that these amine groups were later coupled with the terminal carboxylic acid groups of $[Ru(bpy)_2(caip)](ClO_4)_2$ through amide bonds to form the new metallopolymers.

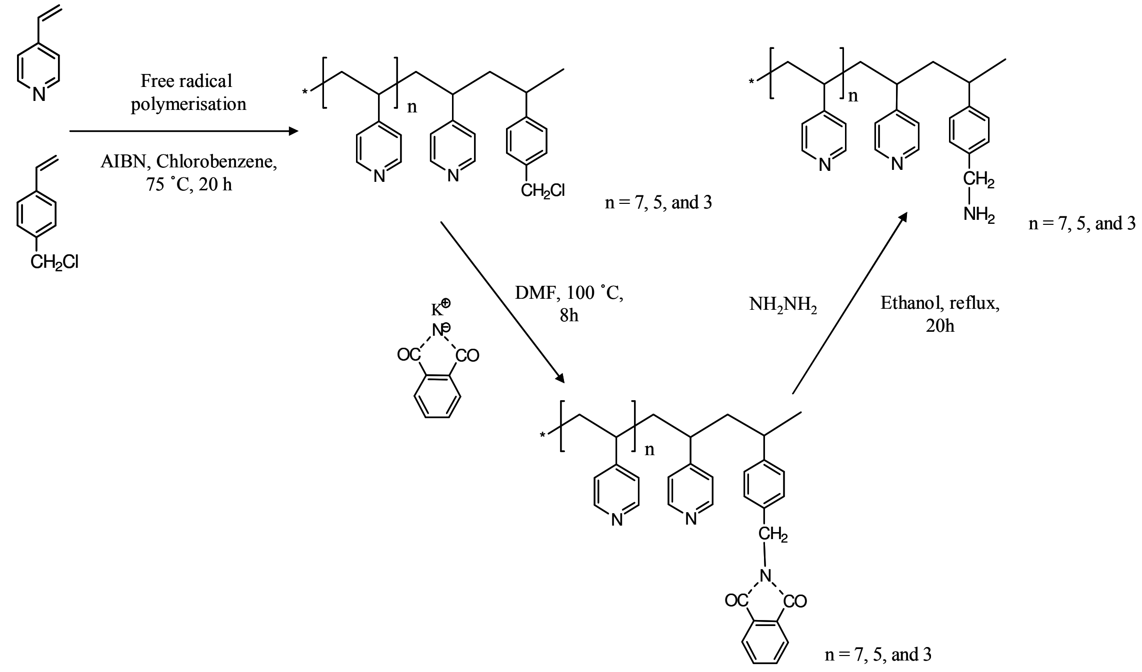

Fig 2.1.1: Synthesis of the copolymer backbones used to make the metallopolymers [Ru(bpy)$_2$(caip co-poly)$_n$](ClO$_4$)$_2$ (n = 5, 7, 9).

The relative ratio of the two monomers in each copolymer backbone could be conveniently calculated from the peak areas of aromatic protons (or backbone protons) and methylene protons in ^{1}H-NMR. These calculated results are very close to the desired ratios and indicates that the target structures of copolymer backbones, with one derivatized styrene monomer every 8, 6, or 4 styrene units, were obtained. Furthermore, the peak areas of aromatic protons and methylene protons can be used to estimate the loading of Ru complexes in the metallopolymer. The extent of loading is consistent with the ratio of the two monomers within the copolymer backbone suggesting that all amine groups are completely coupled with the carboxylic acid containing Ru complexes through amide bonds. FTIR spectroscopy was also used to confirm the formation of the amide. The amide ν(C═O) stretch at 1708 cm^{-1} is observed in the infrared spectrum of the parent Ru complex and is attributed to the pendant carboxylic acid group. In the metallopolymer the band occurring at 1708 cm^{-1} is lost and replaced with a band at 1647 cm^{-1}, which is attributed to the amide carbonyl stretch mode.

The deprotonated form of the 7-1 copolymer, $[Ru(bpy)_2(caip\ co\text{-}poly)_7](ClO_4)$, was synthesized by slow addition of 1.0 M aqueous TBAOH solution to a 1 mM $[Ru(bpy)_2(caip\ co\text{-}poly)_7](ClO_4)_2$ solution in MeCN. The solution turned cloudy and was allowed to sit overnight in the dark. The precipitated $[Ru(bpy)_2(caip\ co\text{-}poly)_7](ClO_4)$ was isolated by centrifugation. The supernatant was removed and the product rinsed thoroughly with MeCN and water. The $[Ru(bpy)_2(caip\ co\text{-}poly)_7]^+$ complex was insoluble in MeCN but soluble in DMSO. The change in protonation state was confirmed by resonance Raman spectroscopy.

The ion-pair composite material $[Ru(bpy)_2(PVP)_{10}]_{4.5}[Mo_{18}O_{54}(SO_4)_2]$ was synthesized by the dropwise addition of a solution of approximately 4.5 mM $[Ru(bpy)_2(PVP)_{10}](NO_3)_2$ dissolved with extensive sonication in DMSO to a solution of 1 mM $[(Hex)_4N]_4[Mo_{18}O_{54}(SO_4)_2]$ fully dissolved in MeCN with vigorous stirring. An orange-brown precipitate was instantly formed, and the mixture was allowed to stand overnight in the dark. The solutions were centrifuged and the supernatant removed, and the solid was then washed with MeCN, to remove any unbound polymer and centrifuged twice more. After the third centrifugation the supernatant was colorless and all soluble unassociated material was deemed removed. The solids were then washed with diethyl ether and centrifuged a final time. After the supernatant was removed the brown solids were dried under a stream of N_2. $[Ru(bpy)_2(caip\ co\text{-}poly)_7]_5[Mo_{18}O_{54}(SO_4)_2]$ was synthesized as above. The solids were characterized by ATR-FTIR and EDX spectroscopies.

The organic soluble analogue $[(But)_4N]_6\alpha\text{-}[P_2W_{18}O_{62}]$ was synthesized by slow addition of a saturated aqueous solution of tetrabutylammonium bromide to a solution of approximately 1 mM $K_6\alpha\text{-}[P_2W_{18}O_{62}]$. The polyoxotungstate solution turned cloudy and was let sit overnight in the dark. The following day a white precipitate was formed and was collected by centrifugation. The solid was washed several times with deionised water to remove any residual aqueous-soluble $K_6\alpha\text{-}[P_2W_{18}O_{62}]$ and was finally dried under a stream of N_2. The molar extinction coefficient of $[(But)_4N]_6\alpha\text{-}[P_2W_{18}O_{62}]$ in MeCN was calculated as $\varepsilon_{305\ nm} = 27400 \pm 550\ M^{-1}.cm^{-1}$. The ion-cluster composite material was synthesized as described in section 2.2.1. The ruthenium to tungsten ratio was quantified by EDX spectroscopy

In order to maximize the amount of data collected for Chapter 6, samples of a wide variety of transition metal complexes were obtained from colleagues in the Keyes research group. Each complex was analyzed by ^{1}H-NMR and/or ESI-MS before synthesis of the composite materials was performed. The following list of complexes was used.

2.2.1 - $[Os(bpy)_2(p0p)_2]^{2+}$: Synthesized by Dr. Yann Pellegrin according to the literature.[6]

2.2.2 - $[Os(bpy)_2(qpy)]^{2+}$: Synthesized by Dr. Yann Pellegrin according to the literature.[11]

2.2.3 - $[Ru(dpp)_3]^{2+}$: Synthesized according to procedure.[7]

2.2.4 - $[Ru(bpy)_2(caip)]^{2+}$: Synthesized by Mr. Ciarán Dolan according to procedure.[8]

2.2.5 - $[Ru(dpp)_2(caip)]^{2+}$: Synthesized by Ms. Lynda Cosgrave according to procedure.[8]

2.2.6 - $[Ru(dppz)_2(caip)]^{2+}$: Synthesized by Ms. Lynda Cosgrave according to procedure.[9]

2.2.7 - $[Os(bpy)_3]^{2+}$: Synthesized according to procedure.[10]

2.2.8 - $[Os(bpy)_2(PVP)_{10}]^{2+}$: Synthesized by Dr. Emmet O' Reilly according to procedure.[5]

2.2.9 - $[Ru(bpy)_2(PVP)_{10}]^{2+}$: Synthesized by Mr. Shane O' Carroll according to procedure.[5]

2.2.10 - $[Ru(bpy)_2(qpy)]^{2+}$: Synthesized by Dr. Yann Pellegrin according to procedure.[11]

2.2.11 - $[Fe(bpy)_3]^{2+}$: Synthesized by Mr. Gavin Sewell according to procedure.[12]

2.2.12 - $[Fe(terpy)_2]^{2+}$: Synthesized by Mr. Gavin Sewell according to procedure.[12]

2.3 – Spectroscopic methods:

UV/Vis spectra were measured using either a Carey 50 spectrophotometer or a Jasco V-670 UV/Vis/NIR spectrophotometer. Solution phase measurements were conducted in Hellma quartz cuvettes of either 1 cm or 0.2 cm optical path lengths. Spectra of self-assembled thin films on ITO electrodes were collected by blanking in air and using a clean, blank ITO electrode as the baseline.

Steady state emission measurements were undertaken using a Cary Eclipse Fluorescence spectrometer with 10 nm emission and 10 nm excitation slits exciting at 450 nm.

Time-correlated single photon counting (TCSPC) measurements were carried out using a Picoquant 'Fluotime 100' compact fluorescence lifetime spectrometer. The 450 nm pulse was generated by Picoquant 'PDL 800-B' pulsed diode laser and a Thurlby Thandar Instruments (TTi) TGP110 10MHz pulse generator. An average of three measurements was taken for each sample. The instrument response function was measured using a scattering Ludox AM-30 colloidal silica solution.

Resonance Raman spectra were collected on a Horiba Jobin Yvon HR800 UV spectrometer. The laser lines were generated by a Coherent Innova 70c tuneable Ar-ion laser (457.9, 488, 514.5 nm), a HeNe laser (633 nm) or a 785 nm diode laser. A 10x or 100x microscope objective was used to focus the laser beam onto a sample ground into a compressed KBr disc. A 600 lines/mm diffraction grating was employed. The x-axis was calibrated versus the Rayleigh line (0 nm) and the phonon mode from silicon wafer (520 cm^{-1}).

FTIR spectroscopy was performed using a Varian 610-IR FTIR microscope with either a slide-on ATR accessory with a germanium crystal tip or with in transmittance mode with samples dispersed in KBr discs. The purified solid powder samples for ATR were mounted on a clean gold substrate and each spectrum acquired consisted of an average of 256 scans.

NMR spectra were recorded on a 600 MHz Bruker Advance series spectrometer operating at 600 MHz (^1H), 150 MHz (^{13}C) 162 MHz (^{31}P) or 61 MHz (^{15}N).

Field emission scanning electron microscopy was performed on a Hitachi S-5500 SEM, and elemental analyses were performed with a coupled EDX spectrometer operating at an accelerating voltage of 10 keV. The sample was either the isolated solid composite mechanically adhered to a carbon tape surface or a composite thin film self-assembled onto an ITO electrode. The instrument was calibrated versus pure cobalt, and ruthenium to molybdenum/tungsten ratios for the composites were calculated from an average of five measurements.

Fluorescence lifetime imaging (FLIM, Zeiss LSM 50) was used to record luminescence images of the metallopolymers on silicon wafers, which were pre-cleaned by rinsing with acetone and ethanol, followed by air-drying. An argon ion laser was used for 488 nm excitation. The scanned images contain 512 × 512 pixels.

Transient absorption measurements were carried out on solid samples in KBr employing a LKS.60 system from Applied Photophysics, Leatherhead, Surrey, UK. A Quantel 'Brilliant Eazy' Q-switched Nd:YAG laser (third harmonic, 355 nm) was used as excitation source. The signal was monitored with a pulsed Oriel 150 W Xe arc lamp. The signal was detected at right angles to the laser source with an R928 5-stage photomultiplier coupled to an Agilent 60 MHz 'Infiniium DSO8064A' digital oscilloscope and a monochromator with slit widths of 0.5 nm. A 355 nm long pass filter was employed to remove laser light.

Electrospray-ionization mass spectra were obtained using a Bruker Daltonics Esquire ESI-ion trap mass spectrometer operating in negative mode.

2.4 - Electrochemical and photoelectrochemical methods:

Solution phase cyclic voltammetry of $K_6\alpha$-$[P_2W_{18}O_{62}]$ was performed in D_2O containing 1 M H_2SO_4. The solution was degassed with N_2 for 20 minutes prior to use. The working electrode was a glassy carbon macro-disk ($A = 0.0717\ cm^2$), the counter electrode was a Pt wire and the reference electrode was Ag/AgCl (calibrated versus SCE). The scan rate used was 10 $mV.s^{-1}$.

Photoelectrochemical measurements were carried out using a standard three-electrode system and a CH Instruments 720b electrochemical workstation. ITO slides (Delta Technologies Ltd., Stillwater, MN) were employed as the working electrodes and were sonicated in ethanol prior to use. The working electrodes were prepared by drop-casting 25 µl of 1 mM (Chapter 3) or 100 µl of 1×10^{-4} M (Chapter 4) acetonitrile suspension/solution of Ru:POM adduct onto an ITO working electrode and allowing it to dry in air. A Pt flag was used as the counter electrode. An Ag wire was employed as the pseudo-reference, which was calibrated versus the IUPAC recommended ferrocene (Fc/Fc^+) internal reference. The potential was either kept constant at + 400 mV (Chapter 3) or systematically from + 400 mV to + 800 mV in repeat experiments (Chapter 4). Neat benzyl alcohol was used as both the solution and sacrificial donor; and no electrolyte was added to avoid ion-pair disruption.

The light source for photochemistry was an Oriel 68811 arc lamp employing a 350 W Xe bulb and a > 400 nm LP filter (Chapter 3) or 480 ± 5 nm narrow band filter (Chapter 4) and was kept at a distance of 10 cm from the sample solution. The optical filters were purchased from Spectrogon UK Ltd.

The photoelectrochemistry in Chapter 5 was performed using self-assembled films on ITO electrodes. The films were prepared by immersing a pre-cleaned ITO electrode into a concentrated solution (approximately 5 mM) of $[Ru(bpy)_2(PVP)_{10}](NO_3)_2$ in 80:20 $EtOH/H_2O$ for 30 minutes. The sample was removed and dried in air, then immersed in a solution of MeCN to remove any unbound surface material. The slide was again dried in air before immersion for another 30 minutes in a 1 mM aqueous solution of $K_6\alpha\text{-}[P_2W_{18}O_{62}]$. The electrode was removed, dried and rinsed as described above. For the films comprised of $\alpha\text{-}[P_2W_{18}O_{62}]^{6-}$ or $[Ru(bpy)_2(PVP)_{10}]^{2+}$ alone the supporting electrolyte used was 0.1 M $(But)_4NBF_4$ in MeCN. However the composite self-assembled film consisting of both ions was unstable in this solvent and hence 0.1 M $(But)_4NBF_4$ in BnOH was used.

UV/Vis/NIR and resonance Raman spectroelectrochemistry were performed using a standard three-electrode system and a CH Instruments 720b electrochemical workstation. The working electrode was a high surface-area Pt mesh; the counter electrode a Pt wire and the pseudo-reference electrode was an Ag wire, calibrated versus the Fc/Fc^+ couple.

2.5 – References:

---

[1] R. A. Palmer and T. S. Piper, *Inorg. Chem.*, 1966, **5**, 864.

[2] D-L. Long, P. K. Gerler and L. Cronin, *Angew. Chem. Int. Ed.,* 2004, **43**, 1817 - 1820.

[3] M. Góral, T. McCormac, E. Dempsey, D-L. Long, L. Cronin and A.M. Bond, *Dalton Trans*, 2009, 6727.

[4] J. B. Cooper, D. M. Way, A. M. Bond and A. G. Wedd, *Inorg. Chem.,* 1993, **32**, 2416.

[5] R. J. Forster and J. G. Vos, *Macromolecules*, 1990, **23**, 4372 - 4377.

[6] T. Albrecht, K. Moth-Poulsen, J. B. Christensen, A. Guckian, T. Bjørnholm, J. G. Vos and J. Ulstrup, *Faraday Discuss.*, 2006, **131**, 265 - 279.

[7] A. Yamagishi, Y. Goto and M. Taniguchi, *J. Phys. Chem.*, 1996**, 100**, 1827 - 1832.

[8] Y. Pellegrin, R. J. Forster and T. E. Keyes, *Inorg. Chim. Acta*, 2009, **362**, 1715 - 1722.

[9] L. Cosgrave, M. Devocelle, R. J. Forster and T. E. Keyes, *Chem. Commun.*, 2010, **46**, 103 - 105.

[10] C. Creutz, M. Chou, T. L. Netzel, M. Okumura and N. Sutin, *J. Am. Chem. Soc.*, 1980, **102**, 1309 - 1319.

[11] R. J. Forster and T. E. Keyes, *J. Phys. Chem. B,* 1998, **102***,* 10004 - 10012.

[12] G. Sewell, R. J. Forster and T. E. Keyes, *J. Phys. Chem. A,* 2008**, 112***,* 880 - 888.

Chapter 3

Photophysical and photochemical properties of $[Ru(bpy)_3]^{2+}$ in the presence of the sulfite Dawson-like type polyoxomolybdates α/β-$[Mo_{18}O_{54}(SO_3)_2]^{4-}$.

3.1 – Introduction:

In the field of photocatalysis, the Dawson polyoxometalate anions (see Fig 3.1.1) are well known as efficient photocatalysts and are capable of multiple proton-coupled redox processes which may be initiated under UV irradiation. In Chapter 1 it was described in detail that $[Ru(bpy)_3]^{2+}$ forms stable electrostatic adducts with the non-reduced Dawson sulfato anions $[M_{18}O_{54}(SO_4)_2]^{4-}$ (where M = Mo, W) to form analytically pure $[Ru(bpy)_3]_2[M_{18}O_{54}(SO_4)_2]$ adducts.[1] The photophysics of these adducts $[Ru(bpy)_3]_2[M_{18}O_{54}(SO_4)_2]$ (where M = Mo, W) have been thoroughly investigated.[2, 3] A remarkable degree of electronic coupling was exhibited between the polyoxoanions and $[Ru(bpy)_3]^{2+}$. This was reflected in the substantial photochemical stability conferred on the normally photolabile $[Ru(bpy)_3]^{2+}$ cation when incorporated into the adduct; and the presence of a new optical transition, assigned as an intramolecular charge-transfer transition from resonance Raman spectroscopy, involving both the polyoxoanion and the $[Ru(bpy)_3]^{2+}$ centres. A separate photoelectrochemical study of $[Ru(bpy)_3]_2[M_{18}O_{54}(SO_4)_2]$ (M = Mo, W) demonstrated that the quantum yield of $[Ru(bpy)_3]_2[Mo_{18}O_{54}(SO_4)_2]$ photoreduction at 420 nm was an order of magnitude higher than that for $[(Hex)_4N]_4[Mo_{18}O_{54}(SO_4)_2]$ in the presence of benzyl alcohol substrate.[4]

In this chapter the photophysical properties of $[Ru(bpy)_3]^{2+}$ in the presence of the sulfite containing Dawson-like anions α/β-$[Mo_{18}O_{54}(SO_3)_2]^{4-}$ are presented. These relatively new structures were first reported in 2004.[5] The replacement of conventional sulfate groups with sulfite groups allows for the possibility of intramolecular electronic communication between the encapsulated sulfur atoms, and indeed α-$[Mo_{18}O_{54}(SO_3)_2]^{4-}$ is more difficult to reduce than the corresponding α-$[Mo_{18}O_{54}(SO_4)_2]^{4-}$ by 105 mV.[6] The differences between the fully oxidized α and β isomers of the sulfite polyoxoanion are minor. The difference in molecular symmetry (see Fig 3.1.1 and also Fig 1.2.4) leads to slight differences in the spectroscopy and electrochemistry of the two ions, which is manifest by the reduction processes occurring between 25 and 55 mV more negative for the β isomer. These differences are unlikely to have a dramatic effect on the binding to $[Ru(bpy)_3]^{2+}$. The unusual distribution of charge within the metal oxide framework results in a distortion of the geometry from the standard Dawson anion to the non-conventional "peanut" configuration, which has also been observed in the non-reduced sulfite polyoxotungstate α-$[W_{18}O_{54}(SO_3)_2]^{4-}$ and in the tin substituted $[H_3SnW_{18}O_{60}]^{7-}$.[7, 8] The sulfite and sulfate containing species exhibit similar spectroscopic properties, however the more recently discovered sulfite anions have not been studied extensively to date. This is likely due to the fact that they are more difficult to synthesize and purify than the corresponding molybdosulfate anion, and that the synthesis of the sulfites was reported far more recently (2004 for the sulfites relative to 1987 for the sulfate).[25] The structures of α-$[Mo_{18}O_{54}(SO_3)_2]^{4-}$, β-$[Mo_{18}O_{54}(SO_3)_2]^{4-}$ and α-$[Mo_{18}O_{54}(SO_4)_2]^{4-}$ are provided in Fig 3.1.1 for comparison.

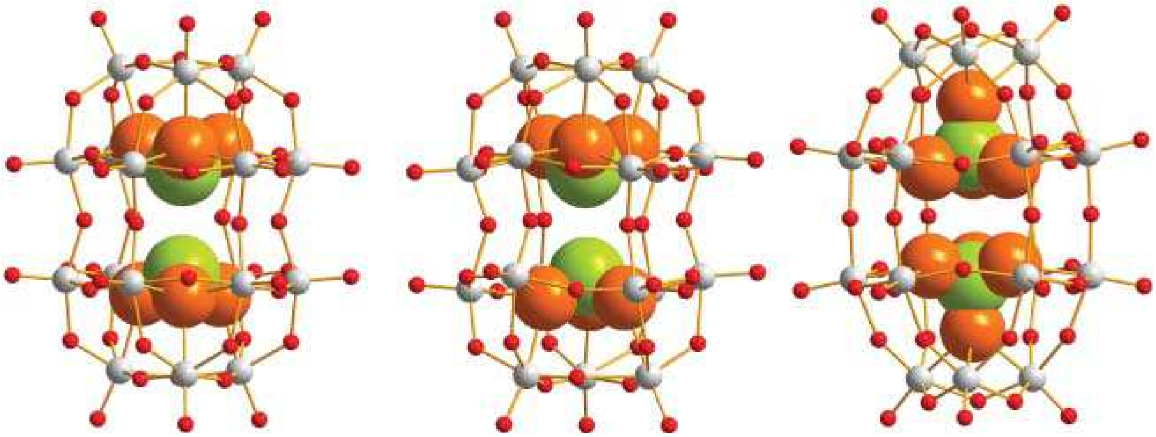

Fig 3.1.1: Structures of the α-SO_3 (left), β-SO_3 (centre) and α-SO_4-based (right) polyoxomolybdate clusters. The encapsulated sulfate and sulfite moieties are not to scale. Reproduced from [9].

The aim of this study, in the context of optimising ruthenium polyoxometalate interactions for sensitized photocatalysis, was to determine how the electronic properties, charge and isomeric structure of these materials influenced their interactions with the $[Ru(bpy)_3]^{2+}$ sensitizer. Our preliminary photoelectrochemical data revealed that $[(Pn)_4N]_4$α-$[Mo_{18}O_{54}(SO_3)_2]$ produced a higher photocurrent than $[(Hex)_4N]_4$α-$[Mo_{18}O_{54}(SO_4)_2]$ under the same conditions. Given the improved photocatalysis evident for the α-$[Mo_{18}O_{54}(SO_3)_2]^{4-}$ anion by comparison with the sulfate analogue, and the improved catalytic efficiency of the sulfate in the presence of $[Ru(bpy)_3]^{2+}$, we were interested to know if these two phenomena could be combined to give even greater photocurrents using $[Ru(bpy)_3]_2$α-$[Mo_{18}O_{54}(SO_3)_2]$.

3.2 – Results and discussion:

3.2.1 - Electronic spectroscopy:

Strong electronic communication between ruthenium polypyridyl complexes and Dawson polyoxometalates has been characterised by significant modification of the UV/Vis spectroscopy of both species. In order to elucidate the presence of any new optical transitions resulting from the electronic interaction between the donor and acceptor moieties, difference electronic spectroscopy was used. This was conducted by adding the absorbance spectra of the individual molecular components electronically at the appropriate concentrations to yield a theoretical sum spectrum and subtracting this from the spectrum of the combined solutions at the same concentrations. This technique is commonly used to reveal subtle spectral changes induced by electronic interaction between the two species.

In this approach, a range of solutions were made up to investigate the effects of varying polyoxometalate concentration on the electronic spectroscopy of a constant concentration of $[Ru(bpy)_3]^{2+}$. Each solution contained 7.3 x 10^{-6} M $[Ru(bpy)_3]^{2+}$ in which the concentration of α or β-$[Mo_{18}O_{54}(SO_3)_2]^{4-}$ was varied between 9.9 x 10^{-7} M to 3.0 x 10^{-5} M in order that the ratio of both metal complexes encompassed the 1:1 and 2:1 range. Fig 3.2.1.1 shows the resulting electronic difference spectra generated by subtracting the electronically combined spectra of separate solutions of $[Ru(bpy)_3]^{2+}$ and α-$[Mo_{18}O_{54}(SO_3)_2]^{4-}$ at its different concentrations from that for the mixtures over the same concentration range.

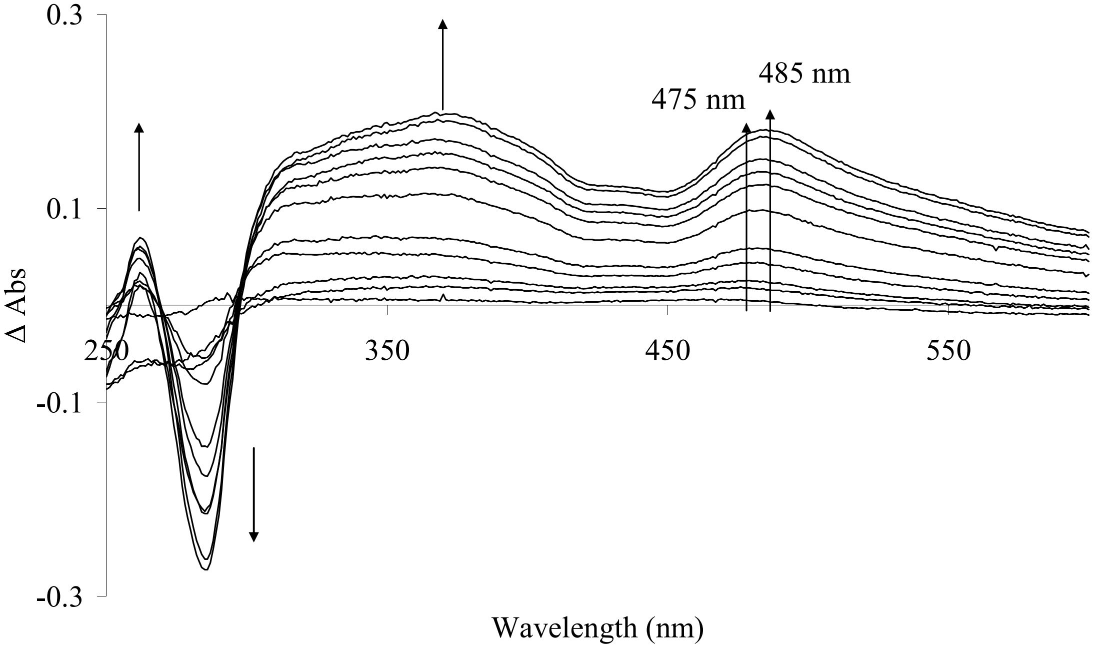

Fig 3.2.1.1: UV/Vis difference spectra of $[Ru(bpy)_3]^{2+}$ (7.3 x 10^{-6} M) upon addition of α-$[Mo_{18}O_{54}(SO_3)_2]^{4-}$ (9.9 x 10^{-7} M – 4.8 x 10^{-6} M) in dry MeCN.

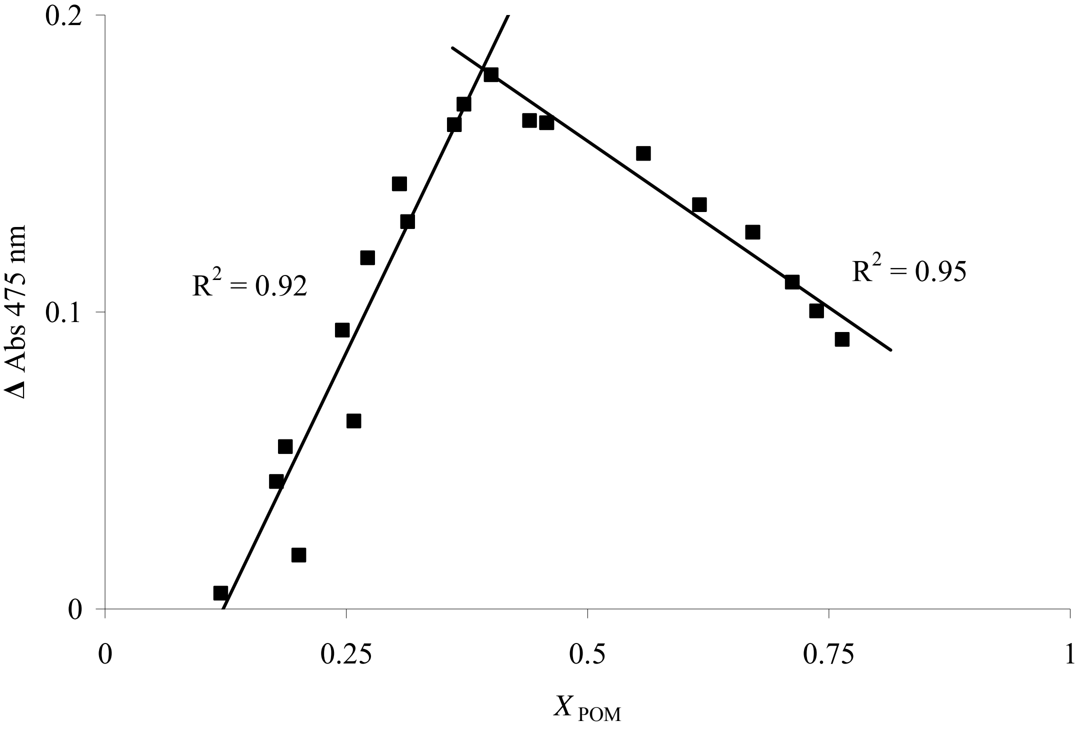

Fig 3.2.1.2: Job's Plot of absorbance change at 475 nm as a function of α-$[Mo_{18}O_{54}(SO_3)_2]^{4-}$ concentration for the data in Fig 3.2.1.1.

Fig 3.2.1.1 shows that titration of the polyoxometalate into the ruthenium solution resulted in a blue shift and reduction in intensity of the feature centred around 280 nm to approximately 260 nm, and the appearance of broad, weak features at approximately 320 nm and 475 nm. These changes are similar to those reported previously for association of $[Ru(bpy)_3]^{2+}$ with the sulfate polyoxometalate, although the extinction coefficient for the new band is approximately 50% smaller in the present case. Interestingly, unlike the sulfato species, when the ratio of $[Ru(bpy)_3]^{2+}$: α-$[Mo_{18}O_{54}(SO_3)_2]^{4-}$ was below 3:1 the λ_{max} of the new visible absorbance band shifted to approximately 485 nm.[2] The feature around 380 nm only appeared at higher polyoxometalate concentrations, which was also observed when the sulfate polyoxoanion was used. As the polyoxometalate was added to $[Ru(bpy)_3]^{2+}$, the ruthenium complex is initially present in a significant excess, so the 2:1 associated species $[Ru(bpy)_3]_2$α-$[Mo_{18}O_{54}(SO_3)_2]$ is predicted to form first. Consequently, the higher energy feature is likely to arise from the 2:1 complex. The corresponding Job's plot in Fig 3.2.1.2 was constructed from the absorbance change at 475 nm.

The maximum of the Job's plot occurred at a polyoxometalate mole fraction (X_{POM}) of approximately 0.375, which corresponds to a α-$[Mo_{18}O_{54}(SO_3)_2]^{4-}$/$[Ru(bpy)_3]^{2+}$ ratio of approximately 0.6:1. This is in good agreement with the expected value of 0.5:1 (X_{POM} = 0.33) and provides strong evidence for a 2:1 complex where the anionic charge on the polyoxometalate is fully compensated for by the dicationic ruthenium complex. When the corresponding isomer β-$[Mo_{18}O_{54}(SO_3)_2]^{4-}$ was investigated slightly different behaviour was observed. These data are presented in Fig 3.2.1.3

.

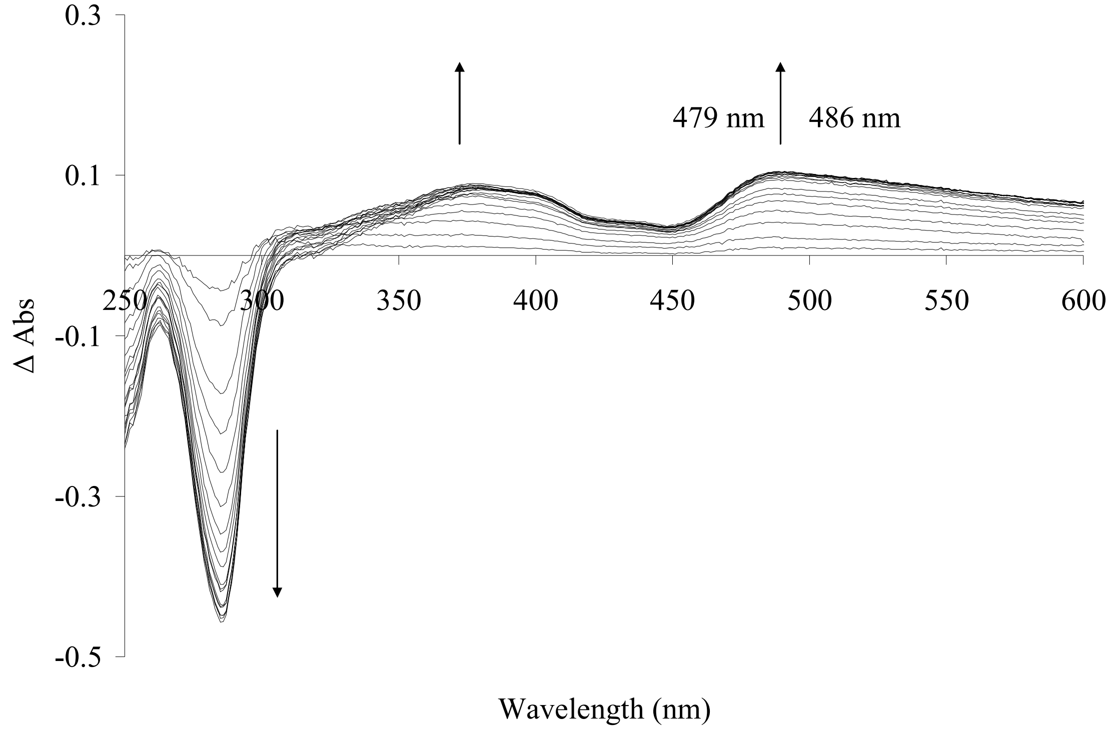

Fig 3.2.1.3: UV/Vis difference spectra of $[Ru(bpy)_3]^{2+}$ (7.3 x 10^{-6} M) upon addition of β-$[Mo_{18}O_{54}(SO_3)_2]^{4-}$ (3.2 x 10^{-7} M – 6.6 x 10^{-6} M) in dry MeCN.

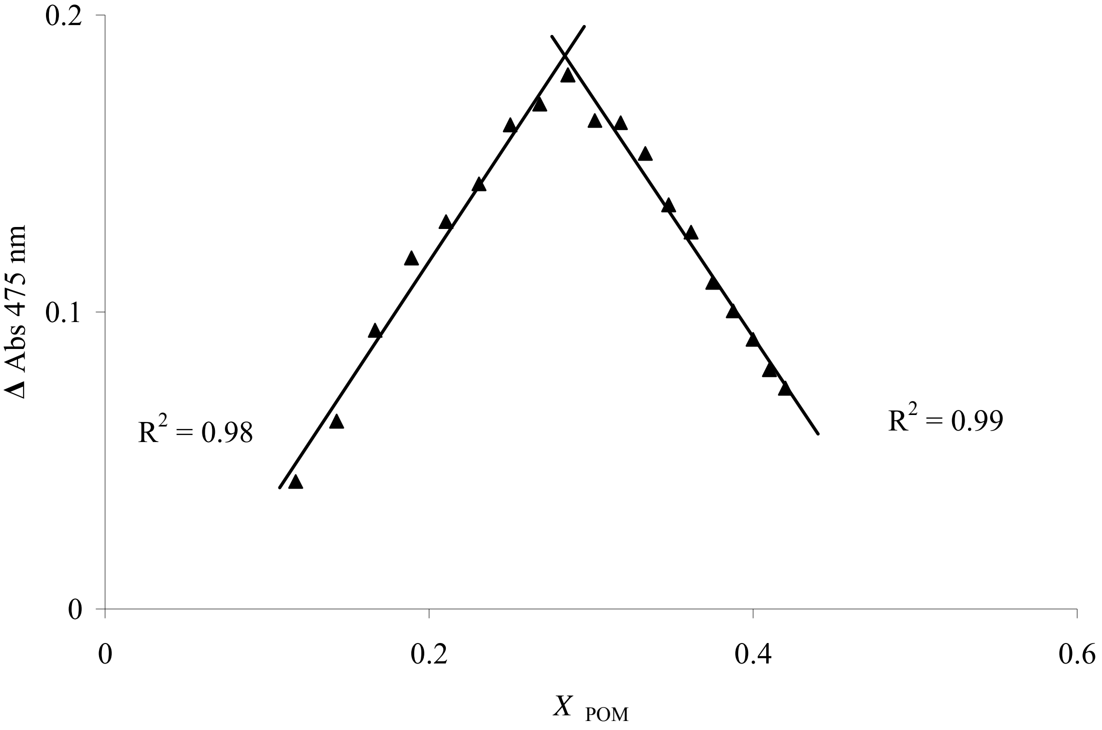

Fig 3.2.1.4: Job's Plot of absorbance change at 475 nm as a function of β-$[Mo_{18}O_{54}(SO_3)_2]^{4-}$ concentration for the data in Fig 3.2.1.3.

Fig 3.2.1.3 shows similar but subtly different behaviour for the association of the β-isomer with $[Ru(bpy)_3]^{2+}$, relative to Fig 3.2.1.1. The new visible feature grew in at 479 nm and shifted to 486 nm at higher concentrations, while the band at 320 nm appears very weak in this case. The Job's plot of the of addition of β-$[Mo_{18}O_{54}(SO_3)_2]^{4-}$ to $[Ru(bpy)_3]^{2+}$ is presented in Fig 3.2.1.4. In the case of the β-isomer the new visible absorbance grew in at 479 nm and shifted to 486 nm upon reaching an X_{POM} value of 0.29, which is close to the expected value of 0.33. These data strongly indicate that $[Ru(bpy)_3]^{2+}$ associates electrostatically with β-$[Mo_{18}O_{54}(SO_3)_2]^{4-}$ in a 2:1 ratio in acetonitrile and that the β-$[Mo_{18}O_{54}(SO_3)_2]^{4-}$/$[Ru(bpy)_3]^{2+}$ adducts have very similar absorption properties to the α-$[Mo_{18}O_{54}(SO_3)_2]^{4-}$/$[Ru(bpy)_3]^{2+}$ adducts.

In order to investigate the formation of the 1:1 adducts the titration was performed in reverse. In these cases the polyoxomolybdate concentration is kept constant and the Ru concentration varied over a large range. Fig 3.2.1.5 (below) shows the titration of increasing the concentration of $[Ru(bpy)_3]^{2+}$ (1.0×10^{-6} M – 4.5×10^{-5} M) in solutions containing a constant concentration (1.0×10^{-5} M) of α-$[Mo_{18}O_{54}(SO_3)_2]^{4-}$.

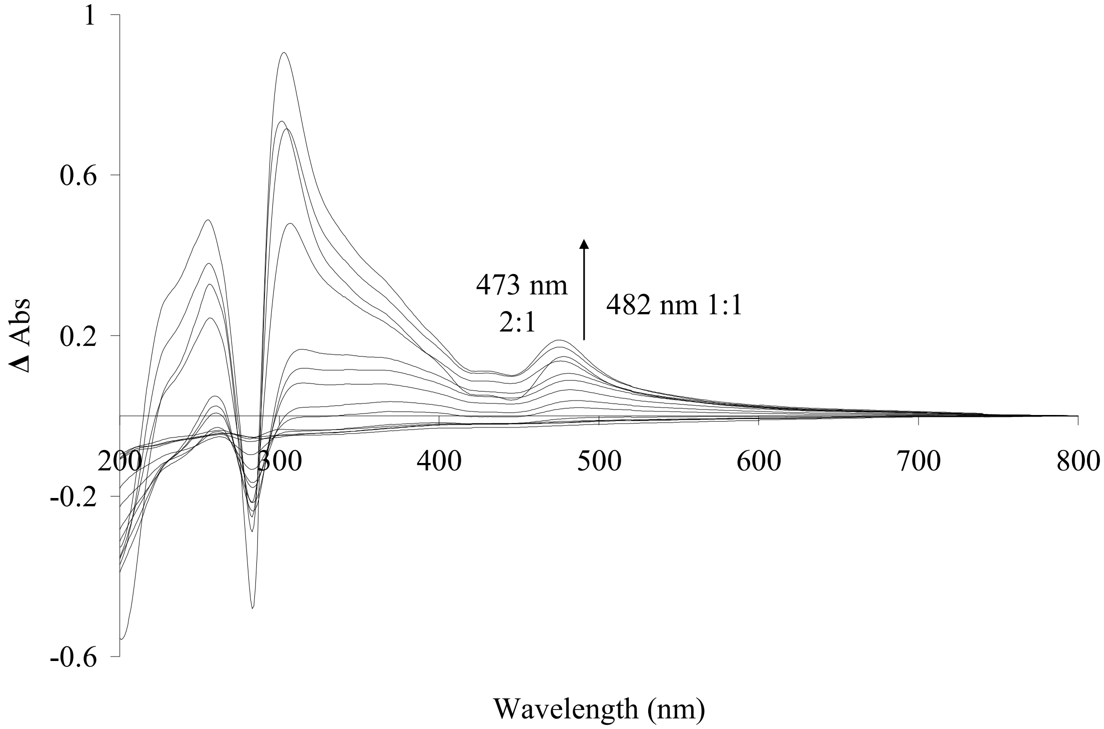

Fig 3.2.1.5: Difference spectroscopy of the reverse titration to observe formation of the 1:1 stoichiometric complex of α-$[Mo_{18}O_{54}(SO_3)_2]^{4-}$/$[Ru(bpy)_3]^{2+}$ in dry MeCN.

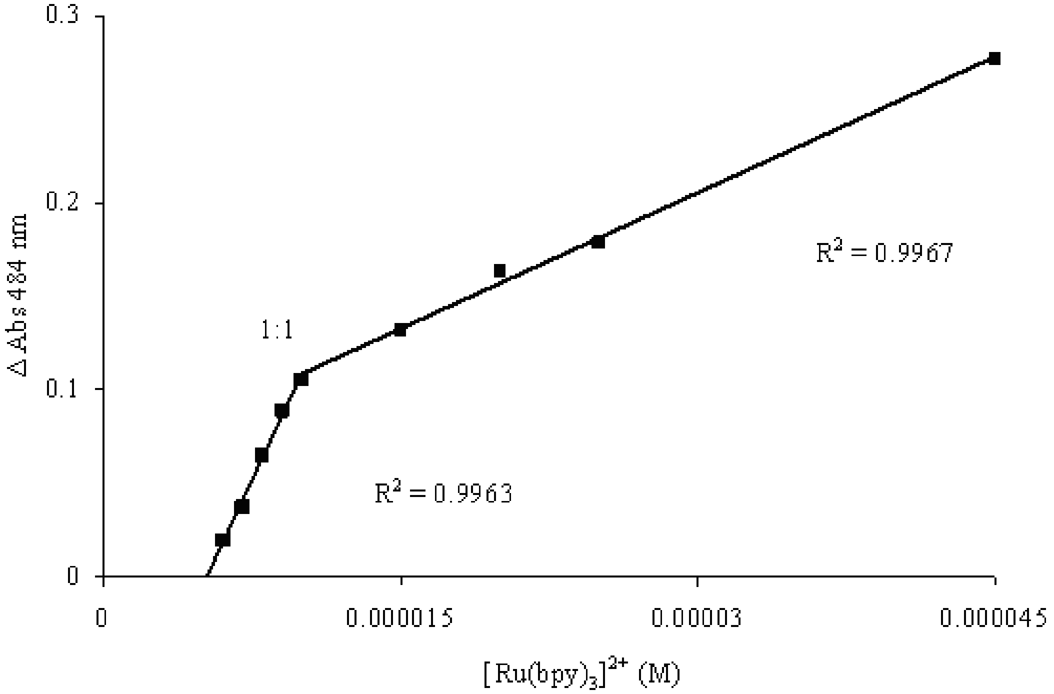

Fig 3.2.1.6: Plot of absorbance at 484 nm change vs $[Ru(bpy)_3]^{2+}$ concentration. Data taken from Fig 3.2.1.5.

In previous photophysical studies of polyoxometalate/$[Ru(bpy)_3]^{2+}$ the concentration of polyoxometalate was varied with respect to constant $[Ru(bpy)_3]^{2+}$ concentration. Initial photophysical measurements were made with a vast excess of $[Ru(bpy)_3]^{2+}$ present; therefore it is the initial formation of the 2:1 species which is observed under these conditions. It was predicted that the 1:1 species would only form when an excess of polyoxometalate is added as the 2:1 species partially dissociates. The formation of the 1:1 complex can be favoured if an initial vast excess of polyoxoanion is used into which $[Ru(bpy)_3]^{2+}$ is titrated. In Fig 3.2.1.5, the initial formation of the 1:1 complex (λ_{max} 482 nm) followed by the 2:1 complex (λ_{max} 473 nm) accurately reflect the λ_{max} values obtained in Fig 3.2.1.1, with minor differences (2 to 3 nm) in the new λ_{max} values were observed. The shapes of the bands in the difference spectra are also different in these spectra, relative to those in Fig 3.2.1.1, with the bands at 320 and 380 nm appearing more intense in this case. The plot of absorbance change in Fig 3.2.1.6 shows two distinct linear regions, and the slope changes at exactly a 1:1 mole ratio.

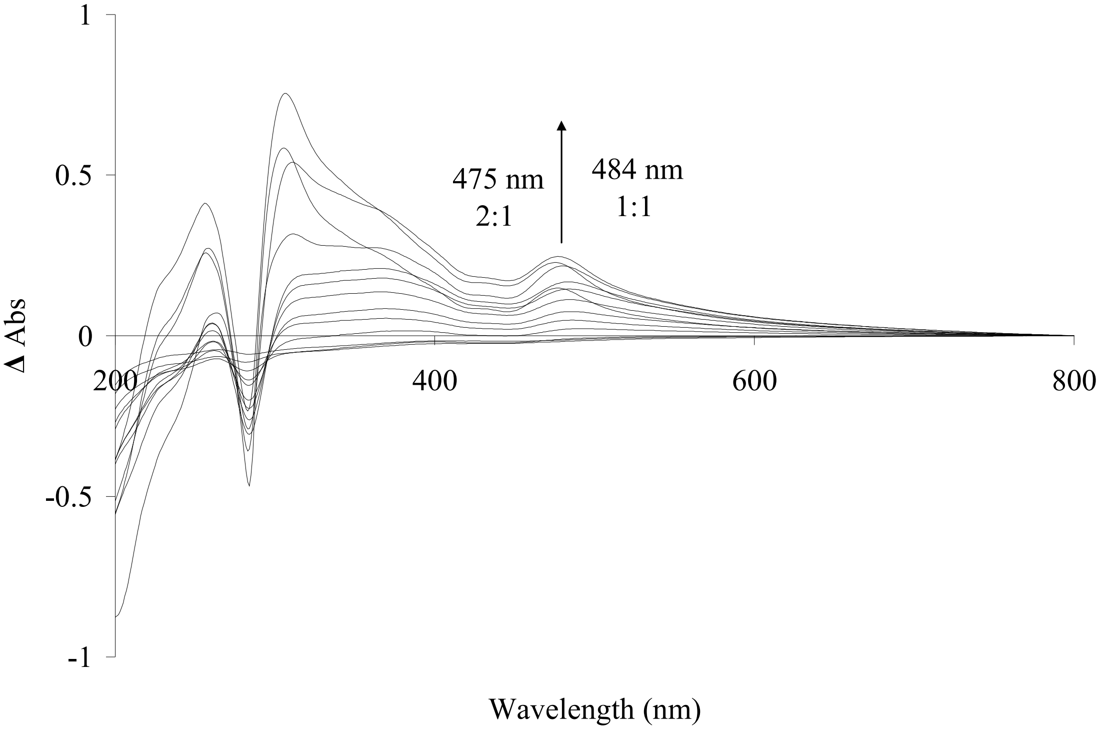

Fig 3.2.1.7: Difference spectroscopy of the reverse titration to observe formation of the 1:1 stoichiometric complex of β-$[Mo_{18}O_{54}(SO_3)_2]^{4-}$/$[Ru(bpy)_3]^{2+}$ in dry MeCN.

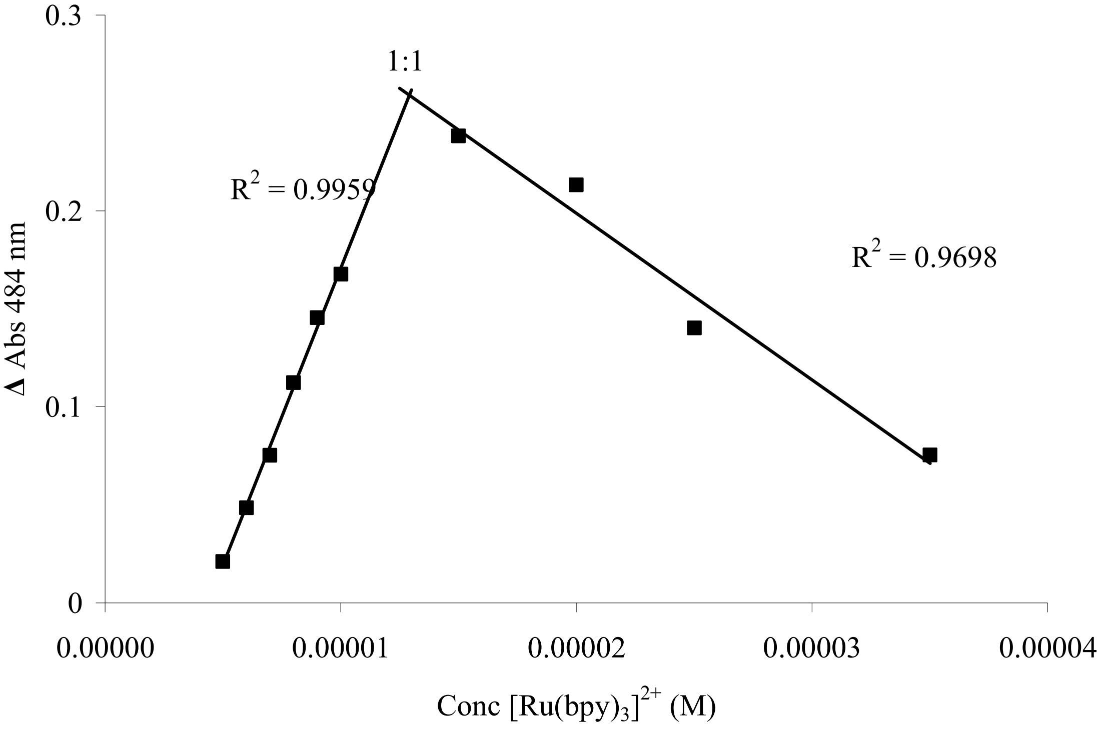

Fig 3.2.1.8: Plot of absorbance change vs $[Ru(bpy)_3]^{2+}$ concentration. Data taken from Fig 3.2.1.7.

Fig 3.2.1.7 reveals that a slightly different trend occurs for the β-isomer. The peaks again grow in at 320 and 380 nm with greater intensity than those in Fig 3.2.1.3 (ie: for the corresponding 2:1 titration). The differences in λ_{max} between the two β-$[Mo_{18}O_{54}(SO_3)_2]^{4-}$/$[Ru(bpy)_3]^{2+}$ titrations are only of the order of 2 to 4 nm. As in the case of the α 1:1 titration, two linear regions are observed which intersect at exactly a 1:1 β-$[Mo_{18}O_{54}(SO_3)_2]^{4-}$/$[Ru(bpy)_3]^{2+}$ mole ratio. However in this case the slope over the high polyoxoanion concentration (ie: 2:1) region appears to be negative. The reason for this apparent difference in slope is unknown but may be due to solubility differences between the two isomers.

3.2.2 – ATR-FTIR spectroscopy:

The ATR-FTIR spectra of the polyoxometalates and their Ru metallo-adducts were obtained to identify any structural changes induced in the complexes on association. Modes characteristic of the polyoxomolybdate anion are shifted by between 3 and 8 cm^{-1} by comparison with the parent anion on association with $[Ru(bpy)_3]^{2+}$. For the composite material, key polyoxometalate modes are observed at 781 cm^{-1} (Mo-O-Mo involving edge-sharing octahedral), 972 cm^{-1} (Mo-O-Mo involving corner-sharing octahedral) and 935 cm^{-1} (Mo=O terminal stretching mode).[10, 11] The sulfite S=O symmetric stretch is observed at 902 cm^{-1}.[10, 12] Interestingly the metal-oxide stretch at 781 cm^{-1} and the bpy out-of-plane C-H bending at 757 cm^{-1} shift in opposite directions upon association relative to their parent ion spectra; while the bipyridine out-of-plane ring bending at 730 cm^{-1} is unaffected.[13, 14] Comparable behaviour has been reported in several other Ru/polyoxometalate electrostatic hybrid systems and has been interpreted as indicating strong electronic interaction.[15, 16] The peaks between 1350 and 1500 cm^{-1} were attributed to the tetrapentylammonium counterion, and the Ru complex PF_6^- counterion mode was observed at 835 cm^{-1}. The fact that none of these peaks are present in the composite material spectrum indicates complete charge compensation of the molybdates by $[Ru(bpy)_3]^{2+}$. The spectra of both isomers and their corresponding Ru adducts are presented in Fig 3.2.2.1 and 3.2.2.2. The primary modes are summarized in Table 3.2.2.

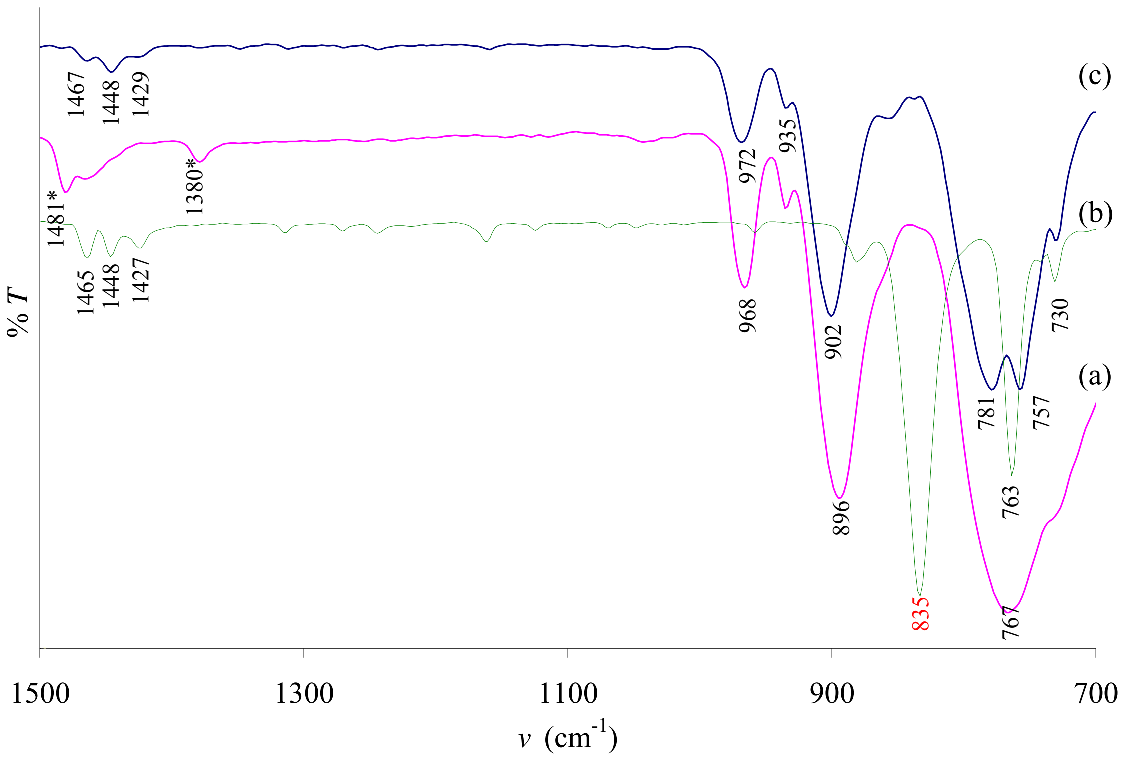

Fig 3.2.2.1: ATR-FTIR spectra of (a) $[(Pn)_4N]_4\alpha\text{-}[Mo_{18}O_{54}(SO_3)_2]$, (b) $[Ru(bpy)_3](PF_6)_2$ and (c) $[Ru(bpy)_3]_2\alpha\text{-}[Mo_{18}O_{54}(SO_3)_2]$. Bands marked with * denote tetrapentylammonium cation modes, and red text denotes a $(PF_6)^-$ mode.

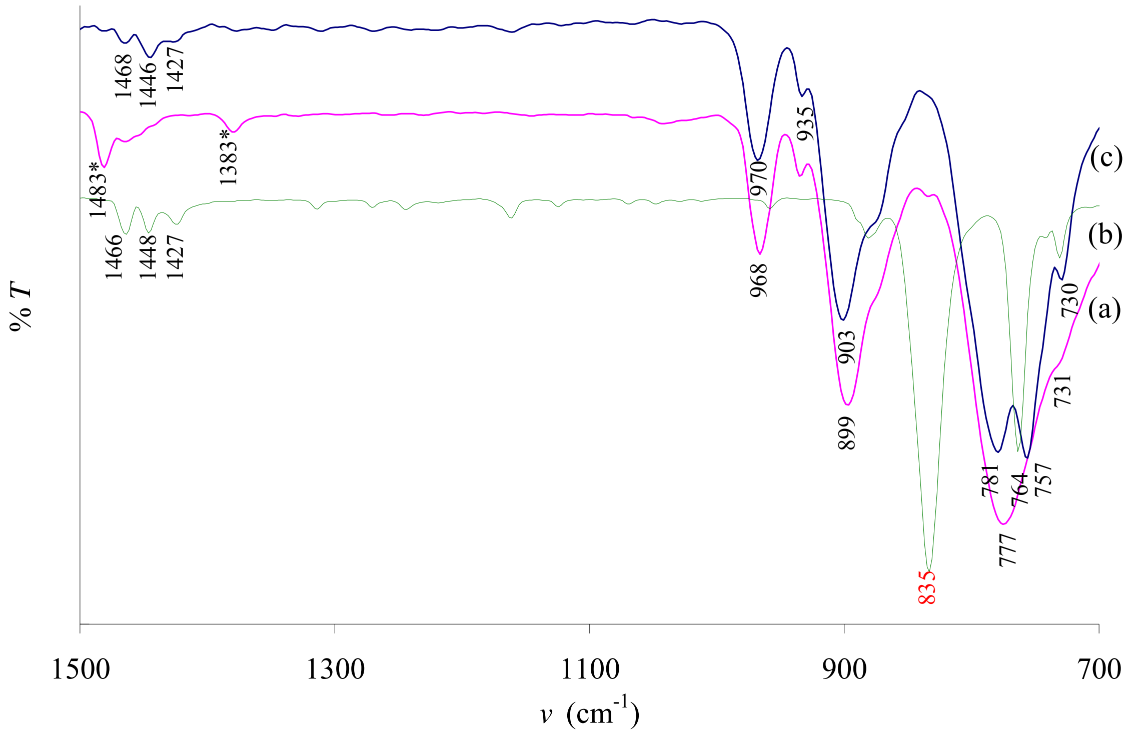

Fig 3.2.2.2: ATR-FTIR spectra of (a) $[(Pn)_4N]_4\beta\text{-}[Mo_{18}O_{54}(SO_3)_2]$, (b) $[Ru(bpy)_3](PF_6)_2$ and (c) $[Ru(bpy)_3]_2\beta\text{-}[Mo_{18}O_{54}(SO_3)_2]$. Bands marked with * denote tetrapentylammonium cation modes, and red text denotes a $(PF_6)^-$ mode.

Mode	**Compound/Wavenumber (cm^{-1})**				
	α	α 2-1	β	β 2-1	$[Ru(bpy)_3]^{2+}$
bpy ring out-of-plane bending		731		731	730
bpy C-H out-of-plane bending		757		757	763
Mo-O-Mo edge-sharing octahedra	767	781	777	781	
S=O symmetric stretch	896	902	899	903	
Mo-O terminal mode	935	935	935	935	
Mo-O-Mo corner-sharing octahedra	968	972	968	970	
bpy ring breathing		1465		1468	1467
bpy ring breathing		1448		1446	1448
bpy ring breathing		1429		1427	1427

Table 3.2.2: Key vibrational modes identified in Figs 3.2.2.1 and 3.2.2.2.

3.2.3 - Luminescence studies:

In order to determine the impact of association of α/β-$[Mo_{18}O_{54}(SO_3)_2]^{4-}$ on the photophysics of $[Ru(bpy)_3]^{2+}$, its luminescence was studied as a function of polyoxometalate concentration in dry acetonitrile.

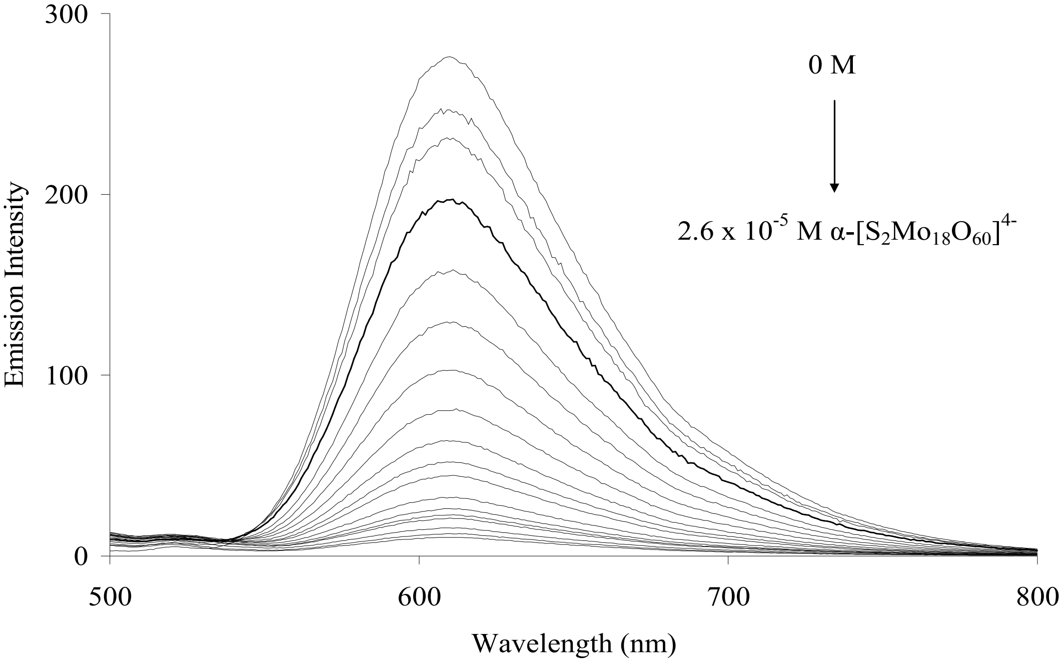

Fig 3.2.3.1: Luminescence quenching of $[Ru(bpy)_3]^{2+}$ (1.0 x 10^{-5} M) by addition of the polyoxometalate α-$[Mo_{18}O_{54}(SO_3)_2]^{4-}$ (1.6 x 10^{-6} M – 2.6 x 10^{-5} M) in dry MeCN.

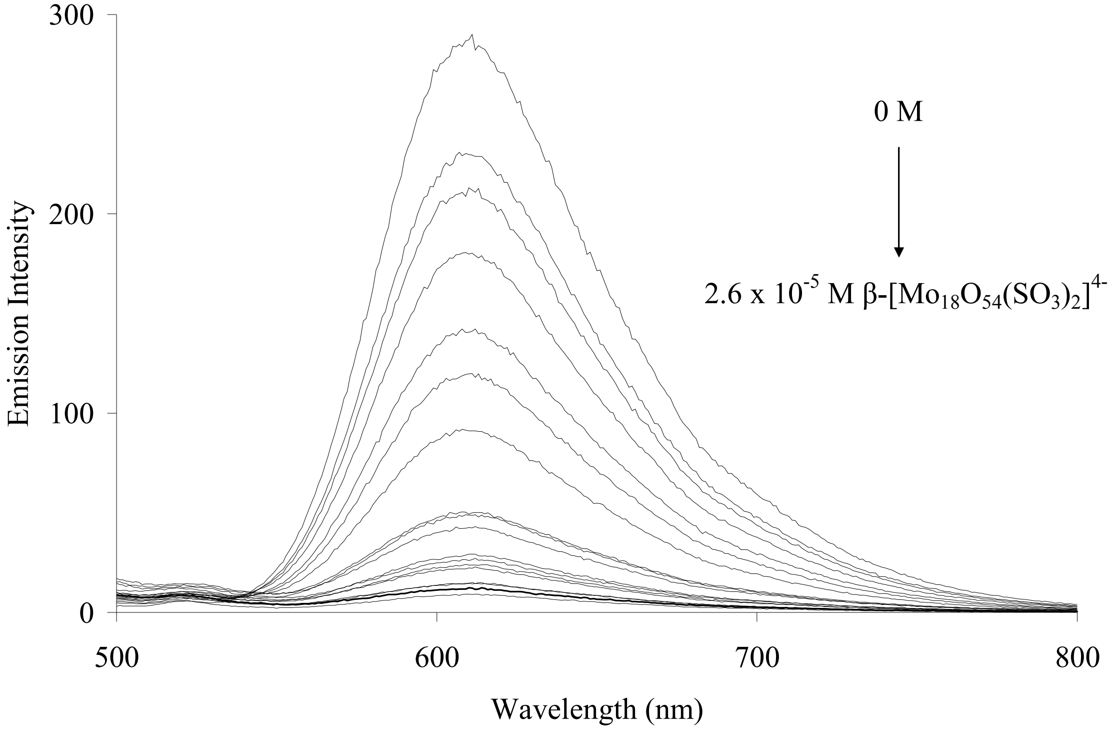

Fig 3.2.3.2: Luminescence quenching of $[Ru(bpy)_3]^{2+}$ (1.0 x 10^{-5} M) by addition of the polyoxometalate β-$[Mo_{18}O_{54}(SO_3)_2]^{4-}$ (1.5 x 10^{-6} M – 2.6 x 10^{-5} M) in dry MeCN.

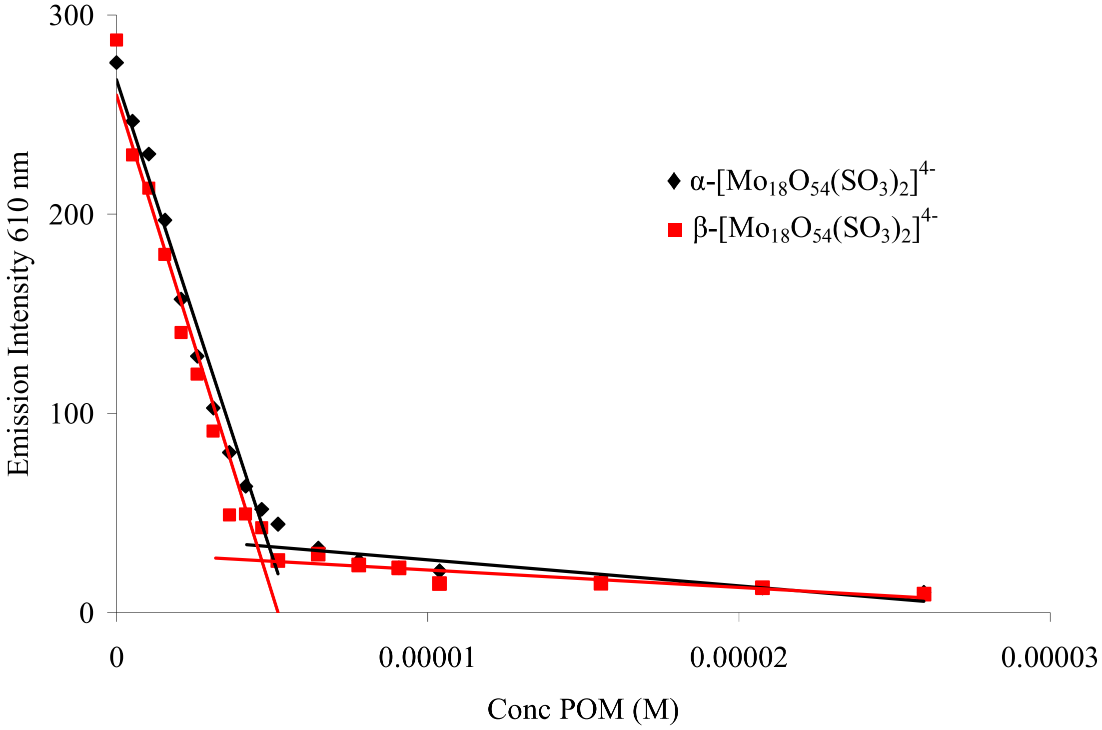

Fig 3.2.3.3: Luminescence intensity quenching of $[Ru(bpy)_3]^{2+}$ by both polyoxomolybdate isomers. Data taken from Fig 3.2.3.1 and Fig 3.2.3.2.

Fig 3.2.3.1 and 3.2.3.2 show that significant quenching of the $[Ru(bpy)_3]^{2+}$ ^{3}MLCT luminescence is observed upon addition of α-$[Mo_{18}O_{54}(SO_3)_2]^{4-}$. The $[Ru(bpy)_3]^{2+}$ phosphorescence centred at 610 nm decreased steadily upon addition of successive quantities of α-$[Mo_{18}O_{54}(SO_3)_2]^{4-}$ or β-$[Mo_{18}O_{54}(SO_3)_2]^{4-}$ as the ions associated, although there was no evidence for a shift in the luminescence λ_{max}. This behaviour contrasts with that of the sulfato polyoxomolybdate $[Mo_{18}O_{54}(SO_4)_2]^{4-}$, where, in addition to quenching, significant changes to the emission spectra were evident. A shoulder observed at ~ 630 nm was formed in the sulfate polyoxomolybdate case, and was attributed to luminescence from the 2:1 associated complex.[2] Even though a very weak residual luminescence at 610 nm remains when the α/β-$[Mo_{18}O_{54}(SO_3)_2]^{4-}$ concentration exceeds that of the ruthenium complex by more that 2.5 times, it is likely that this emission arises from unassociated $[Ru(bpy)_3]^{2+}$ rather than an intrinsic emission from the associated complex. To confirm this, the isolated solids $[Ru(bpy)_3]_2$α/β-$[Mo_{18}O_{54}(SO_3)_2]$ were examined using confocal fluorescence microscopy and this confirmed that the 2:1 complex is non-emissive. These confocal images are shown in Fig 3.2.3.4 and 3.2.3.5. The excitation spectra taken for the weak residual emission confirmed that there was no change to the absorbance giving rise to this weak emission which also suggests that the emission arises from unassociated $[Ru(bpy)_3]^{2+}$. This is again in contrast to the case of the sulfate analogue $[Ru(bpy)_3]_2[Mo_{18}O_{54}(SO_4)_2]$, where the new optical transition seen in the UV/Vis spectra was demonstrated to be the source of the luminescence at 640 nm.

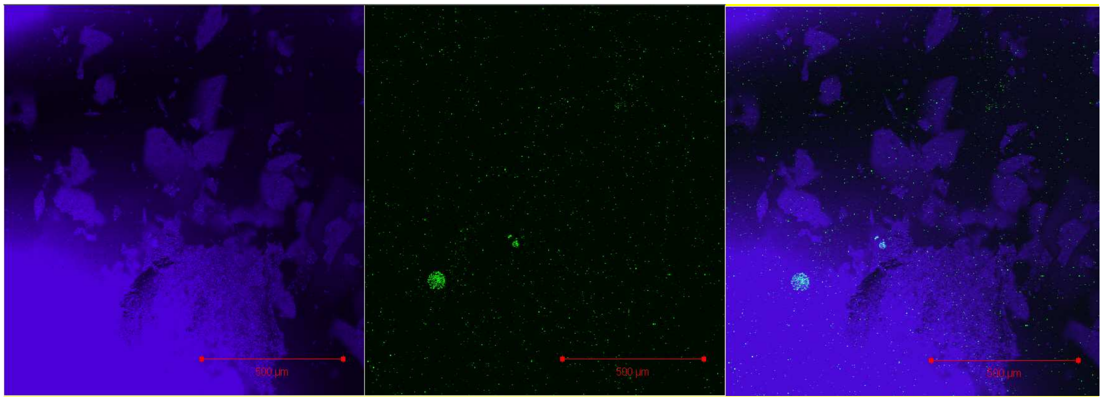

Fig 3.2.3.4: Confocal fluorescence microscopy of solid $[Ru(bpy)_3]_2\alpha$-$[Mo_{18}O_{54}(SO_3)_2]$. Any residual observed luminescence is attributed to free $[Ru(bpy)_3]^{2+}$. Scale: 500 µm/division.

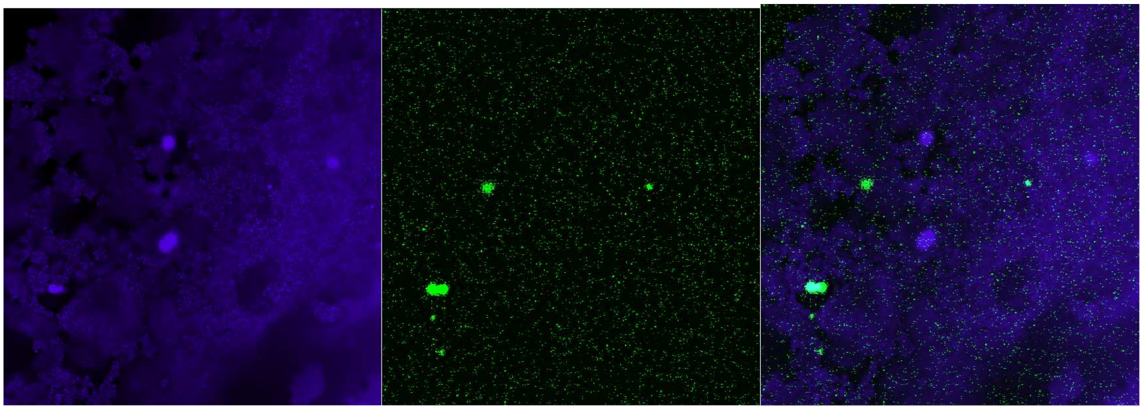

Fig 3.2.3.5: Confocal fluorescence microscopy of solid $[Ru(bpy)_3]_2\beta$-$[Mo_{18}O_{54}(SO_3)_2]$. Any residual observed luminescence is attributed to free $[Ru(bpy)_3]^{2+}$.

Comparison of the behaviour of the luminescence intensity and lifetime as a function of the quencher concentration can yield insights into the nature of the interaction between the two compounds. Dynamic quenching, where interaction between the species is collisional and therefore diffusion controlled, is expected to follow the Stern-Volmer Equation (Equation 1):

$$\frac{I_0}{I} or \frac{\tau_0}{\tau} or \frac{\Phi_0}{\Phi} = 1 + K_{SV}[Q] \qquad \textbf{(1)}$$

where [Q] is the concentration of the quencher; I is the fluorescence intensity; τ is the luminescent lifetime of the fluorophore; and Φ is the fluorescence quantum yield. K_{SV} is the Stern-Volmer constant (Equation 2):

$$K_{SV} = k_q . \tau_0 \qquad \textbf{(2)}$$

where k_q is the experimental rate constant for quenching and τ_0 is the lifetime of the unquenched fluorophore. For purely static quenching, where a non-luminescent association complex forms between the complex an analogous equation is employed (Equation 3), but the physical meaning of the slope, K, is different, according to equation (3)

$$\frac{I_0}{I} = 1 + K[Q] \qquad \textbf{(3)}$$

where *K* is the association constant. In the case of purely static quenching, leading to a non-emitting association complex, the observed lifetime of the luminophore is expected to be unaffected by quencher concentration, so the I_0/I or Φ_0/Φ plots will vary with quencher concentration but τ_0/τ does not. In a mixed static and dynamic scenario, the lifetime will be affected by quencher concentration, but the slope of the I_0/I plot and τ_0/τ plots differ. Consequently, comparison of the luminescence lifetime and intensity as a function of quencher concentration can be used to assess whether quenching is static, dynamic or a combination of both. The I_0/I plots for addition of the sulfite polyoxomolybdates to $[Ru(bpy)_3]^{2+}$ are shown in Fig 3.2.3.6.

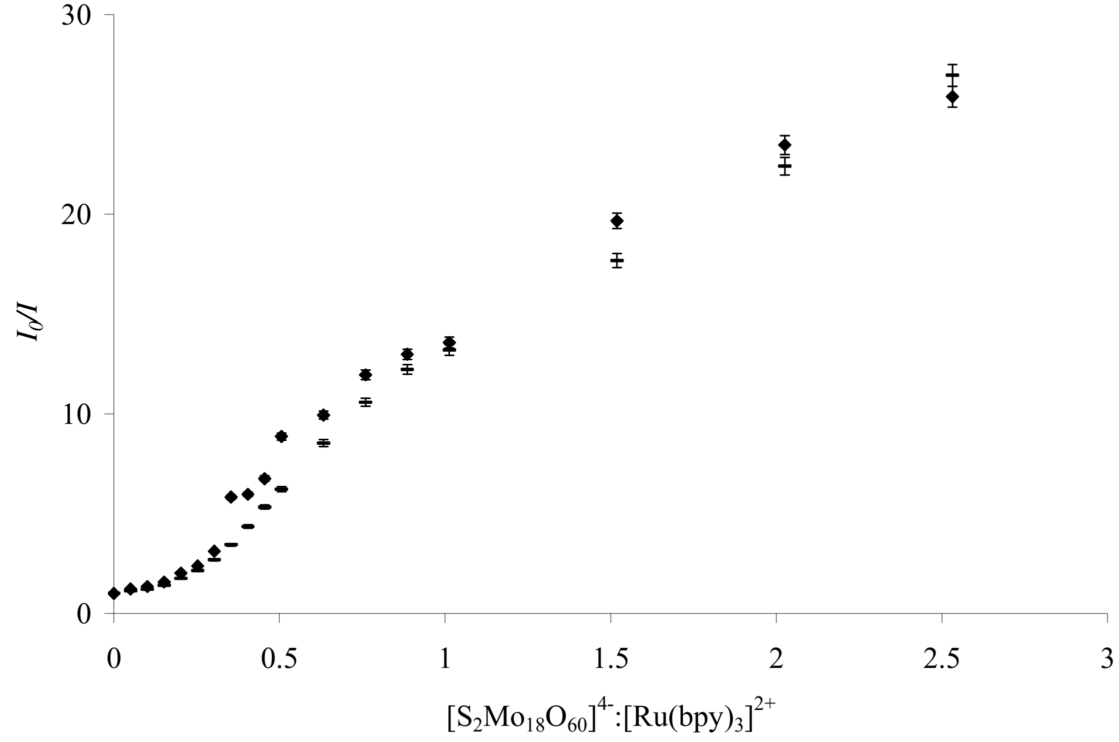

Fig 3.2.3.6: Stern-Volmer plots of the emission quenching of $[Ru(bpy)_3]^{2+}$ (1.0×10^{-5} M) by α-$[Mo_{18}O_{54}(SO_3)_2]^{4-}$ (----) and β-$[Mo_{18}O_{54}(SO_3)_2]^{4-}$ (♦) (1.6×10^{-6} M – 2.6×10^{-5} M) in aerated MeCN.

It is important to remember that the luminophore, $[Ru(bpy)_3]^{2+}$, is present in excess at the beginning of the experiment and that the formation of the associated complex is likely to occur in the following sequence:

$$xs[Ru(bpy)_3]^{2+} + [Mo_{18}O_{54}(SO_3)_2]^{4-} \leftrightarrows [Ru(bpy)_3]_2[Mo_{18}O_{54}(SO_3)_2] + [Ru(bpy)_3]^{2+} \quad \textbf{(4)}$$

$$[Ru(bpy)_3]_2[Mo_{18}O_{54}(SO_3)_2] + [Mo_{18}O_{54}(SO_3)_2]^{4-} \leftrightarrows 2\{[Ru(bpy)_3][Mo_{18}O_{54}(SO_3)_2]\}^{2-} \quad \textbf{(5)}$$

At the initial stages when the ruthenium complex is in a large excess, the 2:1 complex would be expected to form. As shown in Fig 3.2.3.6, the data applied to the SV model is non-linear with significant upward curvature and at least two distinct regions of response, when applied to a Stern-Volmer model. One explanation for such behaviour is that the 2:1 adduct remains luminescent but the 1:1 is not. However, as described above, fluorescence microscopy confirmed this is not the case. Upward curvature in the Stern-Volmer plot is often seen in situations where the quencher can both associate with the luminophore and quench it through molecular collision (ie: mixed static and dynamic quenching).[17]

Although the shape of the plot is somewhat unusual it also coincides well with well-known adaptations of the Stern-Volmer model. Up to a ratio of 2:1 the series slopes upwards, and in fact the application of a quadratic trendline to this portion of the series yielded a fit with a regression coefficient of 0.98 for β and 0.99 for the α-isomer. After a 2:1 ratio it is clear that the SV data changes to a linear relationship. The upwards curvature in this SV plot has also been observed in the quenching of $[Ru(bpy)_3]^{2+}$ phosphorescence by $[PW_{12}O_{40}]^{3-}$ in MeCN/DMSO. The authors attributed this to the formation of non-emissive/very weakly emissive ion-pairs in solution; however they did not perform any time-resolved spectroscopy to investigate this interaction further.

3.2.4 - Time-resolved luminescence:

To investigate the non-linearity of the luminescence intensity data when fitted to the Stern-Volmer model, time-correlated single photon counting was employed to investigate the effect of increasing polyoxometalate concentration on the luminescent lifetime of $[Ru(bpy)_3]^{2+}$ in MeCN. The data obtained are shown in Fig 3.2.4.1.

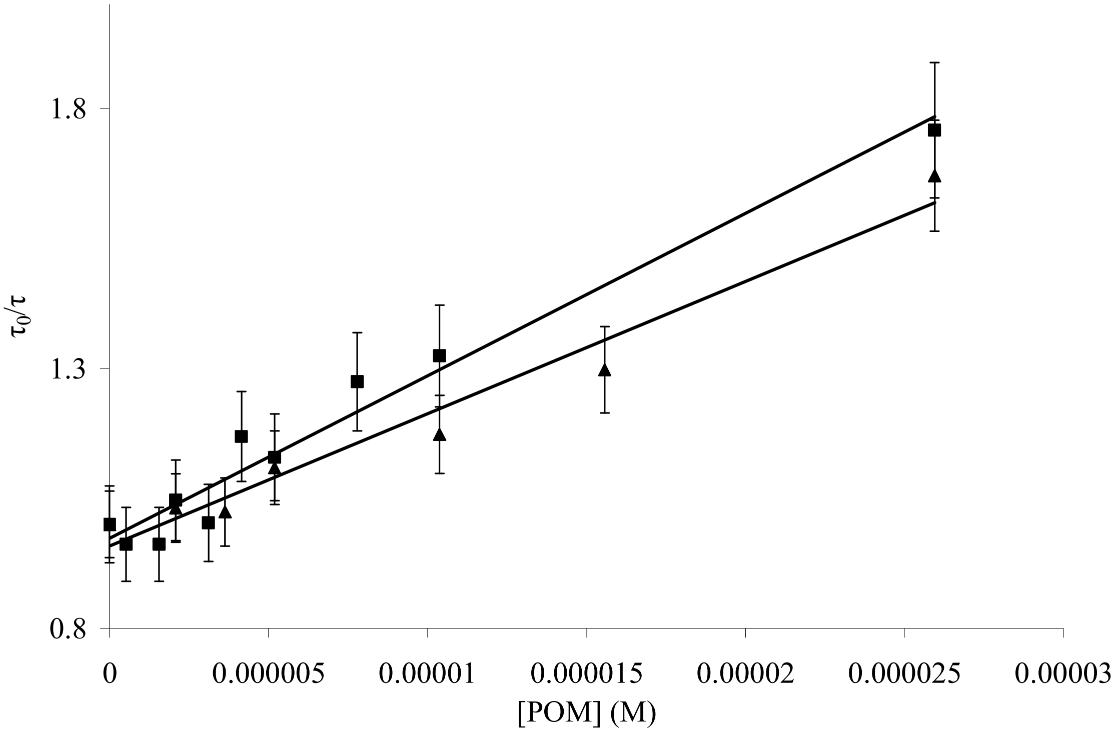

Fig 3.2.4.1: Luminescent lifetime Stern-Volmer plots of 5.0 x 10^{-6} M $[Ru(bpy)_3]^{2+}$ lifetime quenched by α-$[Mo_{18}O_{54}(SO_3)_2]^{4-}$ (■) and by β-$[Mo_{18}O_{54}(SO_3)_2]^{4-}$ (▲) in MeCN.

As data derived from electronic spectroscopy indicated, a 2:1 complex forms between ruthenium and polyoxometalate in MeCN and, on the basis of previous studies, it was expected that the quenching would be purely static. Surprisingly, unlike quenching by the sulfate polyoxometalate analogue where the lifetime was unaffected by the polyoxometalate, consistent with purely static quenching, the sulfite complex did influence the $[Ru(bpy)_3]^{2+}$ lifetime. The lifetime data was applied to a Stern-Volmer plot, i.e. τ_0/τ versus [Q], for both sulfite isomers is shown in Fig 3.2.4.1 which demonstrates that, after an initial plateau region, a reduction in $[Ru(bpy)_3]^{2+}$ lifetime accompanies increasing polyoxometalate concentration. This implies that there is a dynamic component to the quenching of the ruthenium by both sulfite polyoxometalates. This behaviour is likely to be the origin of the upward curvature in the I_0/I plot. The slopes of τ_0/τ versus [Q] are equal to K_{SV}, according to Equation 1 which are 3.1 x 10^4 for α-$[Mo_{18}O_{54}(SO_3)_2]^{4-}$ and 2.5 x 10^4 for β-$[Mo_{18}O_{54}(SO_3)_2]^{4-}$. The quenching rate constants, k_q were estimated according to equation (2) to be 1.9 ± 0.14 x 10^{11} s^{-1} and 1.6 ± 0.10 x 10^{11} s^{-1} for the α and β isomers respectively, which is not consistent with collisional quenching but is for static association. This is because dynamic quenching rate constants are limited by the rate of diffusion through solution, which usually cannot exceed approximately 10^9 s^{-1} at room temperature.

A modified form of the emission intensity Stern-Volmer equation (6) can be used for mixed static and dynamic quenching,[17] equation (6), the parameters are as explained above;

$$\frac{I_0}{I} = 1 + (K_{SV} + K_a)[Q] + K_{SV}K_a[Q]^2 \qquad \textbf{(6)}$$

Therefore, plotting $((I_0/I)-1)/[POM]$ vs [POM] yields a slope equal to $K_{SV}.K_a$. Since the K_{SV} values were obtained from lifetime data, K_a values were derived from these fits as 5.9 ± 0.56 x 10^6 and 1.0 ± 0.09 x 10^7 for the α and β isomers respectively. The K_a value obtained for the association of the corresponding 2:1 sulfate polyoxometalate complex with $[Ru(bpy)_3]^{2+}$ was 1 x 10^6; this suggests the sulfite polyoxomolybdate analogue has a slightly higher affinity for $[Ru(bpy)_3]^{2+}$ compared with the sulfato POM.[2]

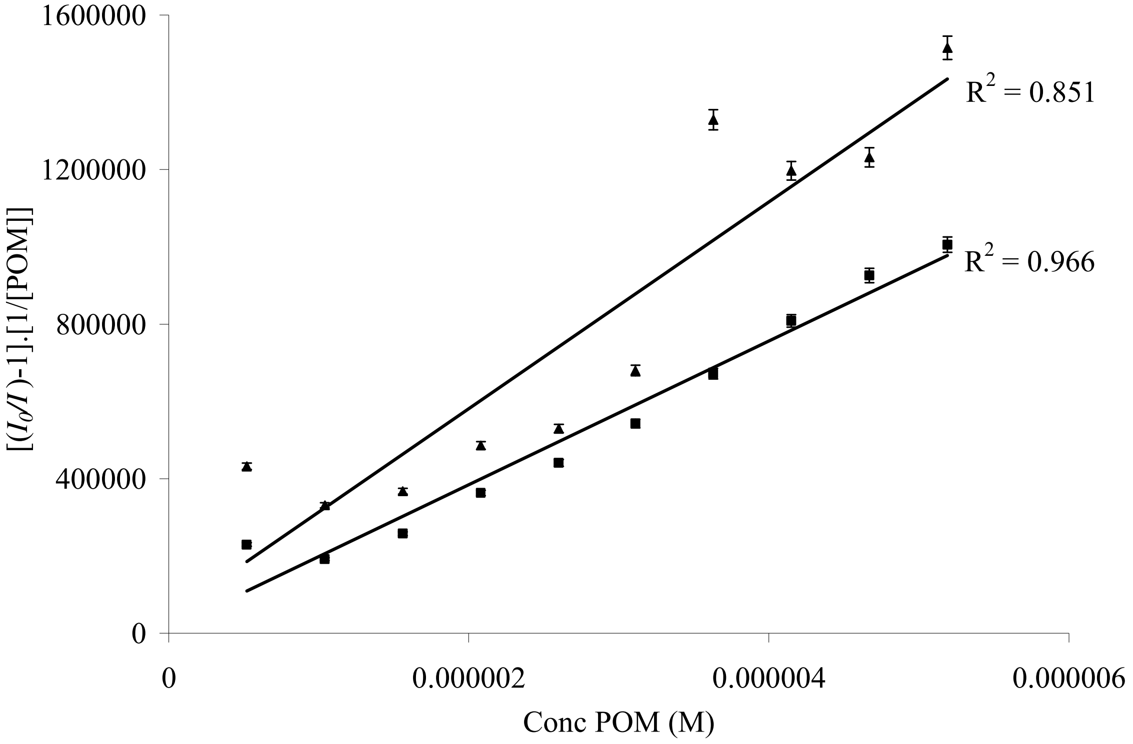

Fig 3.2.4.2: Modified Stern-Volmer plots of the emission quenching of $[Ru(bpy)_3]^{2+}$ (1.0 x 10^{-5} M) by α-$[Mo_{18}O_{54}(SO_3)_2]^{4-}$ (squares) and β-$[Mo_{18}O_{54}(SO_3)_2]^{4-}$ (triangles) (1.6 x 10^{-6} M – 5.2 x 10^{-6} M) in aerated MeCN, from which equilibrium constants were estimated. Slopes equal $K_a.K_{SV}$.

The applied mixed static/dynamic quenching model has never been applied to quenching studies between $[Ru(bpy)_3]^{2+}$ and the Dawson polyoxometalates studies previously, as in each case the Ru luminescent lifetime remained unaffected even at high quencher concetrations.[2, 3, 18] However a dynamic quenching component was observed in the quenching of $[Ru(bpy)_3]^{2+}$ by the substituted Keggin polyoxotungstates $[Co(H_2O)SiW_{11}O_{39}]^{6-}$ and $[Mn(OH)PW_{11}O_{39}]^{6-}$ but these data were for an ion-pair ratio of 1:1, and not for the fully charge compensated species as in the Dawson POM studies.[19]

3.2.5 - Ionic strength and association studies:

To investigate the nature of the association between $[Ru(bpy)_3]^{2+}$ and α-$[Mo_{18}O_{54}(SO_3)_2]^{4-}$ further, the effect of ionic strength on the associated cluster was examined by studying the luminescence recovery with increasing salt concentration. It is well known that ClO_4^- ions have a high propensity to associate with ruthenium complexes, and this salt has been shown to disrupt ion pairing in the case of $[Ru(bpy)_3]^{2+}$ and various other Dawson polyoxometalates.[2, 3, 18] Fig 3.2.5.1 displays the impact of $LiClO_4$ addition on a solution of $[Ru(bpy)_3]_2$β-$[Mo_{18}O_{54}(SO_3)_2]$ containing a tenfold POM excess.

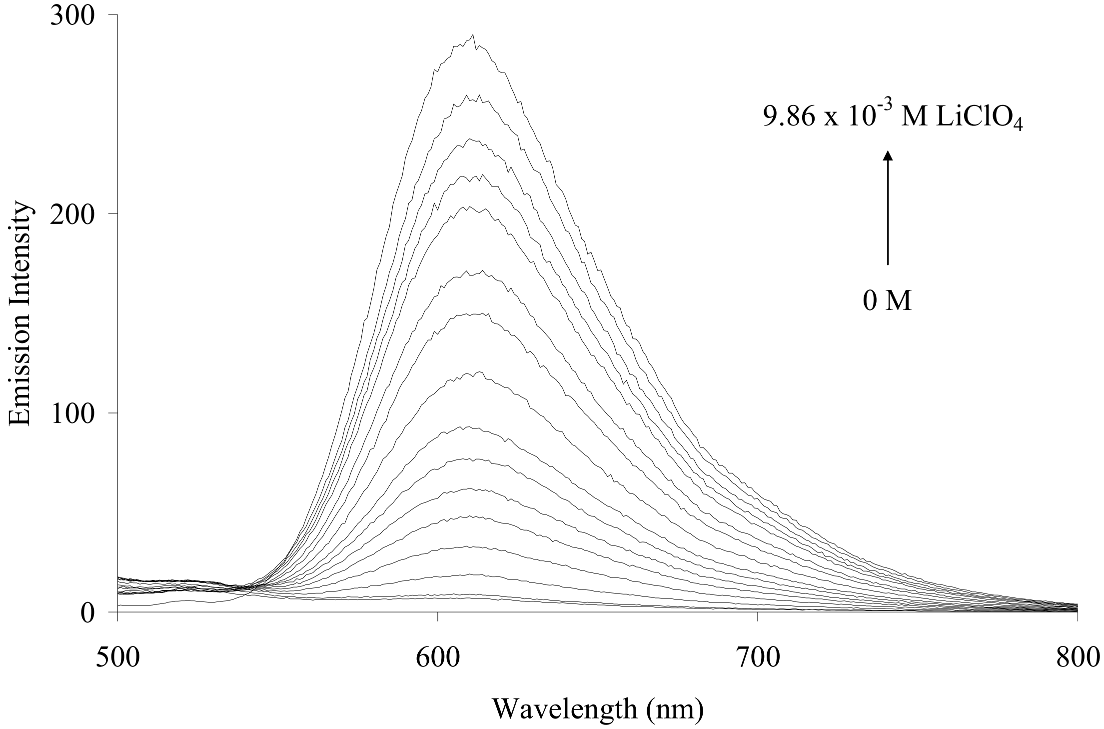

Fig 3.2.5.1: Changes in emission intensity of a solution of 1 x 10^{-5} M $[Ru(bpy)_3]Cl_2$ and 1 x 10^{-4} M $[(Pn)_4N]_4$β-$[Mo_{18}O_{54}(SO_3)_2]$ in dry MeCN upon addition of 1 M $LiClO_4$,

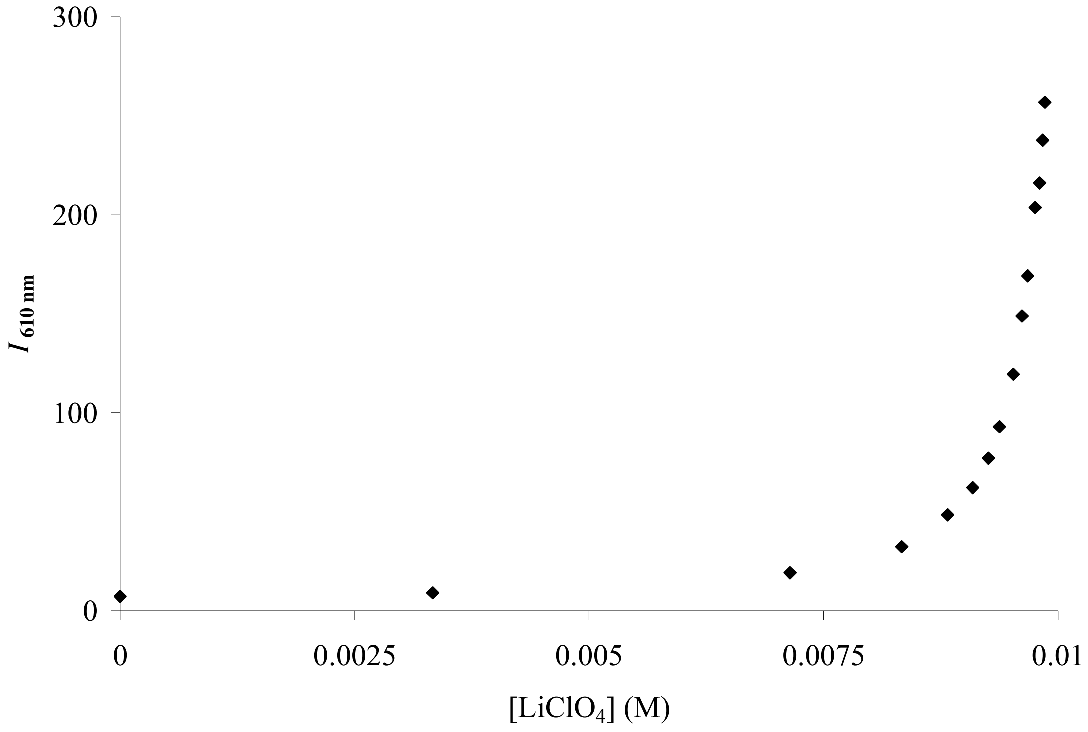

Fig 3.2.5.2: Plot of increasing emission intensity vs LiClO$_4$ concentration taken from data in Fig 3.2.5.1.

This study showed that by a concentration of 9.86 x 10^{-3} M LiClO$_4$ the luminescence of free [Ru(bpy)$_3$]$^{2+}$ was fully recovered. A plot of recovering luminescence intensity as a function of increasing LiClO$_4$ concentration exhibited an upward curvature which was remarkably similar to that for the addition of LiClO$_4$ to a solution of [P$_2$W$_{17}$O$_{61}$(FeOH$_2$)]$^{7-}$ and [Ru(bpy)$_3$]$^{2+}$ recorded by Seery *et al*, although the absolute concentrations used were different.[18] Here a 99-fold excess of LiClO$_4$ over polyoxometalate was required to disrupt the ion-ion association; however in the case of [P$_2$W$_{17}$O$_{61}$(FeOH$_2$)]$^{7-}$ and [Ru(bpy)$_3$]$^{2+}$ a 22500 fold excess of LiClO$_4$ was required to recover the initial luminescence intensity. This difference in required electrolyte concentration is reflected in the difference in both the large excess of POM used in this experiment and the lower K_a value of [Ru(bpy)$_3$]$_2$β-[Mo$_{18}$O$_{54}$(SO$_3$)$_2$] relative to the literature example.

An analogous experiment was then repeated with the α isomer. In this case, addition of $LiClO_4$ to a solution of 1 x 10^{-5} M $[Ru(bpy)_3]^{2+}$ and 1 x 10^{-4} M α-$[Mo_{18}O_{54}(SO_3)_2]^{4-}$ only resulted in partial recovery of the $[Ru(bpy)_3]^{2+}$ luminescence, and at high $LiClO_4$ concentrations a time dependent decrease in luminescence occurred. A UV/Vis spectrum taken before and after the additions showed that the $[Ru(bpy)_3]_2$α-$[Mo_{18}O_{54}(SO_3)_2]$ MLCT at ~ 475 nm had also reduced dramatically in intensity, and the baseline had also shifted. This behaviour was attributed to poor solubility of the complex in acetonitrile which caused precipitation in the presence of the salt. The origin of this difference in solubility observed for the two isomers is unknown as they are isoelectronic and isostructural.

3.2.6 - Resonance Raman spectroscopy:

The new absorbances formed around 475 - 485 nm in the electronic spectrum, on the basis of comparison with other clusters, is thought to be due to absorbance from a new inter-metal charge-transfer within the cluster. In order to confirm this, resonance Raman spectra of the solids dispersed in KBr was explored by exciting with a laser line closely resonant with this state. The resonance Raman spectra of $[Ru(bpy)_3]^{2+}$, $[Ru(bpy)_3]_2$α-$[Mo_{18}O_{54}(SO_3)_2]$ and α-$[Mo_{18}O_{54}(SO_3)_2]^{4-}$ under 488 nm excitation are shown in Fig 3.2.6.1. Spectral intensities are normalized for clarity; the two ruthenium containing complexes are resonant at 488 nm whereas $[(Pn)_4N]_4$α-$[Mo_{18}O_{54}(SO_3)_2]$ is not, so there are large differences in absolute intensity between the spectra. The Raman spectrum of the composite material exciting at 488 nm is shown in Fig 3.2.6.1 (b). The Raman spectra of both sulfite polyoxometalates are very similar. However there are some minor differences; notably the appearance of a broad featureless mode at approximately 1587 cm^{-1} in the β isomer spectrum (Fig 3.2.6.2). A common feature of both POM spectra is the Mo-O mode at ~ 904 cm^{-1}, which is associated with an asymmetric stretching of MoO_2 moieties containing terminal oxygen atoms. The Mo-O bending mode is also observed at 388 cm^{-1}.[20] The ^{3}MLCT resonance Raman spectrum of $[Ru(bpy)_3]^{2+}$ is well known and exhibits signature modes at 1608, 1565, 1492, 1320, 1279, 1178, 1030 and 670 cm^{-1}, all attributed to bpy vibrations, and a Ru-N mode at 375 cm^{-1}.[2]

It is important to note that only the $[Ru(bpy)_3]^{2+}$ modes are expected to be resonantly enhanced under 488 nm excitation. Interestingly, the prominent α-$[Mo_{18}O_{54}(SO_3)_2]^{4-}$ modes at 978 and 991 cm^{-1} which were apparent in the sulfate polyoxometalate complex adduct are not observed in the adducts in this case.[2, 3, 18] This suggests that the weaker 475 nm transition is either too weak to provide a significant resonantly enhanced signal or it is not the same transition as observed in the sulfate polyoxometalates. Nonetheless, a number of new features are detected in the composite, that are not observed for $[Ru(bpy)_3]^{2+}$ alone. In particular, two modes appear at 1433 and 1467 cm^{-1}. These bands appear weakly in the Raman spectrum of $[(Pn)_4N_4]$α-$[Mo_{18}O_{54}(SO_3)_2]$.

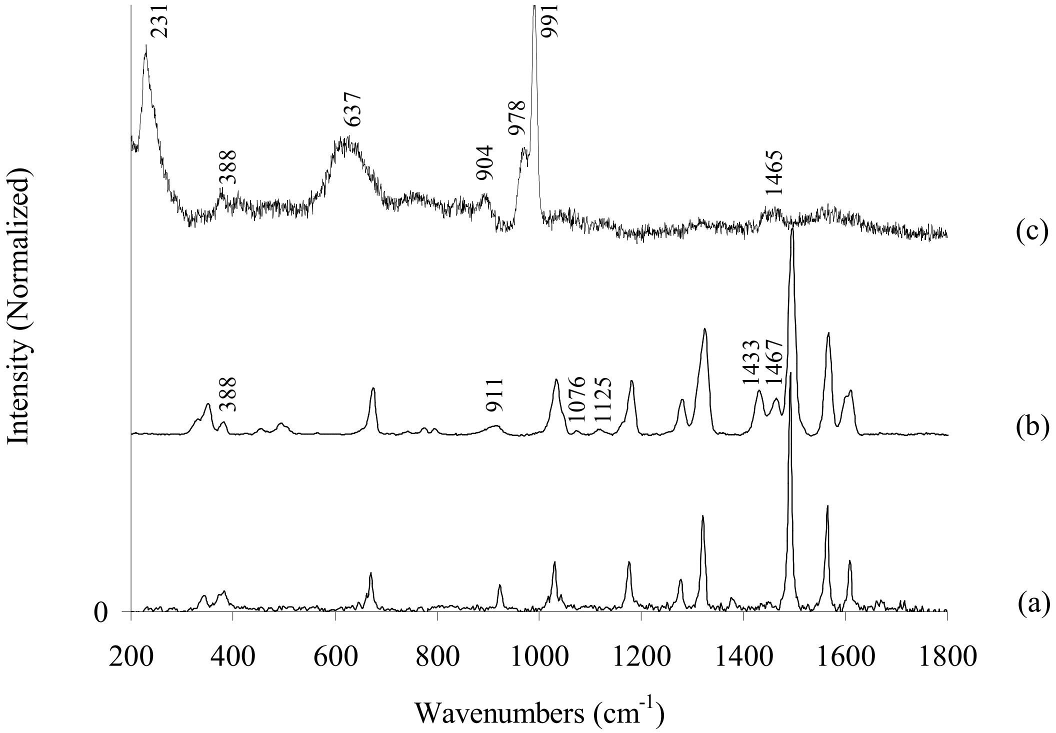

Fig 3.2.6.1: Resonance Raman spectra of (a) $[Ru(bpy)_3](PF_6)_2$, (b) $[Ru(bpy)_3]_2$α-$[Mo_{18}O_{54}(SO_3)_2]$and (c) $[(Pn)_4]$α-$[Mo_{18}O_{54}(SO_3)_2]$ present in KBr discs (~ 5 % w/w) under 488 nm excitation.

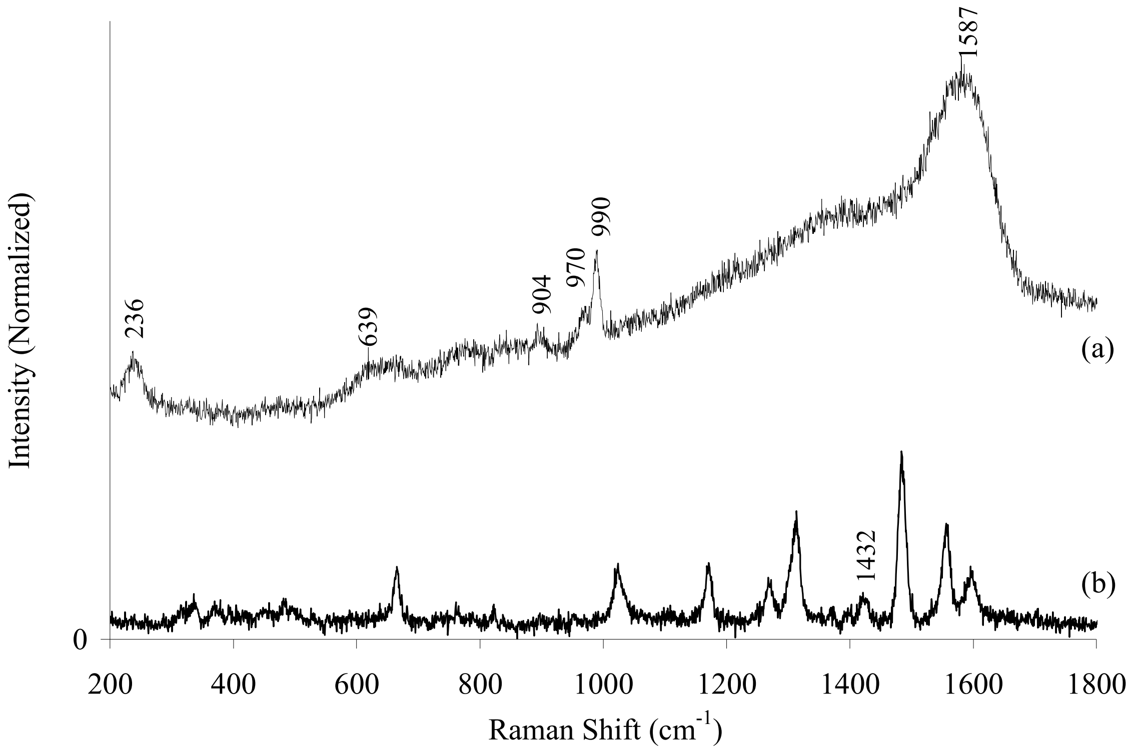

Fig 3.2.6.2: Resonance Raman of (a) [(Pn)$_4$N]β-[Mo$_{18}$O$_{54}$(SO$_3$)$_2$] and (b) [Ru(bpy)$_3$]$_2$β-[Mo$_{18}$O$_{54}$(SO$_3$)$_2$] in KBr discs (~ 5 % w/w) under 488 nm excitation.

The identity of these two modes is unclear. However, given their intensity in relation to the ruthenium polypyridyl modes they are clearly resonant enhanced. The relative intensity of the modes at 1433 and 1467 cm^{-1} increased at longer excitation wavelengths, which may be a function of trace amounts of reduced [POM]$^{5-}$ coming into resonance at longer wavelengths. A weak mode at 388 cm^{-1} appears to be attributable to α-[Mo$_{18}$O$_{54}$(SO$_3$)$_2$]$^{4-}$, while the Ru-N mode at ~360 cm^{-1} appears to be weakly enhanced and red-shifted by approximately 10 cm^{-1} in the adduct spectrum.

The [Ru(bpy)$_3$]$^{2+}$ modes in the composite are affected by association with the polyoxometalate; they are broadened relative to those same features in the parent ion. This is indicative of a heterogeneous environment for the ruthenium cations and is consistent with the association of the metal complex with the polyoxoanion. Previous studies showed both the presence of polyoxometalate modes at non-resonant wavelengths and also showed modification of the $[Ru(bpy)_3]^{2+}$ modes. Spectra of the corresponding isomer β-$[Mo_{18}O_{54}(SO_3)_2]^{4-}$ and its ruthenium adduct $[Ru(bpy)_3]_2$β-$[Mo_{18}O_{54}(SO_3)_2]$ (Fig 3.2.6.2) were very similar to those of the α isomer.

Overall, resonance Raman spectra confirm the association of the ruthenium and polyoxometalate complex, and indicate that the ruthenium polypyridyl modes are perturbed by this association. However, resonance with the weak optical transition observed around 475 nm does not enhance Mo-O modes, as noted with the sulfato complex. Rather new high frequency modes are resonantly enhanced. The possibility that these bands arise from resonance Raman of the photoreduced product of the polyoxometalate was investigated by irradiating the samples for extended periods under the laser lines. No changes to the spectra were noted; so the green one-electron reduced product, $[(Pn)_4N]_5$α-$[Mo_{18}O_{54}(SO_3)_2]$, was electrosynthesized and examined. This colour change from yellow to green is characteristic of reduced Dawson type polyoxomolybdates and arises from low energy $Mo^{V} \rightarrow Mo^{VI}$ intervalence charge-transfer transitions.[5, 21] The spectrum of reduced $[(Pn)_4N]_5$α-$[Mo_{18}O_{54}(SO_3)_2]$ is shown in Fig 3.2.6.3.

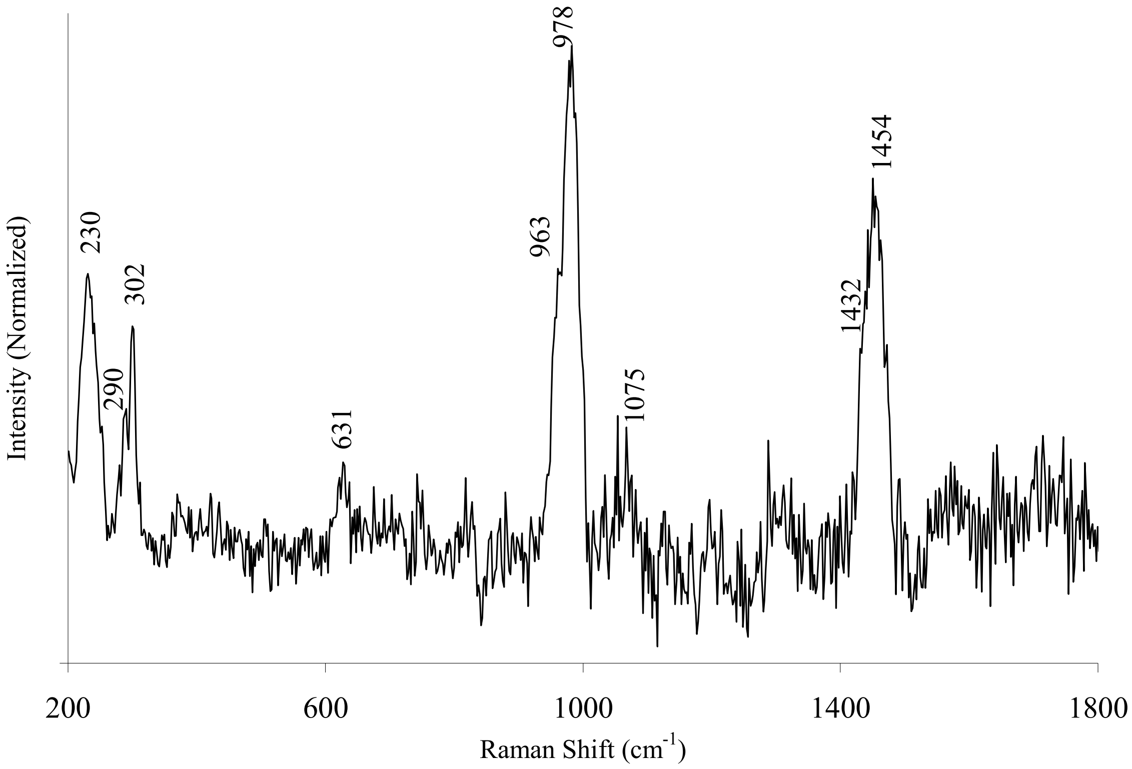

Fig 3.2.6.3: Resonance Raman spectrum of $[(Pn)_4N]_5\alpha\text{-}[Mo_{18}O_{54}(SO_3)_2]$ in KBr (~ 5 % w/w) under 488 nm irradiation.

The spectrum of reduced $\alpha\text{-}[Mo_{18}O_{54}(SO_3)_2]^{5-}$ revealed the appearance of new features at 290, 302, 1075, 1432, 1454 and 1471 cm^{-1} which are not present in the spectrum of $\alpha\text{-}[Mo_{18}O_{54}(SO_3)_2]^{4-}$. These features appear weakly in Fig 3.2.6.1 (b) and this strongly indicates that a small quantity of reduced POM is present in the isolated 2:1 adduct. That this has not been detected by other spectroscopic means indicates an extremely small quantity is present, and only a very sensitive technique such as resonance Raman could reveal its presence.

3.2.7 - Photochemical stability:

Previously studied polyoxometalate-ruthenium polypyridyl ionic composites have been demonstrated to exhibit exceptional photostability under visible irradiation in MeCN, relative to free $[Ru(bpy)_3]^{2+}$.[2, 3, 18] Comparative studies of the novel cluster complexes in acetonitrile were therefore performed using a 300 W Xe arc lamp and a > 400 nm optical filter. A solution containing 1 x 10^{-5} M $[Ru(bpy)_3]^{2+}$ and 5 x 10^{-6} M molybdate was irradiated and the UV/Vis spectrum monitored over a period of 4 hours. In that time, a relatively minor decrease in intensity was observed at 450 nm (approximately an 8 % drop). However in the case of $[Ru(bpy)_3]_2\alpha$-$[Mo_{18}O_{54}(SO_3)_2]$ a decrease of approximately 18 % was observed. The photolability of the $[Ru(bpy)_3]^{2+}$ cation in MeCN is well known,[22] and in comparison an absorbance matched 1 x 10^{-5} M solution of $[Ru(bpy)_3]^{2+}$ showed a decrease in absorbance of almost 30 % over the same timescale. The increased photostability of the POM-Ru adducts relative to free $[Ru(bpy)_3]^{2+}$ has previously been proposed to be due to the perturbation of the dissociative Ru based ^{3}MC state upon association to the POM, as demonstrated by temperature dependant luminescent studies.[3] In this case some photodecomposition of the associated $[Ru(bpy)_3]^{2+}$ (incorporated in 2:1 cluster) was observed over a 4 hour period, while in previous studies this was not reported. This may indicate that the energy levels of the two ions are not as strongly coupled as for the parent and lacunary-substituted Dawson ions, which appears to be confirmed by the resonance Raman spectra. An intramolecular charge-transfer transition is still clearly present in this case, as the electronic spectra demonstrate; however it may be weak in this case, relative to the associated $[Ru(bpy)_3]^{2+}$ sulfato anion cluster.

3.2.8 - Photoelectrochemistry:

The presence of a new charge transfer transition in previous Dawson molybdate and tungstates $[Ru(bpy)_3]^{2+}$ cluster was implicated in the ability of the $[Ru(bpy)_3]^{2+}$ unit to sensitize the photocatalytic activity of $[(Pn)_4N]\alpha$-$[Mo_{18}O_{54}(SO_3)_2]$. We were interested to know, given the enhanced photoelectrochemical activity of the sulfite anions, but also given the weak charge transfer transition and the fact that no associated vibrations appeared in the resonance Raman spectra, if the ruthenium polypyridyl complex could enhance the photocatalytic yield from the POM under visible irradiation. Initial photoelectrochemical studies of $[(Pn)_4N]_4\alpha$-$[Mo_{18}O_{54}(SO_3)_2]$ and $[Ru(bpy)_3]_2\alpha$-$[Mo_{18}O_{54}(SO_3)_2]$ were carried out on an ITO electrode using benzyl alcohol as the donor. The samples were prepared by drop casting the pre-prepared composite onto the pre-cleaned electrode. The modified ITO electrode was immersed into benzyl alcohol and irradiated with > 400 nm white light using a long pass filter. Benzyl alcohol was chosen as the catalytic substrate for these studies. Light-induced homogeneous photocatalytic oxidation of primary alcohols to selectively form aldehydes is a challenging proposition, and the Dawson polyoxometalates have been demonstrated previously to be excellent candidates for this process.[23, 24] In order to ensure that the ion-pair remained associated, photochemical experiments were performed in the absence of any added supporting electrolyte. The absence of electrolyte meant that iR drop is significant, nonetheless photocatalytic current could be observed. The potential was held at 0.4 V to ensure that following photoreduction of polyoxometalate by the benzyl alcohol (Eqns 7 and 8), the reduced polyoxometalate (Eqn 8) was reoxidised back to $[Mo_{18}O_{54}(SO_3)_2]^{4-}$ at the working electrode to generate photocatalytic current. It is expected that photo-oxidation of benzyl alcohol involves proton abstraction to initially form $[Mo_{18}O_{54}(SO_3))]^{5-}$ and H^+, which gives rise to the disproportionation reaction displayed in Eqn (9), as this maintains the polyoxometalate charge. This reduced polyoxometalate ion is finally reoxidized by the applied current at the electrode interface.

$$[Mo_{18}O_{54}(SO_3)_2]^{4-} + h\nu \rightarrow [Mo_{18}O_{54}(SO_3)_2]^{*4-} \qquad \textbf{(7)}$$

$$2[Mo_{18}O_{54}(SO_3)_2]^{*4-} + 2[C_6H_5CH_2OH] \rightarrow 2[Mo_{18}O_{54}(SO_3)_2]^{5-} + 2[C_6H_5CHO] + 2H^+ \qquad \textbf{(8)}$$

$$2[Mo_{18}O_{54}(SO_3)_2]^{5-} + 2H^+ \rightarrow [Mo_{18}O_{54}(SO_3)_2]^{4-} + [Mo_{18}O_{52}(OH)_2(SO_3)_2]^{4-} \qquad \textbf{(9)}$$

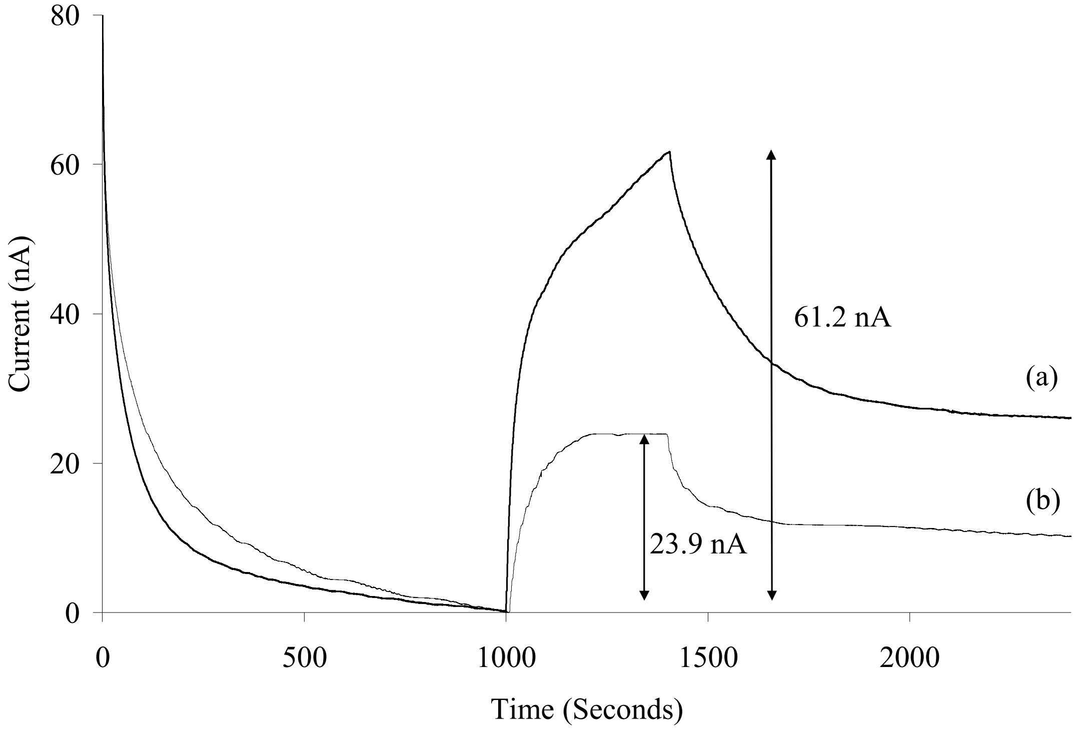

Fig 3.2.8.1: Photocurrents generated by (a) $[(Pn)_4N]_4\alpha\text{-}[Mo_{18}O_{54}(SO_3)_2]$ and (b) $[Ru(bpy)_3]_2\alpha\text{-}[Mo_{18}O_{54}(SO_3)_2]$ modified ITO electrodes in contact with benzyl alcohol (baselines normalized). Each was irradiated for 400 seconds (light on at 1000 seconds, light off at 1400 seconds).

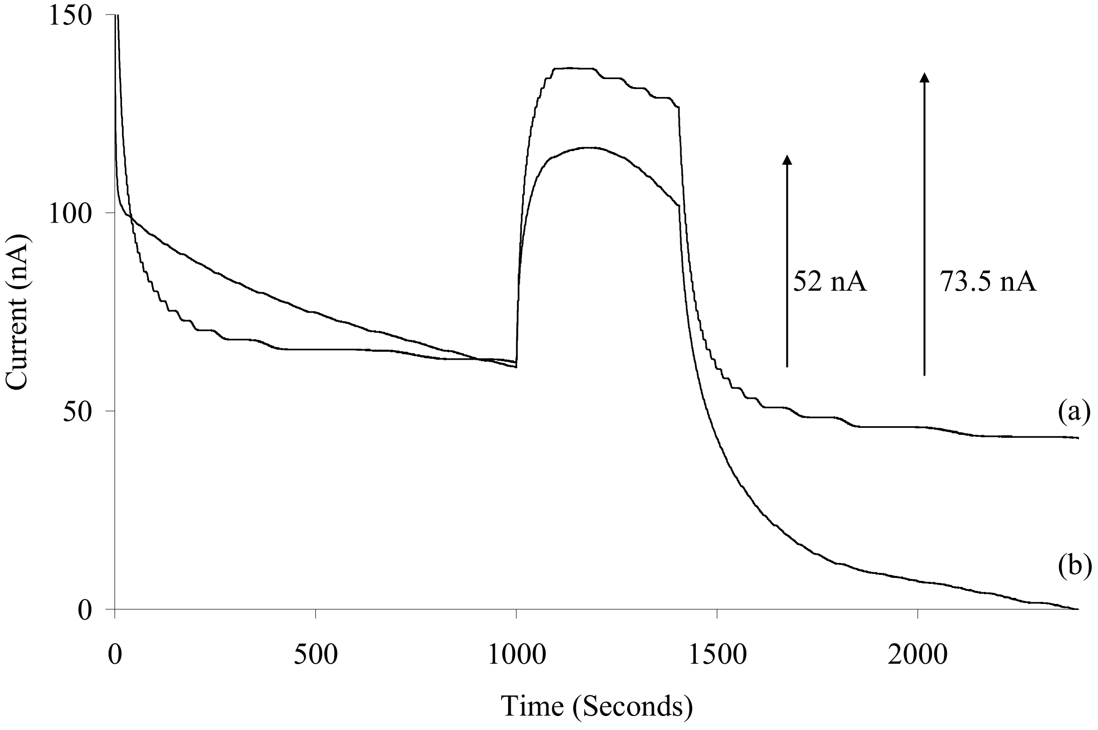

Fig 3.2.8.2: Photocurrents of drop-cast films of (a) $[(Pn)_4N]\beta$-$[Mo_{18}O_{54}(SO_3)_2]$ and (b) $[Ru(bpy)_3]_2\beta$-$[Mo_{18}O_{54}(SO_3)_2]$ modified ITO electrodes in contact with benzyl alcohol (baselines normalized). Each was irradiated for 400 seconds (light on at 1000 seconds, light off at 1400 seconds).

The results of this experiment are striking in that both samples generate significant photocurrents under irradiation with visible light. However, photocurrent generation by the polyoxometalate anion was disappointingly reduced by approximately 60% in the presence of $[Ru(bpy)_3]^{2+}$ (reduction from 61.2 nA to 23.9 nA, Fig 3.2.8.1). The reduction in photocurrent confirms that in the case of the sulfite polyoxometalate, the ruthenium does not sensitize the polyoxometalate and indeed behaves as a filter, reducing the photon flux available to the polyoxomolybdate, resulting in a diminished photocurrent. Comparison with the β-isomer revealed a slightly higher photocurrent (73.5 nA) than that generated by the α form under identical conditions. The associated species, $[Ru(bpy)_3]_2\beta$-$[Mo_{18}O_{54}(SO_3)_2]$, also generated a higher current than the α associated form, producing 52 nA. Interestingly the reduction in current when the Ru was present was not as severe as in the α-isomer case (approximately a 30 % decrease relative to 60 % for the α experiments). These data are presented in Fig 3.2.8.2. Fig 3.2.8.3 demonstrates the degree of spectral overlap between the 2:1 associated species and the POM alone in MeCN solutions.

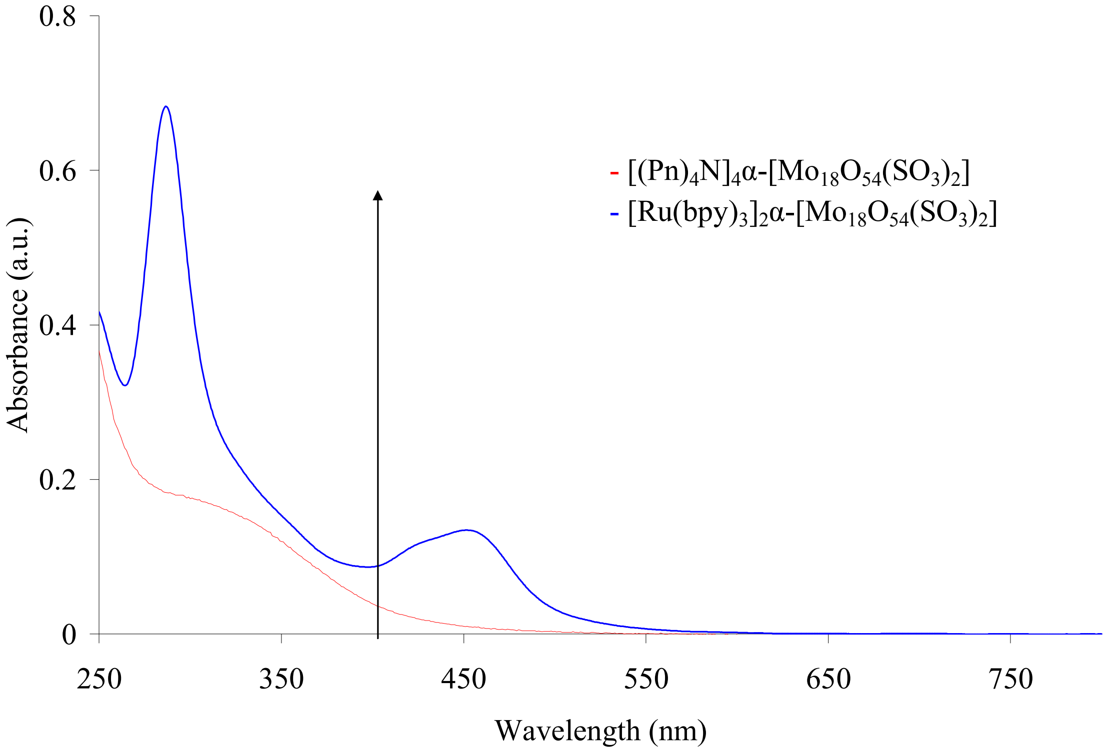

Fig 3.2.8.3: Spectral overlap of [(Pn)$_4$N]$_4$α-[Mo$_{18}$O$_{54}$(SO$_3$)$_2$] (5 x 10^{-6} M) and (b) [Ru(bpy)$_3$]$_2$α-[Mo$_{18}$O$_{54}$(SO$_3$)$_2$] (5 x 10^{-6} M) showing the region of the visible spectrum used as a light source for PEC.

Fig 3.2.8.3 shows that the Ru MLCT band overlaps with the tail of the POM absorbance in the visible region. The absorbance is clearly extended in the case of the composite material; however it is obvious that this absorbance is detrimental to photocurrent generation. It is also noteworthy that blank ITO can also generate a photocurrent under these conditions, as the tail of its absorbance stretches to longer wavelengths than 400 nm. However in each case the POM alone generated a higher current than the ITO alone, and the associated species generated a lower current than the POM alone (of the order of 20 nA).

Fig 3.2.8.4 shows the comparative experiments performed between the sulfite α-$[Mo_{18}O_{54}(SO_3)_2]^{4-}$ and the conventional sulfate containing analogue α-$[Mo_{18}O_{54}(SO_4)_2]^{4-}$. Although the addition of Ru did not result in sensitized POM photochemistry, a comparison of the photocurrent generated by the molybdosulfate $[(Hex)_4N]_4[Mo_{18}O_{54}(SO_4)_2]$ anion with that of the sulfite in the absence of ruthenium confirmed that α-$[Mo_{18}O_{54}(SO_4)_2]^{4-}$ produced a larger photocurrent under identical conditions. Thus, $[(Pn)_4N]_4$α-$[Mo_{18}O_{54}(SO_3)_2]$ produced a photocurrent of magnitude of 61.2 nA, while $[(Hex)_4N]_4[Mo_{18}O_{54}(SO_4)_2]$ generated only 34.5 nA. In a study of the photocatalytic behaviour of $[Mo_{18}O_{54}(SO_4)_2]^{4-}$ dissolved in DMF, it was discovered that the quantum yield of photocatalysis was increased in the visible (420 nm irradiation) in the presence of the ruthenium cation, attributed to sensitization by this species.[4] Apparently, structural differences in the sulfite and sulfate cases have introduced different redox, photochemical and ion association characteristics.

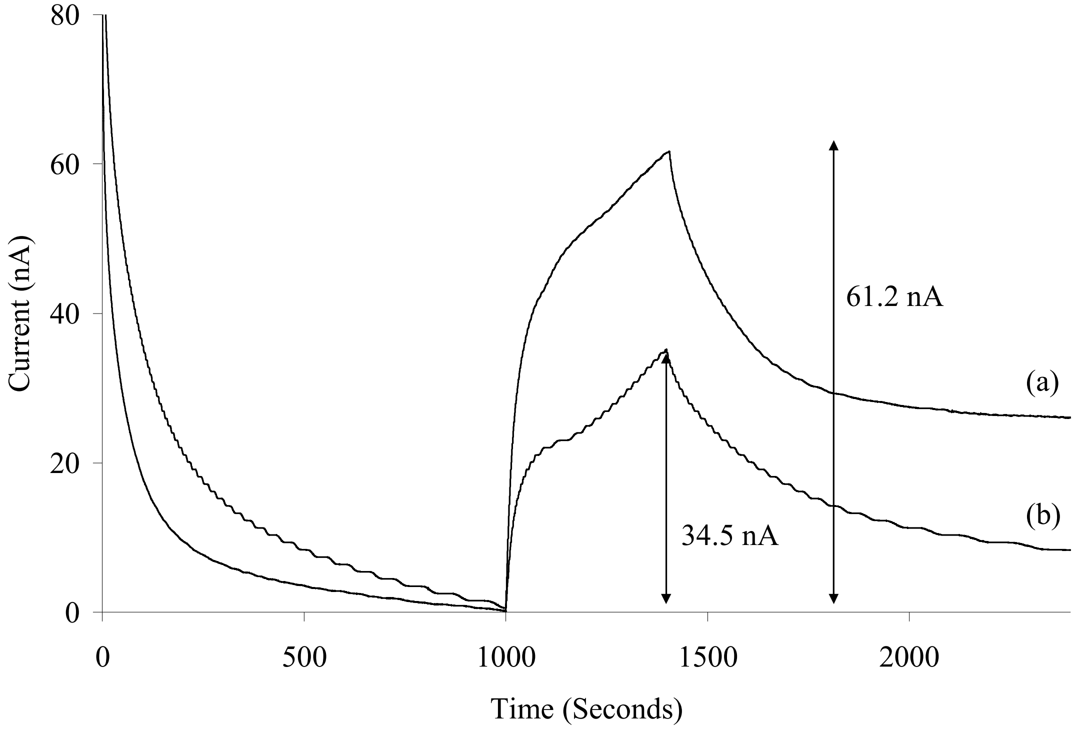

Fig 3.2.8.4: Comparative photocurrents generated by drop-cast POM films on ITO electrodes in the presence of excess benzyl alcohol substrate. (a) $[(Pn)_4N]_4\alpha\text{-}[Mo_{18}O_{54}(SO_3)_2]$ and (b) the conventional $[(Hex)_4N]_4[Mo_{18}O_{54}(SO_4)_2]$.

3.3 – Conclusions:

The photophysics of $[Ru(bpy)_3]^{2+}$ in the presence of the Dawson-like polyoxomolybdates α-$[Mo_{18}O_{54}(SO_3)_2]^{4-}$ and β-$[Mo_{18}O_{54}(SO_3)_2]^{4-}$ have been presented. Both anions associate strongly with $[Ru(bpy)_3]^{2+}$ and efficiently quench the luminescence from this complex. Surprisingly, the quenching observed exhibited mixed static and dynamic behaviour, which has not been observed previously in other studies involving Dawson POMs and $[Ru(bpy)_3]^{2+}$.[2, 3, 4] Difference electronic spectroscopy of the clusters revealed the presence of new electronic transitions which were red-shifted with respect to the $[Ru(bpy)_3]^{2+}$ ^{3}MLCT centred 450 nm and weaker compared to a similar absorbance in the sulfato anions. Resonance Raman spectroscopy, exciting into this new transition, correspondingly showed no contribution from the polyoxometalate, except from a trace amount of reduced species. Furthermore, the adducts showed less photochemical stability than the sulfate adducts with photolability more akin to that of free $[Ru(bpy)_3]^{2+}$, which is indicative of weaker intermolecular electronic interaction in the sulfite containing adduct than that observed in the sulfate analogue. Photo-electrochemical measurements on ITO electrodes with visible light (> 400 nm) irradiation demonstrated that the associated $[Ru(bpy)_3]_2\alpha\text{-}[Mo_{18}O_{54}(SO_3)_2]$, unlike the sulfate analogue $[(Pn)_4N]_4\alpha\text{-}[Mo_{18}O_{54}(SO_3)_2]$, does not sensitize visible light photocatalysis of benzyl alcohol. However, the sulfite molybdate does exhibit a significantly greater photocurrent than found with the sulfato analogue. Structural differences in the sulfite and sulfate containing clusters therefore modify the redox and other physical properties in different ways so that electrochemical and photochemical properties are not analogous.

3.4 – References:

---

[1] V. M. Hultgren, A. M. Bond and A. G. Wedd, *J. Chem. Soc*., *Dalton Trans*., 2001, 1076 - 1082.

[2] T. E. Keyes, E. Gicquel, L. Guerin, R. J. Forster, V. M. Hultgren, A. M. Bond, and A. G. Wedd, *Inorg. Chem.*, 2003, **42**, 7897 - 7905.

[3] M. K. Seery, L. Guerin, R. J. Forster, E. Gicquel, V. M. Hultgren, A. M. Bond, A. G. Wedd, and T. E. Keyes, *J. Phys. Chem. A*, 2004, **108**, 7399 - 7405.

[4] N. Fay, V. M. Hultgren, A. G. Wedd, T. E. Keyes, R. J. Forster, D. Leane and A. M. Bond, *Dalton Trans.*, 2006, 4218 - 4227.

[5] D-L. Long, P. Kögerler and L. Cronin, *Angew. Chem. Int. Ed.,* 2004, **43**, 1817 - 1820.

[6] C. Baffert, J. F. Boas, A. M. Bond, P. Kögerler, D-L. Long, J. R. Pilbrow, and L. Cronin, *Chem. Eur. J.,* 2006, **12**, 8472 - 8483.

[7] D-L. Long, H. Abbas, P. Kogerler, and L. Cronin, *Angew. Chem. Int. Ed*., 2005, **44**, 3415 - 3419.

[8] B. Krebs, E. Droste, M. Piepenbrink and G. Vollmer, *C. R. Acad. Sci., Serie IIc: Chim.,* 2000, **3**, 205.

---

[9] D-L. Long, E. Burkholder and L. Cronin, *Chem. Soc. Rev.*, 2007, **36**, 105 - 121.

[10] M. J. Manos, J. D. Woollins, A. M. Z. Slawin and T. A. Kabanos, *Angew. Chem. Int. Ed.*, 2002, **41**, 2801 - 2805.

[11] D. M. Way, J. B. Cooper, M. Sadek, T. Vu, P. J. Mahon, A. M. Bond, R. T. C. Brownlee and A. G. Wedd, *Inorg. Chem.,* 1997, **36***,* 4227 - 4233.

[12] S. K. Verma and M. K. Deb, *J. Agric. Food Chem.,* 2007, **55***,* 8319 - 8324.

[13] R. M. Silverstein and F. X. Webster, *Spectrometric Identification of Organic Compounds*, 6th Edition, Wiley, pg 143.

[14] P. K. Mallick, G. D. Danzer, D. P. Strommen and J. R. Kincaid, *J. Phys. Chem.,* 1988, **92***,* 5628 - 5634.

[15] Y. Li, H. Zhu and X. Yang, *Talanta*, 2009, **80**, 870 - 874.

[16] L. Bi, H. Wang, Y. Shen, E. Wang, S. Dong, *Electrochem. Commun*., 2003, **5**, 913 - 918.

[17] J. R. Lakowicz, *Principles of Fluorescence Spectroscopy*, 3rd Edition, Springer, p. 282 - 283.

[18] M. K. Seery, N. Fay, T. McCormac, E. Dempsey, R. J. Forster and T. E. Keyes, *Phys. Chem. Chem. Phys*., 2005, **7** , 3426 - 3433.

[19] R. Ballardini, M. T. Gandolfi and V. Balzani, *Inorg. Chem*., 1987, **26**, 862 - 867.

[20] L. Le Bihan, P. Blanchard, M. Fournier, J. Grimblot and E. Payen, *J. Chem. Soc., Faraday Trans.,* 1998, **94**, 937 - 940.

[21] J. B. Cooper, D. M. Way, A. M. Bond and A. G. Wedd, *Inorg. Chem.,* 1993, **32**, 2416.

[22] B. Durham, J. V. Casper, J. K. Nagel and T. J. Meyer, *J. Am. Chem. Soc.,* 1982, **104**, 4803.

[23] T. Rüther, A. M. Bond and W. R. Jackson, *Green Chem*., 2003, **5**, 364 - 366.

[24] T. Rüther, V. M. Hultgren, B. P. Timko, A. M. Bond, W. R. Jackson and A. G. Wedd*, J. Am. Chem. Soc.,* 2003, **125**, 10133 - 10143.

[25] T. Hori and S. Himeno, *Chem. Soc. Jpn. Chem. Lett.,* 1987, **53**.

---

[26] J. Song, Z. Luo, H. Zhu, Z. Huang, T. Lian, A. L. Kaledin, D. G. Musaev, S. Lense, K. I. Hardcastle and C. L. Hill, *Inorg. Chim. Acta*, 2010, **363**, 4381 - 4386.

Chapter 4:

Characterization of novel luminescent metallopolymers and their interactions with the Dawson type polyoxomolybdate α-$[Mo_{18}O_{54}(SO_4)_2]^{4-}$.

4.1 Introduction:

Metallopolymers provide an attractive means of combining the spectroscopic and electrochemical properties of metal complexes with the processability of polymers. They are finding increasing application in molecular electronics,[1] catalysis/electrocatalysis,[2, 3] electrochromic materials,[4, 5] and photo/electroluminescence materials.[6, 7, 8] In particular, metallopolymers containing ruthenium polypyridyl moieties have received significant attention in the areas of electrochemiluminescence (ECL) and photovoltaics due to their long-live excited states, facile electron exchange dynamics and amenability towards thin film assembly.[9, 10, 11]

Extensive effort has been invested in the preparation of ruthenium polypyridyl complexes with optimised photophysical and redox properties. Therefore, a particularly attractive proposition is to chemically incorporate well characterised coordination compounds into a polymer structure in such a way that the metal centre is relatively unperturbed, and largely retains its properties when integrated into the polymeric material. For example the ruthenium metallopolymer $[(\text{polyazabpy})\text{Ru}(\text{bpy})_2]_x^{(2x)+}$ (where polyazabpy = poly[1-(2, 2'-bipyridine-4-yl)-1,4-diazabutadiene-4, 4'-diyl]) has been demonstrated previously to exhibit very similar photophysical and electrochemical characteristics to its parent dimetallic complex $[\{(\text{Ru}(\text{bpy})_2\}_2(\text{DAB})]^{4+}$ (where DAB = diaza-di(5-amino-2,2'-bipyridine)).[12]

In this chapter the characterization of novel co-polymer backbones based on poly(styrene-*p*-(chloromethyl)styrene) which were prepared from the monomers of styrene and 4-vinylbenzylchloride are described. The chlorides within the copolymers were transformed into primary alkyl amines and metallopolymers (Fig 4.1.1) were obtained from the condensation reaction between these amines and carboxylic acid groups pendant on a ruthenium metal complex; $[\text{Ru}(\text{bpy})_2(\text{caip})](\text{ClO}_4)_2$, where caip is 2-(4-carboxyphenyl)imidazo[4,5-f] [1,10]phenanthroline. The objective was to create a hydrogel metallopolymer wherein the metal centre $[\text{Ru}(\text{bpy})_2(\text{caip})](\text{ClO}_4)_2$, retains the properties of its associated monomer. The synthesis, redox and photophysical characteristics of the precursor mononuclear complex; $[\text{Ru}(\text{bpy})_2(\text{caip})](\text{ClO}_4)_2$, have been reported in detail previously. The complex exhibits an intense and pH dependant emission which is long lived and enhanced in aqueous media.[13] A detailed optical spectroscopic and electrochemical study of the novel metallopolymers is presented and the effects of solvent on their optical properties has been investigated and compared with the parent monomer.

In the second half of this chapter the interactions of metallopolymers $[Ru(bpy)_2(PVP)_{10}]^{2+}$ or $[Ru(bpy)_2(caip\ co\text{-}poly)_7]^{2+}$ and the Wells-Dawson structure α-$[Mo_{18}O_{54}(SO_4)_2]^{4-}$ are examined. The metallopolymers exhibit similar spectroscopic, photophysical and electrochemical properties to $[Ru(bpy)_3]^{2+}$ which was demonstrated previously to sensitize $[Mo_{18}O_{54}(SO_4)_2]^{4-}$ photochemistry in solution under visible irradiation.[14] The polymers have the added advantage of improved processability and can bind interfacially to form thin films. The photophysics of the metallopolymer $[Ru(bpy)_2(PVP)_{10}]^{2+}$ have been extensively investigated.[15] It has been shown previously to form stable layers on various electrode surfaces, and therefore it may be possible to use this property to drive discrete LBL multilayer formation or otherwise affect the layer structure.[16] $[Ru(bpy)_2(caip\ co\text{-}poly)_7]^{2+}$ is a novel metallopolymer that has recently been developed by our group and has also been investigated as a potential POM sensitizer. The presence of ionizable imidazole nitrogen atoms on the caip ligand permits facile and reversible changes in electronic properties as a function of pH (see section 4.2). The corresponding monomer complex has been studied previously and provides a useful comparison.[13] We were interested in investigating whether upon polyoxometalate interactions with this polymer could these pH-induced changes potentially alter the degree of electronic interaction with the POM when bound together in the composite film. Indeed, in a recent publication a Ru complex with ionizable imidazole ligands, $[Ru(^tBubpy)_2(biH_2)]^{2+}$ (where ^{t}Bubpy = 4,4'-di-*tert*-butyl-2,2'-bipyridine and biH_2 = 2,2'-biimidazole, doubly protonated), was electrostatically bound to the octamolybdate ion β-$[Mo_8O_{26}]^{4-}$ and dramatic spectroscopic changes were induced upon association.[17] These changes arose as a consequence of the formation of strong N–H---O–Mo hydrogen-bonds, which in turn lead to proton transfer to form N---O–H–Mo. It was hoped that because of the analogous properties of the metallopolymers to $[Ru(bpy)_3]^{2+}$ that comparable interactions with $[Mo_{18}O_{54}(SO_4)_2]^{4-}$ would occur, coupled with the possibility of improved stability of potential interfacial layers. Recently we reported the use of $[Ru(bpy)_2(PVP)_{10}]^{2+}$ and $[Ru(bpy)_2(caip\ co\text{-}poly)_7]^{2+}$ as sensitizers for $[Mo_{18}O_{54}(SO_4)_2]^{4-}$ visible photochemistry, which was the first study employing self-assembled metallopolymer/POM films for this purpose.[11] The purpose of this present chapter is to probe, in detail, the interactions of both polymers with the molybdate and the influence of any association between anion and polymer on the electronic properties and photophysics of the component species.

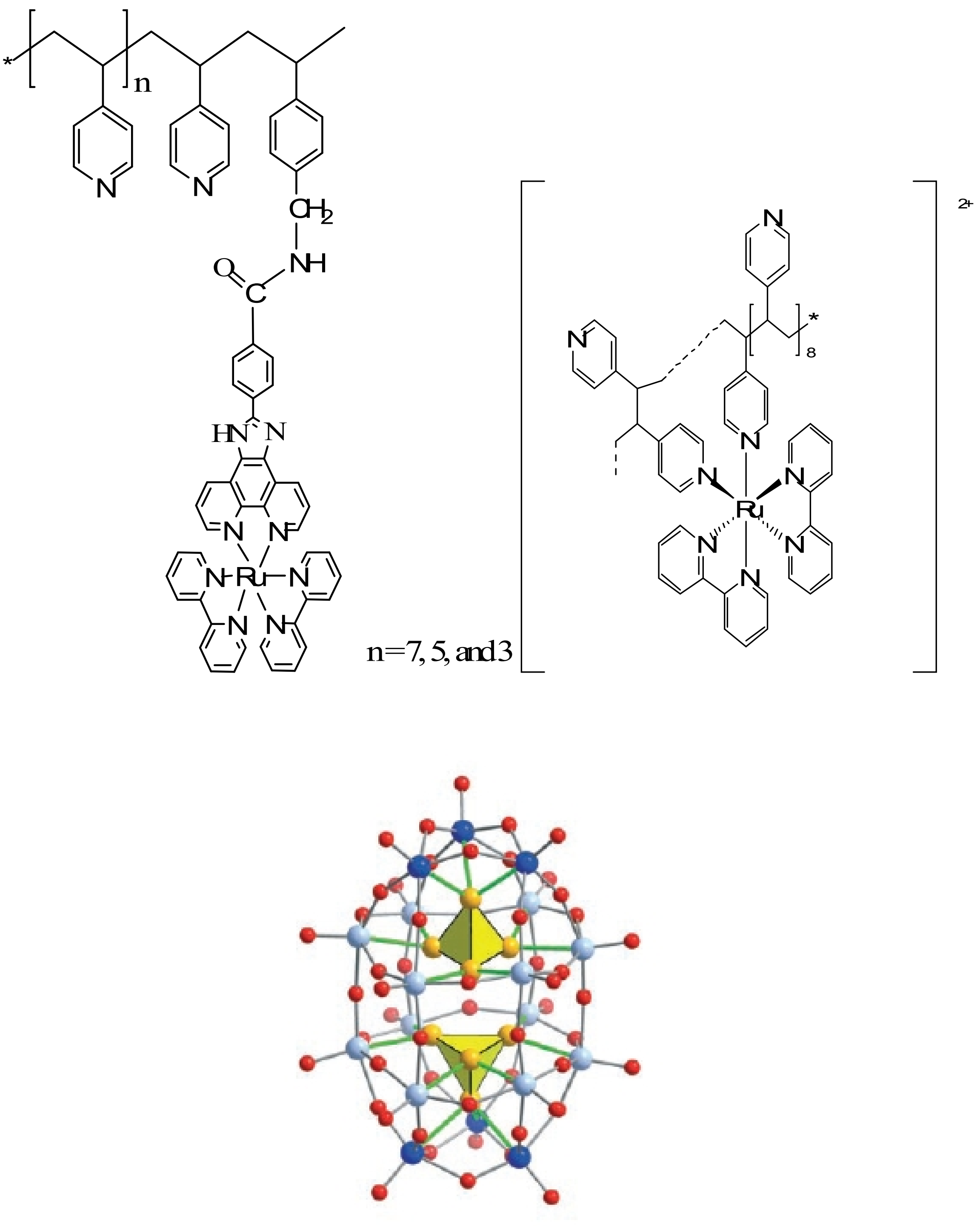

Fig 4.1.1: Structures of the metallopolymers studied in this chapter $[Ru(bpy)_2(caip\ co\text{-}poly)_7]^{2+}$ (n = 5, 7, 9) and $[Ru(bpy)_2(PVP)_{10}]^{2+}$. Structure of α-$[Mo_{18}O_{54}(SO_4)_2]^{4-}$ (below, reproduced from Ref [18]).

4.2 – Characterization of the metallopolymers $[Ru(bpy)_2(caip\ co\text{-}poly)_n]^{2+}$ (n = 5, 7, 9):

4.2.1 Electrochemistry:

The three metallopolymers were synthesized by Dr. Qiang Zeng (see Chapter 2). Table 4.2.1.1 summarizes the electrochemical data for the parent $[Ru(bpy)_2(caip)](ClO_4)_2$ complex and the three metallopolymers. When dissolved in dry DMF with 0.1 M $TBABF_4$ as supporting electrolyte the metallopolymers exhibit a single, one electron, reversible metal centreed oxidation at approximately + 1.0 V. Three reversible one electron reductions are observed around -1.23, -1.91, and -2.37 V, which are assigned to the reduction of the bipyridine and caip ligands. These redox potentials are similar to those of the parent complex obtained under the same conditions and the values are independant of the loading of metal centres in the co-polymers.[13] These data suggest that the coupling between the Ru metal centres and copolymer backbones through the amide linkage and polymer backbone is minimal and higher loadings of metal do not significantly influence the energy of the Ru^{2+}/Ru^{3+} redox process. The effect of the polymer loading on the rate of charge diffusion through metallopolymer films was also investigated by cyclic voltammetry of drop-cast thin films. An example of this voltammetry is shown in Fig 4.2.1.1.

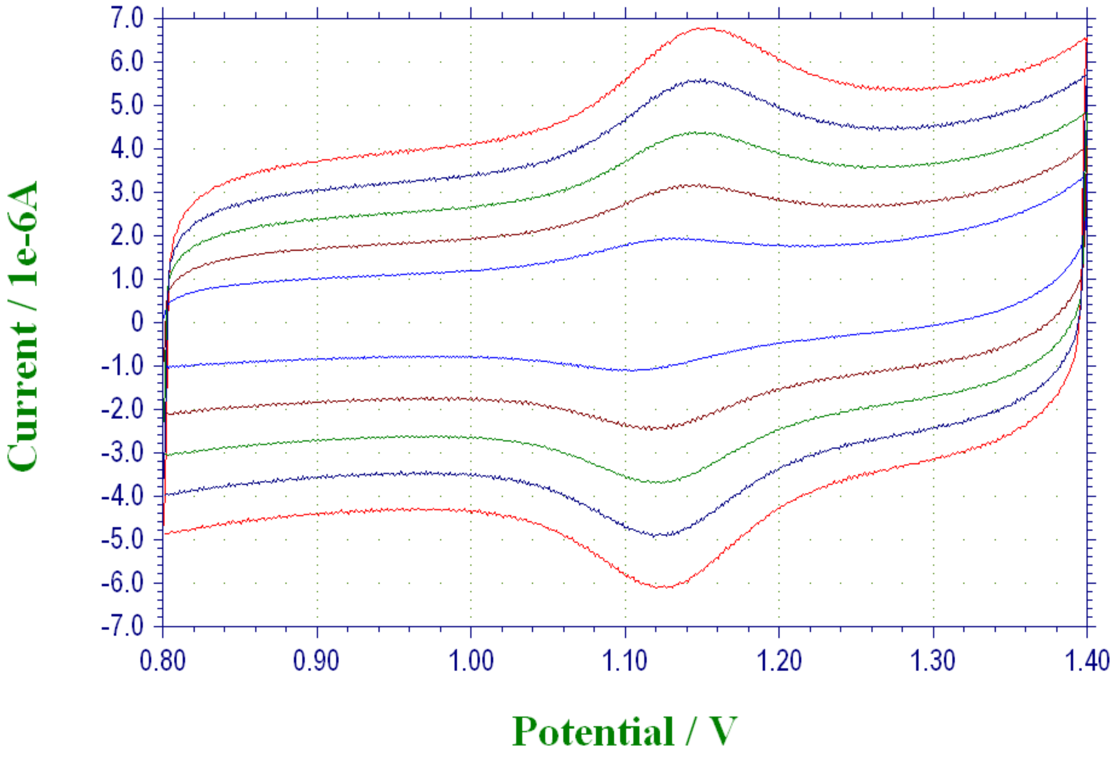

Fig 4.2.1.1: Cyclic voltammograms of drop-cast thin film of [Copolymer (7)–CH_2NHCO-Ru]$^{2+}$ on a glassy carbon working electrode (A = 0.0717 cm^2) with 0.1 M $HClO_4$ in MeCN electrolyte. Scan rates (from lowest) were 100, 200, 300, 400 and 500 mV.s^{-1}. The reference electrode was an Ag wire (+ 400 mV vs Fc/Fc^+) and the counter electrode was a Pt wire.

The films were prepared by drop-casting 10 µl aliquots of a 3 x 10^{-4} M solution of metallopolymer onto a GC working electrode and allowing to dry in air. The voltammograms obtained indicate that there is no evidence for metal-metal interaction at all three loadings as only one Ru redox process is observed. The corresponding experiments with [Copolymer (5)–CH_2NHCO-Ru]$^{2+}$ and [Copolymer (9)–CH_2NHCO-Ru]$^{2+}$ show a similar voltammetric response. Using the peak currents obtained from various scan rates, the homogeneous charge transfer diffusion coefficient, D_{CT}, can be determined using the Randles-Sevçik equation (Equation 1):

$$i_p = (2.69x10^5)n^{3/2}ACD_{CT}{}^{1/2}\nu^{1/2} \qquad \text{(Equation 1)}$$

where n is the number of electrons transferred, A is the area of the electrode (cm^2), C is the concentration of ruthenium centres within the film (mol.cm^{-3}), and i_p is the peak current (Amps). Therefore a plot of i_p vs $\upsilon^{1/2}$ should be linear and the value of D_{CT} can be extracted from the slope, provided the concentration is known. The concentration was calculated from the surface coverage, Γ, and the layer thickness. The surface coverage can be calculated from cyclic voltammetry at slow scan rates according to Equation 2:

$$i_p = \frac{n^2 F^2}{4RT} \nu A \Gamma \qquad \text{(Equation 2)}$$

where F is Faraday's constant (96485 $C.mol^{-1}$), T is the absolute temperature and R is the universal gas constant (8.31 $J.mol^{-1}.K^{-1}$). Combining Equations 1 & 2 it can be seen that the peak current varies linearly with scan rate for a surface confined process, and varies linearly with the square root of scan rate for a diffusion controlled process. The concentration of the three polymer films were calculated as (8.2 ± 1.0) x 10^{-6} $mol.cm^{-3}$ (5-1), (7.3 ± 1.6) x 10^{-6} $mol.cm^{-3}$ (7-1) and (6.3 ± 0.8) x 10^{-6} $mol.cm^{-3}$ (9-1). Using these C values the D_{CT} values were calculated as (2.7 ± 0.5) x 10^{-9} $cm^2.s^{-1}$ (5-1), (5.7 ± 2.4) x 10^{-9} $cm^2.s^{-1}$ (7-1) and (3.5 ± 0.6) x 10^{-9} $cm^2.s^{-1}$ (9-1). These values are significantly higher than those obtained for films of $[Os(bpy)_2(PVP)_{10}]^{2+}$ and $[Ru(bpy)_2(PVP)_{10}]^{2+}$, which were usually of the order of 10^{-11} $cm^2.s^{-1}$. This may indicate higher surface coverages for the caip based polymers, which could be due to the shorter chain lengths of the caip backbones relative to PVP (ie: higher metal centre surface packing density).

4.2.2 Electronic spectroscopy:

The spectroscopic data for the three polymers explored are summarized in Table 4.2.1 along with related data for the parent complex $[Ru(bpy)_2(caip)]^{2+}$. The UV/Vis spectra of the metallopolymers are very similar to that of the parent monomer and display both the characteristic metal to ligand charge transfer (^{1}MLCT) transition centred around 460 nm and the ligand $\pi \rightarrow \pi^*$ transitions at ~ 280 nm. Correspondingly the polymer would be expected to exhibit similar pH dependence as the parent complex, which possesses two ionizable sites on the imidazole ring. These data are shown in Fig 4.2.2.1.

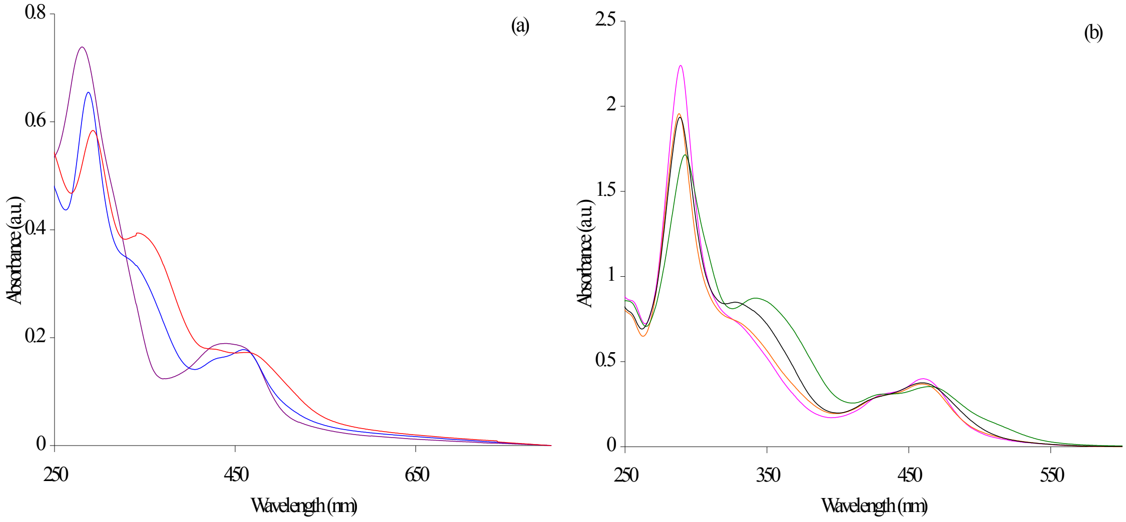

Fig 4.2.2.1 (a): pH induced spectral changes of [Copolymer (7)–CH_2NHCO-Ru]$^{2+}$ (1.1 x 10^{-5} M) in aerated MeCN. Purple: pH = 1.3, blue: pH = 7 and red: pH = 10.9. (b): Spectral changes of 2.2 x 10^{-5} M Copolymer (7)-CH_2NH_2 induced by changing solvent polarities. Pink: dichloromethane, orange: acetonitrile, black: methanol and green: dimethylsulfoxide.

Fig 4.2.2.1 (a) shows the spectral changes induced by changing the pH of the solution wherein deprotonation of the imidazole ring under basic conditions results in a red shift to the MLCT and broadening of this feature out to 600 nm. This response is very similar to that reported for the parent and also for a useful model complex reported previously, [Ru(bpy)$_2$(caip-CONH-adamantyl)](ClO$_4$)$_2$, where the carboxyl pendant is conjugated via an amide linker to amino-adamantyl (see Fig 4.2.2.2).[28] The red shift was attributed to increased σ-donor ability in the deprotonated imidazole moiety, which can lead to destabilisation of the Ru t_{2g} energy levels leading to a decreased $t_{2g} \rightarrow$ bpy(π^*) energy gap. Another peak centreed at approximately 340 nm grows in with increasing pH. This feature was attributed to the caip-based $\pi \rightarrow \pi^*$ transition. Conversely, under acidic conditions, the imidazole becomes fully protonated and this results in a cationic charge on this ring and a blue shift in the MLCT transition. Again, this is consistent with behaviour observed for analogous complexes and attributed to the stabilisation of the t_{2g} levels of the metal with respect to the bipyridyl (π^*) orbitals.

At high pH values (ie: [Copolymer (7)–CH_2NHCO-Ru]$^{+}$) the imidazole ring of the caip ligand is fully deprotonated and this results in a red-shift of both the absorbances at 340 and 450 nm. Previously this has been attributed to increased σ-donor ability in the deprotonated imidazole moiety, which can lead to decreased metal t_{2g} energy levels. In addition, a tail on the MLCT appears which extends the absorption to approximately 550 nm. This feature has been seen in the spectrum of $[Ru(bpy)_2(caip)](ClO_4)_2$ but not that of $[Ru(bpy)_2(caip\text{-}CONH\text{-}adamantyl)](ClO_4)_2$, and has been attributed to a benzocarboxylate → phenanthroline interligand charge-transfer (ILCT) transition. This suggests increased delocalization of the π system occurs, facilitating increased electronic communication between the imidazole and phenanthroline groups. As in previous studies, the changes to the MLCT are relatively minor which suggests that the LUMO of the MLCT is based on the bipyridines and not the caip ligand. However, resonance Raman spectroscopy reveals that both transitions contribute to the broad MLCT (see section 4.2.3). Changing the loading of the metallopolymer increases the value of the extinction coefficient of the MLCT at 455 nm nonlinearly as a function of increasing chain length. However, there is little change to the MLCT wavelengths or band shape which is consistent with the electrochemical data and indicates little electronic interaction between the metal complex moieties. This deviation from linear Beer-Lambert behaviour with metal centre loading, the so-called "hypochromic effect" has been observed previously for a series of ruthenium polypyridyl polymers.[34] This was also seen in the case of poly(2-vinylpyridine), and this was attributed to electronic interactions between neighbouring monomer groups.[19] However significant ground-state electronic communication has been ruled out in this case on the basis of UV/Vis and electrochemical data.

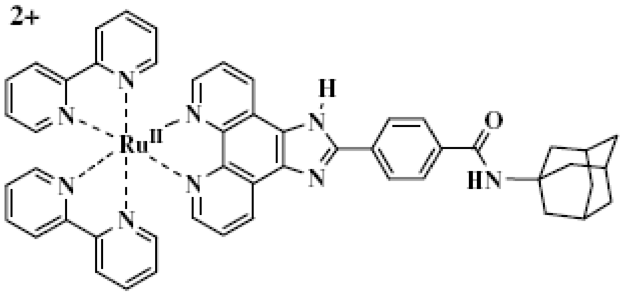

Fig 4.2.2.2: Structure of $[Ru(bpy)_2(caip\text{-}CONH\text{-}adamantyl)]^{2+}$. Reproduced from [28].

Fig 4.2.2.1 (b) shows the impact of changing solvent polarity on the absorption spectra of $[Copolymer\ (7)\text{–}CH_2NHCO\text{-}Ru]^{2+}$. The absorbance spectra of the polymer in MeCN and non-polar DCM show only very minor differences in the relative intensities of the ligand based and MLCT transitions with no evident shift in wavelength of the various transitions present. In the case of a protic solvent, methanol, the caip ($\pi \rightarrow \pi^*$) transition at approximately 330 nm appears along with a slight broadening of the MLCT to the red. In DMSO similar but more extenuated behaviour is observed. Indeed the spectrum of the polymer in DMSO corresponds notably to the complex in the deprotonated state, as the spectrum clearly resembles that of the pH = 10.9 solution from Fig 4.2.2.1 (a). DMSO has a very significant and anomalous impact on the spectroscopy of the polymers. Overall, spectroscopic and electrochemical data in solution indicate that the metal centres within the polymer retain the characteristics of the parent complex with little or no modification.

Materials	**λ_{MLCT} nm (ε 10^{-3}, M^{-1} cm^{-1})^a**	**$E_{1/2}^{ox}$ V^b**	**$E_{1/2}^{red}$ V^b**
$[Ru(bpy)_2(caip)](ClO_4)_2$	455 (17.5)	1.01	-1.24, -1.93, -2.37
Copolymer (9)–CH_2NHCO-Ru	455 (17.1)	1.00^b	-1.23, -1.91, -2.36
Copolymer (7)–CH_2NHCO-Ru	455 (16.7)	1.01^b	-1.23, -1.91, -2.37
Copolymer (5)–CH_2NHCO-Ru	455 (15.4)	1.00^b	-1.24, -1.93, -2.37

Table 4.2.1: Spectroscopic and electrochemical data for the three metallopolymers obtained at room temperature. Comparison with model monomer complex is included. *a* = in spec grade MeCN; *b* = in DMF containing 0.1 M $(But)_4NBF_4$ electrolyte.

4.2.3 - Resonance Raman spectroscopy:

In order to investigate if incorporation of the $[Ru(bpy)_2(caip)]^{2+}$ unit into the polymer influences the origin of the MLCT transition, resonance Raman spectroscopy of the polymers was conducted as a function of pH. Resonance Raman is useful as it permits relatively unambiguous identification of the nature of optical transitions in complex systems. Under resonance excitation in Raman spectroscopy the excitation wavelength coincides with an absorbance, in this instance the ^{1}MLCT of the complex, and this yields a resonance Raman spectrum with a large increase in intensity of the vibronic modes associated with the chromophore under irradiation. Resonance enhancements of 3 to 6 orders of magnitude are typical.[20] The resonance Raman spectra of the three protonation states of [Copolymer (7)–CH_2NHCO-Ru]$^{2+}$ are presented in Fig 4.2.3.1.

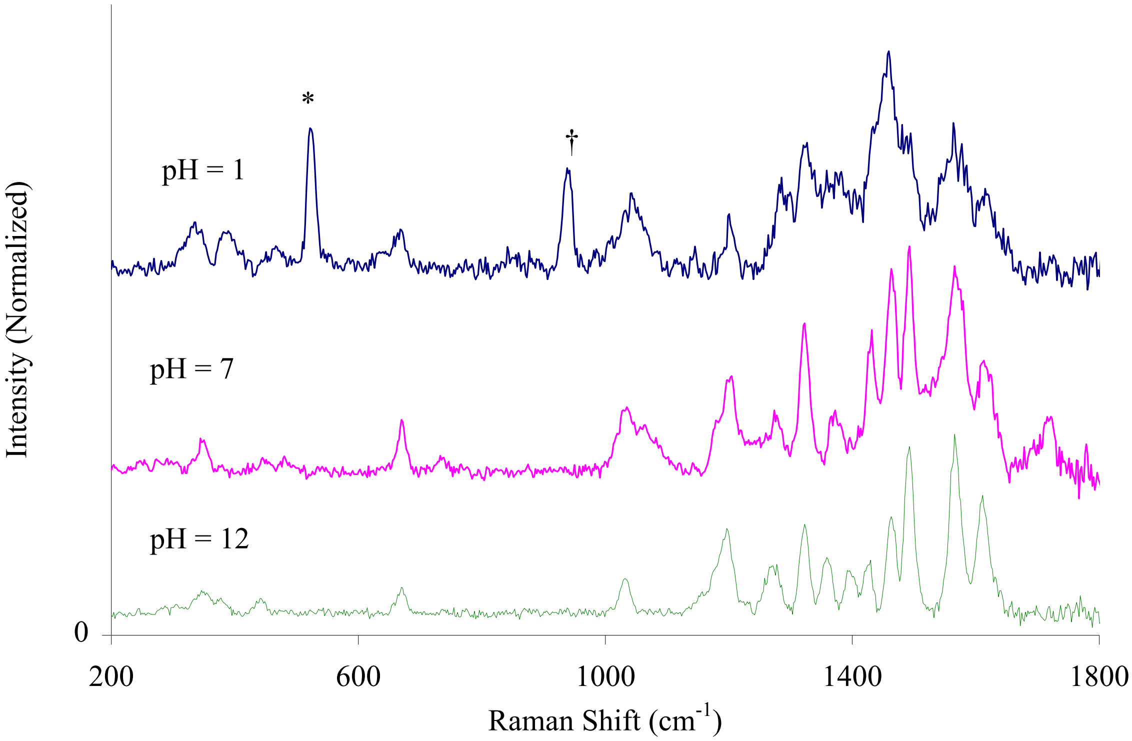

Fig 4.2.3.1: Resonance Raman spectra of thin films of Copolymer (7)-CH_2NH_2 in its various protonation states drop-cast from solutions of MeCN or DMSO onto a clean silicon wafer under 458 nm irradiation. * silicon mode; † $HClO_4$ mode.

The resonance Raman spectra under 458 nm irradiation show significant pH dependence. At pH 10.9, when the imidazole groups are expected to be fully deprotonated (ie: [Copolymer (7)–CH_2NHCO-Ru]$^+$) signature bipyridyl modes can be seen at 1608, 1563, 1491, 1323, 1278, 1180, 1028 and 669 cm^{-1}, and a very weak Ru-N mode appears at 376 cm^{-1}. However other modes, which are not attributable to the Ru(dπ)-bpy(π*) MLCT, are weak but visible at 1463, 1427, 1398 and 1203 cm^{-1}, and are likely due to post-resonance with the caip-based π → π* transition at 330 nm. As the pH is decreased, the spectra of [Copolymer (7)–CH_2NHCO-Ru]$^{2+}$ and [Copolymer (7)–CH_2NHCO-Ru]$^{3+}$ (pH = 7 and pH = 1.3 respectively) become increasingly complex relative to that of [Copolymer (7)–CH_2NHCO-Ru]$^+$ (pH = 10.9); the eight signature bpy modes remain strongly in resonance at pH 7, but although present are strongly dominated by caip modes at 1654, 1628, 1592 and 1035 cm^{-1}. This suggests that the MLCT feature centred around 458 nm contains contributions from both Ru(dπ)-bpy(π*) and Ru(dπ)- caip(π*) when the caip is partially protonated but that when the caip is fully protonated the Ru(dπ)- caip(π*) is the dominant contribution to the MLCT at 458 nm. This is consistent with a situation in which the caip ligand becomes increasingly π-accepting as it gains a positive charge when fully protonated at low pH.

Spectra taken at 488 nm confirm that the relative intensities of the bpy modes decreases significantly relative to those of the caip ligand modes, confirming that the Ru(dπ)- caip(π*) MLCT moves further into resonance at 488 nm. These data would appear to suggest that the energy of the Ru(dπ)- caip(π*) MLCT transition is strongly pH dependant. At high pH values the ligand is completely deprotonated and the energy of the Ru-caip transition moves to higher energy, meaning that irradiation at 458 nm results in the resonant enhancement of the Ru-bpy transition only. As the caip becomes protonated, however, there is an increase in the degree of localization of the π* acceptor state across the entire caip ligand. That the caip contribution to the resonance Raman spectrum at low pH is even greater under 488 nm confirms that switching occurs between the lowest energy transition from Ru(dπ)-bpy(π*) when the caip ligand is deprotonated to Ru(dπ)-caip(π*) when it is fully protonated. The effect of changing the polymer chain length was also investigated, and is shown in Fig 4.2.3.2.

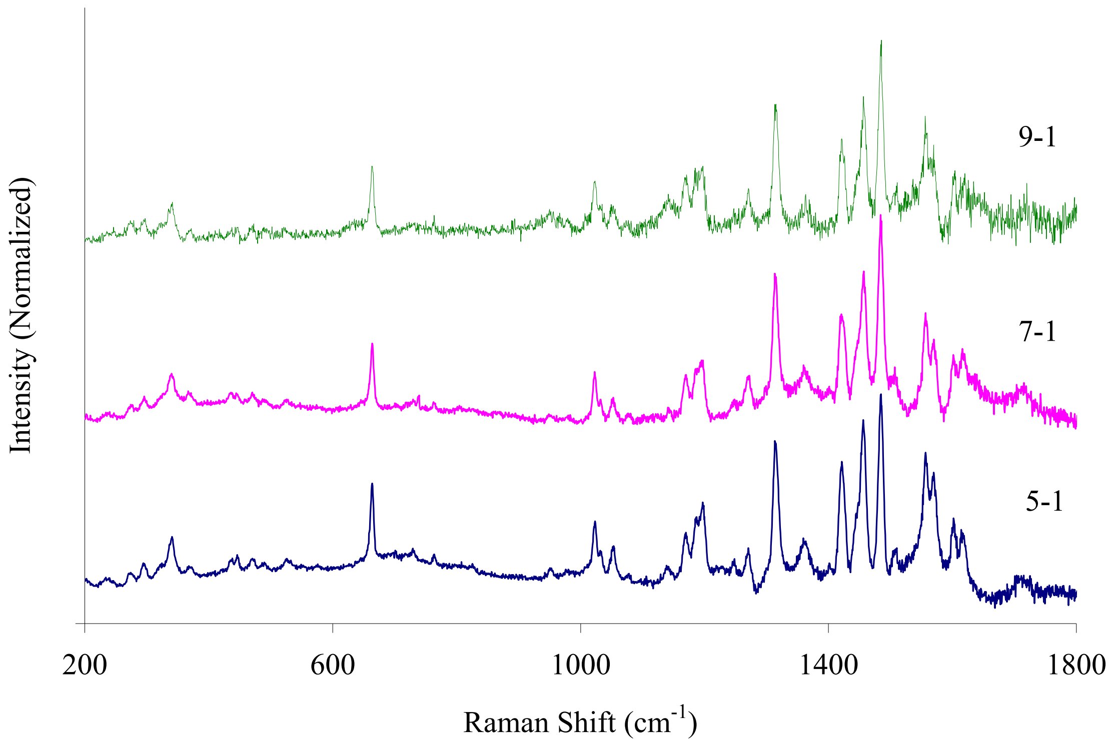

Fig 4.2.3.2: Resonance Raman spectra of the three metallopolymers in their 2+ state dispersed in KBr (~ 5 % w/w) under 458 nm irradiation.

Comparing the spectra of all three metallopolymers under 458 nm irradiation indicates that the polymer, its chain length and metal loading have a negligible effect on the MLCT transitions being probed under resonance. This is also reflected in the electrochemical data. For comparison the spectra of the monomer complex [Ru(bpy)$_2$(caip-CONH-adamantyl)]$^{2+}$ are included in Fig. 4.2.3.3. This complex has very similar pH dependence to the polymers under study.

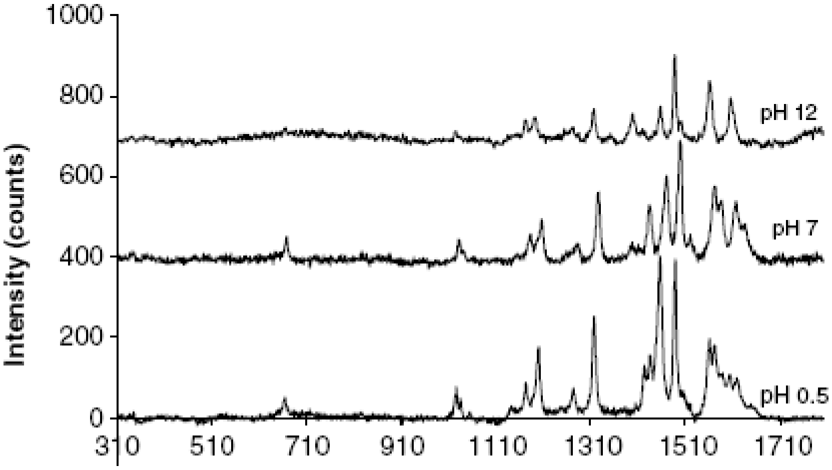

Fig 4.2.3.3: Resonance Raman spectra of [Ru(bpy)$_2$(caip-CONH-adamantyl)]$^{2+}$ at various pH values in buffered aqueous solution under 458 nm irradiation. Reproduced from [28].

The spectrum taken at pH 7 in Fig 4.2.2.3 is very similar to those of the metallopolymers shown in Fig 4.2.2.2, indicating that both the adamantyl group and polymer backbone have very little effect on the spectra of the complexes. This is due to, as discussed, localization of the excited state on the bpy ligands when the complex is not fully protonated. The three spectra in Fig 4.2.3.3 also show that the complexity of the spectra increase with decreasing pH, which is reflected in Fig 4.2.3.1. This is due to the changing electronics of the caip ligand resulting in the Ru-caip MLCT coming into resonance as a function of pH, as discussed previously.

4.2.4 - Emission spectroscopy:

The emission spectra of the metallopolymers have been studied in detail, and these data are presented in Fig 4.2.4.1.

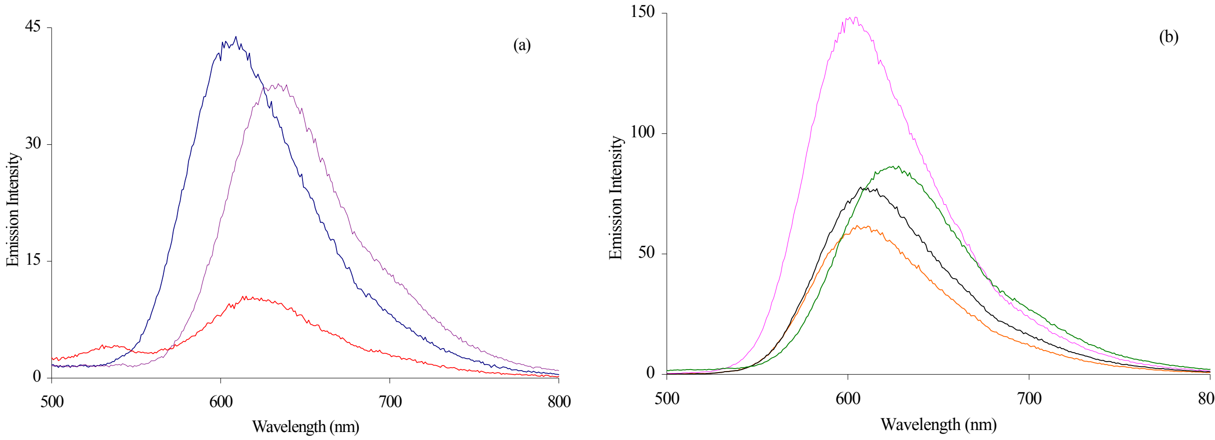

Fig 4.2.4.1 (a): pH induced spectral changes of 1.1 x 10^{-5} M Copolymer (7)-CH_2NH_2 in aerated MeCN. Purple: pH = 1.3, blue: pH = 7 and red: pH = 10.9. (b): Spectral changes of 2.2 x 10^{-5} M Copolymer (7)-CH_2NH_2 induced by changing solvent polarities. Pink: dichloromethane, orange: acetonitrile, black: methanol and green: dimethylsulfoxide. Excitation wavelength was 460 nm.

Fig 4.2.4.1 (a) shows the emission data corresponding to the absorption spectra in Fig 4.2.2.1 (a). Excitation (at 460 nm, absorbance matched) resulted in significant changes to the intensity and λ_{max} of the three pH states of the polymer. In neutral MeCN the emission intensity maximum appeared at 609 nm. Upon acidification this feature red-shifted to 626 nm and its intensity was reduced by approximately 10 %. However upon pH adjustment to 10.9 the intensity dropped dramatically, to only a quarter of the original intensity, and this feature appeared at 626 nm. The pH dependant emission of the metallopolymers is similar to but subtly different from the monomer complex $[Ru(bpy)_2(caip)](ClO_4)_2$.[13] For the monomer complex in MeCN the emission of lowest energy was for the fully protonated complex $[Ru(bpy)_2(caip)]^{3+}$, which exhibited a λ_{max} of 635 nm. The $[Ru(bpy)_2(caip)]^{2+}$ complex, in pH neutral media, exhibited a λ_{max} of 605 nm, which is slightly blue-shifted with respect to the polymer. Although the λ_{max} values of the polymer and monomer are very similar, the relative intensities of emission varied. In the case of the polymer the fully protonated [Copolymer (7)–CH_2NHCO-Ru$]^{3+}$ states exhibit the highest emission intensity, approximately 15 % more intense than that of [Copolymer (7)–CH_2NHCO-Ru$]^{2+}$, whereas in the case of the monomer the $[Ru(bpy)_2(caip)]^{2+}$ state exhibited the more intense emission. The emission of the fully deprotonated [Copolymer (7)–CH_2NHCO-Ru$]^{+}$ occurs at 626 nm, relative to 618 nm in the case of $[Ru(bpy)_2(caip)]^{+}$, which is attributed to solvation/local environment differences between the monomer and polymer. The minor differences in λ_{max} of the polymer and monomer strongly suggest that the photophysical properties of the polymer MLCT based excited states are moderately affected by the presence of the polymer backbone.

Fig 4.2.4.1 (b) presents the effects of changing solvents on the emission properties of the polymer. The least polar solvent, DCM, exhibits by far the highest intensity emission, at about 2.5 times that of the neutral MeCN solution. The emission was also blue-shifted from 609 nm to 604 nm. Changing from MeCN to MeOH resulted in an increase in emission intensity of approximately 25 %, and an accompanying red-shift of 4 nm. Upon changing solvent from MeCN to DMSO the emission was red-shifted by 17 nm, resulting in an emission profile comparable to that observed when the polymer was dissolved in high pH media. In strong contrast to the high pH media, however, the luminescence intensity decreased by approximately 30 % in DMSO. The large changes in UV and luminescence spectra of [Copolymer (7)–CH_2NHCO-Ru]$^{2+}$ in DMSO seem rather anomalous. DMSO is a polar aprotic solvent like acetonitrile and dichloromethane and in terms of its dielectric constant (46.7) it lies above acetonitrile (37.5) and methanol (33). The spectroscopic changes induced in the polymers by DMSO are somewhat reminiscent of its protonation of the benzimidazole ligand. However DMSO is a H-bond acceptor and on this basis might be expected to H-bridge to the benzimidazole proton, hence inducing spectral changes more reminiscent of deprotonation.[21] Luminescent lifetimes of the polymer also increase significantly upon changing from acetonitrile to DMSO. Fluorescence anisotropic measurements are currently underway to investigate this further.

4.2.5 - Time-resolved emission and microscopy:

The excited state lifetimes of the metallopolymers have been studied as a function of solvent and pH as both have been shown above to have a strong influence on the emission characteristics of the polymers. The luminescent decays of the polymers fitted best to a biexponential function. For example, the luminescence decay of [Copolymer (7)–CH_2NHCO-Ru]$^{2+}$ in deaerated DCM is presented in Fig 4.2.5.1. This multi-exponential decay behaviour is common for polymers due to the microheterogeneous environment they display.[31] The luminescent lifetimes of the three copolymers and the parent monomer complex under different solvent and pH conditions are presented in Table 4.2.5.

Complex/Solvent	**λ_{max} abs (nm)**	**λ_{max} emit (nm)**	**$\tau_{1\ aerated}$ (ns) (% cont.)**	**$\tau_{2\ aerated}$ (ns) (% cont.)**	**$\tau_{1\ deaerated}$ (ns) (% cont.)**	**$\tau_{2\ deaerated}$ (ns) (% cont.)**
$[Ru(bpy)_2(caip)]^{2+}$	455^a	605^a		N/A	973 ± 3^a	N/A
$[Ru\ co\text{-}p\ 5]^{2+}$/MeCN	455	609	241 ± 6 (61)	142 ± 3 (39)	404 ± 17 (82)	177 ± 5 (18)
MeOH	458	611	213 ± 8 (72)	112 ± 12 (28)	694 ± 25 (86)	212 ± 18 (14)
DCM	459	604	444 ± 3 (71)	168 ± 3 (29)	953 ± 38 (76)	269 ± 29 (24)
DMSO	465	626	496 ± 16 (89)	167 ± 21 (11)	920 ± 37 (82)	337 ± 24 (18)
Thin film			236 ± 4 (84)	42 ± 2 (16)		
$[Ru\ co\text{-}p\ 5]^{3+}$	440^b	634^b				
$[Ru\ co\text{-}p\ 5]^{+}$	468^b	627^b				
$[Ru\ co\text{-}p\ 7]^{2+}$/MeCN	455	609	208 ± 5 (63)	102 ± 5 (37)	424 ± 5 (85)	117 ± 2 (15)
MeOH	458	613	273 ± 3 (95)	148 ± 4 (5)	542 ± 46 (95)	114 ± 17 (5)
DCM	459	604	422 ± 2 (94)	106 ± 7 (6)	994 ± 1 (94)	241 ± 3 (6)
DMSO	464	626	405 ± 1 (94)	140 ± 1 (6)	844 ± 1 (95)	285 ± 7 (5)
Thin film			321 ± 9 (71)	70 ± 4 (29)		
$[Ru\ co\text{-}p\ 7]^{3+}$	437^b	635^b				
$[Ru\ co\text{-}p\ 7]^{+}$	461^b	626^b				
$[Ru\ co\text{-}p\ 9]^{2+}$/MeCN	455	610	203 ± 4 (72)	98 ± 4 (28)	341 ± 24 (88)	118 ± 5 (12)
MeOH	458	615	214 ± 12 (65)	112 ± 19 (35)	709 ± 56 (82)	193 ± 10 (18)
DCM	459	603	425 ± 11 (77)	111 ± 25 (23)	971 ± 61 (77)	216 ± 23 (23)
DMSO	465	632	337 ± 2 (87)	98 ± 21 (13)	790 ± 44 (82)	324 ± 48 (18)
Thin film			259 ± 9 (84)	51 ± 4 (16)		
$[Ru\ co\text{-}p\ 9]^{3+}$	440^b	635^b				
$[Ru\ co\text{-}p\ 9]^{+}$	463^b	627^b				

Table 4.2.5: Effects of solvent polarity and pH on the photophysics of all three copolymers and their parent monomer. *a*: data reproduced from [13], *b*: Complex was dissolved in 100 µl MeCN and made up to 3 ml with solvent listed (approx 3.3 % v/v); pH was adjusted by titrating 5 µl of either 1.0 M $HClO_4$ or 1.0 M $(But)_4NOH$ into 3 ml of MeCN complex solution in order to prevent precipitation. Dissociation of acid/base is almost quantitative in MeCN.[22]

The data in Table 4.2.5 shows that, as predicted on the basis of the behaviour of the parent monomer, the presence of O_2 in solution has a dramatic effect on the luminescent lifetime. As expected the long component of the decay is most affected, while the influence on the short component depended on its lifetime. In DCM and DMSO where the short component of the decay exceed 200 ns it was strongly influenced by O_2, due presumably to diffusion rate of O_2 through the polymer in solution, whereas this effect was not as pronounced in the cases of MeCN and MeOH. The lifetime of the polymer varies strongly with solvent ranging from 424 ns in deaerated acetonitrile to 994 ns in dichloromethane. Interestingly, the lifetime in polar DMSO was also high at 844 ns. The luminescent decay of [Copolymer (7)–CH_2NHCO-Ru]$^{2+}$ in deaerated DCM is shown in Fig 4.2.5.1.

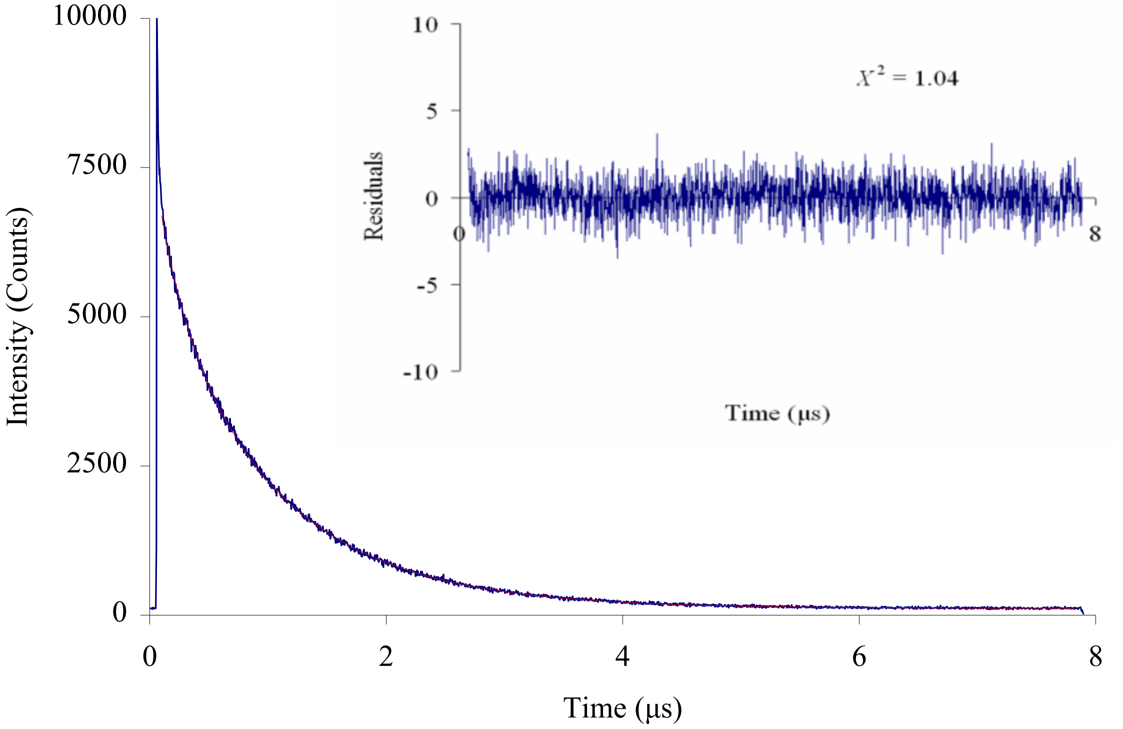

Fig 4.2.5.1: Luminescence decay from [Copolymer (7)–CH_2NHCO-Ru]$^{2+}$ in deaerated DCM at room temperature. The overlaid trace shows the fitted line to a biexponential model.[23] Inset: Residual of biexponential tailfit with regression coefficient of 1.04.

Fig 4.2.5.1 presents the long luminescence lifetime of [Copolymer (7)–CH_2NHCO-Ru]$^{2+}$ in DCM when O_2 is removed. Interestingly the lifetimes of the other chain-length polymers under the same conditions of solvent, temperature and O_2 concentration are comparable to [Copolymer (7)–

CH_2NHCO-$Ru]^{2+}$. This appears to suggest that the large distance from the metal centre to the polymer backbone leads to negligible changes in lifetime due to environment or metal-metal interaction.

Thin films of the polymers remain luminescent, so their lifetimes were also explored as an understanding of their behaviour in this state is important in any layer-by-layer assembly. In all three cases the major component is largely similar and resembles the lifetimes observed in MeCN or MeOH. However the shorter component is drastically reduced relative to those measured in solution. This may be attributed to the fact that the polymer film is fully exposed to O_2, or due to their being less microenvironment homogeneity Studies into the thin film topology of [Copolymer (7)–CH_2NHCO-$Ru]^{2+}$ are shown in Fig 4.2.5.2.

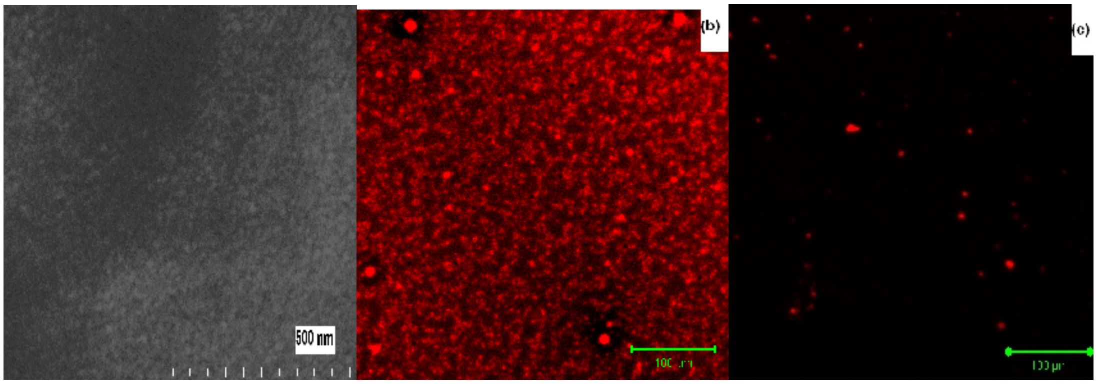

Fig 4.2.5.2 (a): FeSEM image of a thin film of [Copolymer (7)–CH_2NHCO-$Ru]^{2+}$ drop-cast onto an ITO electrode. Magnification times 110000, scale 50 nm/division; (b) Fluorescence lifetime imaging (FLIM) microscopy of a [Copolymer (7)–CH_2NHCO-$Ru]^{2+}$ thin film drop-cast onto silicon wafer. Scale was 100 µm; (c) FLIM microscopy of a $[Ru(bpy)_2(caip)]^{2+}$ monomer complex thin film drop-cast onto silicon wafer. Scale was 100 µm. FLIM images were recorded by Dr. Qiang Zeng.

The images in Fig 4.2.5.2 are striking. The FeSEM image (left) shows a high-resolution image of the film on the sub-micron scale. The film was prepared by drop-casting 100 µl of a 1 x 10^{-4} M acetonitrile solution of polymer onto an ITO, followed by drying in air and rinsing with acetonitrile. The film shows homogeneous deposition of polymer, with no obvious cracks or large pores. Fig 4.2.5.2 (b) shows the confocal luminescence image which demonstrates that the polymer has a similar appearance on the macro-scale. The orderly packing of Ru metallopolymer films on surfaces is well known as the free pyridyl nitrogen atoms display a propensity to bind strongly to surfaces. Fig 4.2.5.2 (c) is a comparative image of the parent monomer complex film prepared under the same conditions. Clearly the monomer complex does not form dense films as it lacks the free pyridyl groups to bind itself strongly to the surface.

4.3 – Photophysics of adducts of the metallopolymers $[Ru(bpy)_2(caip\ co\text{-}poly)_7]^{2+}$ and $[Ru(bpy)_2(PVP)_{10}]^{2+}$ with the Dawson type polyoxomolybdate $\alpha\text{-}[Mo_{18}O_{54}(SO_4)_2]^{4-}$.

4.3.1 - Electronic spectroscopy:

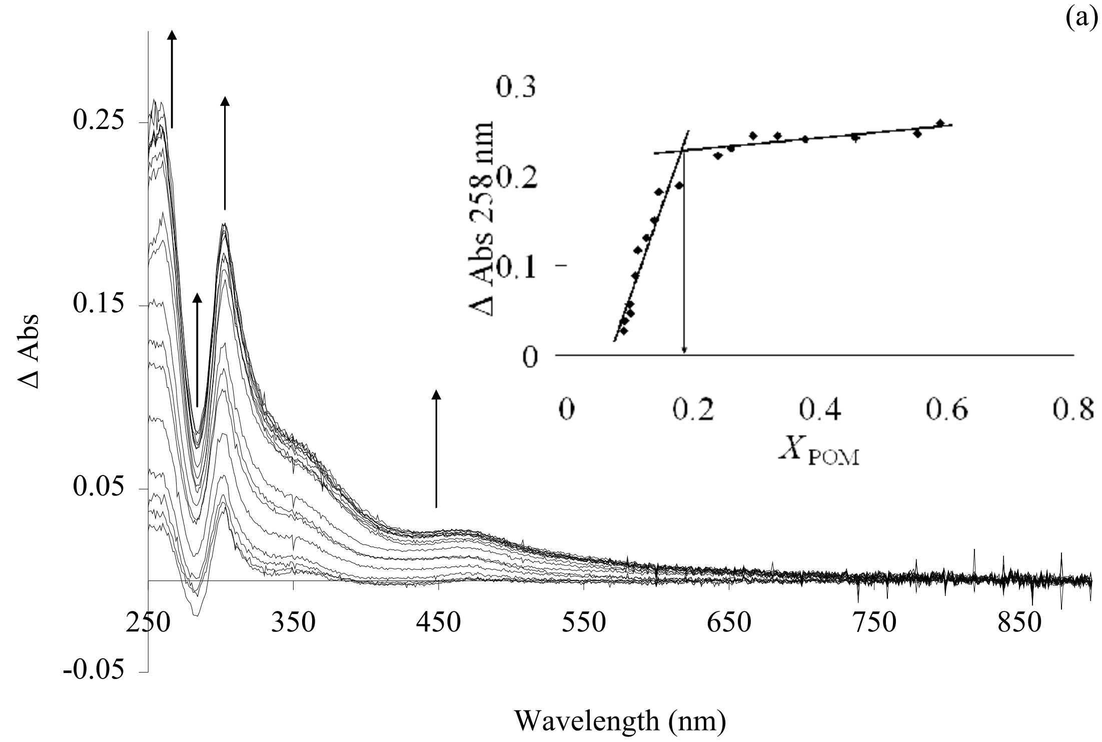

Fig 4.3.1.1 (a): Difference electronic spectra (experimental-calculated) of $[Ru(bpy)_2(PVP)_{10}]^{2+}$ in the presence of increasing concentrations of $[Mo_{18}O_{54}(SO_4)_2]^{4-}$ in MeCN. Inset: Job's Plot of absorbance change at 258 nm versus increasing mole fraction of $[Mo_{18}O_{54}(SO_4)_2]^{4-}$.

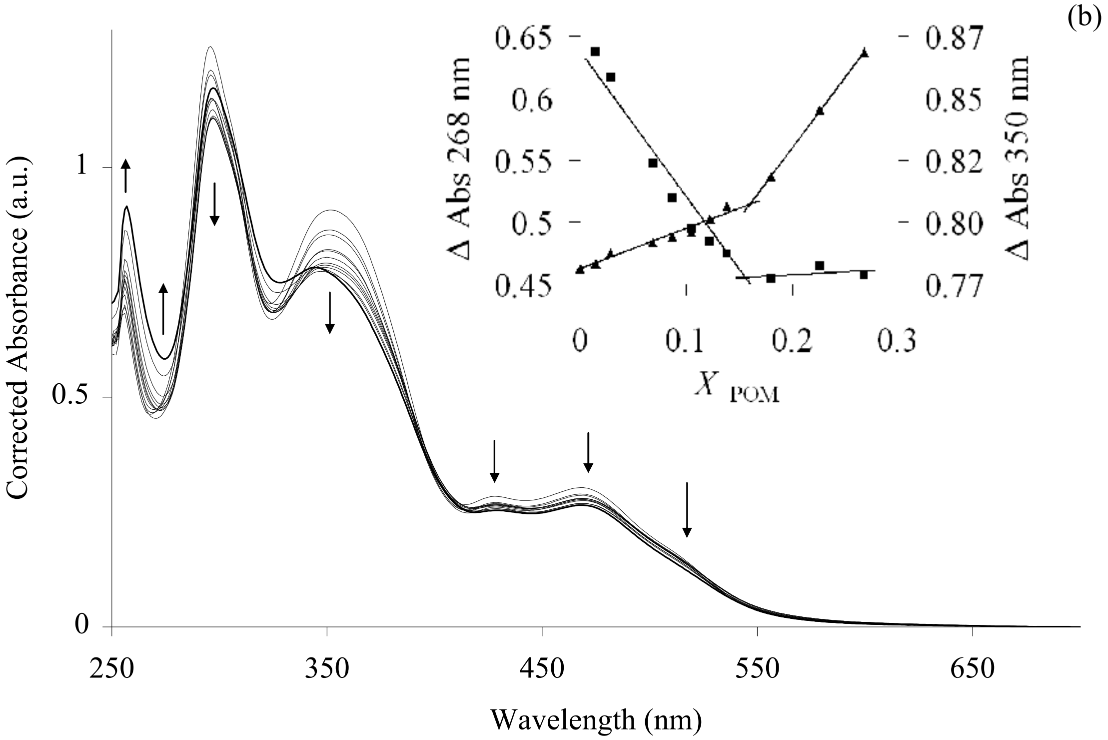

Fig 4.3.1.1 (b): Electronic spectra of $[Ru(bpy)_2(caip\ co\text{-}poly)_7]^+$ (1.8 x 10^{-5} M, DMSO) titrated with $[Mo_{18}O_{54}(SO_4)_2]^{4-}$ (3.75 x 10^{-4} M, MeCN). Spectra were baseline corrected at 700 nm. Inset: Absorbance changes as a function of increasing POM mole fraction.

UV/Vis spectroscopy was used to monitor electronic changes induced by association between the anion and polymers. As each Ru centre in the polymer carries a positive charge, the association was expected to be electrostatically charge-neutral as reported for the association of $[Mo_{18}O_{54}(SO_4)_2]^{4-}$ with $[Ru(bpy)_3]^{2+}$.[24] Fig 4.3.1.1 (a) shows the difference spectra obtained on combining $[Ru(bpy)_2(PVP)_{10}](PF_6)_2$ and $[N(Hex)_4]_4[Mo_{18}O_{54}(SO_4)_2]$ at various concentrations in MeCN. As mentioned previously, this approach has been used extensively in photophysical studies of electrostatic cluster formation involving Dawson polyoxometalates and cationic ruthenium (II) polypyridyl complexes.[24, 25, 26] In each case significant changes to the UV/Vis spectroscopy of the parent ions were observed indicating electronic perturbation of the metal centres on association. In Fig 4.3.1.1 (a) shifts and a grow-in of intensity in the UV attributed to polymer ligands and the polyoxometalate LMCT band were observed between 258 and 350 nm. In addition, a broad new band grows in at approximately 470 nm which tailed to approximately 700 nm. Although new features have been observed on association between $[Ru(bpy)_3]^{2+}$ and the polyoxomolybdates

$[Mo_{18}O_{54}(SO_4)_2]^{4-}$, α-$[Mo_{18}O_{54}(SO_3)_2]^{4-}$ and β-$[Mo_{18}O_{54}(SO_3)_2]^{4-}$ (see Chapter 3), these features were invariably narrow and did not exhibit the long tail to the red observed here.[24, 27]

The Fig 4.3.1.1 (a) inset shows a Job's Plot from spectral data shown in Fig 4.3.1.1 (a), where the increase in absorbance at 258 nm with increasing POM mole fraction yielded two linear regions. The intersection of the two lines occurs at a POM mole fraction (X_{POM}) of 0.18, which is approximately a 4.5:1 Ru centres:POM ratio. A Job's plot of absorbance change at 475 nm confirmed that the behaviour of the new absorbance changed at the same mole fraction as at 258 nm. Interestingly this suggests that the binding stoichiometry is different than anticipated based on charge compensation of the ruthenium centres by the polyoxomolybdate. In previous studies involving $[Ru(bpy)_3]^{2+}$ and Dawson POMs the thermodynamically favoured product was the adduct formed in which the polyoxometalate anion was fully charge compensated by the ruthenium cation leading to charge-neutral adduct with respect to Ru and POM. Even in the case of $[Ru(bpy)_3]_5[P_2W_{17}O_{61}]$, where the association constant was orders of magnitude lower than that of the closely related $[Ru(bpy)_3]_3[P_2W_{17}O_{61}(FeBr)]$ due to steric repulsion, Stern-Volmer plots still indicated that the favoured stoichiometry of ion-pairing was that which resulted in ion-cluster neutrality.[26]

Fig 4.3.1.1 (b) shows the absorbance changes occurring as a solution of $[Ru(bpy)_2(caip\ co\text{-}poly)_7]^+$ is titrated with aliquots of $[Mo_{18}O_{54}(SO_4)_2]^{4-}$. This is because addition of POM to a solution of $[Ru(bpy)_2(caip\ co\text{-}poly)_7]^{2+}$, in which the polymer was synthesized in its protonated form, resulted in an instantaneous shift in emission wavelength due to proton transfer to the polyoxometalate, which significantly complicated the Stern-Volmer data. In this experiment a set of difference spectra could not be reliably obtained due to insolubility of the resulting adduct, which resulted in changes in the absorbance baseline due to scatter. The spectra show that the POM based bands at 255 and 272 nm increase in intensity whereas all of the Ru based bands decrease as the POM concentration increases (see inset). Although there is some dilution with addition of $[Mo_{18}O_{54}(SO_4)_2]^{4-}$ the volumes of POM added were extremely small so as to minimize this effect (the final solution was only 1.8 % MeCN v/v). Overall the volume of POM in MeCN added to the DMSO solution increased by 1.8 % over the course of the titration, and this dilution was taken into account when calculating mole ratios). The changes to the absorbance are tentatively attributed to alterations of polarity of the solvent mixture changes throughout the experiment, which has been shown before to dramatically affect the polymer spectroscopy, as well as the spectroscopy of the corresponding monomer complex.[28, 13] Inspection of the visible spectral region shows no evidence for the appearance of new features in the visible region as a consequence of cluster formation with the POM, in contrast to those observed for the PVP polymer. This implies weak or no electronic communication between the two ions in DMSO/MeCN solution.

From the change in slopes in Fig 4.3.1.1 (b) inset it appears as though electrostatic association is favoured at $X_{\mathrm{POM}} \sim 0.16$, which would suggest a ratio of 5 Ru per POM centre. This ratio is also different than expected, given that full charge-compensation would result in a 4:1 ratio, when the polymer is in the form $[\mathrm{Ru(bpy)_2(caip\ co\text{-}poly)_7}]^{+}$. Alternatively, if the polymer was in the form $[\mathrm{Ru(bpy)_2(caip\ co\text{-}poly)_7}]^{2+}$ then a 2:1 ratio would be expected. This 5:1 ratio is unusual given the reported data for Ru monomer associations with polyoxoanions, but is quite similar to that seen for $[\mathrm{Ru(bpy)_2(PVP)_{10}}]^{2+}/[\mathrm{Mo_{18}O_{54}(SO_4)_2}]^{4-}$ in Fig 4.3.1.1 (a), and it is possible that these ratios are the same within error. These data also correlate with relative stoichiometric ratios obtained from graphical integration of the redox processes in the cyclic voltammetry of self-assembled thin films.[29] To gain further insight into these interesting observations, luminescence quenching of the two metallopolymers by $[\mathrm{Mo_{18}O_{54}(SO_4)_2}]^{4-}$ was conducted.

4.3.2 - Luminescence spectroscopy:

The electrostatic association of cationic Ru (II) polypyridyl complexes with anionic Dawson polyoxometalates has been shown to lead to significant quenching of the luminescence of the Ru centre upon addition of increasing concentrations of polyoxometalate to a solution of the Ru complex.[24, 25, 26] This has, in all but one case to date, been attributed to purely static quenching due to the formation of a charge-neutral Ru/polyoxometalate electrostatic cluster.[27] The data for emission quenching of $[\mathrm{Ru(bpy)_2(PVP)_{10}}]^{2+}$ and $[\mathrm{Ru(bpy)_2(caip\ co\text{-}poly)_7}]^{+}$ by $[\mathrm{Mo_{18}O_{54}(SO_4)_2}]^{4-}$ are presented in Fig 4.3.2.1.

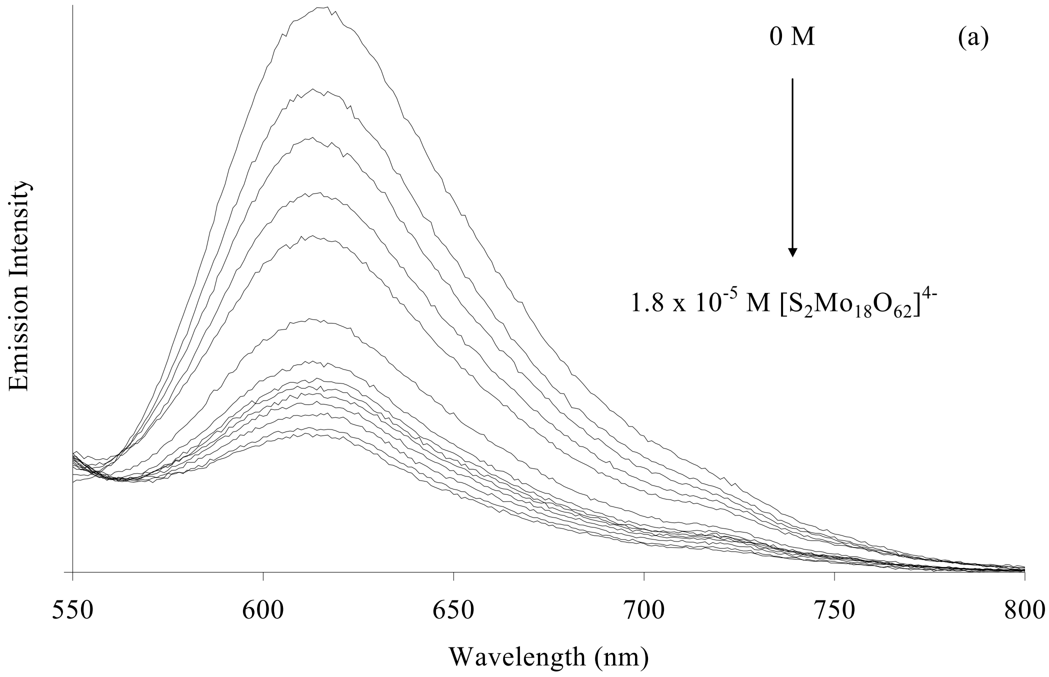

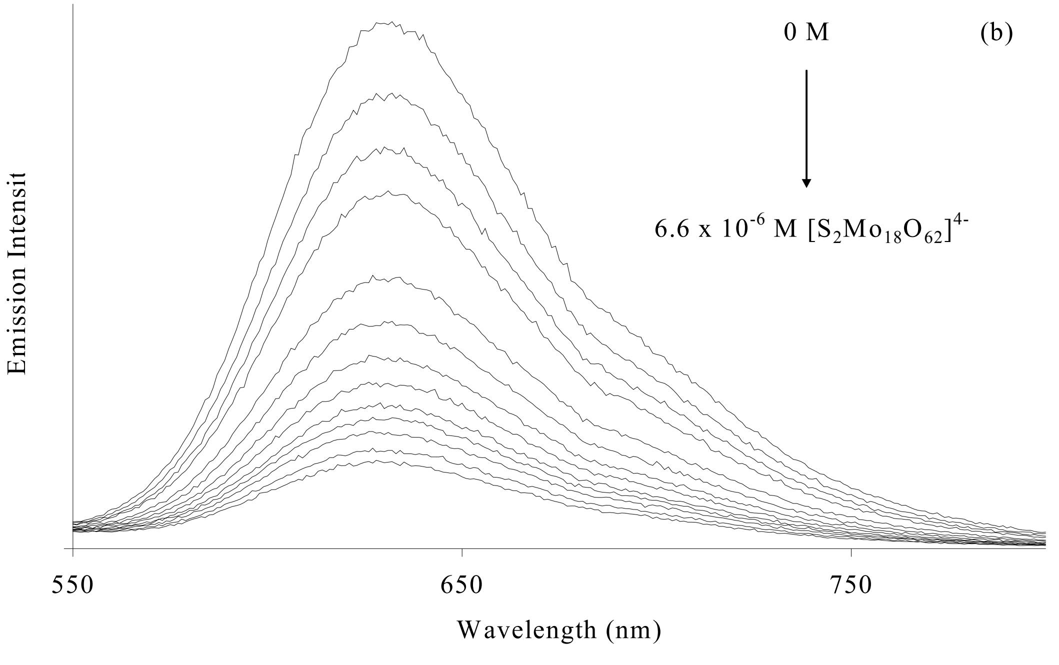

Fig 4.3.2.1: (a) Luminescence quenching of $[Ru(bpy)_2(PVP)_{10}]^{2+}$ (1.9 x 10^{-5} M) in the presence of increasing concentrations of $[Mo_{18}O_{54}(SO_4)_2]^{4-}$ in MeCN and (b) Quenching of $[Ru(bpy)_2(caip\ co\text{-}poly)_7]^+$ (1.83 x 10^{-5} M, in DMSO) by $[Mo_{18}O_{54}(SO_4)_2]^{4-}$ (3.75 x 10^{-4} M, in dry MeCN, final MeCN volume was 1.8 % v/v). λ_{exc} = 450 nm; both slit widths 10 nm.

Fig 4.3.2.1 (a) shows the effect of adding aliquots of 1.13 x 10^{-3} M $[Mo_{18}O_{54}(SO_4)_2]^{4-}$ to a solution of $[Ru(bpy)_2(PVP)_{10}]^{2+}$ (1.9 x 10^{-5} M) in MeCN. The strong ^{3}MLCT luminescence centred at 616 nm decreased with addition of successive POM quantities. Interestingly, no shift in emission wavelength was observed throughout the titration and an isoemissive point was maintained at 557 nm. In a study by Keyes *et al* involving $[Mo_{18}O_{54}(SO_4)_2]^{4-}$ and $[Ru(bpy)_3]^{2+}$, which is energetically analogous to $[Ru(bpy)_2(PVP)_{10}]^{2+}$, the λ_{max} red shifted until a broad shoulder appeared centred at approximately 640 nm when the cation to anion ratio was ~3:1 (X_{POM} ~0.25).[24] However in this case no such shoulder was observed and excitation spectra taken at 600, 640 and 700 nm confirmed that the chromophore responsible for maximum emission was absorbing at ~ 465 nm without change. These data indicate that the interaction between the two ions has little or no effect on the Ru based excited state responsible for emission, and that no new emissive state was observed for the composite material.

Fig 4.3.2.1 (b) shows the quenching of $[Ru(bpy)_2(caip\ co\text{-}poly)_7]^{+}$ by $[Mo_{18}O_{54}(SO_4)_2]^{4-}$. As in Fig 4.3.1.1 (b) the deprotonated form of the Ru complex was employed. The differences in the luminescent properties of $[Ru(bpy)_2(caip\ co\text{-}poly)_7]^{2+}$ relative to $[Ru(bpy)_2(caip\ co\text{-}poly)_7]^{+}$ have been thoroughly studied as a function of pH (see section 4.2). In this case, addition of the POM results in significant Ru based quenching and, as for the PVP metallopolymer, no shift in emission λ_{max} or change in the excitation spectrum was observed.

The Stern-Volmer quenching model has been widely used in the study of Ru complexes with POMs (see page 92-93). The Stern-Volmer data of the luminescence quenching are presented in Fig 4.3.2.2. It is clear that two distinct equilibria were reached for each metallopolymer throughout the experiment. Interestingly the ion pair ratios at which changes in Stern-Volmer behaviour are seen are very different from previous cases involving polyoxometalates and Ru polypyridyl complexes. In the case of $[Ru(bpy)_2(PVP)_{10}]^{2+}$ the ratios appear to be very different than expected, with likely Ru-POM binding ratios of 9:1 and ~4.7:1 (approximately 9:2). The third linear region is a plateau which corresponds to the fully-quenched species. The similarities in both the Stern-Volmer and Job's plots would appear to confirm these ratios. It is possible that the flexible PVP chain has some bearing on the electrostatic association with POM; however why a ratio of 4.5:1 is favoured over the predicted 2:1 is unknown. It may be that ion cluster formation results in extra Ru centres accompanying those binding directly to the POM. According to the static Stern-Volmer model the slopes of such plots are equal to the association constant of the ion-pairs (or, in this case, higher-order ion-clusters). This would indicate that the 9:1 and 4.5:1

complexes, presumably in the forms $\{[Ru(bpy)_2(PVP)_{10}]_9[Mo_{18}O_{54}(SO_4)_2]^{4-}\}^{14+}$ and $\{[Ru(bpy)_2(PVP)_{10}]_{4.5}[Mo_{18}O_{54}(SO_4)_2]\}^{5+}$, exhibit K_a values of 2.7 x 10^5 and 6.2 x 10^5 M^{-1} respectively. These K_a values are an order of magnitude higher than those reported for the formation of 1:1 and 2:1 clusters between $[Ru(bpy)_3]^{2+}$ and $[Mo_{18}O_{54}(SO_4)_2]^{4-}$.[24] However the applicability of the Stern-Volmer is in general poor when polymers are involved and hence the another model must be used to accurately explain the quenching behaviour. It is also clear from these data that the associated clusters are still luminescent to a moderate degree, but that this luminescence is unchanged from that of free Ru. Presumably this luminescence is from unquenched Ru centres in the polymer, so it is reasonable to conclude that each POM is not capable of quenching emission from 4.5 Ru centres simultaneously. The formation of the 4.5:1 clusters may be due to constraints such as the penetrability of the polyoxometalate to the polymer structure, or the association of Ru with POM brings additional ruthenium centres not necessary for electroneutrality into the ion-cluster with the remaining charge compensated by existing counterions in solution.

In the case of $[Ru(bpy)_2(caip\ co\text{-}poly)_7]^+$ and $[Mo_{18}O_{54}(SO_4)_2]^{4-}$ quenching the Stern-Volmer behaviour changes at POM mole fractions of approximately 0.06 and 0.16. This would appear to indicate Ru:POM ratios of approximately 15:1 and 5:1 respectively, presumably in the forms $\{[Ru(bpy)_2(caip\ co\text{-}poly)_7)]^+_{15}[Mo_{18}O_{54}(SO_4)_2]^{4-}\}^{9+}$ and $\{[Ru(bpy)_2(caip\ co\text{-}poly)_7]^+_5[Mo_{18}O_{54}(SO_4)_2]^{4-}\}^+$. The K_a values inferred for these clusters were 6.5 x 10^5 and 1.1 x 10^6 M^{-1} respectively. The formation of the 5:1 cluster reflects the UV/Vis data in Fig 4.3.1.1 (b). The slopes of this SV plot demonstrate that quenching is more efficient in the case of this polymer. This may be due to the shorter polymer chain length and thus closer proximity of Ru centres to each other, as each POM may be able to quench more Ru units simultaneously if they are less sterically hindered by the backbone.

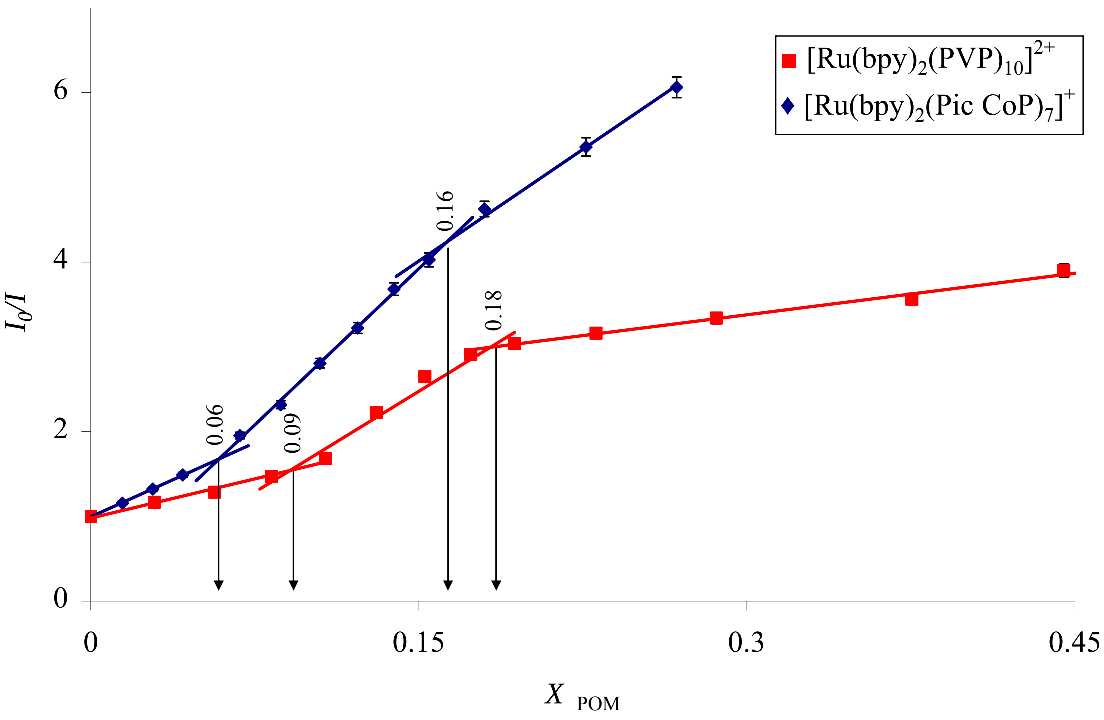

Fig 4.3.2.2: Stern-Volmer plots of luminescence quenching data in Fig 4.3.3.1.

In polymer systems electrostatic association is considered to occur in a rigid matrix, and in such cases the Perrin equation (Eqn. 4) may be applied to estimate the volume within which quenching may occur. The Perrin model is the most commonly applied to quenching in polymer systems. It assumes static quenching between immobile (on the quenching timescale) fluorophores with quenchers randomly in proximity. Within a certain quenching sphere around the fluorophore the efficiency of quenching is assumed to be 100 %, and therefore no quenching occurs outside of the quenching sphere. The slope of the Perrin equation can be used to estimate the electron transfer distance of a static quenching reaction.

$$\ln\left(\frac{I_0}{I}\right) = V.N_A.[Q] = \frac{4}{3}\pi.R_S^3.N_A.[Q] \qquad \textbf{(4)}$$

Where I_0 and I are the emission intensities of the quenched and unquenched samples respectively, Q is the concentration of polyoxometalate quencher and R_S is the radius of the quenching sphere. The Perrin plots of the quenching data in Fig 4.3.2.1 are shown in Fig 4.3.2.3.

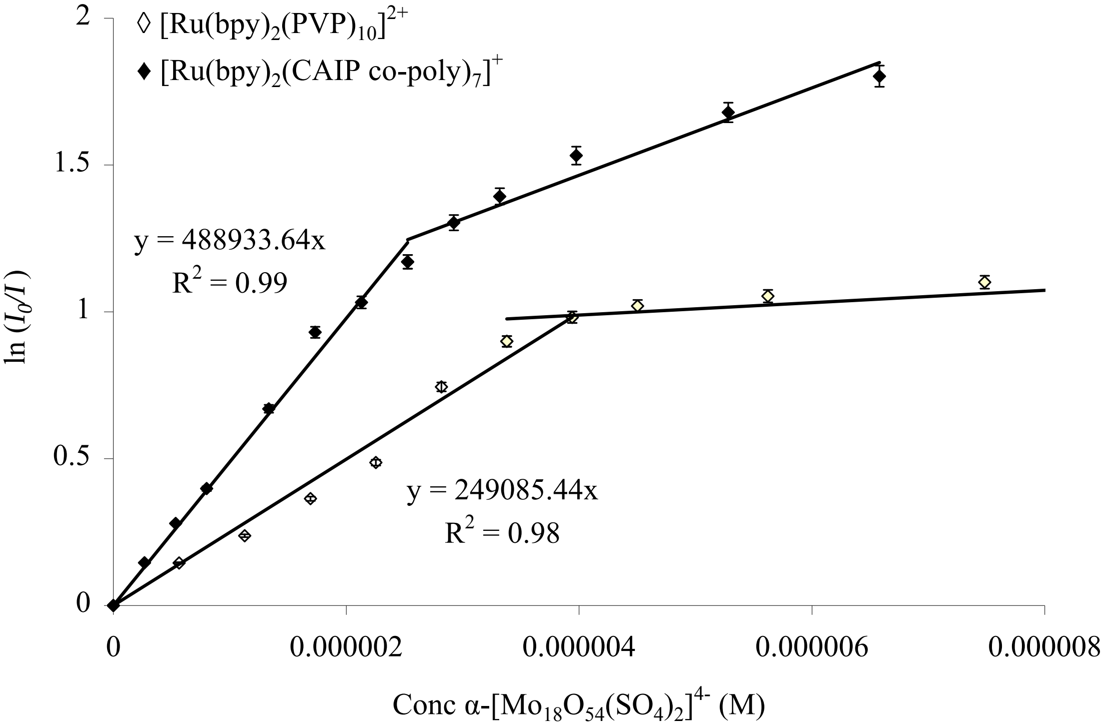

Fig 4.3.2.3: Perrin plots of luminescence quenching data in Fig 4.3.3.1.

Fig 4.3.2.3 demonstrates that the Perrin model fits the polymer quenching well, over the low POM concentration region. The model was not fitted over the high POM concentration region where the data reached a plateau. The slopes of the lines indicate that the radii of the quenching spheres, R_S, are approximately 4.6 Å and 5.8 Å for of $[Ru(bpy)_2(PVP)_{10}]^{2+}$ and $[Ru(bpy)_2(caip\ co\text{-}poly)_7]^+$ respectively. These numbers correspond well with static electron transfer distances, and are shorter than in a study of $[Ru(bpy)_3]^{2+}$ dispersed in a poly(ethyleneoxide) polymer matrix being quenched by co-dispersed molecules of 2-methyl-4-(*N*,*N*-dibenzylamino)-benzaldehyde-*N*-2-benzothiazolyl-*N*-*n*-butylhydrazone in proximity to the fluorophore a static electron transfer distance of 1.9 nm was obtained.[30]

4.3.3 - Time-resolved luminescence:

To assess the impact of quencher addition on the luminescence of the metallopolymers, the luminescent lifetime was measured as a function of increasing quencher concentration. If quenching is purely static then the lifetime should remain unaffected by the presence of quencher;

however if the lifetime is reduced then a dynamic component may also be present. The luminescent lifetime quenching data are shown in Fig 4.3.3.1.

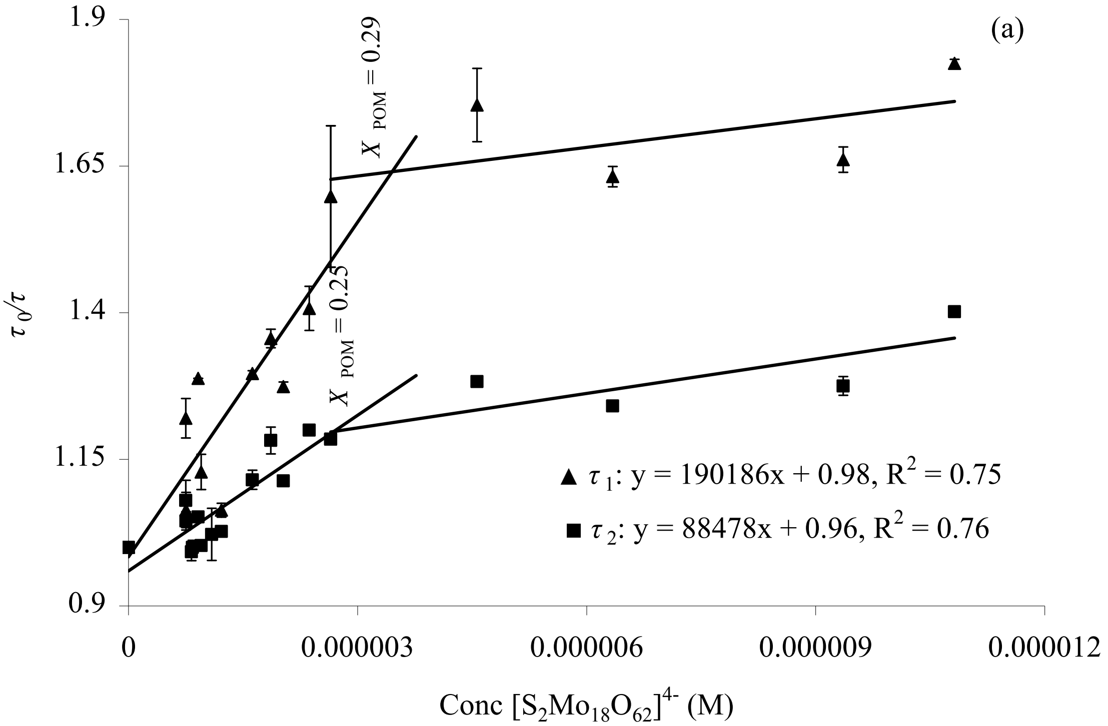

Fig 4.3.3.1 (a): Luminescent lifetime Stern-Volmer plots for the long component (triangles) and the short component (squares) of $[Ru(bpy)_2(PVP)_{10}]^{2+}$ by $[Mo_{18}O_{54}(SO_4)_2]^{4-}$ in aerated MeCN.

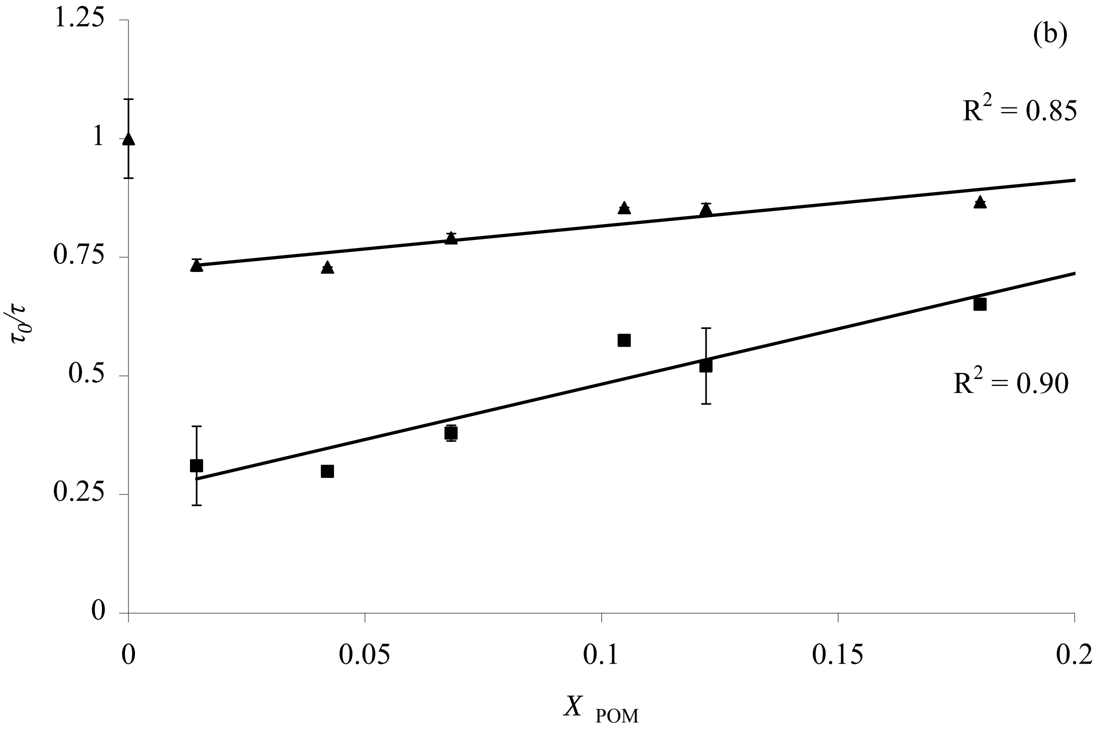

Fig 4.3.3.1 (b) modified luminescent lifetime Stern-Volmer plots for the long component (triangles) and the short component (squares) of $[Ru(bpy)_2(caip\ co\text{-}poly)_7]^+$ by $[Mo_{18}O_{54}(SO_4)_2]^{4-}$ in aerated DMSO/MeCN. Luminescent decays were recorded by TCSPC, $\lambda_{exc} = 450$ nm.

The results in Fig 4.3.3.1 (a) clearly show a small but significant reduction in τ for the quenching of $[Ru(bpy)_2(PVP)_{10}]^{2+}$ by $[Mo_{18}O_{54}(SO_4)_2]^{4-}$. All plots were fitted using a biexponential tailfit method, and fit the model well ($0.85 \leq \chi^2 \leq 1.30$). As described previously, biexponential lifetime decays are commonly observed when working with Ru polymers in MeCN, and this is due to heterogeneity arising from cross-linking.[31] Both components were dynamically quenched weakly at low POM concentrations, however little or no change was observed after a certain concentration of polyoxometalate ($X_{POM} = 0.25$) was reached. This plateau was estimated to be over the same region as that in Fig 4.3.3.2, within experimental error. The lower sloping region corresponds to the same region over which the Perrin model was applied. The contribution of the long component of the decay decreased from 72 % for the unquenched sample to approximately 66 % for the highly quenched samples.

In the case of $[Ru(bpy)_2(caip\ co\text{-}poly)_7]^+$ quenching by $[Mo_{18}O_{54}(SO_4)_2]^{4-}$ there is also a notable decrease in luminescent lifetime. As for $[Ru(bpy)_2(PVP)_{10}]^{2+}$ biexponential decays were observed. Upon addition of a very small quantity of POM to $[Ru(bpy)_2(caip\ co\text{-}poly)_7]^+$ a large decrease in both lifetime components was observed. The origin of this initial change could be due to the formation of non-emissive centres in the composite as the quantity of POM present was so low ($X_{POM} \sim 0.015$). This change is more likely due to solvent effects arising from the addition of the POM (ie: MeCN solution), which would affect the solution pH and polarity, as the luminescent lifetimes of $[Ru(bpy)_2(caip\ co\text{-}poly)_7]^+$ are extremely sensitive to the microenvironment of the sample. In this case the contribution from the longer component, τ_1, underwent a small initial decrease, which accompanied the decrease in τ_1, from 89 % to 83 %. This value recovered to 88 ± 2 % above $X_{POM} = 0.1$.

Overall these plots show that there is, surprisingly, a weak dynamic component to the quenching at low concentrations. This implies that the purely static Perrin model applied in Fig 4.3.3.3 does not fully explain the behaviour. However, the overall dynamic component is fairly small in relation to the static, which is expected due to the highly associative nature of the quenching process. However, given the slopes present in Fig 4.3.3.1 it must be concluded that some collisional quenching may occur at high polyoxomolybdate concentrations. Mixed static and dynamic quenching has been observed previously in quenching of Dawson-like polyoxometalates by $[Ru(bpy)_3]^{2+}$ in solution (see Chapter 3).

4.3.4 - Resonance Raman spectroscopy:

The Stern-Volmer data and the Job's plot indicate that an ion-pair ratio of approximately 4.5:1 is favoured in these experiments in solution. In order to analyze the properties of the isolated complex a solution of 4.5 mM Ru was added to a solution of 1 mM POM with stirring. The isolated solid (see Chapter 2) was dried carefully under nitrogen and ground into a disc with oven dried KBr. The resonance Raman spectra are presented in Fig 4.3.4.1.

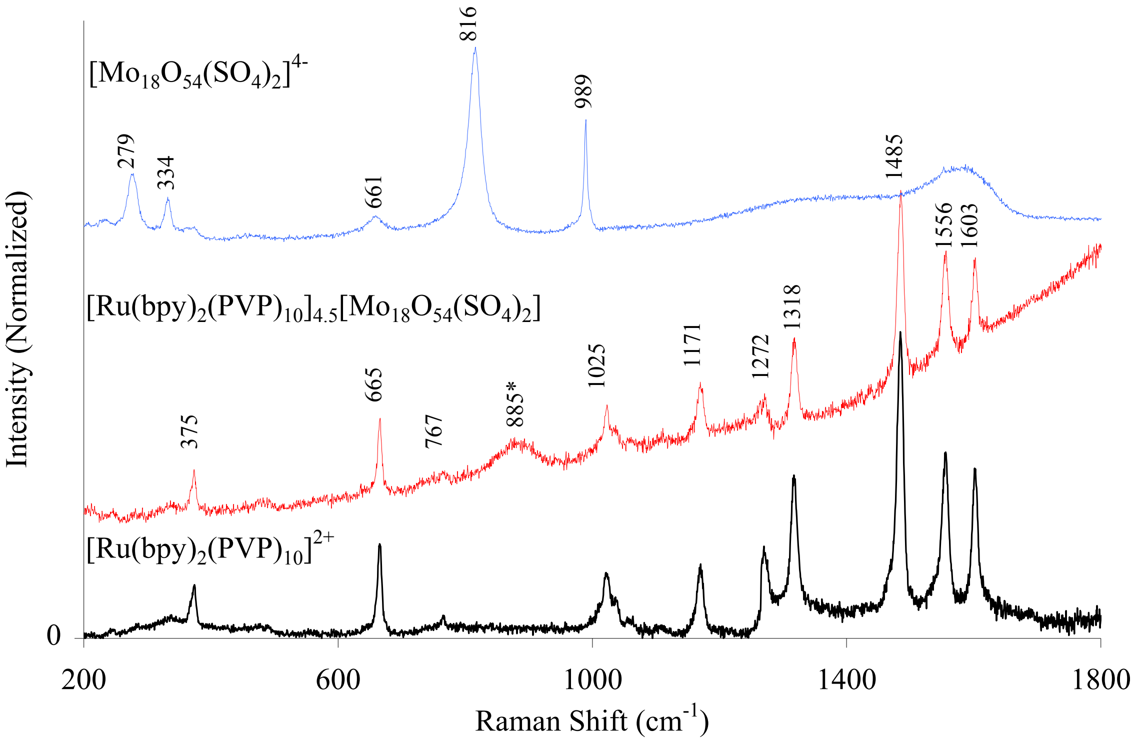

Fig 4.3.4.1 (a): Resonance Raman spectra (normalized, uncorrected baselines) of $[Ru(bpy)_2(PVP)_{10}]^{2+}$, $[Mo_{18}O_{54}(SO_4)_2]^{4-}$ and $[Ru(bpy)_2(PVP)_{10}]_{4.5}[Mo_{18}O_{54}(SO_4)_2]$ in KBr (~ 5 % w/w) under 514 nm excitation. Mode marked with * is POM based.

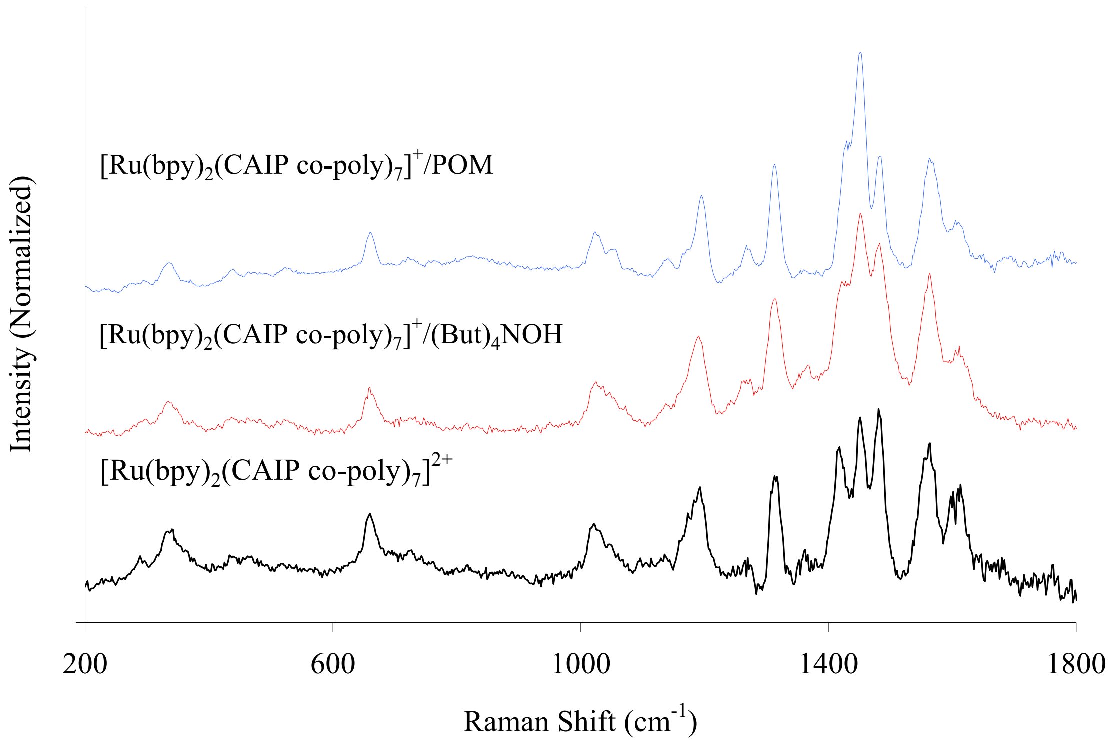

Fig 4.3.4.2: Resonance Raman spectra of the metallopolymer [Ru(bpy)$_2$(caip co-poly)$_7$]$^+$ in both its 2+ and 1+ forms and the electrostatically formed 4:1 POM cluster in KBr (~ 5 % w/w) under 488 nm irradiation.

Resonance Raman permits identification of vibronic modes associated with the electronic transition under scrutiny by a resonant enhancement effect of those modes. This resonance is extremely strong, and enhancement factors of the order of 10^6 have been observed.[20] Fig 4.3.4.1 (a) shows the spectra of [Ru(bpy)$_2$(PVP)$_{10}$](NO$_3$)$_2$, [N(Hex)$_4$]$_4$[Mo$_{18}$O$_{54}$(SO$_4$)$_2$], and their associated ion cluster of 4.5:1 stoichiometry. The spectrum of [Mo$_{18}$O$_{54}$(SO$_4$)$_2$]$^{4-}$ is similar to that of other Dawson polyoxometalates, and is dominated by Mo-O stretching modes at 816 and 989 cm^{-1}.[24] This spectrum is post-resonant under 514 nm excitation so is far less intense than the Ru based spectra; hence the spectra were normalized here for clarity. The Raman spectrum of [Ru(bpy)$_2$(PVP)$_{10}$]$^{2+}$ is well known.[32] The characteristic pyridine breathing modes associated with ruthenium polypyridyl complexes are observed at 1603, 1556, and 1485 cm^{-1}; and the Ru-N mode at 375 cm^{-1} is also seen. The Ru-based modes are all present in the adduct spectrum. In addition to these modes, however, a broad new feature centred at approximately 885 cm^{-1} appeared which is not present in the parent Ru ion spectrum. Based on its width and frequency this feature is attributed to the polyoxometalate

Mo-O stretching mode, although it is blue-shifted from its initial 816 cm^{-1} and its shape is distorted. That this mode is observed in this case despite the fact that the polyoxomolybdate is non-resonant under 514 nm irradiation indicates that both ions participate in the new optical transition seen in Fig 4.3.1.2 (a). It is interesting to note that only the presumably H-bonded Mo-O mode is enhanced under visible excitation into the new optical transition, which indicates that it may play a vital role in mediating charge-transfer. When $[Ru(bpy)_3]^{2+}$ was studied with $[Mo_{18}O_{54}(SO_4)_2]^{4-}$ a similar transition suggested to be an intramolecular charge-transfer transition was identified by resonance Raman excitation at 488 nm; but in that instance no changes in Mo-O mode peak shape or wavelength were observed.[24] However Seery *et al* have demonstrated that electrostatic adducts of $[Ru(bpy)_3]^{2+}$ and the lacunary substituted Dawson polyoxotungstate $[P_2W_{17}O_{61}(FeBr)]^{6-}$ displayed a shift in W-O mode similar to the one observed in this case when excited at 488 nm.[26] Why exactly the band is shifted is unclear but we tentatively ascribe this shift to Mo-O---H hydrogen-bond formation between the bipyridyl ligand and the terminal POM oxygen atoms. In the case of $K_5\{[Ru(bpy)_3][PW_{11}O_{39}]\}^{5-}$ and $K\{[Ru(bpy)_3][PW_{12}O_{40}]\}^{-}$ small shifts (7 cm^{-1} relative to the tungstate alone) were seen in the infrared W-O terminal stretching modes, and X-ray crystallography of these cluster complexes revealed H-bonding at three sites.[33] In addition, the absence of peak shifts for the pyridine modes indicate the absence of a quaternary pyridinium species; therefore the spectral changes and unusual stoichiometry induced on binding due to the POM cannot be due to protonation of free pyridine nitrogen atoms in the polymer chains.[35] Excitation of the $[Ru(bpy)_2(PVP)_{10}]_{4.5}[Mo_{18}O_{54}(SO_4)_2]$ cluster at 488 nm revealed the same polyoxomolybdate-based mode, but it was significantly less intense relative to the bpy vibrational modes. This suggests that the new optical transition comes more strongly into resonance at wavelengths higher than 488 nm, which reflects the long tail in Fig 4.3.1.1 (a). The rising baseline in the 4.5-1 spectrum also demonstrates that the Ru based emission has not been fully quenched, which correlates well with the emission quenching data in Fig 4.3.2.1 (a).

It was interesting to compare the resonance Raman spectra of the $[Ru(bpy)_2(PVP)_{10}]^{2+}/[Mo_{18}O_{54}(SO_4)_2]^{4-}$ composites with those of $[Ru(bpy)_2(caip\ co\text{-}poly)_7]^{+}/[Mo_{18}O_{54}(SO_4)_2]^{4-}$, as in the latter case no new significant optical transitions were observed (Fig 4.3.2.1 (b)). Fig 4.3.4.1 (b) demonstrates that no POM based features are apparent in the spectrum of $[Ru(bpy)_2(caip\ co\text{-}poly)_7]_5[Mo_{18}O_{54}(SO_4)_2]$, under 488 nm irradiation. The Ru-based spectral changes observed upon association with the POM were due to a change from Ru^{2+} to Ru^{+}, due to proton abstraction by the POM, as demonstrated by isolation of $[Ru(bpy)_2(caip\ co\text{-}poly)_7]^{+}$ via addition of excess base ($(But)_4NOH$) to a solution of $[Ru(bpy)_2(caip\ co\text{-}poly)_7]^{2+}$. The POM modes at 816 or 989 cm^{-1} are not seen in the adduct spectrum in this case, whereas they clearly are resonantly enhanced in Fig 4.3.4.1 (a).

4.3.5 - Transient absorption spectroscopy:

To further investigate the intramolecular charge-transfer transient absorption spectroscopy of the isolated solids was performed. Transient spectroscopy is a powerful tool in tracking reactive intermediates as it can provide both mechanistic and kinetic information. The transient data are shown in Fig 4.3.5.1.

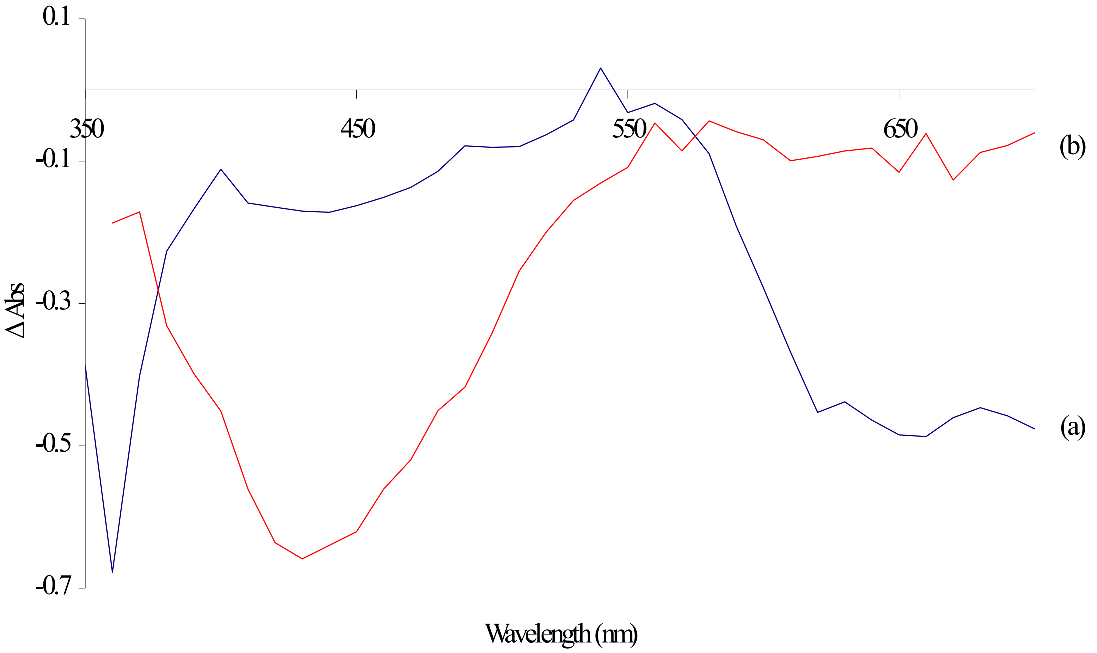

Fig 4.3.5.1: Diffuse reflectance transient absorption spectra of (a) $[Ru(bpy)_2(PVP)_{10}].2NO_3$ and (b) $[Ru(bpy)_2(PVP)_{10}]_{4.5}[Mo_{18}O_{54}(SO_4)_2]$ ground into KBr discs (~ 5 % w/w) under 355 nm irradiation 104 ns after laser pulse excitation.

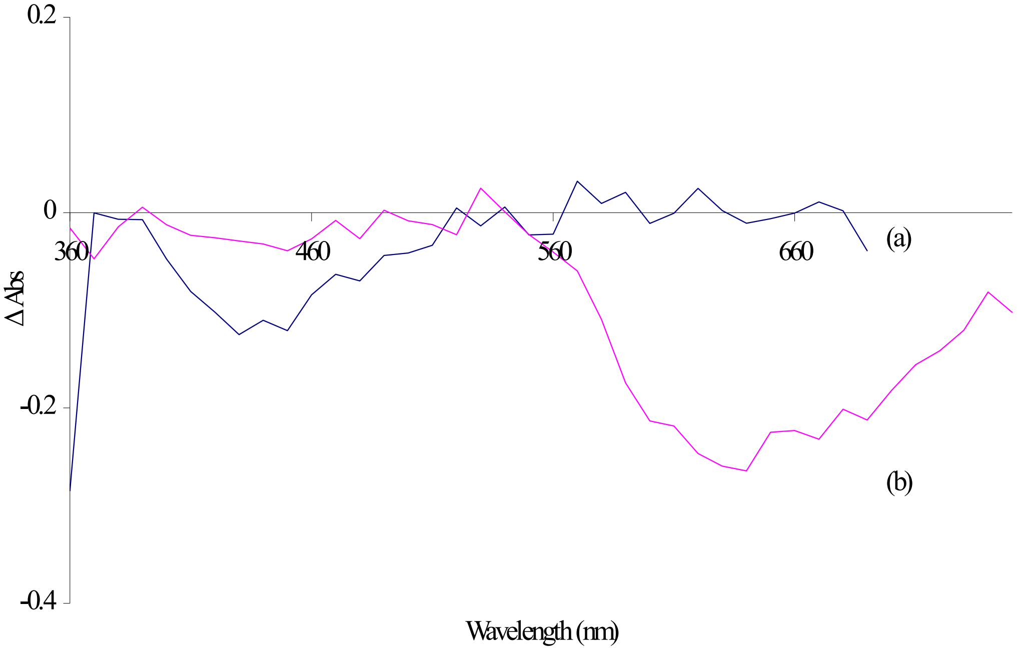

Fig 4.3.5.2: Diffuse reflectance transient absorption spectra of (a) $[Ru(bpy)_2(caip\ co\text{-}poly)_7]_5[Mo_{18}O_{54}(SO_4)_2]$ and (b) $[Ru(bpy)_2(caip\ co\text{-}poly)_7](ClO_4)_2$ in KBr discs (~ 5 % w/w) 104 ns after laser pulse excitation.

Fig 4.3.5.1 shows the transient spectra of $[Ru(bpy)_2(PVP)_{10}](NO_3)_2$ and $[Ru(bpy)_2(PVP)_{10}]_{4.5}[Mo_{18}O_{54}(SO_4)_2]$ as solids dispersed in KBr discs. In each case the MLCT depletion centred at ~ 440 nm can be clearly seen. Interestingly this feature does not exhibit a tail into the red for $[Ru(bpy)_2(PVP)_{10}]_{4.5}[Mo_{18}O_{54}(SO_4)_2]$ as it does in Fig 4.3.1.1 (a); however the feature is far more intense as a consequence of the large Ru excess (4.5 times present). The grow-in of a bipyridine ligand based radical intermediate peak was unfortunately obscured by the laser pulse at 355 nm. The emission of each sample can be seen clearly at 600 nm, which correlates with the phosphorescence data seen in Fig 4.3.2.1 (a). The strong emission of unquenched $[Ru(bpy)_2(PVP)_{10}](NO_3)_2$ can be seen in Fig 4.3.5.1; whereas the weak residual emission of free Ru is present in the spectrum of $[Ru(bpy)_2(PVP)_{10}]_{4.5}[Mo_{18}O_{54}(SO_4)_2]$. There is no evidence for the presence of the formation of the reduced polyoxomolybdate $[Mo_{18}O_{54}(SO_4)_2]^{5-}$ as a consequence of charge transfer, as there was in the spectrum of $[Mo_{18}O_{54}(SO_4)_2]^{4-}$ and $[Ru(bpy)_3]^{2+}$ in MeCN 20 ns after excitation.[24] However given the resonance Raman and photoelectrochemical data (discussed later) it is likely that either the new optical transition is non-luminescent or photoinduced supramolecular electron transfer is the mechanism by which quenching occurs. If this is the case the process may be too fast for our instrumentation (laser pulse duration approx 5 ns).

The transient spectra of $[Ru(bpy)_2(caip\ co\text{-}poly)_7]_5[Mo_{18}O_{54}(SO_4)_2]$ and $[Ru(bpy)_2(caip\ co\text{-}poly)_7]^{2+}$ are presented in Fig 4.3.5.2. As in Fig 4.3.5.1, the MLCT absorption depletion at 450 nm is visible at this timescale, while the emission band at 650 nm is quenched when the POM is present. The grow-in of the bpy radical is not observable, and no POM based radical grow in is observed. Since the Ru emission of both metallopolymers is quenched on addition of POM it can be concluded that deactivation of the Ru excited state occurs through one of three mechanisms: (1) Ultrafast electron transfer from the Ru based ^{1}MLCT before ISC occurs; (2): Electron transfer from the ^{3}MLCT state before phosphorescence occurs; or (3) direct population of a non-luminescent charge-transfer state from the ground state. Direct population of a CT state is still likely in the case of $[Ru(bpy)_2(caip\ co\text{-}poly)_7]^+$ and $[Mo_{18}O_{54}(SO_4)_2]^{4-}$, even given the absence of a new CT band upon ion-cluster association. All of these proposed mechanisms would almost certainly occur on a timescale too fast for our instrumentation. Whatever the mechanism, the population of a charge-transfer state is clearly different in the cases of the two different metallopolymers, as indicated by the resonance Raman and photoelectrochemical data. It may be that these two deactivation mechanisms compete with one another, and only one leads to a photocatalytically active state. Why these different pathways are favoured over one another in these two thermodynamically analogous systems is unclear, but steric effects and/or donor-acceptor orbital overlap may play a vital role.

4.3.6 - Photoelectrochemistry:

Addition of $[Mo_{18}O_{54}(SO_4)_2]^{4-}$ to $[Ru(bpy)_2(PVP)_{10}]^{2+}$ resulted in a new absorbance band in the UV/Vis, while adding the POM to $[Ru(bpy)_2(caip\ co\text{-}poly)_7]^+$ apparently did not we were interested in investigating whether or not this new transition resulted in visible sensitised POM photochemistry. To achieve this, photoelectrochemical studies of the metallopolymer/POM thin films were performed. In a previous contribution we demonstrated that self-assembled thin films of $[Ru(bpy)_2(PVP)_{10}]_{4.5}[Mo_{18}O_{54}(SO_4)_2]$ could effectively decompose benzyl alcohol under visible (480 nm) irradiation with greater efficiency than a film of $[(Hex)_4N]_4[Mo_{18}O_{54}(SO_4)_2]$ under the same conditions.[29] These studies were performed in the presence of 0.1 M $(But)_4NBF_4$ electrolyte in order to enhance the conductivity through the film and hence increase the current magnitude; however electrolyte is well known to disrupt ionic association between Ru complexes and POMs (see Chapter 3). $(But)_4NBF_4$ was the only electrolyte tested that did not result in disruption of the films in this case, as was demonstrated by stable and reproducible film voltammetry obtained when this electrolyte was used.[29] These experiments were performed by drop-casting 100 µl of 1 x 10^{-4} M solutions/suspension of either $[(Hex)_4N]_4[Mo_{18}O_{54}(SO_4)_2]$ or $[Ru(bpy)_2(PVP)_{10}]_{4.5}[Mo_{18}O_{54}(SO_4)_2]$ onto ITO working electrodes and performing photo-electrochemistry in 0.1 M $(But)_4NBF_4$ in MeCN. Under the same conditions of irradiation as in the case of the self-assembled films, the net current generated under 480 nm irradiation actually decreased from approximately 6 nA/400 seconds to 0.7 nA/400 seconds when Ru was present, a decrease of a factor of 8. These data are shown in Fig 4.3.6.1.

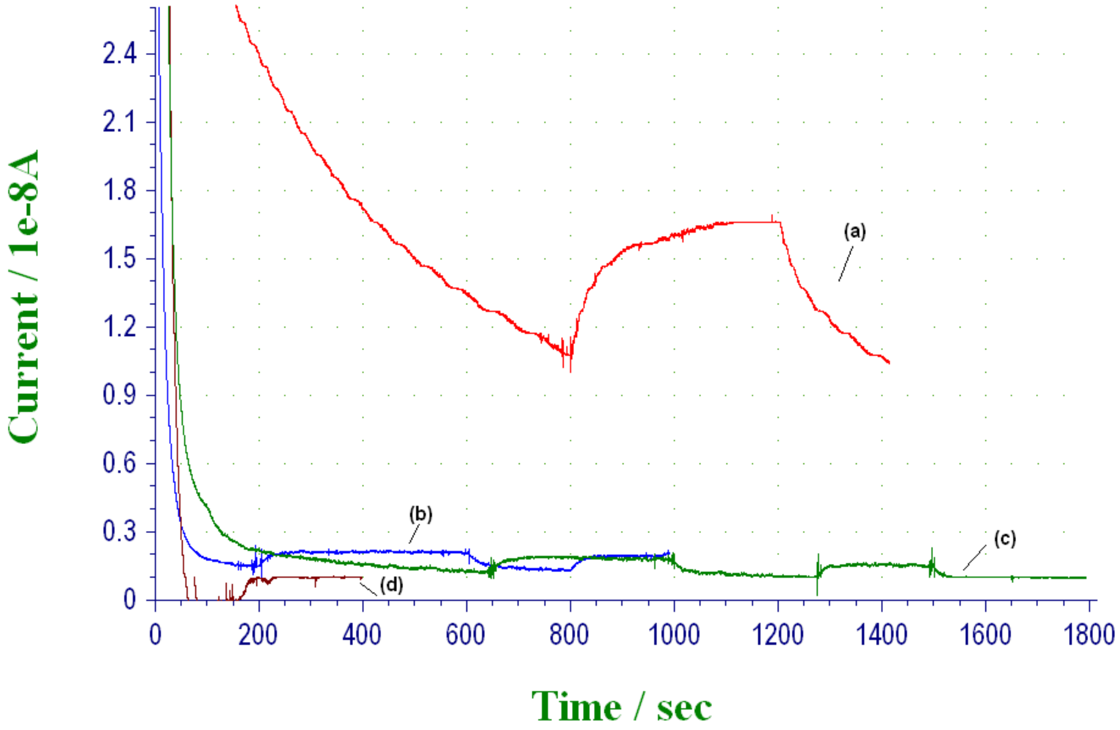

Fig 4.3.6.1: Photocurrent responses of dropcast films on ITO working electrodes using a Xe arc lamp operating at 350 W and a 480 ± 5 nm narrow band optical filter. The electrolyte was in 0.1 M $(But)_4NBF_4$ in MeCN. The counter electrode was a Pt flag and the reference electrode was an Ag wire (+ 400 mV vs Fc/Fc^+). Potential was held constant at + 400 mV. (a) - $[(Hex)_4N]_4[SO_4\text{-POM}]$ (red): Current 5.9 nA; (b) - $[Ru(bpy)_2(PVP)]_{4.5}[SO_4\text{-POM}]$ (blue):Current 0.7 nA. 8 x smaller than POM alone; (c) - $[Ru(bpy)_2(PVP)].(NO_3)_2$ (green): Current 0.6 nA; and (d) - Blank ITO (purple): Practically zero current.

Fig 4.3.6.1 highlights the failure of drop-cast films to generate a sensitized photocurrent under visible irradiation. This was in sharp contrast to the self-assembled films, where the current increased from approximately 10 nA/100 secs for POM alone to 38 nA/100 secs when Ru was present. These data are shown in Fig 4.3.6.2.

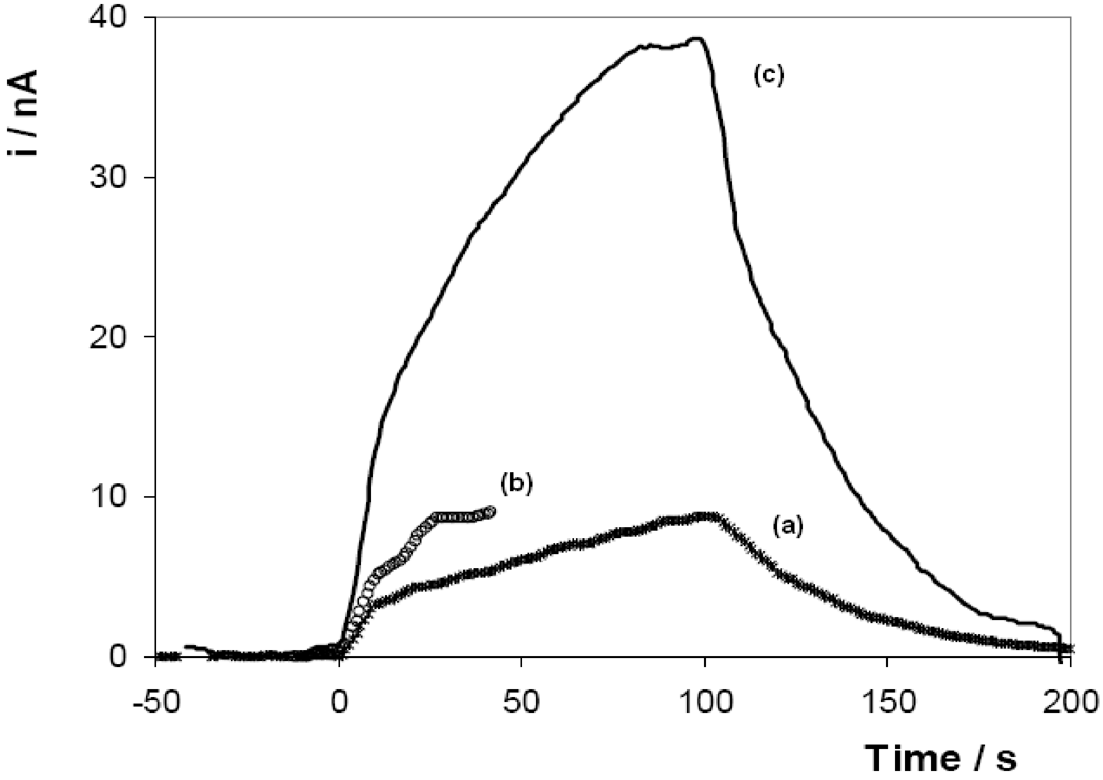

Fig 4.3.6.2: Enhanced photocurrents generated self-assembled films of (a) $[(Hex)_4N]_4[Mo_{18}O_{54}(SO_4)_2]$, (b) $[Ru(bpy)_2(PVP)]_{4.5}[Mo_{18}O_{54}(SO_4)_2]$ and (c) $[Ru(bpy)_2(caip\ co\text{-}poly)_7]_5[Mo_{18}O_{54}(SO_4)_2]$ on ITO. Light source was a Xe arc lamp operating at 350 W and a 480 ± 5 nm narrow band optical filter. The electrolyte was in 0.1 M $(But)_4NBF_4$ in MeCN. The counter electrode was a Pt flag and the reference electrode was an Ag wire (+ 400 mV vs Fc/Fc^+). Potential was held constant at + 400 mV. Reproduced from [11].

In addition, both drop-cast and self-assembled films of $[Ru(bpy)_2(caip\ co\text{-}poly)_7]_2[Mo_{18}O_{54}(SO_4)_2]$ resulted in poor photocurrent generation. In each case the current magnitude produced by $[Mo_{18}O_{54}(SO_4)_2]^{4-}$ decreased in the presence of this metallopolymer, indicating a lack of sensitization under visible irradiation. These data strongly indicate that electrostatic self-assembly is the only viable method for producing visible-light activated photocatalytic films using Dawson polyoxometalates. Preliminary studies suggest that effective photocurrent generation is a function of film thickness, as the value of D_{CT} decreases with increasing surface coverage.[29] Therefore drop cast films are likely too thick to be used in future photovoltaic applications.

4.4 - Conclusions:

In this chapter was explored the photophysics of a new family of luminescent metallopolymer, $[Ru(bpy)_2(caip\ co\text{-}poly)_n]^{2+}$ (n = 5, 7, 9), and compared their ability to bind to the polyoxomolybdate $[Mo_{18}O_{54}(SO_4)_2]^{4-}$ with the ability of the well known polymer $[Ru(bpy)_2(PVP)_{10}]^{2+}$. The photophysics of the metallopolymers $[Ru(bpy)_2(caip\ co\text{-}poly)_n]^{2+}$ (n = 5, 7, 9) have been reported in a variety of solvent systems. The polymer spectroscopy and electrochemistry was found to be primarily independent of chain length. It was observed that the polymer spectroscopy had a strong dependence on pH, which was also observed in the corresponding monomer complex $[Ru(bpy)_2(caip)]^{2+}$. Upon increasing the pH the polymer charge increases from 3+ → 2+ → 1+, and a new band correspondingly grows in at low energy. This has been attributed to a benzocarboxylate → phenanthroline interligand charge-transfer (ILCT) transition, which suggests a more increased delocalization of the π system, facilitating increased electronic communication between the imidazole and phenanthroline groups, when the imidazole ligand is fully deprotonated. The relative contributions of the Ru → bpy and Ru → caip MLCT transitions were probed by resonance Raman spectroscopy, and it was demonstrated that the Ru → caip comes more strongly into resonance when fully protonated under 458 nm irradiation. This indicates that the relative energy levels of the caip ligand are changed significantly upon changing pH.

The polymer optical spectroscopy also exhibited strong solvent dependence. In particular dissolution of the metallopolymers in dimethylsulfoxide induced significant spectral changes relative to MeCN. The UV/Vis spectrum appeared to indicate a situation where the DMSO solvent molecules underwent strong H-bonding with the imidazole ligand, and hence the spectrum had the appearance of the fully deprotonated polymer in MeCN. The emission spectroscopy in DMSO also reflected this trend, and the luminescent lifetime of DMSO was also abnormally long given the values obtained in MeCN and MeOH, which have similar dielectrics. It was postulated that DMSO affects the free pyridyl nitrogen atoms in the polymer backbone, causing it to swell, and hence affecting the spectroscopy. Investigation into the fluorescence anisotropy of the polymers in various solvents is currently underway in order to confirm this hypothesis.

The photophysics of the metallopolymers $[Ru(bpy)_2(caip\ co\text{-}poly)_7]^+$ and $[Ru(bpy)_2(PVP)_{10}]^{2+}$ in the presence of the Dawson polyoxomolybdate $\alpha\text{-}[Mo_{18}O_{54}(SO_3)_2]^{4-}$ has been thoroughly investigated in MeCN solutions. Both the $[Ru(bpy)_2(PVP)_{10}]^{2+}$ and $[Ru(bpy)_2(caip\ co\text{-}poly)_7]^+$ polycations associate strongly with $[Mo_{18}O_{54}(SO_3)_2]^{4-}$ and form MeCN-insoluble electrostatic adducts of highly unusual stoichiometry (4.5: and 5:1 respectively) at high concentrations (approximately mM), but at lower concentrations (ie: ~ 10^{-5} M) the solubility is maintained. UV/Vis and difference electronic spectroscopy of cluster formation revealed the presence of a new intramolecular electronic transition in the case of $[Ru(bpy)_2(PVP)_{10}]^{2+}/[Mo_{18}O_{54}(SO_3)_2]^{4-}$ that tailed significantly into the red (to approximately 700 nm); but no new features were observed in the case of $[Ru(bpy)_2(caip\ co\text{-}poly_7]^+/[Mo_{18}O_{54}(SO_3)_2]^{4-}$. Luminescence quenching experiments revealed strong quenching in both cases that did not adequately fit to the linear static Stern-Volmer model. Application of the Perrin model for static quenching yielded linear fits with excellent regression coefficients; and the values obtained for quenching sphere radii were acceptable at 4.6 Å and 5.8 Å for $[Ru(bpy)_2(PVP)_{10}]^{2+}$ and $[Ru(bpy)_2(caip\ co\text{-}poly)_7]^+$ quenching respectively. Resonance Raman spectroscopy, exciting into the new transition, showed no contribution from the polyoxometalate in the case of $[Ru(bpy)_2(caip\ co\text{-}poly)_7]^+/[Mo_{18}O_{54}(SO_3)_2]^{4-}$. However, a resonantly enhanced polyoxometalate based Mo-O stretching mode was clearly resonantly enhanced in the spectrum of $[Ru(bpy)_2(PVP)_{10}]_{4.5}[Mo_{18}O_{54}(SO_4)_2]$. This mode was blue-shifted significantly with respect to the same vibration of the parent ion and this was tentatively ascribed to strong intramolecular H-bonding with the Ru complex. This mode also came more strongly into resonance at 514 nm relative to 488 nm, which reflects the long tail observed in the electronic difference spectra. Diffuse reflectance transient absorption spectra of the solid adducts at 355 nm did not reveal the presence of the transient reduced species $[Mo_{18}O_{54}(SO_3)_2]^{5-}$ in either metallopolymer adduct. Photo-electrochemical measurements on ITO electrodes with 480 nm irradiation demonstrated that the associated ion-cluster $[Ru(bpy)_2(PVP)_{10}]_{4.5}[Mo_{18}O_{54}(SO_4)_2]$ generated a lower current than $[Mo_{18}O_{54}(SO_3)_2]^{4-}$ under the same conditions. This was in sharp contrast to the photocurrents generated by self-assembled films reported by us previously; and this has been attributed to excessive layer thickness produced by drop-casting.[11] In both drop-casting and self-assembly, $[Ru(bpy)_2(caip\ co\text{-}poly)_7]_5[Mo_{18}O_{54}(SO_4)_2]$ generated a lower photocurrent than $[Mo_{18}O_{54}(SO_3)_2]^{4-}$ alone and was therefore deemed to be non-sensitizing. The reason for the difference between the effectiveness if the two metallopolymers is not known; however since the thermodynamics of charge transfer are very similar the difference likely lies in sterics and/or orbital overlap. We therefore conclude that resonance Raman spectroscopy can be use to identify potential donor-acceptor electrostatic ion-clusters that exhibit enhanced photochemistry under visible irradiation.

4.5 - References:

---

[1] C. E. D. Chidsey and R. W. Murray, *Science*, 1986, **103**, 5007.

[2] D. J. Caruana and A. Heller, *J. Am. Chem. Soc.*, 1999, **121**, 769.

[3] N. Gajovic, G. Binyamin, A. Warsinke, F. W. Scheller and A. Heller, *Anal. Chem.*, 2000, **72**, 2963.

[4] R. J. Mortimer, A. L. Dyer and J. R. Reynolds, *Displays*, 2006, **27**, 2.

[5] Q. Zeng, A. McNally, T. E. Keyes and R. J. Forster, *Electrochem. Commun.*, 2008, **10**, 466.

[6] L. Dennany, R. J. Forster and J. F. Rusling, *J. Am. Chem. Soc.*, 2003, **125**, 5213.

[7] L. Dennany, R. J. Forster, B. White, M. R. Smyth and J. F. Rusling, *J. Am. Chem. Soc.*, 2004, **126**, 8835.

[8] L. Dennany, C. F. Hogan, T. E. Keyes and R. J. Forster, *Anal. Chem.*, 2006, **78**, 1412 - 1417.

[9] A. M. Spehar-Délèze, U. Neugebauer, Y. Pellegrin, T. E. Keyes and R. J. Forster, *Electrochem. Commun.*, 2008, **10**, 984.

[10] A. Venkatanarayanan, A-M. Spehar-Délèze, L. Dennany, Y. Pellegrin, T. E. Keyes and R. J. Forster, *Langmuir*, 2008, **24**, 11233.

[11] J. Zhu, S. O' Carroll, A. M. Bond, T. E. Keyes and R. J. Forster, *Electrochem. Commun.*, 2011, In Print, doi: 10.1016/j.elecom.2011.02.010

[12] S. C. Rasmussen, D. W. Thompson, V. Singh and J. D. Petersen, *Inorg. Chem.,* 1996**, 35***,* 3449 - 3450.

[13] Y. Pellegrin, R. J. Forster and T. E. Keyes, *Inorg. Chim. Acta*, 2009, **362**, 1715.

[14] N. Fay, V. M. Hultgren, A. G. Wedd, T. E. Keyes, R. J. Forster, D. Leane and A. M. Bond, *Dalton Trans.*, 2006, 4218 - 4227.

[15] R. J. Forster and J. G. Vos, *Macromolecules*, 1990, **23**, 4372 - 4377.

[16] C. F. Hogan and R. J. Forster, *Anal. Chim. Acta*, 1999, **396**, 13 - 21.

[17] K. Heussner, K. Peuntinger, N. Rockstroh, L. C. Nye, I. Ivanovic-Burmazovic, S. Rau and C. Streb, *Chem. Commun.,* 2011, in press, DOI: 10.1039/c1cc11859e

[18] C. Baffert, J. F. Boas, A. M. Bond, P. Kögerler, D-L. Long, J. R. Pilbrow and L. Cronin, *Chem. Eur. J.*, 2006, **12**, 8472 - 8483.

[19] J. Kowal, *Polymer*, 1997, **38**, 5059 - 5062.

---

[20] J. R. Ferraro, *Introduction to Raman Spectroscopy*, Academic Press, New York, 1994.

[21] S. Nad and H. Pal, *J. Phys. Chem. A*, 2001, **105**, 1097.

[22] For acetonitrile solutions, the formal definition of pH does not, of course, apply. However, the perchloric acid and tetrabutylammonium hydroxide employed in these studies are anticipated to dissociate close to 100% in MeCN (for example see: I. M. Kolthoff, S. Bruckenstein and M. K. Chantooni, *J. Am. Chem. Soc.,* 1961, **83**, 3927 - 3935). Thus we define pH here as -log[$HClO_4$] or 14--log[TBAOH].

[23] Biexponential decay fitted using $I(t) = (I)_0[\alpha_1 e^{-t/\tau 1} - \alpha_2 e^{-t/\tau 2}]$, where τ_1 and τ_2 are the decay times and α_1 and α_2 are the fractional amplitudes of the components at $t = 0$. See N. Keswani, S. Choudhary and N. Kishore, *J. Biochem.*, 2010, **148**, 71 - 84.

[24] T. E. Keyes, E. Gicquel, L. Guerin, R. J. Forster, V. M. Hultgren, A. M. Bond, and A. G. Wedd, *Inorg. Chem.*, 2003, **42**, 7897 - 7905.

[25] M. K. Seery, L. Guerin, R. J. Forster, E. Gicquel, V. M. Hultgren, A. M. Bond, A. G. Wedd, and T. E. Keyes, *J. Phys. Chem. A*, 2004, **108**, 7399 - 7405.

[26] M. K. Seery, N. Fay, T. McCormac, E. Dempsey, R. J. Forster and T. E. Keyes, *Phys. Chem. Chem. Phys*., 2005, **7** , 3426 - 3433.

[27] J. J. Walsh, D-L. Long, L. Cronin, A. M. Bond, R. J. Forster and T. E. Keyes, *Dalton Trans.*, 2011, **40**, 2038 - 2045.

[28] Y. Pellegrin, R. J. Forster and T. E. Keyes, *Inorg. Chim. Acta*, 2008, **361**, 2683 - 2691.

[29] Jie Zhu PhD thesis, DCU, 2011.

[30] K. Nagai, T. Nishijima, N. Takamiya, M. Tada and M. Kaneko, *J. Photoch. Photobio. A*, 1995, **92**, 47 - 51.

[31] L. Dennany, T. E. Keyes and R. J. Forster, *Analyst*, 2008, **133**, 753 - 759.

[32] A. P. Taylor, J. A. Crayston and T. J. Dines, *J. Chem. Soc., Faraday Trans.*, 1997, **93**, 1803 - 1812.

[33] J. Song, Z. Luo, H. Zhu, Z. Huang, T. Lian, A. L. Kaledin, D. G. Musaev, S. Lense, K. I. Hardcastle and C. L. Hill, *Inorg. Chim. Acta*, 2010, **363**, 4381 - 4386.

[34] L. M. Dupray and T. J. Meyer, *Inorg. Chem.*, 1996, **35**, 6299.

[35] S. W. Hedges and L. H. Bowen, *Inorg. Chem.*, 1984, **23**, 615 - 618.

Chapter 5:

Photophysics and photoelectrochemistry of $[Ru(bpy)_2(PVP)_{10}]^{2+}$ in the presence of the α-$[P_2W_{18}O_{62}]^{6-}$ anion.

5.1: Introduction:

Zhu *et al.* recently reported that $[Ru(bpy)_2(PVP)_{10}]^{2+}$ and α-$[Mo_{18}O_{54}(SO_4)_2]^{4-}$ could be employed to produce interfacial LBL self-assembled multilayer films with the ability to photooxidize benzyl alcohol substrate under visible (480 nm) irradiation. These films were more efficient at photocurrent generation than films consisting of either $[Ru(bpy)_2(PVP)_{10}]^{2+}$ or α-$[Mo_{18}O_{54}(SO_4)_2]^{4-}$ alone under the same conditions of irradiation. Furthermore, detailed studies of the film stability, electrolyte concentration, layer thickness and substrate concentration were performed.[1] The data reported in Chapter 4 and by Zhu *et al.* strongly suggest that film morphology and thickness are critical in determining photocurrent generating efficiency.[10] Collectively, these studies demonstrated that:

(a) Photocurrent generation initially increases with an increasing number of deposition cycles (ie: increasing surface coverage, Γ).
(b) After a certain number of deposition cycles layer growth becomes non-linear and photocurrent generation becomes adversely affected as D_{CT} drops.
(c) Drop-cast films have very poor photocurrent generating ability, which is attributed to their thickness.
(d) Photocurrent generation could be increased by addition of electrolyte to the films to improve conductivity. However most electrolytes investigated disrupted the electrostatic association of the films, causing them to rapidly disassociate.
(e) Photocurrent generation increases as a non-linear function of increasing applied potential.

It was concluded that one of the limiting factors of current generation was the reoxidation of the reduced $[Mo_{18}O_{54}(SO_4)_2]^{5-}$ moieties in the Ru-molybdate film after catalysis. Polyoxotungstates have a more negative initial reduction potential and therefore a larger overpotential for reoxidation may be applied to a Ru-POW system relative to a Ru-POM system. α-$[P_2W_{18}O_{62}]^{6-}$ was the polyoxotungstate chosen for this study as it is isostructural with other polyoxometalates studied in this thesis. To exploit the potentially preferable properties of the tungstate, this chapter therefore focuses on the photophysics of adducts formed between α-$[P_2W_{18}O_{62}]^{6-}$ and $[Ru(bpy)_2(PVP)_{10}]^{2+}$, and the photoelectrochemical studies of self-assembled $[Ru(bpy)_2(PVP)_{10}]^{2+}$/α-$[P_2W_{18}O_{62}]^{6-}$ films at ITO electrodes.

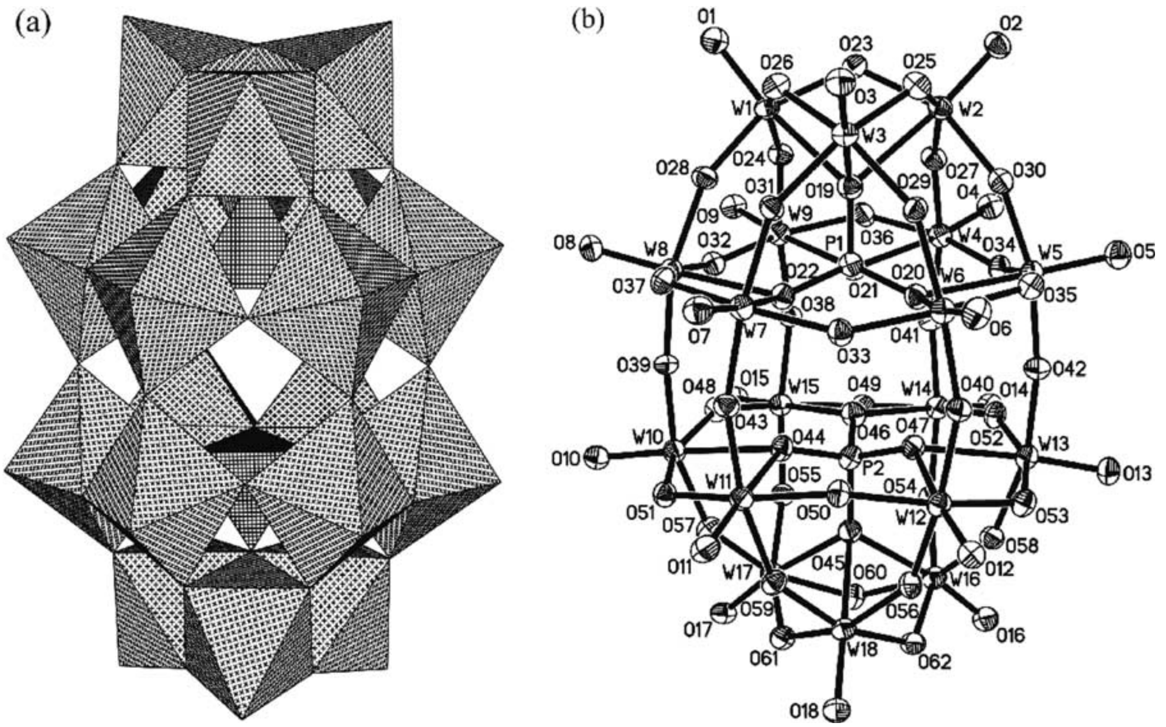

Fig 5.1.1: (a) Polyhedral representation of α-$[P_2W_{18}O_{62}]^{6-}$ where each octahedron represents a WO_6 unit and (b) ORTEP diagram of α-$[P_2W_{18}O_{62}]^{6-}$ with thermal ellipsoids at 50% probability. Reproduced from [2].

5.2 – Synthesis and characterization:

The polyoxotungstate K_6α-$[P_2W_{18}O_{62}]$ was synthesized according to the method of Mbomekalle *et al*.[3] The compound was characterized by CV, UV/Vis spectroscopy, ATR-FTIR spectroscopy, Raman spectroscopy and mass spectrometry.[4] This synthetic procedure afforded excellent isomeric purity, as demonstrated by ^{31}P-NMR spectroscopy. The cyclic voltammetry (CV) of the polyoxotungstate is shown in Fig 5.2.1.1.

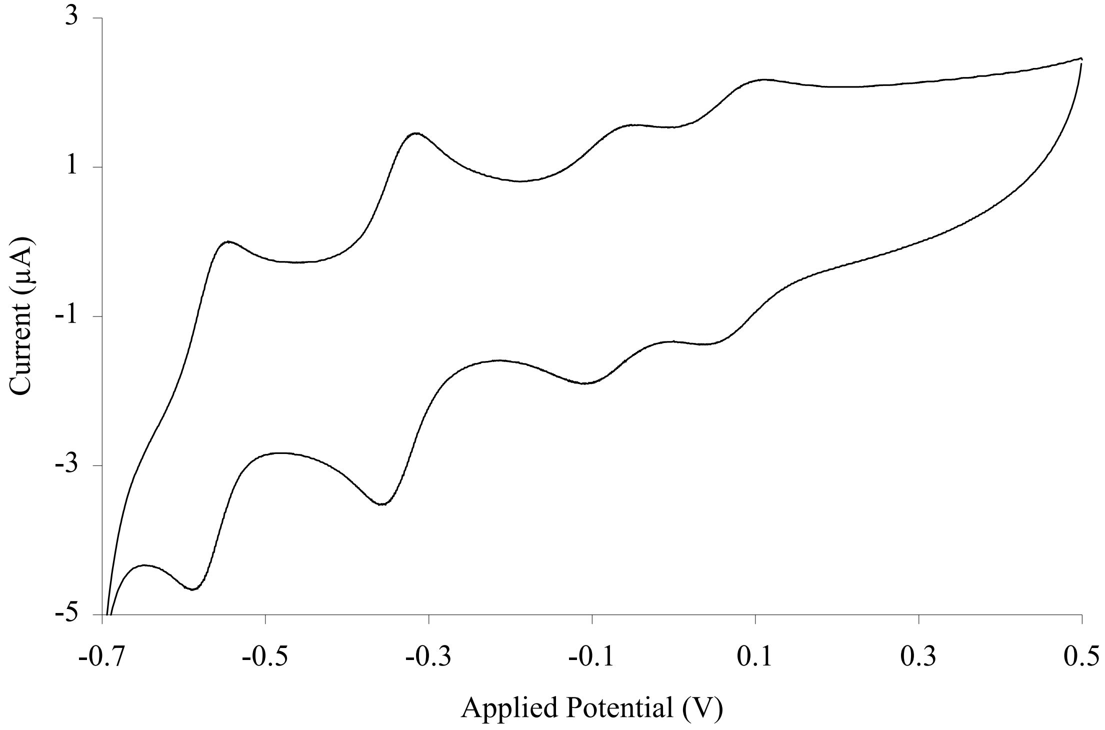

Fig 5.2.1.1: Cyclic voltammogram of 2 x 10^{-4} M $K_6\alpha$-$[P_2W_{18}O_{62}]$ in 0.5 M H_2SO_4. Working electrode: glassy carbon disk; scan rate: 10 mV/s; solution pH: 0.33. Counter electrode was a large surface area Pt flag. Reference electrode was Ag/AgCl.

The CV in Fig 5.2.1.1 demonstrates the purity of the α-$[P_2W_{18}O_{62}]^{6-}$ synthesis. The other isomer, β-$[P_2W_{18}O_{62}]^{6-}$, has similar but subtly different electrochemical properties. The first two reductions (1 electron processes) appear at more positive potentials and the second two (2 electron processes) at more negative potentials, so that in a mixture of the two isomers all 4 peaks would be expected to appear quite broadened. CV, however, is insensitive to approximately 10 % isomeric impurities, so the isomeric purity was confirmed by NMR. Fig 5.2.1.2 shows the ^{31}P-NMR of α-$[P_2W_{18}O_{62}]^{6-}$. The α-isomer exhibits one peak at -12 ppm, whereas the β-isomer has lower symmetry (D_{3d} for β relative to D_{3h} for α) and exhibits two well separated ^{31}P resonances of equal intensity, and the absence of these peaks indicates that the quantity of β isomer is low.

$[(But)_4N]_6\alpha$-$[P_2W_{18}O_{62}]$ was synthesized as described in Chapter 2.

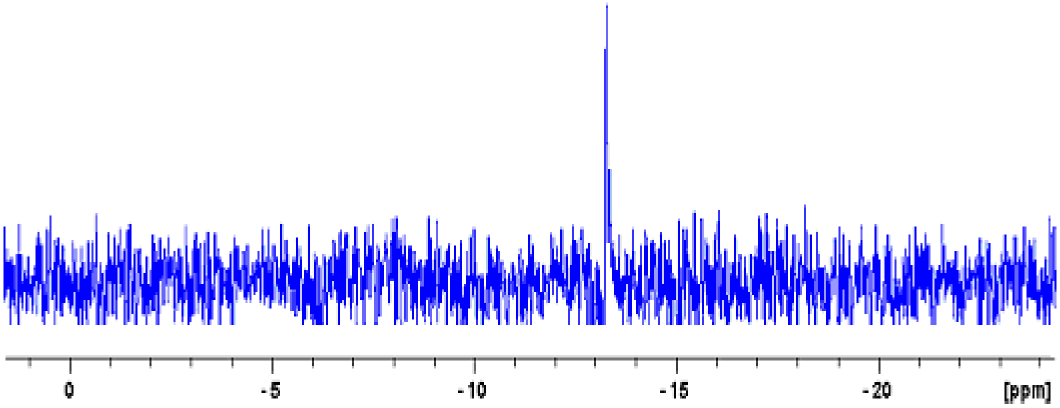

Fig 5.2.1.2: ^{31}P-NMR spectrum (162 MHz) of isomerically pure $K_6\alpha$-[$P_2W_{18}O_{62}$] in 1 M $LiClO_4$ in D_2O.

5.3 – Ion-cluster photophysics and spectroscopy:

5.3.1 - UV/Vis spectroscopy:

Ion-cluster formation between Dawson polyoxometalates and Ru (II) polypyridyl complexes has previously been shown to result in the appearance of a new electronic absorption band in the visible region, attributed to an intramolecular charge-transfer transition between the two ions.[5, 6, 7] These low energy features tail significantly into the red in the case of molybdates but not in the case of tungstates. In previous cases difference spectroscopy was employed in order to clearly see these often subtle spectral changes, as they can be obscured by more-intense adjacent parent-ion features. However in this present case poor solubility has limited our spectral analyses of ion-cluster formation; the degree of baseline drift observed in the UV spectra would suggest at least partial precipitation of the $[Ru(bpy)_2(PVP)_{10}]^{2+}/\alpha$-$[P_2W_{18}O_{62}]^{6-}$ composites, or aggregation of the polymer leading to light scatter. The corrected UV spectra of a solution of $[Ru(bpy)_2(PVP)_{10}](PF_6)_2$ in the presence of increasing concentrations of $[N(But)_4]_6\alpha$-$[P_2W_{18}O_{62}]$ are presented in Fig 5.3.1.1.

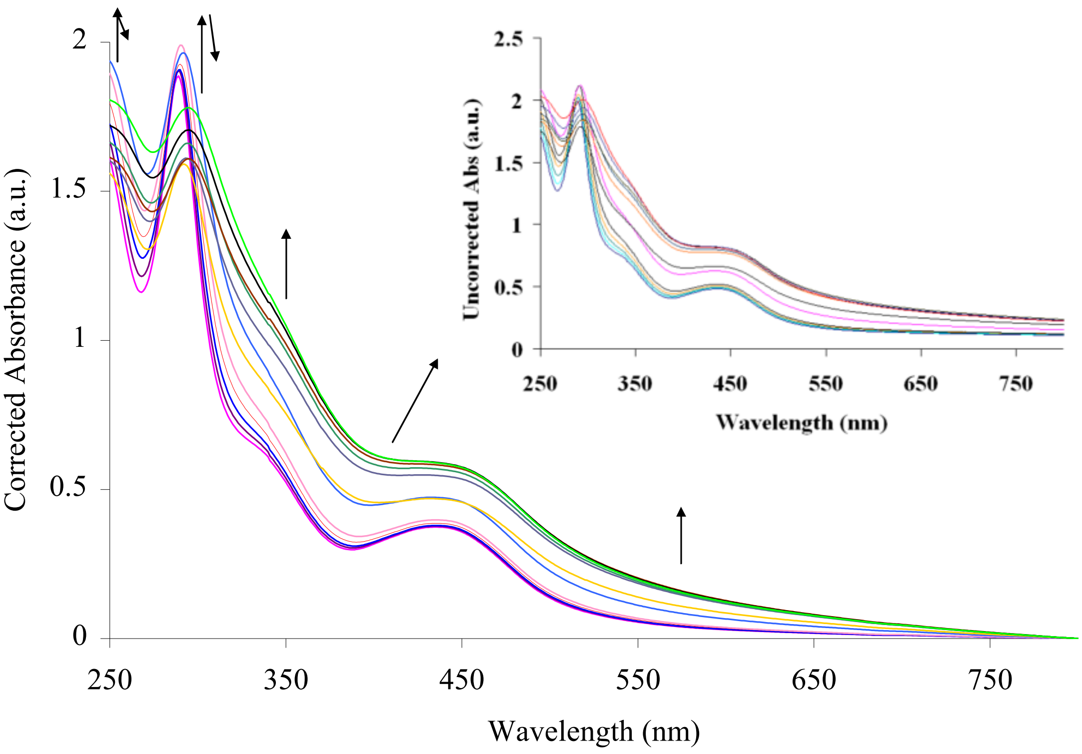

Fig 5.3.1.1: UV/Vis spectra (corrected) of $[Ru(bpy)_2(PVP)_{10}]^{2+}$ (4.5 x 10^{-5} M) titrated with α-$[P_2W_{18}O_{62}]^{6-}$ (2.89 x 10^{-4} M) in dry MeCN. Inset: The same series of spectra uncorrected.

The spectra in Fig 5.3.1.1 are not consistent with previous related studies involving polyoxometalates and Ru monomeric complexes. The baseline drift appears to be significant in this case, indicating significant scatter from the electrostatic product formed in MeCN. The new low-energy intramolecular charge-transfer band appears as a shoulder on the $[Ru(bpy)_2(PVP)_{10}]^{2+}$ MLCT absorbance centered around 445 nm, and this feature tails significantly into the red. The $[Ru(bpy)_2(PVP)_{10}]^{2+}$ $\pi \rightarrow \pi^*$ transition at 288 nm also broadens, decreases in intensity, and red-shifts by approximately 6 nm to 294 nm. It also appears as though the Ru MLCT transition increases in intensity upon association. This is highly unlikely to be a true increase, and is more likely due to scattered light from the associated product. The polyoxotungstate holds a 6- charge and therefore will significantly increase the ionic strength of the solution upon its addition. This change in ionic strength could lead to initial swelling or contraction of the polymer, resulting in unusual initial association behaviour. The change in behavior could otherwise possibly be due to polymer particle formation. The conformation of conjugated polymers in solution has been studied previously as a function of ionic strength. When the polymer poly[5-methoxy-2-(4-sulfobutoxy)-1,4-phenylvinylene] (MBL–PPV) was dissolved in aqueous solution, small-angle neutron scattering

(SANS) was used to demonstrate that the polymer formed aggregates that are stable in low ionic strength media but dissociate in the presence of excess salt.[8] In this present case the polyoxotungstate carries a 6- charge and 6 tetrabutylammonium counterions, so its addition to solutions of $[Ru(bpy)_2(PVP)_{10}]^{2+}$ would result in significant ionic strength alteration. This means that metallopolymer aggregation could be favoured in this case, which is likely to reduce the number of available binding sites for the quencher and hence affect the associative behaviour. Further investigation into this behaviour will be undertaken in future by dynamic light scattering (DLS) measurements.

In previous related studies, Job's method for calculating binding stoichiometry has been successfully employed by using difference spectral data. In this case no difference spectra were acquired so the raw data were employed instead. These data are presented in Fig 5.3.1.2.

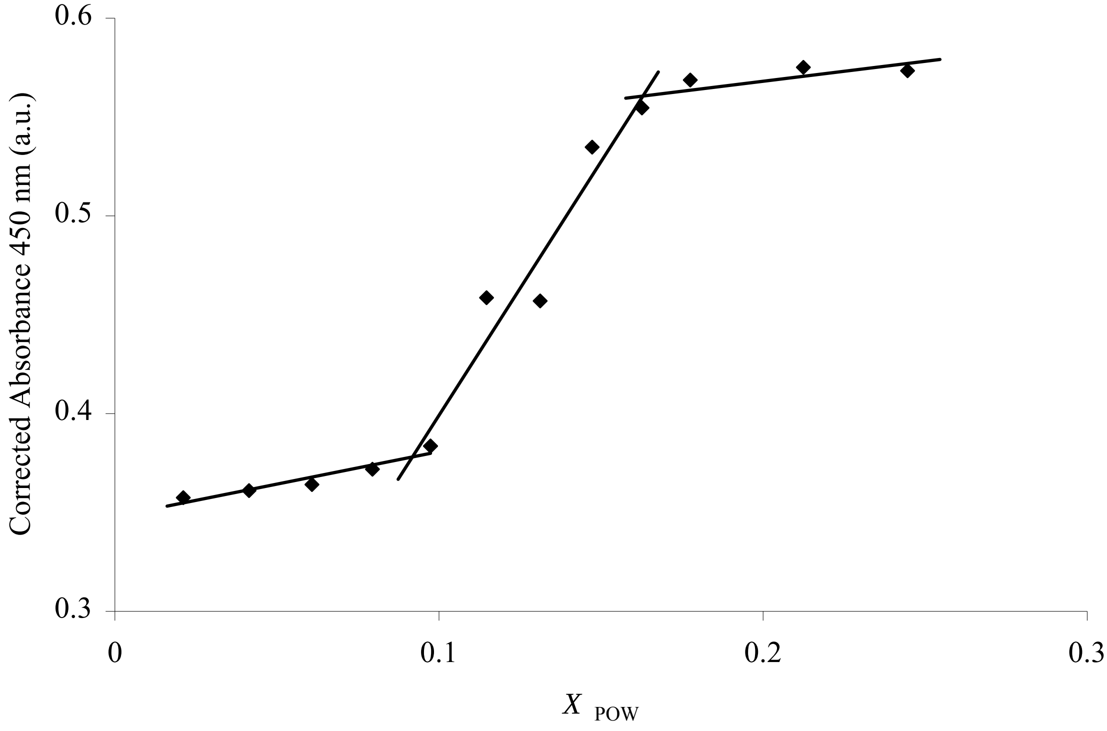

Fig 5.3.1.2: Plot of α-$[P_2W_{18}O_{62}]^{6-}$ mole fraction versus absorbance change at 450 nm as a function of increasing α-$[P_2W_{18}O_{62}]^{6-}$ concentration, data taken from Fig 5.3.1.1.

The plot in Fig 5.3.1.2 is strikingly similar to the shape of the I_0/I Stern-Volmer plot obtained for quenching of $[Ru(bpy)_2(PVP)_{10}]^{2+}$ by the related Wells-Dawson polyoxomolybdate α-

$[Mo_{18}O_{54}(SO_4)_2]^{4-}$ (see Chapter 4). The intersections of the lines indicate the molar ratios at which the spectroscopy changes and different ion-clusters may form at these ratios. In the case of $[Ru(bpy)_2(PVP)_{10}]^{2+}$ and α-$[Mo_{18}O_{54}(SO_4)_2]^{4-}$ ion-cluster formation occurred at a ratio of 4.5:1 (Ru to Mo), which was demonstrated both spectroscopically (UV/Vis, emission quenching, EDX) and by cyclic voltammetry (see Chapter 4).[9, 10] This was, to our knowledge, the first reported instance in which the ion-cluster ratio formed did not result in a full stoichiometric pairing of Ru and POW. In the present case, the spectroscopy changes at the same stoichiometry (~ 4.5:1 Ru:POW ratio, X_{POW} ~ 18 %), and also at a lower X_{POW} ~ 9 % (approximately a 9:1 Ru:POW ratio). Presumably the ion-clusters exist in the forms $\{[Ru(bpy)_2(PVP)_{10}]_9\alpha\text{-}[P_2W_{18}O_{62}]\}^{12+}$ and $\{[Ru(bpy)_2(PVP)_{10}]_{4.5}\alpha\text{-}[P_2W_{18}O_{62}]\}^{3+}$. These data are somewhat unexpected as α-$[P_2W_{18}O_{62}]^{6-}$ has been shown previously to form 3:1 charge neutral electrostatic adducts with $[M(bpy)_3]^{2+}$ (where M = Fe, Ru, Os).[11, 12, 13] Since the expected 3:1 ratio (ie: charge neutral overall with respect to Ru-POW cluster formation) was not observed in this case it may be the case that ion-pair formation is not driven purely by electrostatic attraction between $[Ru(bpy)_2(PVP)_{10}]^{2+}$ and the Dawson polyoxometalates that results in formation of the thermodynamically most favoured product, and that different stoichiometric products can form at different ion-cluster ratios.

The UV/Vis spectra of thin films of $[Ru(bpy)_2(PVP)_{10}]^{2+}$ and $[Ru(bpy)_2(PVP)_{10}]^{2+}$/α-$[P_2W_{18}O_{62}]^{6-}$ on ITO electrodes have also been recorded. The pre-cleaned ITO slide was dipped into a 1 mM solution of $[Ru(bpy)_2(PVP)_{10}]^{2+}$ for 30 minutes, removed from the solution and dried in air. The slide was then rinsed with MeCN to remove any non surface-bound material. After drying in air again the UV/Vis spectrum was recorded. The slide was then dipped into a solution of 1 mM α-$[P_2W_{18}O_{62}]^{6-}$ for another 30 minutes to allow the POW to electrostatically bind to the Ru film. The slide was removed, dried in air, and again rinsed with MeCN. The slide was dried and the UV/Vis spectrum was recorded. These spectra are shown in Fig 5.3.1.4.

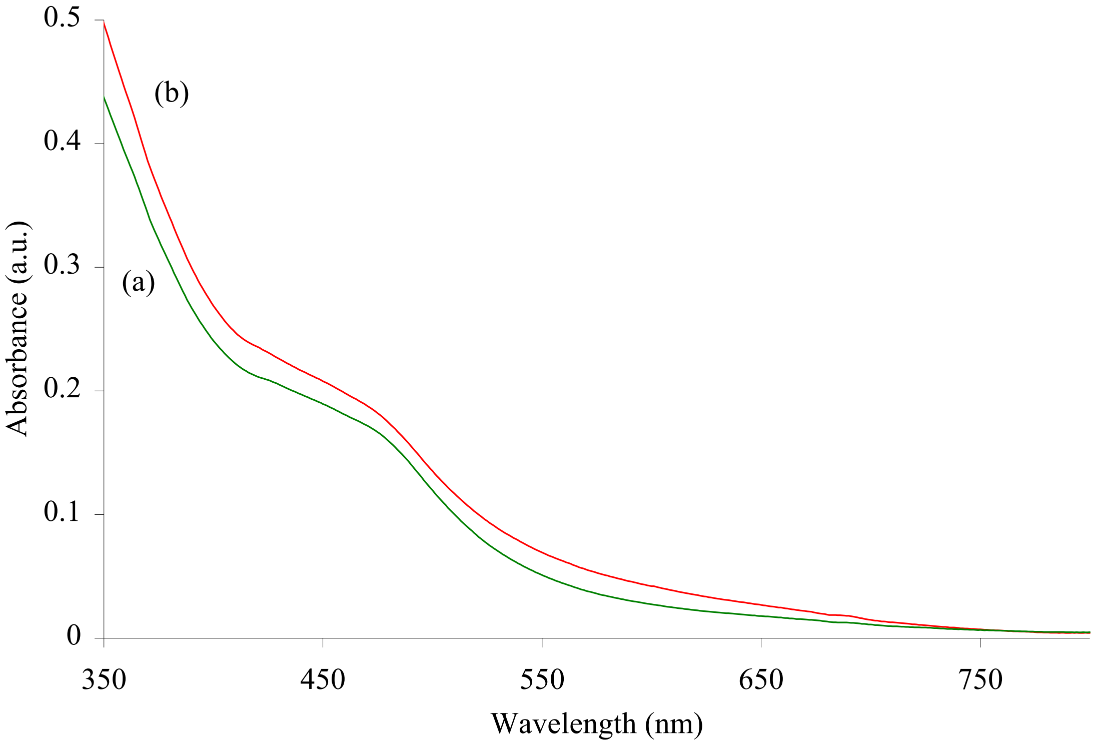

Fig 5.3.1.3: UV/Vis spectra of a (a) thin film of $[Ru(bpy)_2(PVP)_{10}]^{2+}$ dip-coated onto an ITO electrode and (b) thin film of the same electrode after subsequent dip-coating of α-$[P_2W_{18}O_{62}]^{6-}$

Unfortunately these spectra could not be recorded below 300 nm as the ITO substrate absorption filters all light from reaching the detector below this wavelength, therefore the drop in spectral intensity observed for $[Ru(bpy)_2(PVP)_{10}]^{2+}$ $\pi \rightarrow \pi^*$ transition at 288 nm in Fig 5.3.1.1 could not be monitored here. However the apparent increase in absorbance at approximately 470 nm seen in Fig 5.3.1.1 is also observed here, as is an absorbance that tails into the red. These changes are likely to be due to the presence of a new optical transition, on the basis of previous studies of Dawson polyoxometalates and Ru (II) polypyridyl complexes; however this is not as clear as in this case. Nonetheless, participation of both ions in the electronic absorption at > 480 nm is confirmed by resonance Raman spectroscopy (*vide infra*).

5.3.2 - FTIR spectroscopy:

FTIR spectra of α-$[P_2W_{18}O_{62}]^{6-}$, $[Ru(bpy)_2(PVP)_{10}]^{2+}$ and the isolated ion-composite material were examined to identify any structural changes that occur upon ionic association. The polyoxotungstate (spectrum (a)) exhibits signature P-O stretching modes at 1090 and 1024 cm^{-1}, a terminal W-O stretch at 960 cm^{-1} and two W-O-W (bridging oxygen) stretches at 914 and 777 cm^{-1}.[4] Upon association to the Ru polymer these modes all shift slightly, and the largest shift sees the mode at 777 move to 792 cm^{-1} (spectrum (c)). Modes associated with the metallopolymer are also clearly visible in the adduct spectrum; in particular a series of bipyridine ring breathing modes are observed between 1400 and 1600 cm^{-1}, with no significant shifts observable on association. This is not surprising as due to the high Ru:tungstate ratio not all Ru centers will be coupled directly to a polyoxotungstate molecule. The band at 1340 cm^{-1} (spectrum (b)) is attributed to the nitrate counterion and the absence of this mode in the composite material (spectrum (c)) is interesting as it indicates full ion-exchange. This is unexpected, as on the basis of the UV/Vis and emission data there appears to be an excess of Ru and therefore some residual NO_3 should be observed. Overall the spectra indicate full association of α-$[P_2W_{18}O_{62}]^{6-}$ with $[Ru(bpy)_2(PVP)_{10}]^{2+}$, and removal of the NO_3^- counterions. The spectra also indicate that the W-O structure of the POW is perturbed upon association, while the encapsulated PO_4 moieties exhibit little change. This is expected given the shielded environment of these anions relative to the metal-oxide framework and the possibility of H-binding between the peripheral oxygen atoms and the bipyridine protons. The FTIR spectra are presented in Fig 5.3.2.1.

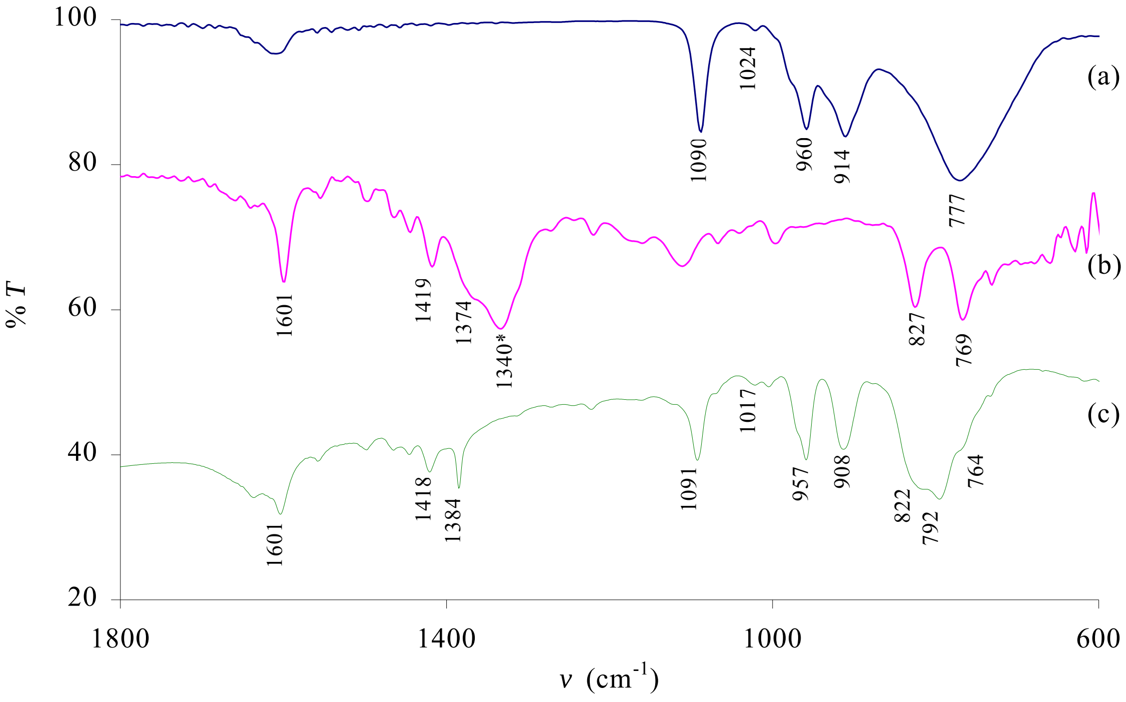

Fig 5.3.2.1: ATR-FTIR spectra of (a) $K_6\alpha$-$[P_2W_{18}O_{62}]$, (b) $[Ru(bpy)_2(PVP)_{10}](NO_3)_2$ and (c) $[Ru(bpy)_2(PVP)_{10}]_{4.5}\alpha$-$[P_2W_{18}O_{62}]$.

5.3.3 - Emission spectroscopy:

The electrostatic association between Dawson polyoxometalates and Ru (II) polypyridyl complexes has been shown to result in significant quenching of the Ru (II) luminescence intensity.[5, 6, 7] The quenching mechanism has usually been observed to be purely static quenching via intramolecular charge transfer to a non-emissive state; however in one particular case mixed static/dynamic quenching was observed.[16] The emission from $[Ru(bpy)_2(PVP)_{10}]^{2+}$ in the presence of increasing concentrations of α-$[P_2W_{18}O_{62}]^{6-}$ in MeCN is shown in Fig 5.3.3.1. The quenching behaviour of this system appeared at first to be unusual in that the apparent emission intensity of $[Ru(bpy)_2(PVP)_{10}]^{2+}$ actually increased upon addition of α-$[P_2W_{18}O_{62}]^{6-}$. As described previously this change in absorbance is attributed to likely initial formation of light-scattering polymeric aggregates at initially high ionic strength, and since only those fluorophores at the surface of the aggregate will be physically accessible to the quencher, the quenching behaviour will alter over the course of the reaction as the increasing ionic strength unfolds the aggregate to allow quenching of internal Ru fluorophores. Cross-linking in polymer The quenching data were fitted to various models in an effort to understand this behaviour. When the uncorrected absorbance data obtained from Fig 5.3.1.2 (relative absorbance changes at 450 nm) are used to normalize the emission intensity values then a I_0/I Stern-Volmer plot was obtained. These data are shown in Fig 5.3.3.1.

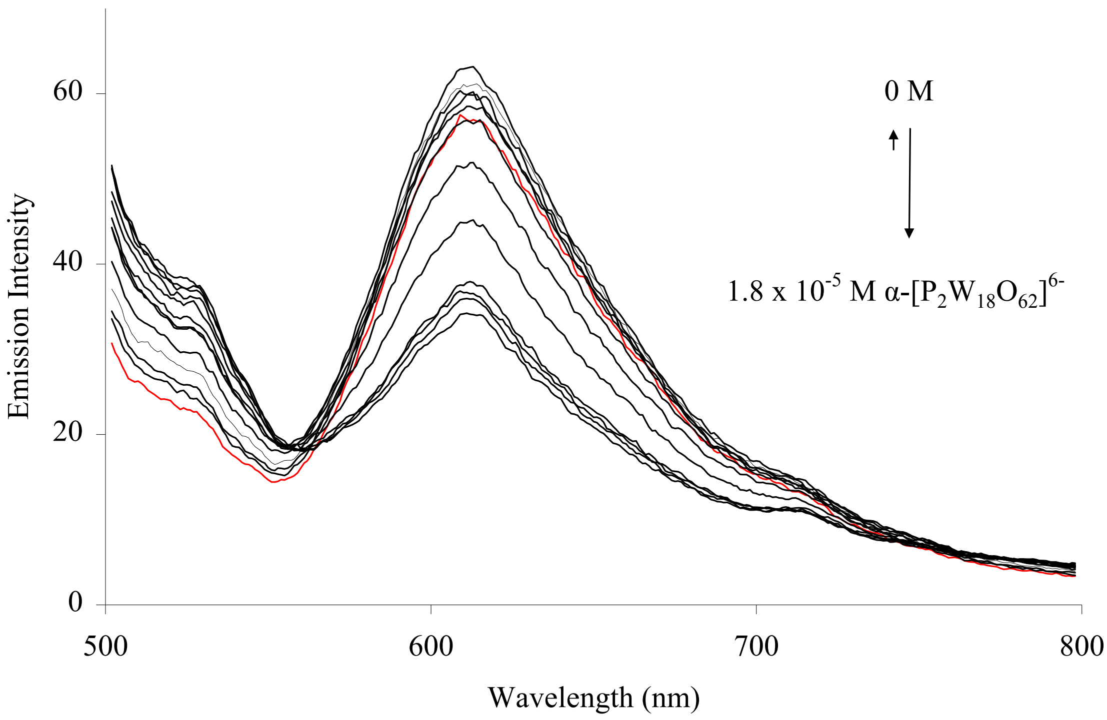

Fig 5.3.3.1: Uncorrected emission spectra of [$Ru(bpy)_2(PVP)_{10}$]$^{2+}$ in the presence of increasing concentrations of [$P_2W_{18}O_{62}$]$^{6-}$ in MeCN. Initial emission before addition of tungstate is in red. Excitation wavelength 450 nm.

The Stern-Volmer relationship has been employed extensively in the study of photoinduced electron transfer mechanisms that results in fluorescence quenching. The Stern-Volmer relationship is described in Chapter 3 (pages 82 – 83). The S-V plot of the data in Fig 5.3.3.1 (corrected using Fig 5.3.1.1) is shown in Fig 5.3.3.2.

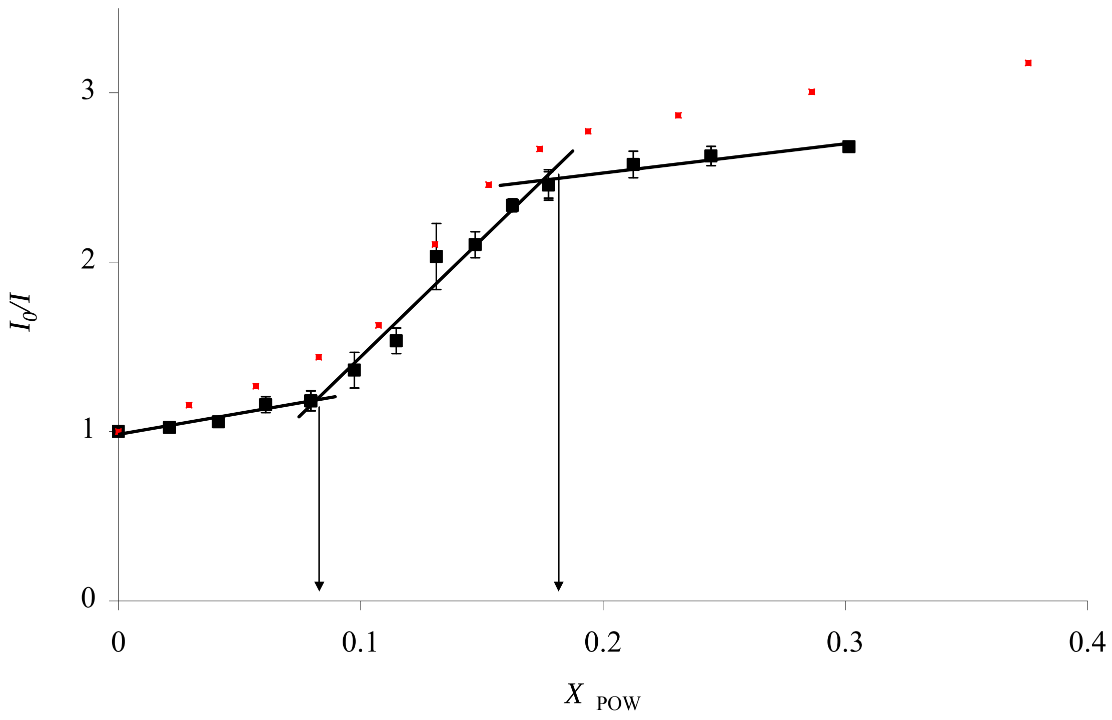

Fig 5.3.3.2: Modified fluorescence quenching Stern-Volmer plot of $[\text{Ru(bpy)}_2(\text{PVP})_{10}]^{2+}$ by α-$[P_2W_{18}O_{62}]^{6-}$ in MeCN. Plot was normalized using absorbance changes at 450 nm based on Fig 5.3.1.2 The red trace is the corresponding Stern-Volmer plot (uncorrected) of $[\text{Ru(bpy)}_2(\text{PVP})_{10}]^{2+}$ quenching by α-$[\text{Mo}_{18}O_{54}(SO_4)_2]^{4-}$ in MeCN (reproduced from Chapter 4 for comparison). Excitation wavelength was 450 nm for both series.

The data presented in Fig 5.3.3.2 show the changes in emission behaviour as a function of changing Ru/POW molar ratios. As for the absorbance data three linear regions are observed, indicating binding stoichiometries of approximately 9:1 and 4.5:1 Ru:POW. The K_a values inferred for these ion ratios were 2.7×10^4 and 2.8×10^5 M^{-1} respectively. Interestingly these same ratios were also obtained upon complexation of $[\text{Ru(bpy)}_2(\text{PVP})_{10}]^{2+}$ with the analogous polyoxomolybdate α-$[\text{Mo}_{18}O_{54}(SO_4)_2]^{4-}$ in MeCN (red series). However these values may not reflect true stoichiometric ratios but rather average situations where some Ru centers are fully charge compensated and are inaccessible to the POW quencher. As mentioned this may indicate that the stoichiometric binding of $[\text{Ru(bpy)}_2(\text{PVP})_{10}]^{2+}$ to Dawson polyoxometalates is not driven by the electrostatics of forming neutral ionic composites. This 4.5:1 stoichiometry may arise because the cation is polymeric in nature, so that the association of a Ru:polyoxometalate neutral 2:1 cluster brings additional ruthenium centers not necessary to maintain electroneutrality. It may also be due to penetrability of polymer aggregates to the polyoxometalate quencher, which is a quite a large anion. It is interesting that this phenomenon is independent of polyoxometalate charge (ie: both the 4- molybdate and 6- tungstate resulted in the same Ru:polyoxometalate ratios forming). It must be noted that the use of a polymer as the fluorophore effects the applicability of the purely static Stern-Volmer model. The Perrin model can be used to investigate the applicability of "sphere of action" quenching to this system, and is widely used in studying the quenching of polymers

A more appropriate model to describe static quenching between a luminescent polymer and a small quencher is likely to be the Perrin model. Used both with polymers and for proteins, the Perrin model describes static quenching between randomly distributed and immobile fluorophores with quenchers which are randomly in proximity. In this model, one presumes that there is instantaneous quenching of an excited donor (D^*, ie: $[\mathrm{Ru(bpy)_2(PVP)_{10}}]^{2+}*$) by a quencher ($Q$, ie: α-$[\mathrm{P_2W_{18}O_{62}}]^{6-}$) if this quencher is within a spherical volume V centered on D^*; and that no quenching occurs when the quencher is outside of this volume.[14] Since Ru monomer complexes are mobile in solution the model cannot be applied in those cases; however Ru metallopolymers have sufficiently constrained mobility to be considered for this "sphere of action" model. The Perrin equation (Equation 6) is given below.

$$\ln\left(\frac{I_0}{I}\right) = V.N_A.[Q] = \frac{4}{3}\pi.R_S^3.N_A.[Q] \qquad (6)$$

Where V is the volume of the quenching sphere of action and R_S is the radius of the quenching sphere. The quenching data fitted to the Perrin model is shown in Fig 5.3.3.4.

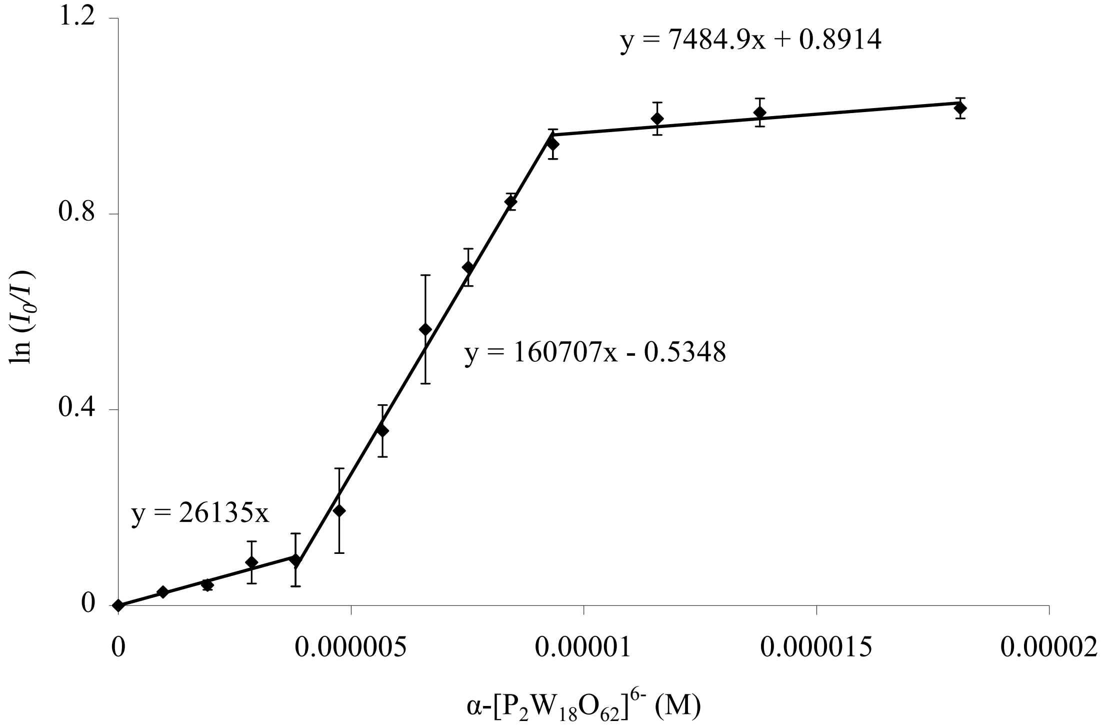

Fig 5.3.3.4: Perrin plot of the quenching data in Fig 5.3.3.1.

Again, the data showed three linear portions and slopes of these regions in Fig 5.3.3.4 were analyzed using the Perrin model. Unlike for the quenching of the corresponding molybdate in Chapter 4, the data did not fit the model well. For the Perrin equation to be employed in calculating the radius of the quenching sphere the intercept of the equation must equal zero; therefore only the lowest concentration region has been applied. This is somewhat speculative as if the Perrin model fits the quenching behaviour then only one linear region should be observed until the quenching plateaus (see Chapter 4). This unexpected change in slope is attributed to the polymer structure changing as a function of increasing ionic strength (as discussed in section 5.3.1), which resulted in light scatter and altered emission intensity being recorded. POW-bridged cross-linking between polymer chains is also a possibility, as they polymer could uncoil as the ionic strength changes, allowing access to previously inaccessible fluorophores. Nonetheless, the initial slope has been employed in this case as an estimate. Inserting this number (26135 $cm^3.mol^{-1}$) into the Perrin equation gives a quenching sphere radius R_S of 2.2 ± 0.1 Å. This number is a reasonable estimate for static electron transfer distance involving Ru (II) polypyridyl fluorophores in a polymer matrix, and corresponds to a very short distance (ie: one or two bond lengths). If the second slope of 160707 $cm^3.mol^{-1}$ is used then a R_S value of 4.0 ± 0.1 Å was obtained, which is closer to the values obtained in Chapter 4 for the corresponding molybdate study. In either case, these distances are both reasonable estimates for static quenching charge-transfer.

5.3.4 - Time-resolved emission:

Time-resolved luminescence spectroscopy can reveal further insight into the nature of the quenching mechanism. If the luminescent lifetime remains unaffected over the same quencher concentration range that results in luminescence intensity quenching then the photoinduced electron transfer is purely static in nature. If the τ_0/τ plot has a slope then a dynamic quenching component may be present. The τ_0/τ plot of $[Ru(bpy)_2(PVP)_{10}]^{2+}$ quenching by α-$[P_2W_{18}O_{62}]^{6-}$ is given in Fig 5.3.4.1.

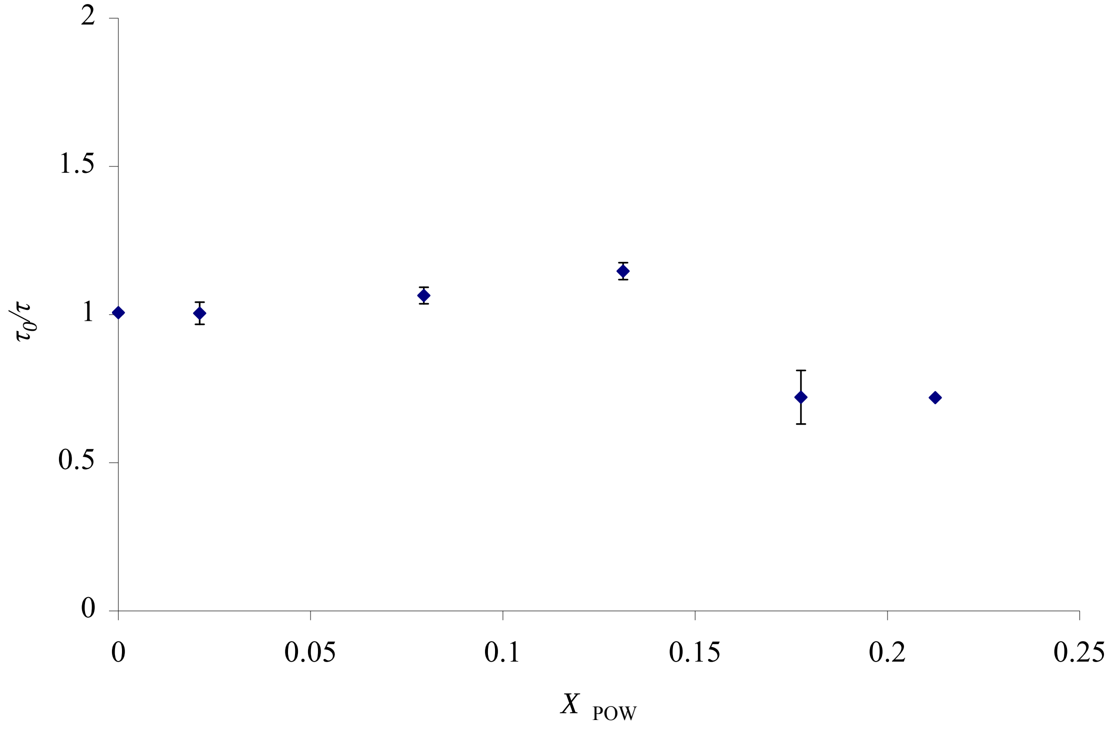

Fig 5.3.4.1: Luminescence lifetime quenching of $[Ru(bpy)_2(PVP)_{10}]^{2+}$ (long component) by α-$[P_2W_{18}O_{62}]^{6-}$ in MeCN. Recorded by TCSPC exciting at 450 nm.

In the case of purely static quenching no slope is observed in the τ_0/τ plot; whereas if there is a dynamic quenching component also present an upwards slope would be expected. In this case of Fig 5.3.4.1 it appears as though there is little or no initial slope, consistent with predominantly static quenching; however at the ion-cluster ratio of 4.5:1 there appears to be a change in behaviour. At this ratio the τ_0/τ plot slopes downwards, and indeed the lifetime increased to 162 ± 5 ns from its initial 116 ns. The reason for this apparent increase in lifetime is unknown, but may be due to the changes in polymer structure with increasing ionic strength mentioned previously. Interestingly, the short component of the decay also increased from 13 ns for free $[Ru(bpy)_2(PVP)_{10}]^{2+}$ to 22 ns for $[Ru(bpy)_2(PVP)_{10}]_{4.5}\alpha\text{-}[P_2W_{18}O_{62}]$. It is difficult to draw meaningful conclusions from the slope in Fig 5.3.4.1 as the luminescent intensity decreased with increasing POW concentration, and hence the error bars are substantial.

5.3.5 - Resonance Raman spectroscopy:

As discussed in previous chapters, resonance Raman spectroscopy may be used to identify polyoxometalate/Ru complex ion-clusters in which both ions participate in the new intercomponent lowest-energy optical transition centered on 475 nm (Fig 5.3.1.1). Assuming an ion-cluster stoichiometry of 4.5:1 Ru:POW as demonstrated by UV/Vis and fluorescence quenching solution titrations, the associated cluster $[Ru(bpy)_2(PVP)_{10}]_{4.5}\alpha\text{-}[P_2W_{18}O_{62}]$ was synthesized as described in Chapter 2. The solid was ground into oven-dried KBr for resonance Raman analysis, in order to prevent any unwanted photooxidation under laser irradiation. The resonance Raman spectra of the associated cluster and the parent ions are shown in Fig 5.3.5.1.

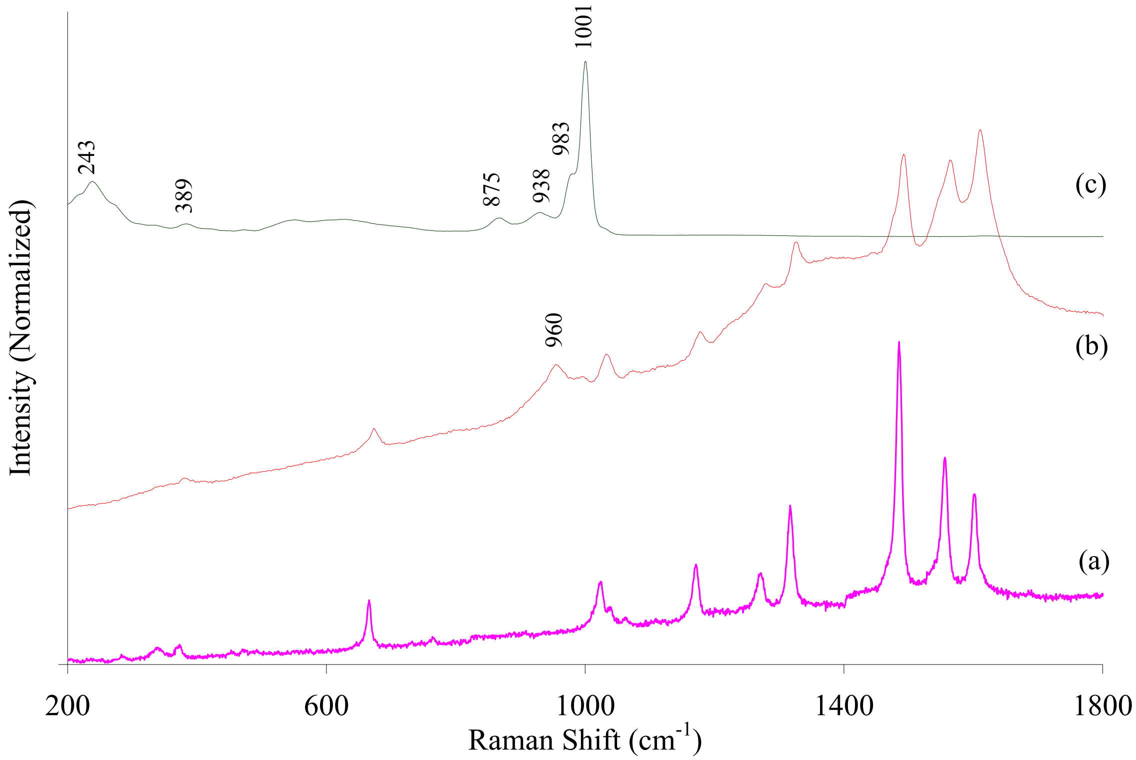

Fig 5.3.5.1: Resonance Raman spectra of (a) $[Ru(bpy)_2(PVP)_{10}](NO_3)_2$, (b) $[Ru(bpy)_2(PVP)_{10}]_{4.5}\alpha$-$[P_2W_{18}O_{62}]$ and (c) $K_6\alpha$-$[P_2W_{18}O_{62}]$ in KBr discs (~ 5 % w/w) under 488 nm irradiation.

This technique was employed to investigate the origin of the weak changes seen in the UV/Vis spectra upon Ru-POW association. Resonance Raman spectroscopy is an extremely useful tool which can be used to elucidate which vibrational modes are associated with a chromophore. An optical transition in resonance with laser excitation will exhibit large enhancement of its vibronic modes, and enhancement factors of up to 10^7 have been observed.[15] Investigations of polyoxometalate/transition metal complex electrostatic adducts have demonstrated that a new feature is commonly observed in the UV/Vis spectra of the adducts. These new optical transitions were shown, via resonance Raman spectroscopy, to involve both polyoxometalate and Ru-based modes and hence were attributed to Ru to polyoxotungstate charge transfer transitions. In this case the use of Raman is absolutely necessary in characterizing the charge-transfer character of the $[Ru(bpy)_2(PVP)_{10}]_{4.5}\alpha$-$[P_2W_{18}O_{62}]$ composite as the UV/Vis changes viewed upon association were ambiguous, relative to those seen in Chapters 3 and 4.

Although a wide variety of polyoxometalate/transition metal complex ion-clusters have been studied using resonance Raman spectra (see Chapter 6) most studied to date have not shown the presence of polyoxometalate bands under visible excitation (458, 488 or 514 nm).[16] It is thought that the presence of resonantly enhanced polyoxometalate modes in the resonance Raman of the new optical transitions is important in identifying which ion-clusters will result in sensitization, as it is likely that this transition participates in sensitization. Therefore all candidate ion-pairs for photochemistry were identified by checking for polyoxometalate modes in the resonance Raman spectra of their solid ionic composites under visible irradiation.

The resonance Raman spectra of the two parent ions and of the $[Ru(bpy)_2(PVP)_{10}]_{4.5}\alpha$-$[P_2W_{18}O_{62}]$ composite are presented in Fig 5.3.5.1. The spectrum of $[Ru(bpy)_2(PVP)_{10}](NO_3)_2$ (Fig 5.3.5.1 (a)) exhibits modes characteristic of resonance with a Ru-bpy MLCT transition with modes at 1603, 1557, 1485, 1318, 1272, 1172, 1026 and 665 cm^{-1} attributed to bpy vibrations, and a Ru-N mode is clearly visible at 376 cm^{-1}. The differences between the Raman spectra of $[Ru(bpy)_2(PVP)_{10}]^{2+}$ and $[Ru(bpy)_3]^{2+}$ are very minor, as the excited state (ie: resonantly enhanced chromophore) is localized on bpy only in both cases. Fig 5.3.5.1 (c) shows the spectrum of $K_6\alpha$-$[P_2W_{18}O_{62}]$. The Raman spectrum is typical of Dawson polyoxometalates without resonant enhancement, with the P-O stretching mode at 1001 cm^{-1} dominating the spectrum. The W-O (terminal oxygen) stretch is observable as a shoulder at 983 cm^{-1}, and the W-O-W (bridging oxygen) stretch exhibits two bands at 938 and 875 cm^{-1}. Interestingly, Fig 5.3.5.1 (b) demonstrates that both bpy and POW modes participate in the optical transition in resonance at 488 nm. Since the POW is non-resonant at this wavelength but the metallopolymer is, the Ru signal will be orders of magnitude higher than that of the POW, and since the intensity of the POW mode at 960 cm^{-1} and is well within an order of magnitude of those of the bpy modes it may be concluded that the POW modes are resonantly enhanced under 488 nm irradiation. Importantly, the absence of other POW modes, including the most intense feature at 1001 cm^{-1} indicates that the presence of the POW features in the resonance Raman spectrum of the composite is not merely due to post resonance with POW transition. Interestingly the terminal W-O stretch shifts to lower energy upon binding to $[Ru(bpy)_2(PVP)_{10}]^{2+}$, which may be due to H-bonding with the bipyridine protons. We can conclude that since the POW itself is non-resonant at this wavelength that the new optical transition at 480 nm involves both Ru and POW ions and assign this transition to an intramolecular charge-transfer state.

5.4 – Thin film characterization:

5.4.1 – Cyclic voltammetry:

Since the resonance Raman spectra revealed the presence of a supramolecular charge-transfer transition it was decided to examine the $[Ru(bpy)_2(PVP)_{10}]_{4.5}\alpha\text{-}[P_2W_{18}O_{62}]$ composite materials for photoelectrochemical current generation. Previous photoelectrochemical studies of polyoxometalate/sensitizer combinations have generally been performed in solution, but a drive towards using thin films is crucial if the true potential of these materials is to be achieved in a practical application. Our group have already published the photoelectrochemistry of thin films of $[Ru(bpy)_2(PVP)_{10}]_{4.5}\alpha\text{-}[S_2Mo_{18}O_{62}]$.[10]

$[Ru(bpy)_2(PVP)_{10}]^{2+}$ is well known for its ability to form stable layers on metal electrode surfaces.[17] The free pyridine nitrogen atoms in the polymer backbone can adsorb quite strongly to electrode surfaces such as silver and indium-doped tin oxide (ITO).[10, 18] It has also been demonstrated that polyoxometalates can be employed in the formation of self-assembled multilayers in conjunction with large cationic polymers.[19] The primary goal of this project is to attempt to optimize the photoelectrochemical properties of some of these interfacial films. Therefore a detailed understanding of the surface redox processes and surface coverage of the films is crucial in quantifying the efficiency of photocurrent generation. The thin film cyclic voltammetry of films of $[Ru(bpy)_2(PVP)_{10}]^{2+}$, $\alpha\text{-}[P_2W_{18}O_{62}]^{6-}$ and one “bilayer” (ie: one LBL deposition cycle of both materials) of $[Ru(bpy)_2(PVP)_{10}]_{4.5}[P_2W_{18}O_{62}]$ on ITO working electrodes are shown in Figs 5.4.1.1 – 5.4.1.4.

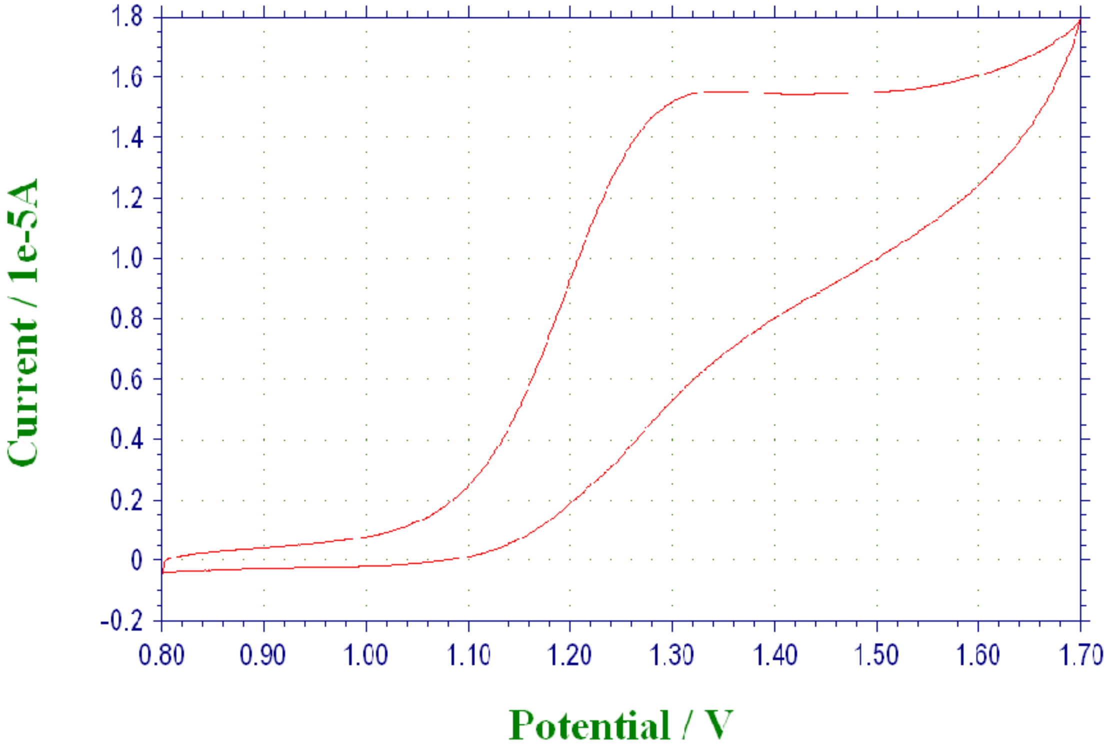

Fig 5.4.1.1: Cyclic voltammogram of self-assembled film of $[Ru(bpy)_2(PVP)_{10}]^{2+}$ on an ITO working electrode. The supporting electrolyte was 0.1 M $(But)_4NBF_4$ in MeCN; scan rate was 10 $mV.s^{-1}$. Reference electrode was an Ag wire (+ 400 mV vs Fc/Fc^+).

The CV of a film of $[Ru(bpy)_2(PVP)_{10}]^{2+}$ alone is presented in Fig 5.4.1.1. It reveals atypical redox behaviour for a Ru polypyridyl complex. A single redox process is observed at + 1.2 V which is attributed to the Ru^{2+}/Ru^{3+} redox couple, but the couple does not appear to be completely reversible at this scan rate. The sigmoidal shape of the voltammogram resembles that of a species adsorbed on a microelectrode, and may indicate low surface coverage of the film in the form of islands of material. Otherwise it may be that the rate of oxidation is much greater than the corresponding rate of reduction; however this is less likely at 10 $mV.s^{-1}$. Either way this shape is unusual given the well behaved voltammetric behaviour of $[Ru(bpy)_2(PVP)_{10}]^{2+}$ adsorbed on surfaces such as gold.[20] The absence of a shoulder on the negative side of the oxidation peak indicates that the purity of the Ru polymer is at least 90% (ie: only one type of Ru center is present, and synthesis of the N_6 coordinated metallopolymer rather than the corresponding N_5Cl has been primarily achieved). This indicates that deposition of $[Ru(bpy)_2(PVP)_{10}]^{2+}$ from a concentrated MeCN/EtOH solution onto ITO followed by extensive cycling in 0.1 M $(But)_4NBF_4$ does not affect film stability. The ease and reproducibility of film preparation, coupled with the stability of the film itself, demonstrate the usefulness of Ru metallopolymers over their corresponding monomers in thin film research.

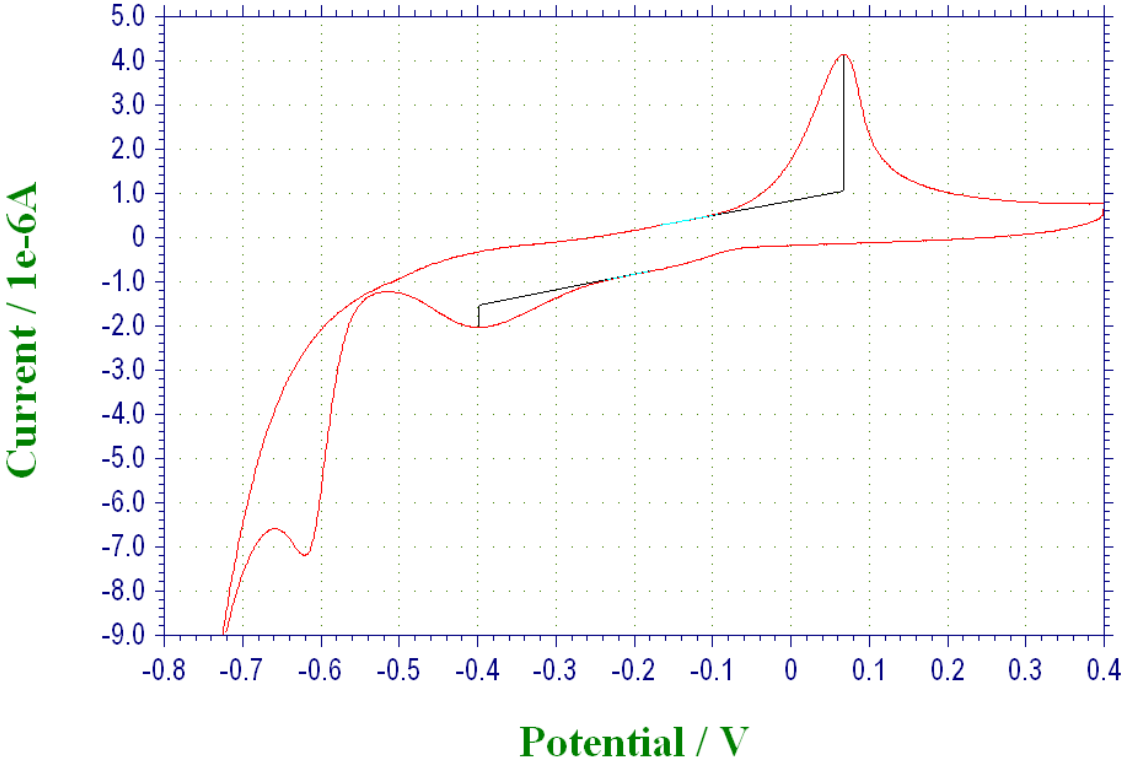

Fig 5.4.1.2: Cyclic voltammogram of self-assembled film of α-$[P_2W_{18}O_{62}]^{6-}$ on an ITO working electrode. Supporting electrolyte was 0.1 M $(But)_4NBF_4$ in MeCN; scan rate was 10 mV.s^{-1}. Reference electrode was an Ag wire (+ 400 mV vs Fc/Fc$^+$).

For comparison, ITO electrodes were dipped into concentrated aqueous solutions of K_6α-$[P_2W_{18}O_{62}]$. Polyoxotungstates are not known for their ability to form stable layers on electrodes by themselves, and are often electrostatically attached to surfaces that have been modified to carry a positive charge, such as glassy carbon surfaces modified with 4-aminobenzoic acid.[24] In the case of $[Ru(bpy)_2(PVP)_{10}]^{2+}$ the free pyridyl nitrogens are coordinating ligands which can bind to the surface, driving film formation. However in the case of α-$[P_2W_{18}O_{62}]^{6-}$ the film forms as it dries to the surface and is likely only bonded via very weak Van der Waals forces. In fact, the surface of ITO is covered in polar oxo and hydroxyl functional groups, which are likely to repel the anionic POW molecules.[21] Fig 5.4.1.2 demonstrates that the amount of α-$[P_2W_{18}O_{62}]^{6-}$ deposited on ITO by dip-coating is relatively small, compared with the $[Ru(bpy)_2(PVP)_{10}]^{2+}$. The redox processes of α-

$[P_2W_{18}O_{62}]^{6-}$ are also greatly affected by adhering to the surface, as demonstrated by the significant changes in voltammetry relative to that of the molecule in solution (see Fig 5.2.1.1). The reason for this change is unknown but may be due to weak interactions between POW and the surface. The solution phase voltammetry was also performed in the presence of acid, which has been reported to alter the redox chemistry of Dawson polyoxotungstates.[22]

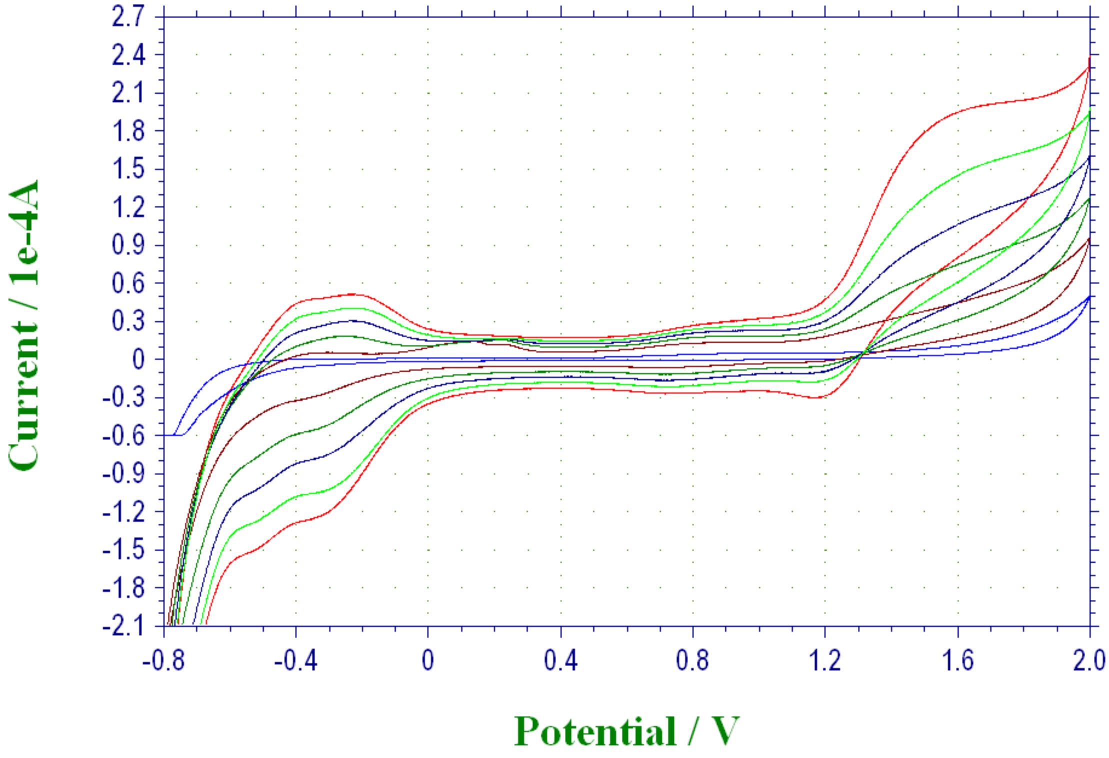

Fig 5.4.1.3: Cyclic voltammogram of self-assembled "bilayer" film on an ITO working electrode, unstable in MeCN containing 0.1 M $(But)_4NBF_4$; scan rates from most intense 500, 400, 300, 200, 100 and 10 mV.s^{-1}. Reference electrode was an Ag wire (+ 400 mV vs Fc/Fc$^+$).

Fig 5.4.1.3 shows the voltammetry of one "bilayer" of $[Ru(bpy)_2(PVP)_{10}]_{4.5}[P_2W_{18}O_{62}]$ self-assembled on an ITO working electrode when MeCN containing 0.1 M $(But)_4NBF_4$ is used as the supporting electrolyte. The film was formed by assembling a layer of $[Ru(bpy)_2(PVP)_{10}]^{2+}$ on ITO via free pyridyl N atoms adsorbing strongly to the surface, followed by electrostatic adsorption of a α-$[P_2W_{18}O_{62}]^{6-}$ layer to the $[Ru(bpy)_2(PVP)_{10}]^{2+}$. Although this electrolyte system was perfectly adequate for obtaining voltammetry for films of both $[Ru(bpy)_2(PVP)_{10}]^{2+}$ and α-$[P_2W_{18}O_{62}]^{6-}$ alone, as well as for films of $[Ru(bpy)_2(PVP)_{10}]_{4.5}[S_2Mo_{18}O_{62}]$,[10] the composite film was unstable under these conditions. With each voltammetric sweep more material was lost off the surface until little or no electroactive material was in contact with the ITO surface. The reason for this is attributed to disruption of the electrostatics via competitive electrolyte binding. The loss of the polyoxotungstate was accompanied by a loss in Ru, which is somewhat surprising since the Ru film was demonstrated to be stable under these voltammetric conditions (see Fig 5.4.1.1). Both ions are therefore likely to be removed from the surface as electrostatic clusters, which indicate the strength of this association.

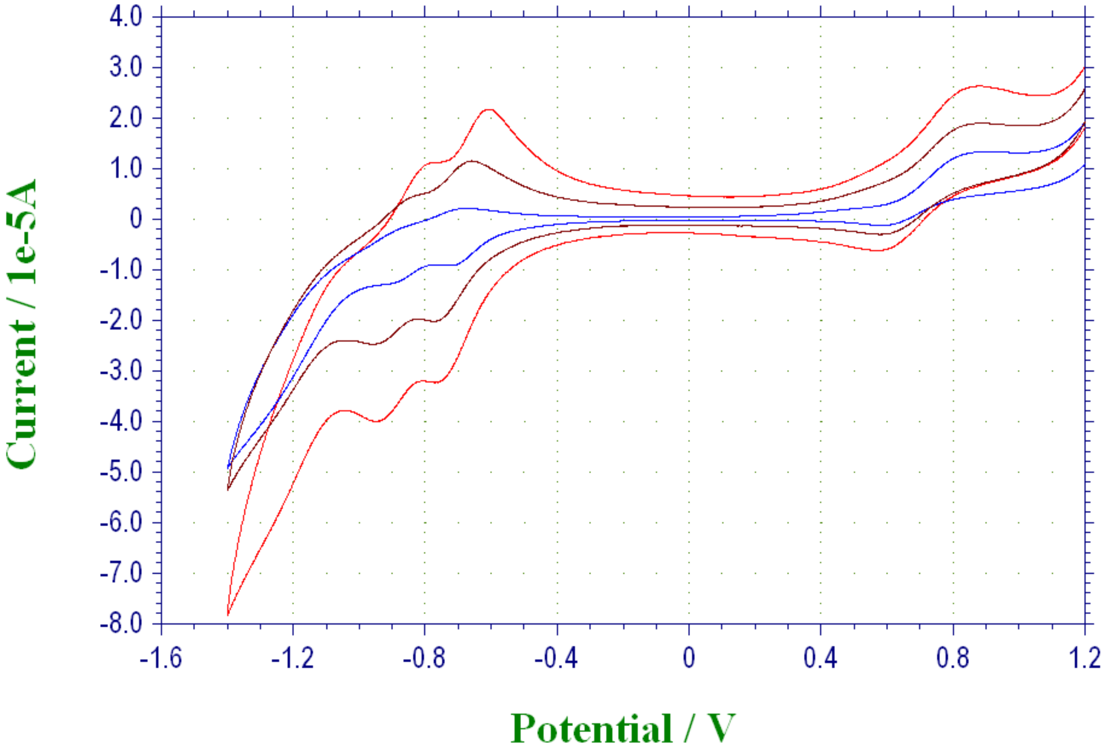

Fig 5.4.1.4: Cyclic voltammogram of self-assembled "bilayer" film on ITO, stable in BnOH containing 0.1 M $(But)_4NBF_4$; scan rates from largest peak currents: 100, 50 and 10 mV.s^{-1}. Reference electrode was an Ag wire (+ 400 mV vs Fc/Fc$^+$).

Fig 5.4.1.4 demonstrates that the self-assembled film of $[Ru(bpy)_2(PVP)_{10}]_{4.5}[P_2W_{18}O_{62}]$ is stable to voltammetric cycling in 0.1 M $(But)_4NBF_4$ in BnOH at a variety of different scan rates. Using the different peak currents obtained at different scan rates, the charge-transfer diffusion coefficient of the film can be calculated. The surface coverage of each species can also be calculated from the charge passed at slow scan rates using Equation 7:

$$\Gamma = \frac{Q}{nFA} \qquad (7)$$

Where Γ is the surface coverage of redox active species ($mol.cm^{-2}$), Q is the charge passed (in Coulombs), n is the number of electrons transferred (in this case 1), F is Faraday's constant (charge per mole of electrons, 96485 $C.mol^{-1}$) and A is the working electrode area (cm^2). In the case of both $[Ru(bpy)_2(PVP)_{10}]^{2+}$ and α-$[P_2W_{18}O_{62}]^{6-}$ MeCN (0.1 M $(But)_4NBF_4$) was used as the supporting electrolyte, whereas in the bilayer case the electrolyte was BnOH (0.1 M $(But)_4NBF_4$). The surface coverages are given in Table 5.4.1.

Film	**Γ ($mol.cm^{-2}$)**
$[Ru(bpy)_2(PVP)_{10}]^{2+}$	$(9.83 \pm 3.38) \times 10^{-10}$
α-$[P_2W_{18}O_{62}]^{6-}$	$(1.66 \pm 0.77) \times 10^{-12}$
$[Ru(bpy)_2(PVP)_{10}]_{4.5}[P_2W_{18}O_{62}]$ Ru	$(6.11 \pm 0.32) \times 10^{-10}$
$[Ru(bpy)_2(PVP)_{10}]_{4.5}[P_2W_{18}O_{62}]$ POW	$(1.44 \pm 0.39) \times 10^{-10}$

Table 5.4.1: Surface coverage calculated from cyclic voltammetric data ($10mV.s^{-1}$) of self-assembled thin films of $[Ru(bpy)_2(PVP)_{10}]^{2+}$, α-$[P_2W_{18}O_{62}]^{6-}$ and $[Ru(bpy)_2(PVP)_{10}]_{4.5}[P_2W_{18}O_{62}]$ on ITO electrodes.

The data in Table 5.4.1 shows that both the $[Ru(bpy)_2(PVP)_{10}]^{2+}$ and $[Ru(bpy)_2(PVP)_{10}]_{4.5}[P_2W_{18}O_{62}]$ thin films displayed relatively low surface coverage, of the order of 10^{-10} $mol.cm^{-2}$. These numbers correspond to several monolayers of material. The polyoxotungstate surface coverage is extremely low (10^{-12} $moles.cm^{-2}$), and is indicative of sub-monolayer coverage. This is not surprising as the nature of POW-ITO binding is likely to be only physisorption or weak chemisorption.

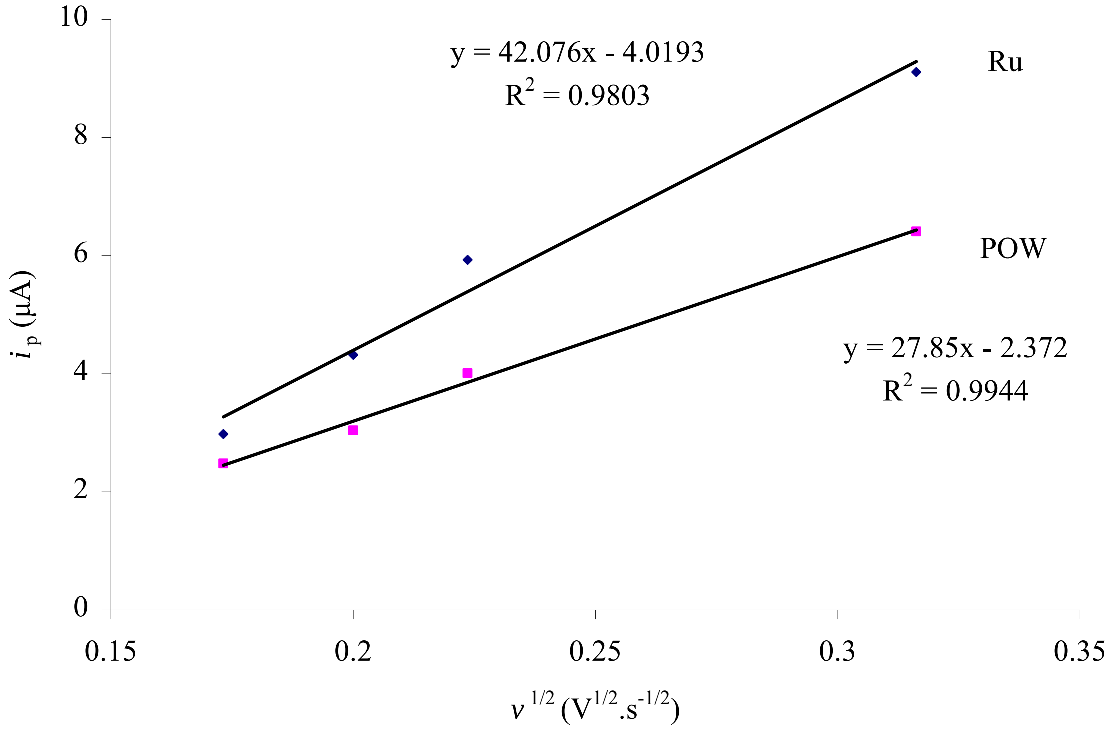

Fig 5.4.1.5: Scan rate dependence of cyclic voltammograms of self-assembled “bilayer” film on ITO (shown in Fig 5.4.1.4), stable in BnOH containing 0.1 M $(But)_4NBF_4$. Reference electrode was an Ag wire (+ 400 mV vs Fc/Fc^+).

The scan rate dependence of the film is presented in Fig 5.4.1.5. The peak current of a redox process plotted versus the square root of scan rate ($v^{1/2}$) gives the value for the D_{CT} of the film. D_{CT} is a measure of how fast an electron or ion can diffuse through a film and can be calculated using the Randles-Sevçik equation (Equation 8).

$$i_p = (2.69x10^5)n^{3/2}.A.D_{CT}{}^{1/2}.C_i.v^{1/2} \qquad (8)$$

Where i_p is the peak current (Amps), n is the number of electrons transferred in the redox process, A is the geometric electrode area (cm^2), D_{CT} is the diffusion coefficient ($cm^2.s^{-1}$), C_i is the bulk concentration of redox species ($mol.cm^{-3}$) and v is the scan rate ($V.s^{-1}$). If the area of the electrode is accurately measured and the film thickness measured then C can be calculated and hence D_{CT}. Using the slope for the Ru oxidation in Fig 5.4.1.5, D_{CT} can be calculated from the Γ value in Table

5.4.1. In the case of $[Ru(bpy)_2(PVP)_{10}]_{4.5}[S_2Mo_{18}O_{62}]$ the mean layer thickness was measured by AFM to be approximately 200 nm. Assuming the same film thickness of 200 nm for the $[Ru(bpy)_2(PVP)_{10}]_{4.5}[P_2W_{18}O_{62}]$ films, the concentration of Ru in the composite film was calculated as 0.03 M, which yielded a D_{CT} value of (2.62 ± 0.10) x 10^{-11} $cm^2.s^{-1}$. This was a factor of two larger than that reported for a film of $[Ru(bpy)_2(PVP)_{10}]_{4.5}[S_2Mo_{18}O_{62}]$.[7] The value obtained for D_{CT} was assessed using the following equations:

$$\tau = \frac{RT}{Fv} \qquad (9)$$

$$\delta = \sqrt{D_{CT}.\tau} \qquad (10)$$

Where v is the scan rate ($V.s^{-1}$), τ is the experimental timescale (s) and δ is the depletion layer thickness. Using our D_{CT} value of 2.62 x 10^{-11} $cm^2.s^{-1}$ and scan rates of 10 $mV.s^{-1}$ and 100 $mV.s^{-1}$ (the lowest and highest scan rates used in measurements of D_{CT} and Γ), values of τ obtained were 2.57 s and 0.26 s respectively. Insertion of these values into Equation 10 yielded a depletion layer thickness between 26 and 82 nm. It is highly desirable that the value of δ is less than half the film thickness and these numbers therefore appear to confirm that the value obtained for D_{CT} in this case is a reasonable one.

5.4.2 – Photoelectrochemistry:

The photocurrent generation ability of the films was examined using 480 ± 5 nm irradiation from a Hg/Xe arc lamp. The prepared films were immersed in a solution of pure BnOH containing 0.1 M $(But)_4NBF_4$ electrolyte, as this electrolyte system was shown previously to not adversely affect layer stability. Some selected photocurrents are shown below.

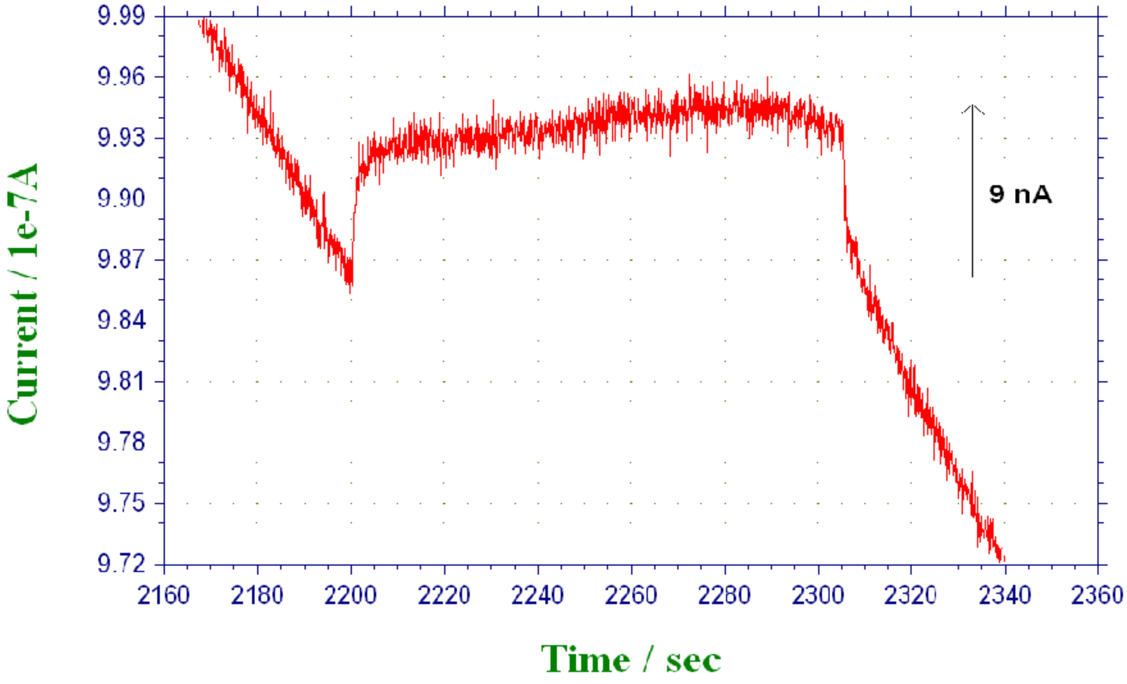

Fig 5.4.2.1: Photocurrent generated by blank ITO in pure BnOH containing 0.1 M $(But)_4NBF_4$ electrolyte at 0.5 V under 480 nm irradiation.

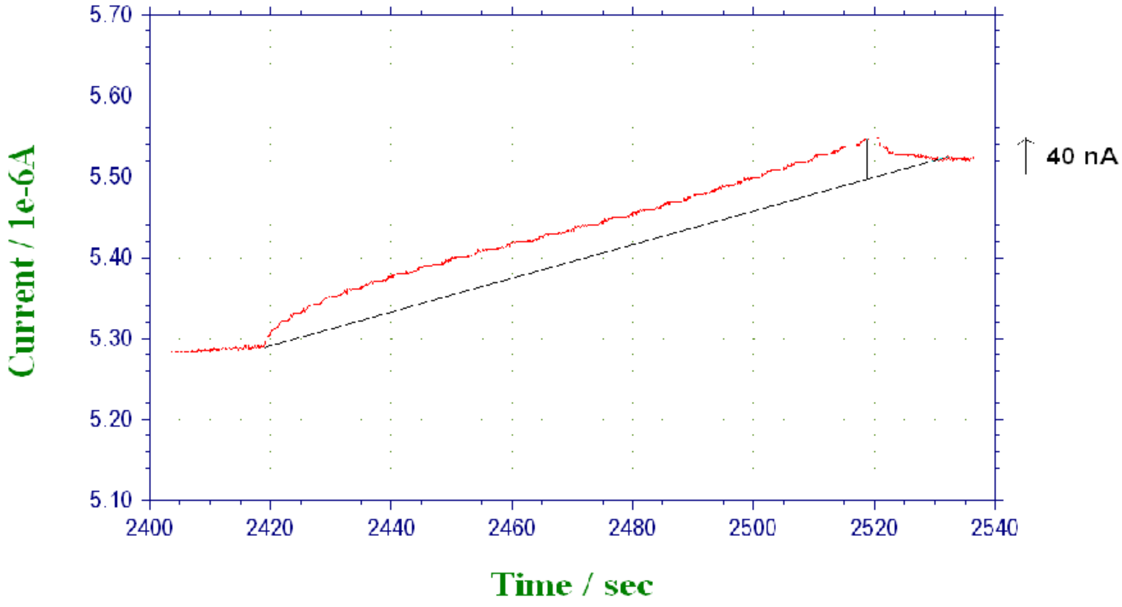

Fig 5.4.2.2: Photocurrent generated by $[Ru(bpy)_2(PVP)_{10}]^{2+}$ in pure BnOH containing 0.1 M $(But)_4NBF_4$ electrolyte at 0.6 V under 480 nm irradiation.

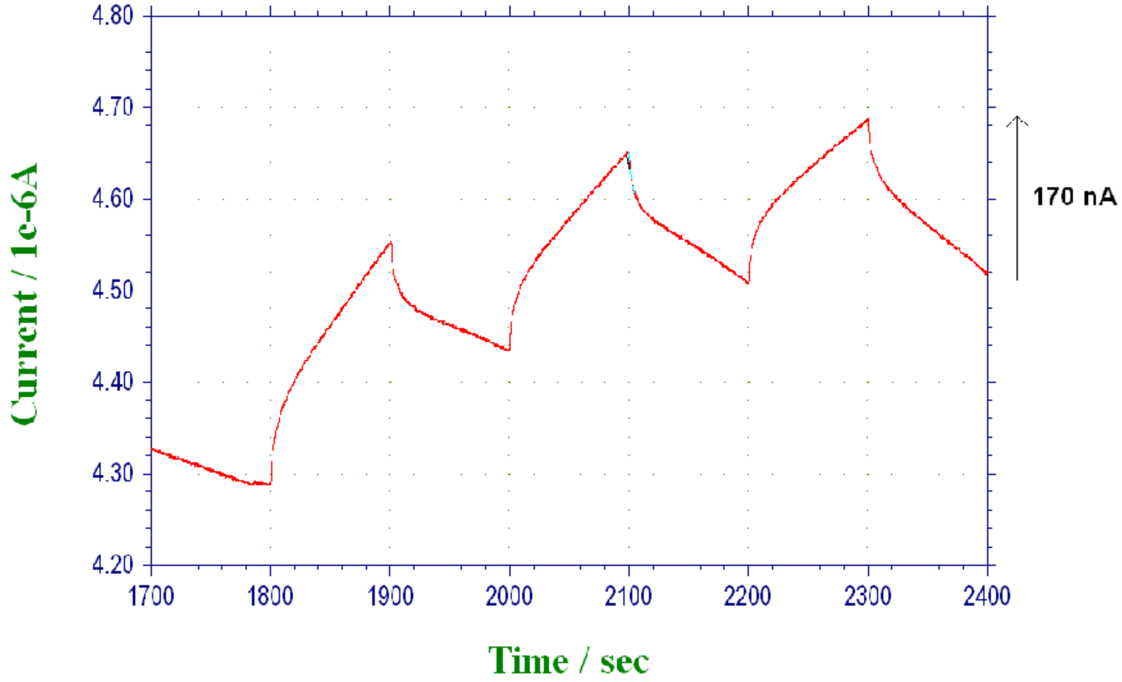

Fig 5.4.2.3: Photocurrent generated by one "bilayer" of $[Ru(bpy)_2(PVP)_{10}]^{2+}/[P_2W_{18}O_{62}]^{6-}$ dip-coated onto an ITO working electrode in pure BnOH containing 0.1 M $(But)_4NBF_4$ electrolyte. Potential held at + 0.7 V, irradiation at 480 nm.

The photocurrents shown in Figs 5.4.2.1 – 5.4.2.3 show that a clear pattern emerges in the data. The blank ITO and α-$[P_2W_{18}O_{62}]^{6-}$ alone generate tiny currents, of the order of 10 nA. This is due to the almost negligible spectral absorptivity of these materials at 480 nm. The Ru metallopolymer alone does generate a current under these conditions and has been examined in the past as a photocatalyst by itself. In fact, $[Ru(bpy)_2(PVP)_5]^{2+}$ coated on TiO_2 was shown previously to generate a photocurrent of 45 nA under 450 nm irradiation (ie: non-incident with TiO2 absorption);[23] and although the surface coverage was far higher in that case (~10^{-7} mol.cm^{-2}) the photocurrent generated here under similar conditions is of comparable magnitude. The data in Fig 5.4.2.3 clearly show that there is a substantial increase in photocurrent generated when the composite film is employed, as the current increase from 40 nA.cm^{-2} to 170 nA.cm^{-2}. In addition, the surface coverage of Ru^{2+} centers in the composite film is actually 30 % lower than for the film comprised of $[Ru(bpy)_2(PVP)_{10}]^{2+}$ alone.

A potential dependence study was performed to optimize the driving force for this process. The data are presented in Fig 5.4.2.4.

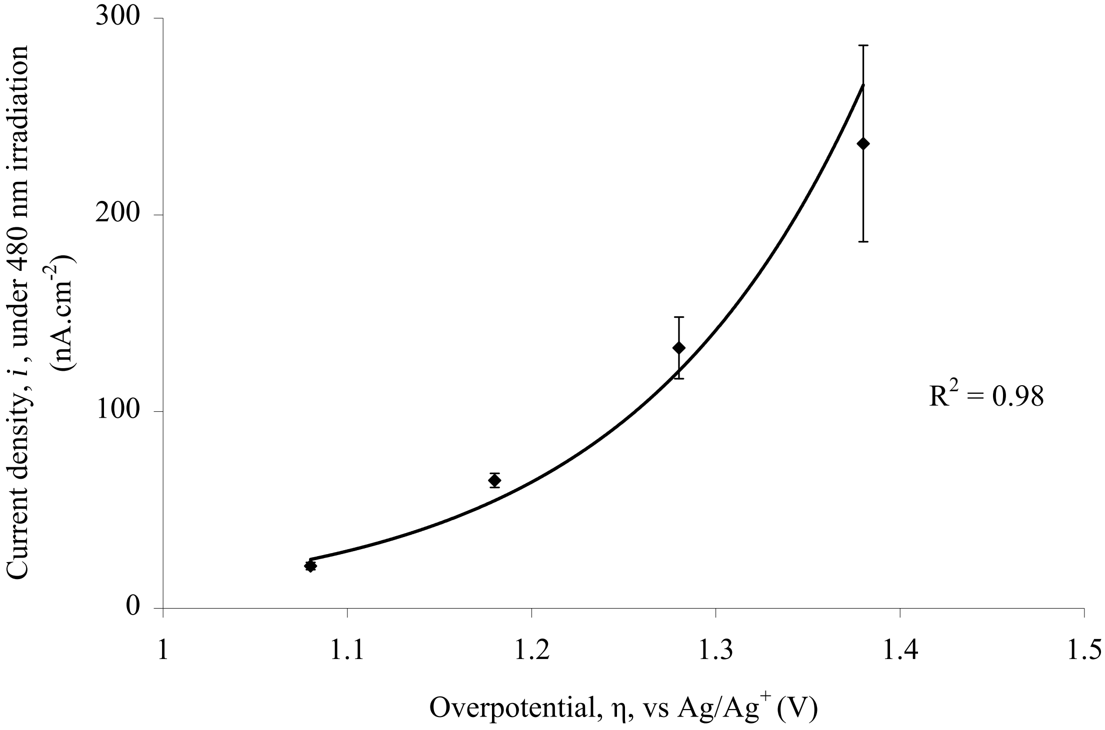

Fig 5.4.2.4: Plot of photocurrent generation versus applied overpotential of one "bilayer" of $[Ru(bpy)_2(PVP)_{10}]^{2+}/[P_2W_{18}O_{62}]^{6-}$ dip-coated onto an ITO working electrode, fitted to an exponential model.

The overpotential, η, was calculated as the difference between the experimental applied potential and the formal E_0 value of the first polyoxotungstate (electron acceptor) reduction. It is clear that the data follows an exponential trend, and the log plot of the data can be used to calculate the transfer coefficient of the potential energy barrier, α, using the Equation 11.

$$\log\frac{i}{1-e^{nf\eta}} = \log i_0 - \frac{\alpha nF\eta}{2.3RT} \qquad (11)$$

Where α is a measure of the symmetry of the potential energy barrier for the photoreductive process, and *i* is the current density (Amps) and i_0 is the current density at E_0 (for first tungstate reduction). When α is greater then 0.5, then the activation energy for the reduction process is decreased while the activation energy for the oxidation process is increased. The plot in Fig 5.4.2.5 was used to calculate α and i_0 and is shown below.

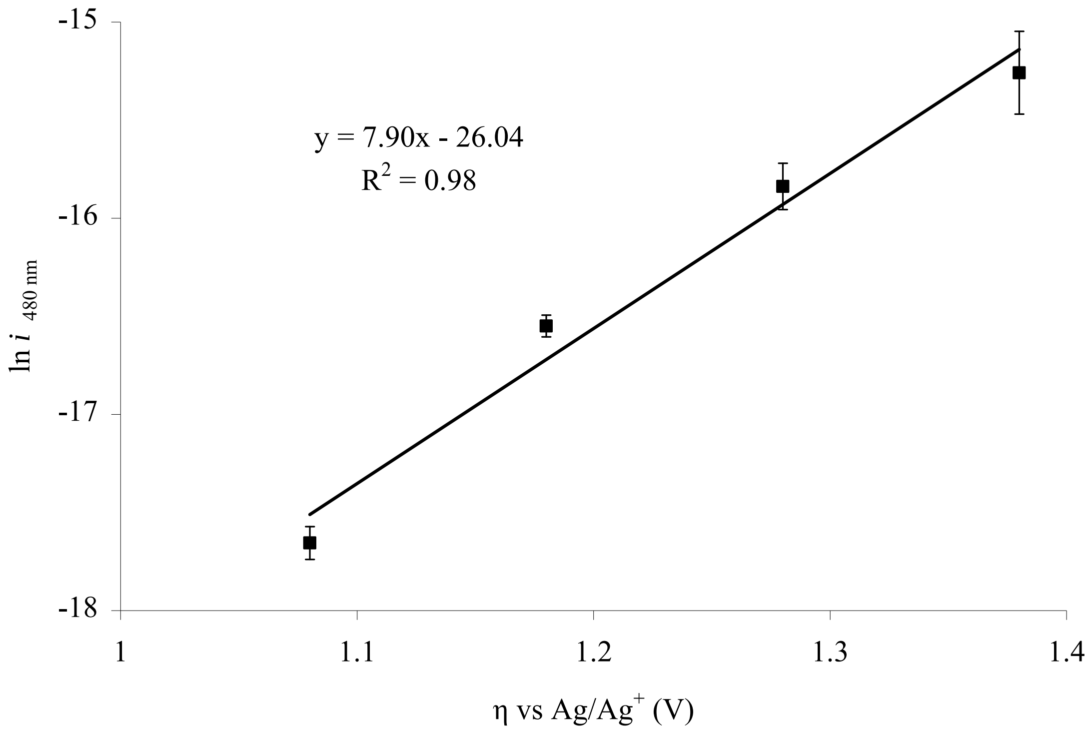

Fig 5.4.2.5: Tafel plot of the photocurrent data in Fig 5.4.2.4.

According to Equation 11 the value for α is approximately 0.52, indicating that the polyoxometalate redox process is highly reversible. This is reflected in the shape of the CVs in Fig 5.4.1.4. The value for i_0, the current generated at equilibrium (POW E_0) was determined to be 0.36 nA. This kind of behaviour was not observed by Jie Zhu in the case of $[Ru(bpy)_3]_2[S_2W_{18}O_{62}]$, where a higher α value of 0.92 was obtained.[1] In this case the value of α simply indicates that the photocatalytic reaction under investigation is fully reversible and therefore reoxidizing the reduced POW molecules to close the catalytic cycle is unlikely to be a determining factor in the rate of photocurrent generation. Indeed, the value of D_{CT} for a film hundreds of nm thick is likely to be a limiting factor in current generating efficiency.[1]

5.4.3 – Electron microscopy and EDX spectroscopy:

The data obtained in Chapter 4 and detailed studies performed by our group strongly suggest that film morphology and thickness are critical in determining photocurrent generating efficiency for self-assembled films of $[Ru(bpy)_2(PVP)_{10}]^{2+}$ and α-$[Mo_{18}O_{54}(SO_4)_2]^{4-}$. Assuming the morphology of the films comprised of $[Ru(bpy)_2(PVP)_{10}]^{2+}$ and α-$[P_2W_{18}O_{62}]^{6-}$, also influence photoelectrochemical performance through parameters such as ion transport, the microscopy of the films has been investigated.

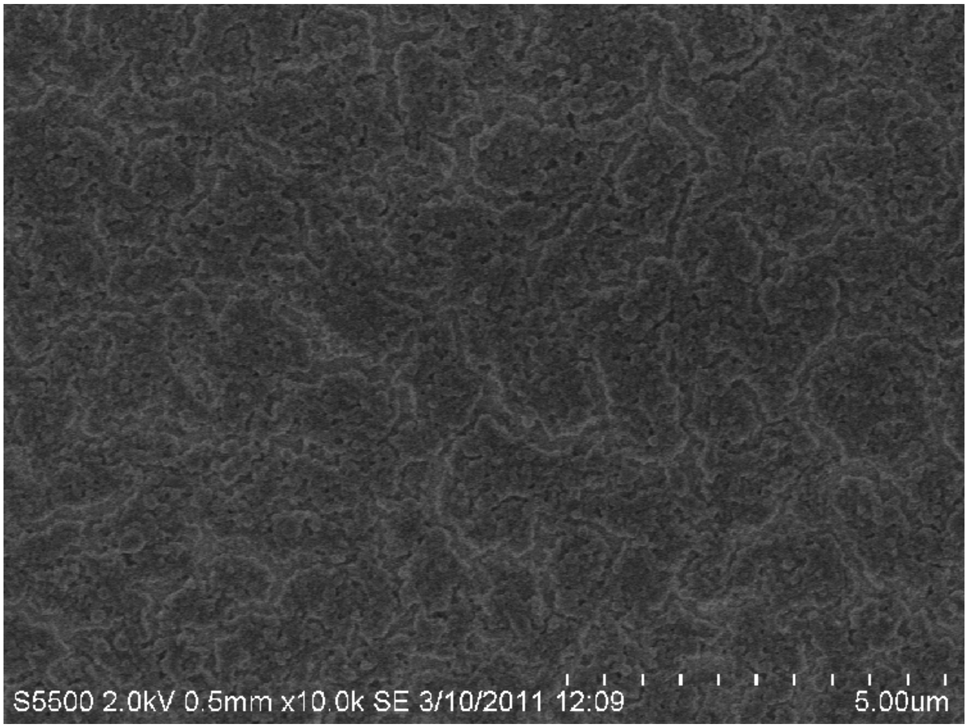

Fig 5.4.3.1: FeSEM image of $[Ru(bpy)_2(PVP)_{10}]^{2+}$ thin film self-assembled on ITO. Scale: 500 nm/division.

Firstly the feSEM of the thin films of $[Ru(bpy)_2(PVP)_{10}]^{2+}$ was recorded. Ru based metallopolymers with free pyridine groups in the polymer backbone are well known to form stable films on most electrode surfaces, as the disordered and flexible polyvinylpyridine chain bonds directly to the surface via a series of pyridyl nitrogen-substrate coordination bonds.[10, 20] As expected, Fig 5.4.3.1 shows a relatively homogenous film that is fairly densely packed. It was difficult to get an image of greater magnification image of the film due to its high organic content, but it was apparent that the film had cracks in it of the order of 100 – 500 nm across. These cracks likely formed during the drying process.

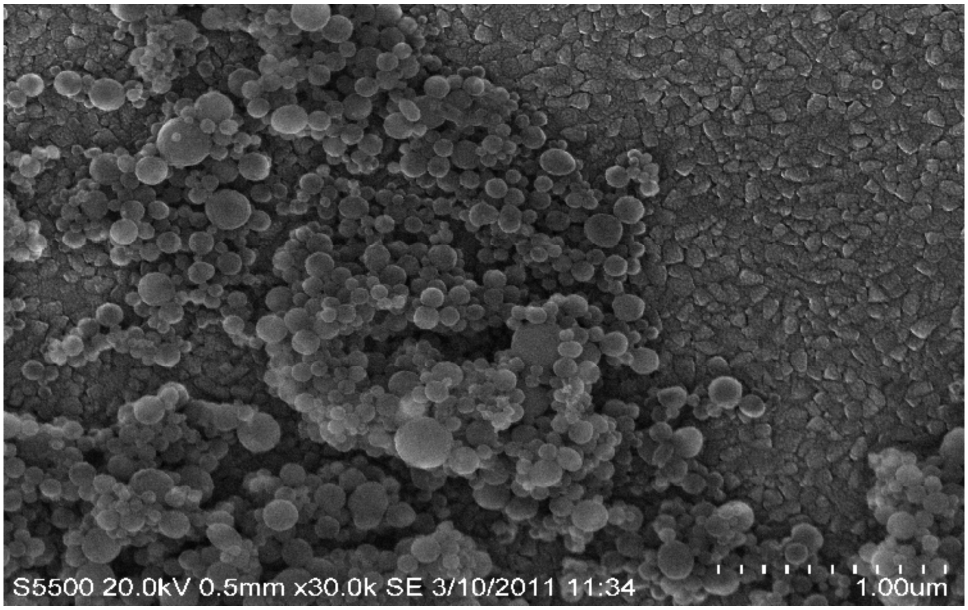

Fig 5.4.3.2: FeSEM image of α-$[P_2W_{18}O_{62}]^{6-}$ thin film self-assembled on ITO. Scale: 100 nm/division.

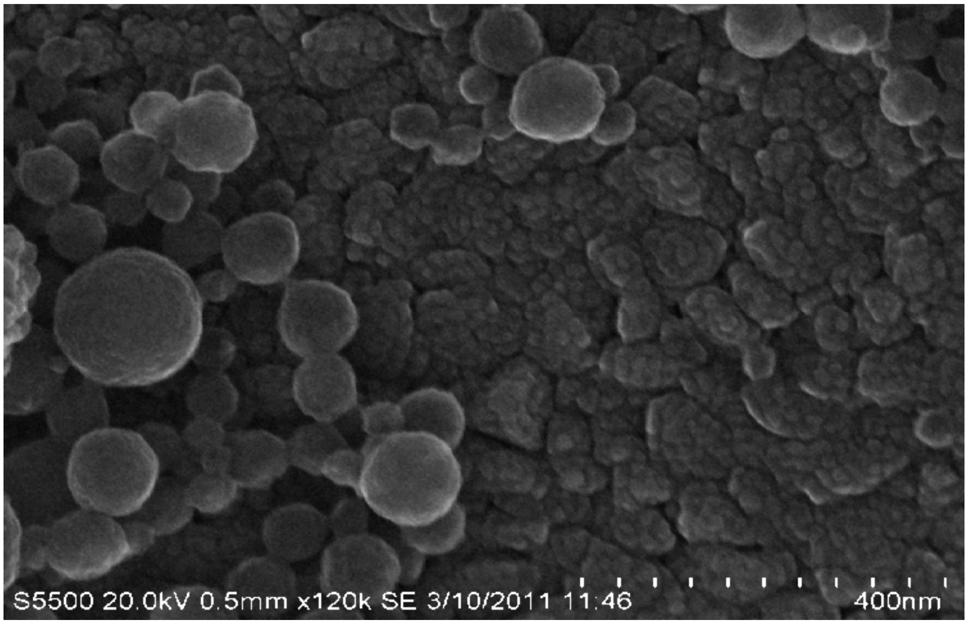

Fig 5.4.3.3: FeSEM image of α-$[P_2W_{18}O_{62}]^{6-}$ thin film self-assembled on ITO. Scale: 40 nm/division.

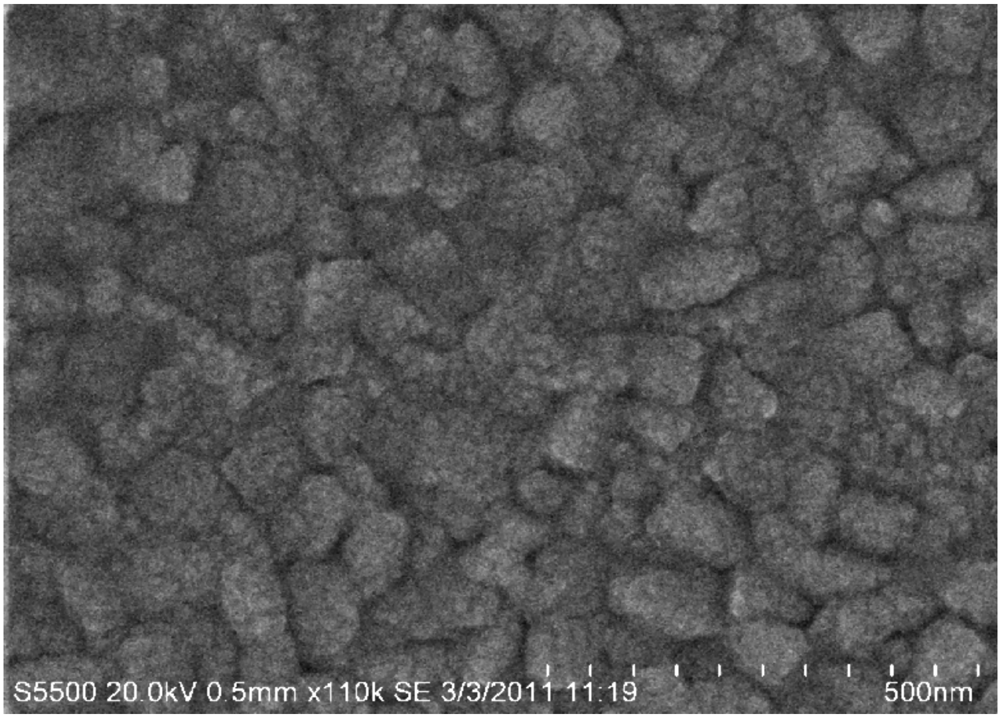

Fig 5.4.3.4: FeSEM image of a clean, unmodified ITO electrode. Scale: 50 nm/division.

The two Figs 5.4.3.2 and 5.4.3.3 show the self-assembled film of $K_6\alpha$-$[P_2W_{18}O_{62}]$ on an ITO surface at different magnifications. Fig 5.4.3.2 revealed that the polyoxotungstate did not form a densely packed monolayer on ITO. Homogeneous surface adsorption is not favoured in this case as covalent bond formation is not a driving force for assembly; in fact the POW is likely only held to the surface via weak Van der Waals forces. The rough ITO substrate can clearly be seen on the right hand side of both images, and a blank ITO electrode is also shown in Fig 5.4.3.4 for comparison. The POW molecules cluster together in sub-micron sized spheres, which in turn clump together to form islands of material on the electrode surface. These spheres are roughly 100 nm to 300 nm in diameter. The patchy self-assembled film of α-$[P_2W_{18}O_{62}]^{6-}$ as revealed by feSEM is consistent with the low surface coverages obtained in electrochemical studies of these films.

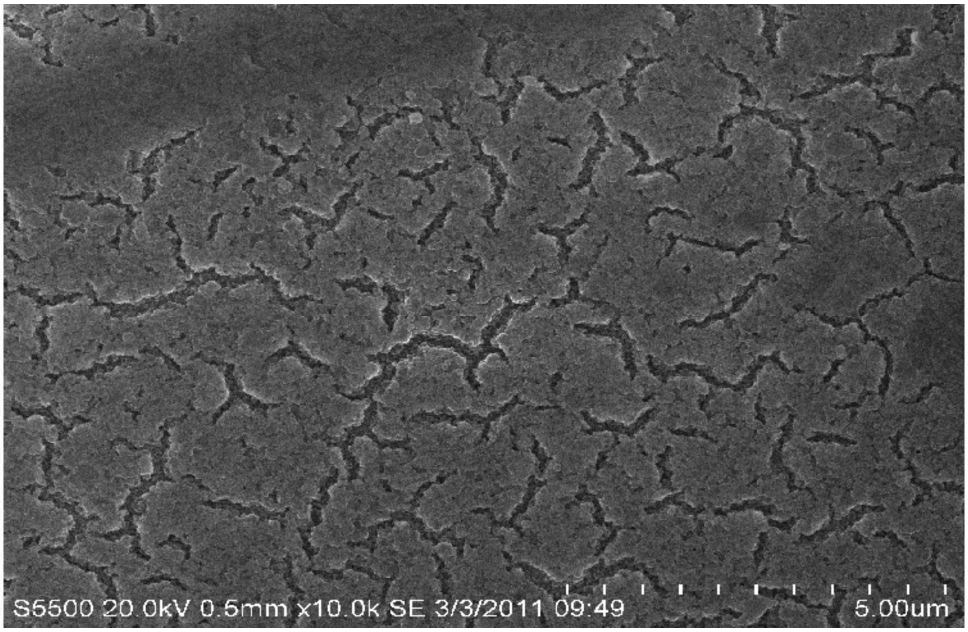

Fig 5.4.3.5: FeSEM image of $[Ru(bpy)_2(PVP)_{10}]_{4.5}\alpha\text{-}[P_2W_{18}O_{62}]$ thin film self-assembled on ITO. Scale: 500 nm/division.

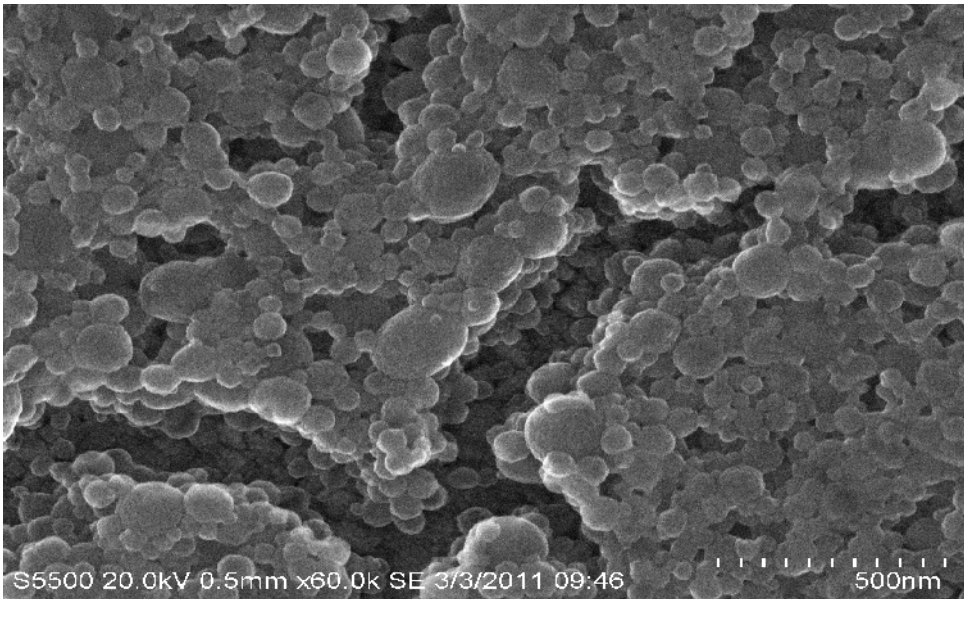

Fig 5.4.3.6: FeSEM image of $[Ru(bpy)_2(PVP)_{10}]_{4.5}\alpha\text{-}[P_2W_{18}O_{62}]$ thin film self-assembled on ITO. Scale: 50 nm/division.

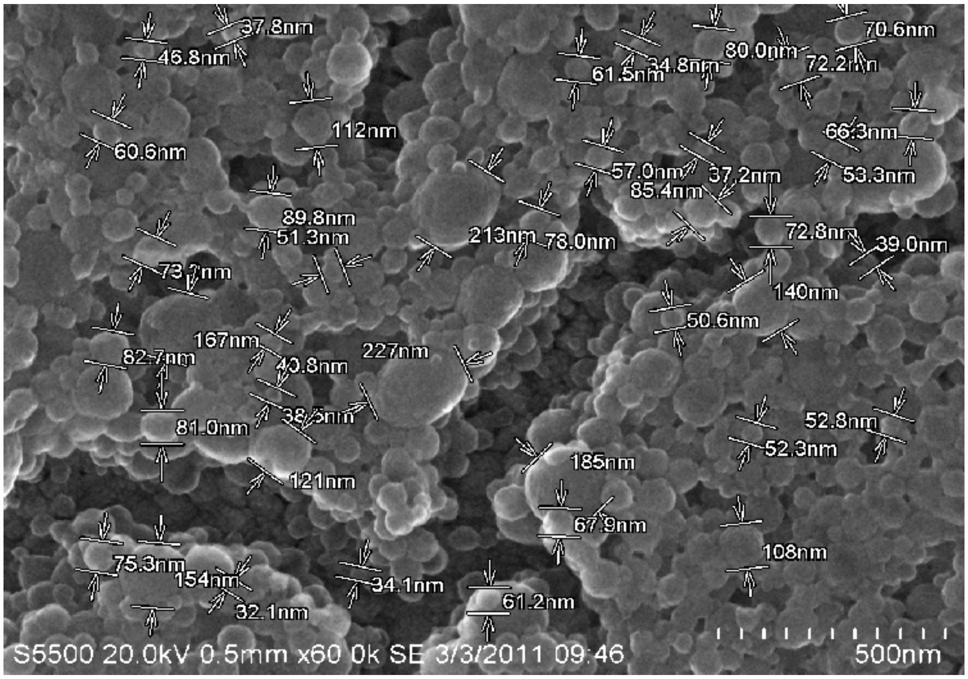

Fig 5.4.3.7: FeSEM image of $[Ru(bpy)_2(PVP)_{10}]_{4.5}\alpha\text{-}[P_2W_{18}O_{62}]$ thin film self-assembled on ITO. Scale: 50 nm/division.

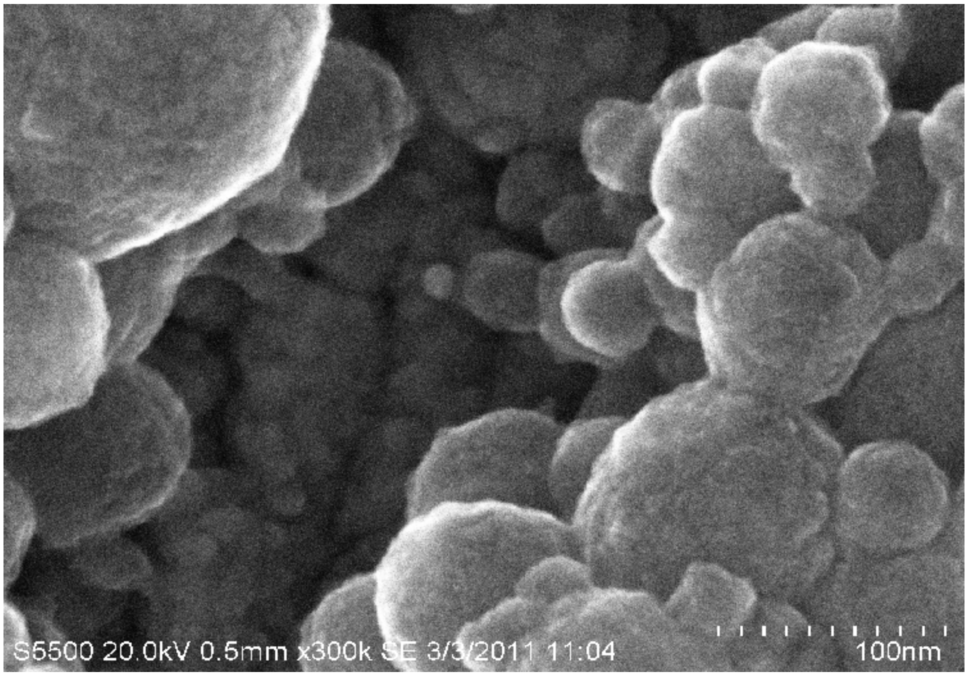

Fig 5.4.3.8: FeSEM image of $[Ru(bpy)_2(PVP)_{10}]_{4.5}\alpha\text{-}[P_2W_{18}O_{62}]$ thin film self-assembled on ITO. Scale: 10 nm/division.

Figs 5.4.3.5 to 5.4.3.8 show the feSEM images of a composite self-assembled film of $[Ru(bpy)_2(PVP)_{10}]^{2+}$ and α-$[P_2W_{18}O_{62}]^{6-}$ at different magnifications. The differences between this film and the two parent ion films are striking. The associated ion-clusters seem to form spherical clumps upon association, reminiscent of the structures formed by the α-$[P_2W_{18}O_{62}]^{6-}$ alone. The sphere surfaces were themselves rough and were on the 5 nm scale, which is approaching the resolution of the instrument. These spheres fell roughly into three size categories. Using the crude graphical integration in Fig 5.4.3.6 the three particle sizes were estimated to be 45 ± 8, 74 ± 9 and 161 ± 41 nm. Whether or not these numbers represent meaningful properties of the clusters on the nanoscale is unclear; however it is clear that the clusters in Fig 5.4.3.6 are smaller than those in Fig 5.4.3.2. Their smaller size is therefore likely a consequence of ion-cluster formation.

The composite film was probed by EDX spectroscopy to assess the ratio of $[Ru(bpy)_2(PVP)_{10}]^{2+}$ to α-$[P_2W_{18}O_{62}]^{6-}$ in the film. EDX spectroscopy is a very useful tool for obtaining quantitative elemental analyses of thin films. Exact quantitation can be difficult, particularly with lighter elements, but in this case only a relative ratio (Ru:W) was required. The absolute numbers provided below for all elements are not quantitatively accurate and should not be treated as such; however the relative ratio of Ru:W is very accurate. The EDX spectra were acquired over a large area in Fig 5.4.3.4 to avoid burning of the film. The numerical data provided is an average of 3 independent spectral acquisitions.

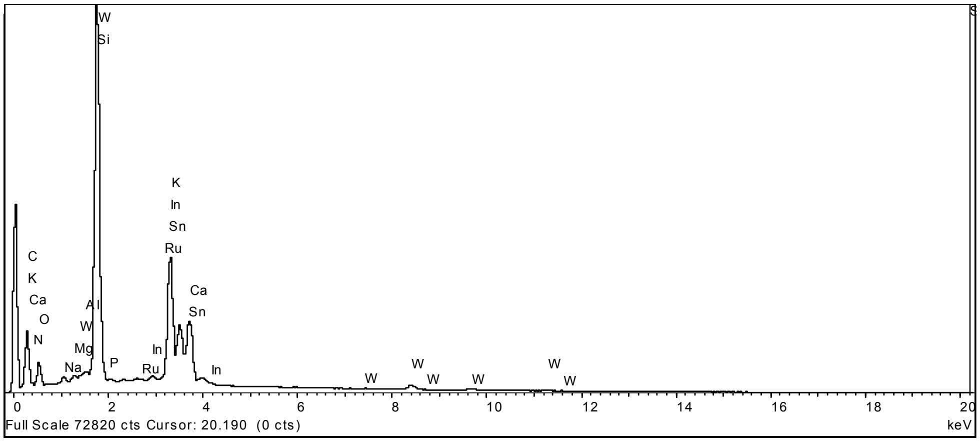

Element	**C**	**N**	**O**	**Na**	**Mg**	**Al**	**Si**	**P**	**S**	**K**	**Ca**	**Ru**	**In**	**Sn**	**W**
Mean	56.76	8.02	19.16	0.43	0.24	0.15	10.06	0.04	0.06	0.29	1.29	0.053	2.79	0.17	0.473

Fig 5.4.3.8: EDX spectrum of self-assembled film of $[Ru(bpy)_2(PVP)_{10}]^{2+}$ and α-$[P_2W_{18}O_{62}]^{6-}$. Values in table are mean atomic percentages and were calculated as an average of 3 spectra.

The results obtained in Fig 5.4.3.8 were somewhat surprising. Firstly the presence of magnesium and aluminium peaks were attributed to trace quantities in the underlying glass. The sodium was a trace impurity from the synthesis of the polyoxotungstate (starting material was sodium tungstate). The calcium, indium, tin and silicon are present in the EDX spectrum of blank ITO. Most importantly, the average Ru:W atomic ratio was 0.053:0.473. This is exactly a ratio of 2 Ru per 17.8 W atoms, or 2 Ru centers per polyoxotungstate molecule (W_{18}). This ratio is surprising for three reasons. Firstly, the UV/Vis and emission spectroscopy, as well as electrochemistry, appeared to indicate a favoured 4.5:1 ratio for this cluster in solution; secondly the metallopolymer formed 4.5:1 ratios with the isostructural polyoxomolybdate α-$[Mo_{18}O_{54}(SO_4)_2]^{4-}$ and thirdly a 2:1 ratio would not be expected to result in ion-cluster neutrality. The reason for this difference is unknown. It may be that more than one ion-cluster ratio may be favoured at the electrode interface as a function of deposition time. It is possible that the formation of a kinetically controlled 2:1 product is favoured as a disproportionation product when an excess of polyoxotungstate is present. The formation of disproportionation products has been postulated in previous studies involving $[Ru(bpy)_3]^{2+}$ and $[S_2M_{18}O_{62}]^{4-}$ (M = Mo, W) in which the charge-neutral 2:1 adducts dissociate to form the 1:1 products. These 1:1 products have never need isolated. However in the case of $[Ru(bpy)_3]^{2+}$ and the Keggin ion $[PW_{12}O_{40}]^{3-}$ adducts of both 1:1 and 3:2 ratios have been isolated by different authors.[25, 26] In this case the 1:1 adduct was grown slowly by recrystallization whereas the 3:2 adduct was isolated using the same centrifugation method we have used (see Chapter 2). Therefore it may be possible to isolate different stoichiometric products by controlling the rate of reaction between the two ions. It certainly appears, in our experience, that addition of stoichiometric solutions to one another results in the most stable product precipitating almost instantaneously; however slow diffusion has also been demonstrated to yield 1:1 crystals.[25] This observation merits further study in future.

5.5 – Conclusions:

The photophysics of $[Ru(bpy)_2(PVP)_{10}]^{2+}$ in the presence of the polyoxotungstate anion α-$[P_2W_{18}O_{62}]^{6-}$ have been investigated. The two ions form electrostatic composites of unusual ratios in acetonitrile. UV/Vis association data appear to suggest that the solubility of the adducts changes at two distinct ion-cluster ratios corresponding to $\{[Ru(bpy)_2(PVP)_{10}]_9\alpha\text{-}[P_2W_{18}O_{62}]\}^{12+}$ and $\{[Ru(bpy)_2(PVP)_{10}]_{4.5}\alpha\text{-}[P_2W_{18}O_{62}]\}^{3+}$, which may indicate the formation of adducts of these compositions in solution. A new absorbance band was also seen upon ion-cluster formation, which tailed into the red. Luminescence quenching was observed between the two ions and the quenching data was fitted to various models. The Stern-Volmer model was applied but has limited applicability to polymer systems. The Perrin model, which is the most commonly applied polymer quenching model, did not give a great fit to the data. In all three quenching models the presence of three different linear regions was again observed. Using the Perrin equation to fit the initial data gives a quenching sphere radius R_S of 2.2 ± 0.1 Å, which is a reasonable estimate for polymeric quenching distance. A luminescent lifetime Stern-Volmer plot appeared to reveal that the quenching is purely static in nature; however there was an abrupt increase in luminescent lifetime at a POW mole fraction of 0.18, which corresponds to the $\{[Ru(bpy)_2(PVP)_{10}]_{4.5}\alpha\text{-}[P_2W_{18}O_{62}]\}^{3+}$ species observed in the absorbance and emission intensity plots. Resonance Raman spectra of the isolated cluster revealed the presence of a polyoxotungstate mode under visible (488 nm) irradiation, which is coincident with the new optical transition seen in the UV/Vis spectra, and the new optical transition was hence assigned to an intramolecular charge-transfer transition.

Cyclic voltammetry revealed that $[Ru(bpy)_2(PVP)_{10}]^{2+}$ forms stable films when dip-coated onto ITO working electrodes whereas $\alpha\text{-}[P_2W_{18}O_{62}]^{6-}$, which lacks the free pyridyl nitrogen atoms to drive thin film formation, formed very patchy films with sub-monolayer coverage. Composite self-assembled films of $[Ru(bpy)_2(PVP)_{10}]^{2+}$ and $\alpha\text{-}[P_2W_{18}O_{62}]^{6-}$ were formed electrostatically and were stable to voltammetric cycling in BnOH electrolyte but not MeCN. The photoelectrochemistry of the films was recorded under visible (480 ± 5 nm) irradiation using BnOH as the catalytic substrate. It was found that the composite film produced a significantly higher photocurrent than that of $[Ru(bpy)_2(PVP)_{10}]^{2+}$ alone under the same conditions of irradiation and surface coverage. The driving force for photocurrent generation was increased by applying increased overpotential to the system and this resulted in an exponential increase in current density as a function of increased applied potential. A Tafel plot was employed to estimate the value for α, which is a measure of the symmetry of the potential energy barrier for the photoreductive process and is used to indicate if a reaction is favoured or not. The value of 0.8 obtained was lower than the 0.92 obtained for analogous films of $[Ru(bpy)_2(PVP)_{10}]_{4.5}\alpha\text{-}[S_2Mo_{18}O_{62}]$ reported by Jie Zhu; however the photocurrents obtained in this case were significantly higher as a higher overpotential could be employed. This is due to the more negative reduction potential of tungstates relative to their analogous molybdates. Field-emission scanning electron microscopy revealed that the composite films were mesoporous, and EDX spectroscopy revealed a Ru:POW ratio of 2:1 It is postulated that the 2:1 ratio is possibly favoured at high concentrations of polyoxotungstate due to a disproportionation reaction.

5.6 - References:

---

[1] Jie Zhu, PhD thesis, DCU, 2011.

[2] Z. Li, B-Z. Lin, J-F. Zhang, F. Geng, G-H. Han and P-D. Liu, *J. Mol Struct.*, 2006, **783**,176 - 183.

[3] I-M. Mbomekalle, Y. Wei Lu, B. Keita and L. Nadjo, *Inorg. Chem. Commun.*, 2004, **7**, 86 - 90.

[4] C. M. Granadeiro, R. A. S. Ferreira, P. C. R. Soares-Santos, L. D. Carlos and H. I. S. Nogueira, *Eur. J. Inorg. Chem.,* 2009, 5088 - 5095.

[5] T. E. Keyes, E. Gicquel, L. Guerin, R. J. Forster, V. M. Hultgren, A. M. Bond, and A. G. Wedd, *Inorg. Chem.*, 2003, **42**, 7897 - 7905.

[6] M. K. Seery, L. Guerin, R. J. Forster, E. Gicquel, V. M. Hultgren, A. M. Bond, A. G. Wedd, and T. E. Keyes, *J. Phys. Chem. A*, 2004, **108**, 7399 - 7405.

[7] M. K. Seery, N. Fay, T. McCormac, E. Dempsey, R. J. Forster and T. E. Keyes, *Phys. Chem. Chem. Phys*., 2005, **7** , 3426-3433.

[8] W. N. George, M. Giles, I. McCulloch, J. C. de Mello and J. H. G. Steinke, *Soft Matter*, 2007, **3**, 1381 - 1387.

[9] "Photophysics of unusual electrostatic adducts of the metallopolymers $[Ru(bpy)_2(caip\ co\text{-}poly)_7]^{2+}$ and $[Ru(bpy)_2(PVP)_{10}]^{2+}$ with the Dawson type α-$[Mo_{18}O_{54}(SO_4)_2]^{4-}$." Manuscript in preparation; see also Chapter 4.

[10] J. Zhu, Q. Zeng, S. O'Carroll, T. E. Keyes and R. J. Forster, *Electrochem. Commun.,* 2011, **13**, 899 - 902.

[11] N. Fay, E. Dempsey and T. McCormac, *J. Electroanal. Chem.*, 2005, **574**, 359 - 366.

[12] N. Fay, E. Dempsey, A. Kennedy and T. McCormac, *J. Electroanal. Chem.*, 2003, **556**, 63 - 74.

[13] N. Fay, E. Dempsey and T. McCormac, *Electrochim. Acta*, 2005, **51**, 281 - 288.

[14] J. Yang and M. A. Winnik, *Chem. Phys. Lett.*, 1995, **238**, 25 - 30.

[15] J. R. Ferraro, *Introduction to Raman Spectroscopy*, Academic Press, New York, 1994.

[16] J. J. Walsh, D-L. Long, L. Cronin, A. M. Bond, R. J. Forster and T. E. Keyes, *Dalton Trans.*, 2011, **40**, 2038 - 2045.

[17] L. Dennany, R. J. Forster and J. F. Rusling, *J. Am. Chem. Soc.*, 2003, **125**, 5213 - 5218.

[18] A. P. Taylor, J. A. Crayston and T. J. Dines, *J. Chem. Soc., Faraday Trans.*, 1997, **93**, 1803 - 1812.

[19] T. McCormac, D. Farrell, D. Drennan and G. Bidan, *Electroanal.*, 2001, **13**, 836 - 842.

[20] A. Devadoss, C. Dickinson, T. E. Keyes and R. J. Forster, *Anal. Chem.*, 2011, **83**, 2383 - 2387.

[21] P. J. Hotchkiss, H. Li, P. B. Paramonov, S. A. Paniagua, S. C. Jones, N. R. Armstrong, J-L. Brédas and S. R. Marder, *Adv. Mater.*, 2009, **21**, 4496 - 4501.

---

[22] P. J. S. Richardt, R. W. Gable, A. M. Bond and A. G. Wedd, *Inorg. Chem*., 2001, **40**, 703 - 709.

[23] J. M. Calvert, J. V. Caspar, R. A. Binstead, T. D. Westmoreland and T. J. Meyer, *J. Am. Chem. Soc.* 1982, **104**, 6620 - 6627.

[24] L-H. Bi, K. Foster, T. McCormac and E. Dempsey, *J. Electroanal. Chem.*, **2007**, 605, 24 - 30.

[25] J. Song, Z. Luo, H. Zhu, Z. Huang, T. Lian, A. L. Kaledin, D. G. Musaev, S. Lense, K. I. Hardcastle and C. L. Hill, *Inorg. Chim. Acta*, 2010, **363**, 4381 - 4386.

[26] Y. Li, H. Zhu and X. Yang, *Talanta*, 2009, **80**, 870 - 874.

Chapter 6:

Combinatorial approach to identifying potentially sensitized clusters using resonance Raman spectroscopy.

6.1 – Introduction:

The failure of $[Ru(bpy)_3]^{2+}$ to effectively sensitise the Dawson-like sulfite α/β-$[Mo_{18}O_{54}(SO_3)_2]^{4-}$ ions (Chapter 3) was unexpected given the thermodynamic similarities between $[Ru(bpy)_3]_2\alpha/\beta$-$[Mo_{18}O_{54}(SO_3)_2]$ and the sulfate analogue $[Ru(bpy)_3]_2\alpha$-$[Mo_{18}O_{54}(SO_4)_2]$, as the latter resulted in effective visible sensitisation under 480 nm irradiation as identified by resonance Raman (see Fig 6.1.1).[1] Although in both cases a new optical transition was observed in the visible spectrum of the electrostatic adducts, it appeared weaker in $[Ru(bpy)_3]_2\alpha/\beta$-$[Mo_{18}O_{54}(SO_3)_2]$ than in the sulphate analogue composites. A key distinction between assemblies which showed photosensitization by the ruthenium centre and the sulfite polyoxomolybdates, which did not, was in the resonance Raman spectroscopy of the associated assemblies. For example $[Ru(bpy)_3]_2\alpha$-$[Mo_{18}O_{54}(SO_4)_2]$ showed that resonantly enhanced vibrations from both cation and anion participation in the new optical transition; however this was not true of $[Ru(bpy)_3]_2\alpha/\beta$-$[Mo_{18}O_{54}(SO_3)_2]$.[2, 3] We rationalised that the presence of a new optical transition and associated involvement of the polyoxometalate in this transition was indicative of photosensitization as this optical transition is likely to play a role in the sensitization process. In this chapter we explored this premise by using resonance Raman to take a combinatorial approach to identifying transition metal complex/polyoxometalate ion-clusters with potential visible-sensitizing ability.

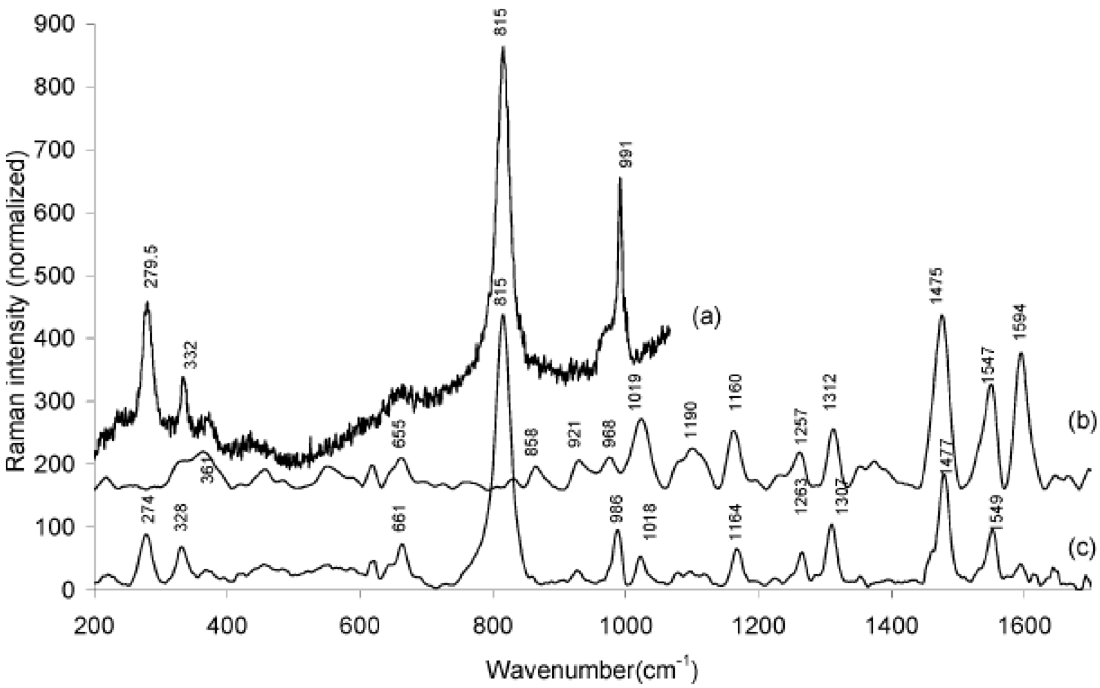

Fig 6.1.1: Resonance Raman spectrum of solids dispersed in KBr discs (~ 5 % w/w) excited at 488 nm: (a) $[(But)_4N]_4\alpha\text{-}[Mo_{18}O_{54}(SO_4)_2]$; (b) $[Ru(bpy)_3]Cl_2$; (c) $[Ru(bpy)_3]_2\alpha\text{-}[Mo_{18}O_{54}(SO_4)_2]$. Reproduced from [3].

The inherently low solubility of transition metal complex/polyoxometalate ion-clusters in MeCN renders them easy to isolate. Concentrated solutions of both parent ions in MeCN at appropriate molar ratios required for ion-cluster neutrality are added together slowly and the insoluble composite material collected by centrifugation. The solids are then washed repeatedly, dried under a stream of N_2 and ground into a KBr disc for Raman analysis. Since both ruthenium polypyridyl complexes and polyoxometalates are photoactive, the use of dry KBr as a matrix minimises the chances of either ion undergoing undesirable side reactions during spectral acquisition.

6.2 - Synthesis and characterization:

In order to maximise the amount of data collected, a range of transition metal complexes which had been studied and characterised previously by our group were assembled. Each monomer complex (except the Fe complexes, which are paramagnetic) was analyzed by ^{1}H-NMR (Appendix 1) before synthesis of the composite materials was performed. In total 14 metal cations were explored in conjunction with three Dawson polyoxometalates. The cationic complexes used are shown in Table 6.2.1. The synthetic procedures are outlined in Chapter 2.

Ru (II)	**Os (II)**	**Fe (II)**
$[Ru(bpy)_2(PVP)_{10}]^{2+}$	$[Os(bpy)_3]^{2+}$	$[Fe(bpy)_3]^{2+}$
$[Ru(bpy)_2(qpy)]^{2+}$	$[Os(bpy)_2(qpy)]^{2+}$	$[Fe(terpy)_2]^{2+}$
$[Ru(bpy)_2(caip)]^{2+}$	$[Os(bpy)_2(p0p)_2]^{2+}$	
$[Ru(dpp)_2(caip)]^{2+}$	$[Os(bpy)_2(PVP)_{10}]^{2+}$	
$[Ru(dppz)_2(caip)]^{2+}$		
$[Ru(bpy)_2(caip\text{-}NH_2)]^{2+}$		
$[Ru(bpy)_2(caip\text{-}NO_2)]^{2+}$		
$[Ru(dpp)_3]^{2+}$		

Table 6.2.1: List of transition metal complexes employed in this combinatorial study.

The Dawson polyoxometalates α-$[Mo_{18}O_{54}(SO_4)_2]^{4-}$, γ*-$[W_{18}O_{54}(SO_4)_2]^{4-}$ and α-$[W_{18}O_{54}(PO_4)_2]^{6-}$ were synthesized as described previously.[4, 5, 6] The electrostatic adduct materials were synthesized according to the procedure of Hultgren *et al.*[7] In brief 0.75 ml of metal complex solution (either 2 mM or 4.5 mM depending on the complex) was added dropwise to 1 ml of 1 mM polyoxometalate solution with vigorous stirring. At these concentrations the adduct materials are very insoluble in MeCN and thus precipitate almost immediately. The solid powders were isolated via centrifugation. The supernatant was removed and the material was washed with fresh MeCN, to remove any residual starting materials. This was performed in triplicate. The solid was then washed with diethyl ether and dried under a stream of N_2.

6.3 – Resonance Raman spectroscopy of novel ion-clusters with Ru complexes:

The Raman spectra of the isolated solids in KBr discs were performed under visible irradiation (458, 488 and 514 nm). As described, the intensity of Raman spectra can be enhanced dramatically if the excitation wavelength is coincident with an optical absorbance, and enhancements of the order of 10^6 are commonly observed for chromophore vibrational modes.[8] This permits relatively unambiguous identification of the underlying optical transition, if it is isolated from other absorbances as chromophore modes can be selectively tracked as the laser lines come in and out of resonance. Importantly the fully oxidized polyoxometalates employed in this thesis only absorb below 400 nm and hence give very weak intensity Raman spectra under visible irradiation, whereas the Ru complexes absorb strongly in the visible and give intense resonantly enhanced spectra.

In almost every case studied to date, addition of a polyoxometalate solution to a solution of Ru complex resulted in quenching of the Ru luminescence. The sole exception to this was in the case of $[Ru(bpy)_2(biq)]^{2+}$---$[Co(H_2O)SiW_{11}O_{39}]^{6-}$, where no quenching was observed, which was attributed to the positive free energy of electron transfer for this system (+ 0.35 eV).[9] The association of a number of cationic Ru complexes with anionic Dawson polyoxometalates also resulted in the appearance of a new optical transition at low energies in the UV/Vis spectra and these transitions were assigned to intramolecular charge-transfer transitions on the basis of resonance Raman data, as described in previous chapters. However the new charge-transfer transitions observed did not always result in the appearance of polyoxometalate modes under visible irradiation.[2] The reason for this is not precisely known, however in the large majority of cases examined in this study no polyoxometalate modes were seen under visible excitation. The polypyridyl complexes of ruthenium (II) employed in this study are discussed in this section.

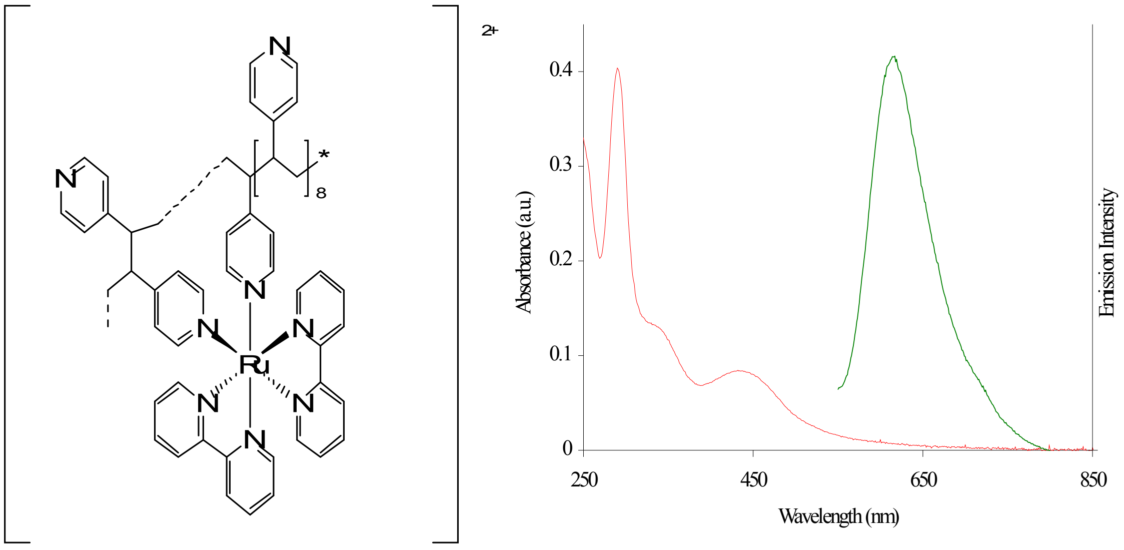

Fig 6.3.1: Structure of $[Ru(bpy)_2(PVP)_{10}]^{2+}$ (left) and UV/Vis and emission spectroscopy (~ 9 x 10^{-6} M) of $[Ru(bpy)_2(PVP)_{10}]^{2+}$ in MeCN (right). Excitation wavelength was 450 nm.

Fig 6.3.1 shows the structure of the metallopolymer $[Ru(bpy)_2(PVP)_{10}]^{2+}$, which has been used extensively throughout this thesis. The bidentate coordination of the two polymer pyridines to the Ru center does not induce major spectral changes relative to $[Ru(bpy)_3]^{2+}$, as the UV/Vis and emission spectra indicate. The MLCT Ru dπ – bpyπ* absorption is centered at around 450 nm and exciting into this band generates an intense phosphorescence band at 615 nm. The phosphorescence intensity has been normalized for clarity.

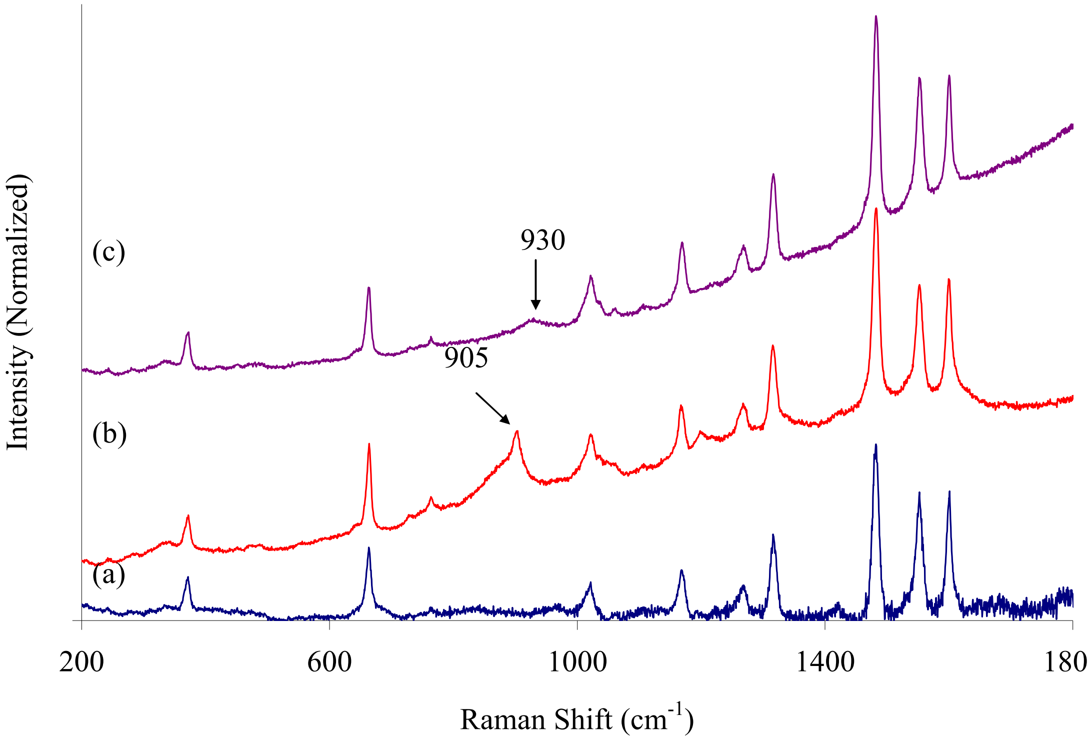

Fig 6.3.2: Resonance Raman spectra of (a) $[Ru(bpy)_2(PVP)_{10}](NO_3)_2$, (b) $[Ru(bpy)_2(PVP)_{10}]_{4.5}\alpha$-$[Mo_{18}O_{54}(SO_4)_2]$ and (c) $[Ru(bpy)_2(PVP)_{10}]_{4.5}\gamma^*$-$[W_{18}O_{54}(SO_4)_2]$ in oven-dried KBr (~ 5 % w/w) under 514 nm excitation.

The spectra in Fig 6.3.2 show the changes in the Raman spectrum of $[Ru(bpy)_2(PVP)_{10}]^{2+}$ upon electrostatic cluster formation with various Dawson polyoxometalates. In these spectra the bipyridine ligand modes at 1603, 1556 and 1485 cm^{-1} are unaffected by counterion exchange, as is the Ru-N stretch at 375 cm^{-1}. However some new modes that are not attributable to the Ru metallopolymer are visible in the adduct spectra. In the case of the polyoxomolybdate cluster $[Ru(bpy)_2(PVP)_{10}]_{4.5}\alpha$-$[Mo_{18}O_{54}(SO_4)_2]$ a new mode appeared at 905 cm^{-1}, which has previously been attributed to the Mo-O stretching mode of α-$[Mo_{18}O_{54}(SO_4)_2]^{4-}$.[10] However it appears as though a polyoxotungstate mode at 930 cm^{-1} is also resonantly enhanced in the case of $[Ru(bpy)_2(PVP)_{10}]_2\gamma^*$-$[W_{18}O_{54}(SO_4)_2]$. This is likely the W-O stretching mode, although the resonance enhancement appears to be weaker in this case. These data imply a different type of intramolecular electronic communication to those in the literature, which focused on the resonance Raman of $[Ru(bpy)_3]_2\alpha$-$[Mo_{18}O_{54}(SO_4)_2]$ and $[Ru(bpy)_3]_2\gamma^*$-$[W_{18}O_{54}(SO_4)_2]$, and which revealed the resonance enhancement of more than one polyoxometalate band.[1, 11] These differences are not unusual given the difference in polyoxometalate binding between the polymer and monomer. The enhancement of so many modes is not observed in this case, nevertheless the spectra do appear to confirm that both ions participate in an optical transition based around 514 nm in the cases of both molybdate and tungstate. Resonance enhancement of the Ru-bpy modes is expected at this wavelength, given that the tail of the MLCT mentioned previously is under irradiation; however enhancement of the polyoxometalate modes at this wavelength indicates that the polyoxoanions participate in the underlying transition at 514 nm.

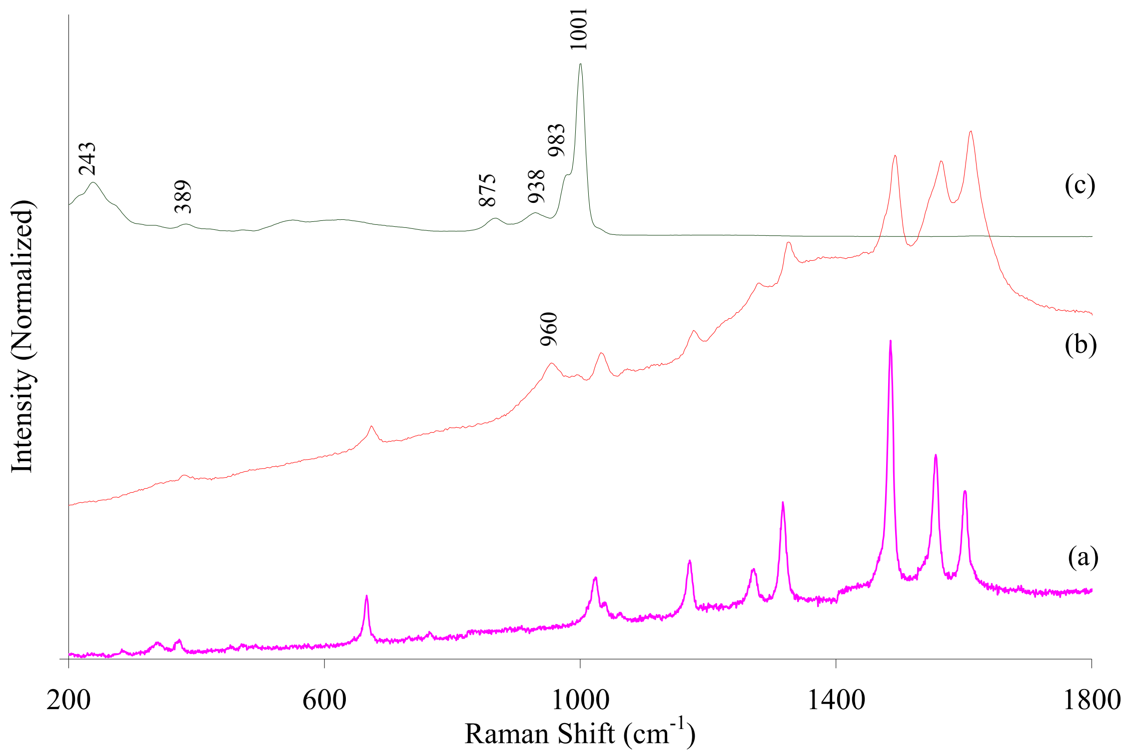

Fig 6.3.3: Resonance Raman spectra of (a) $[Ru(bpy)_2(PVP)_{10}](NO_3)_2$, (b) $[Ru(bpy)_2(PVP)_{10}]_2\alpha$-$[W_{18}O_{54}(PO_4)_2]$ and (c) $K_6\alpha$-$[W_{18}O_{54}(PO_4)_2]$ in oven-dried KBr (~ 5 % w/w) under 488 nm excitation.

Fig 6.3.3 shows the Raman spectra of the phosphotungstate Dawson anion α-$[W_{18}O_{54}(PO_4)_2]^{6-}$, $[Ru(bpy)_2(PVP)_{10}]^{2+}$ and the associated metallopolymer composite $[Ru(bpy)_2(PVP)_{10}]_{4.5}$α-$[W_{18}O_{54}(PO_4)_2]$. In the case of this polyoxometalate a new feature appeared at 960 cm^{-1} in the adduct spectrum. This feature has been attributed to the W-O stretching mode, which has undergone a peak shift upon binding to metallopolymer. This peak shift may be due to intramolecular H-bonding, which has been seen before in the infrared spectrum and crystal structure of $K_5\{[Ru(bpy)_3][PW_{11}O_{39}]\}^{5-}$.[12] What Figs 6.3.2 and 6.3.3 demonstrate is that $[Ru(bpy)_2(PVP)_{10}]^{2+}$ appears to be an excellent candidate for Dawson polyoxometalate sensitization, for both molybdates and tungstates, and this has since been demonstrated in the photoelectrochemical studies in the literature and in Chapters 4 and 5.[13]

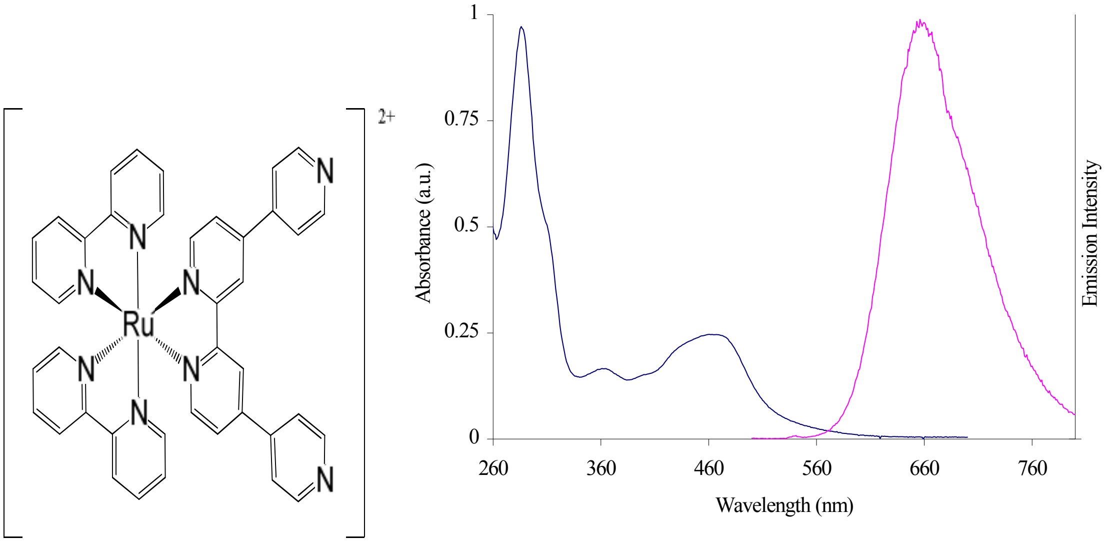

Fig 6.3.4: Structure of $[Ru(bpy)_2qpy]^{2+}$ (left) and UV/Vis and emission spectroscopy of $[Ru(bpy)_2(PVP)_{10}]^{2+}$ in DMSO (right). Excitation wavelength was 465 nm.

Fig 6.3.4 shows the structure of $[Ru(bpy)_2qpy]^{2+}$ and its optical spectroscopy in DMSO. The Ru-bpy MLCT is clearly visible at approximately 465 nm and exciting into this band produced an emission at 660 nm, which is red-shifted with respect to $[Ru(bpy)_3]^{2+}$. The MLCT is also broadened towards the red and hence is likely to be an overlap of the Ru-bpy and Ru-qpy MLCT transitions. The free pyridyl nitrogen atoms can form coordination bonds with other molecules and with electrode surfaces.

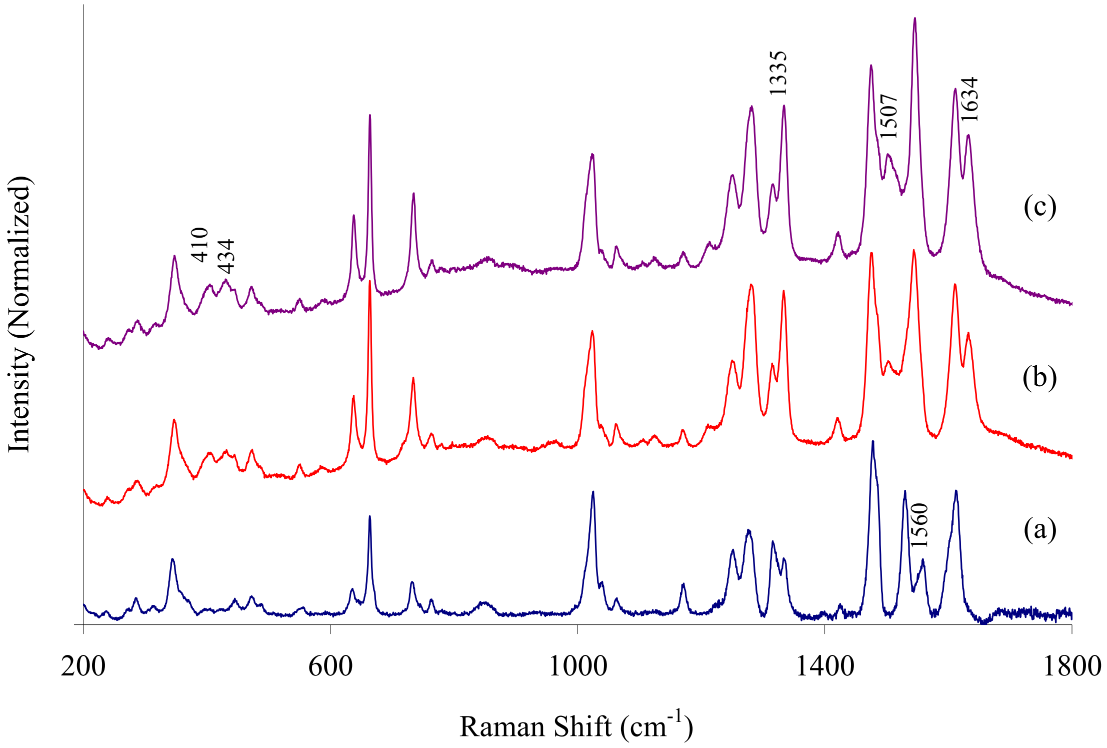

Fig 6.3.5: Resonance Raman spectra of (a) $[Ru(bpy)_2(qpy)]^{2+}$, (b) $[Ru(bpy)_2(qpy)]_2$α-$[Mo_{18}O_{54}(SO_4)_2]$ and (c) $[Ru(bpy)_2(qpy)]_2$γ*-$[W_{18}O_{54}(SO_4)_2]$ in oven-dried KBr (~ 5 % w/w) under 514 nm excitation.

Fig 6.3.1.5 shows the resonance Raman spectra of $[Ru(bpy)_2(qpy)]^{2+}$, $[Ru(bpy)_2(qpy)]_2$α-$[Mo_{18}O_{54}(SO_4)_2]$ and $[Ru(bpy)_2(qpy)]_2$γ*-$[W_{18}O_{54}(SO_4)_2]$ under visible irradiation. At this wavelength it is clear that both bpy and qpy modes are resonantly enhanced, which confirms that MLCT transitions to both ligands are resonant at 514 nm. Some interesting changes are seen in the adduct spectra. A major band at 1560 cm^{-1}, assigned to a pyridine C-C stretching mode, disappeared whereas new bands grew in at 1634 and 1507 cm^{-1}.[14] Other bipyridyl based modes were enhanced at 1335, 434 and 410 cm^{-1}. Interestingly, addition of either molybdate (b) or tungstate (c) resulted in the same spectral changes, which confirms that they are not polyoxometalate based and therefore cannot be explained in terms of resonantly enhanced Ru-polyoxometalate charge-transfer transition as in Fig 6.3.2. We tentatively assign the changes to arise as a result of the free pyridyl nitrogen atoms interacting with the polyoxometalates, and thus experiencing significant changes in electron density. However without X-ray crystal diffraction or

NMR data this for the moment is speculative. The resonance Raman spectroscopy of a range of similar complexes is presented in Figs 6.3.7, 6.3.9 and 6.3.11.

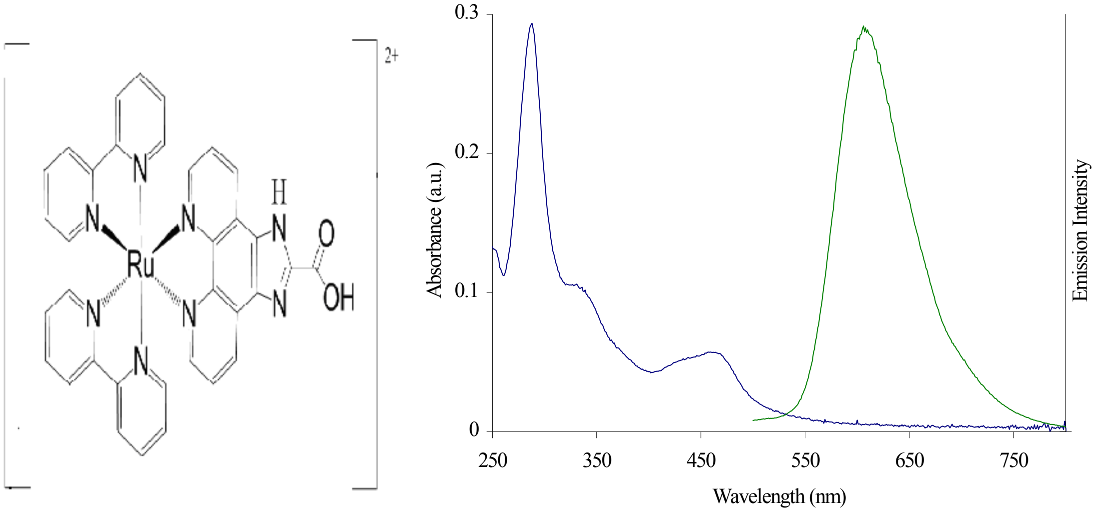

Fig 6.3.6: Structure of $[Ru(bpy)_2(caip\text{-}COOH)]^{2+}$ (left) and UV/Vis and emission spectroscopy of $[Ru(bpy)_2(PVP)_{10}]^{2+}$ in MeCN (right). Excitation wavelength was 460 nm.

Fig 6.3.6 shows the structure and optical spectra of $[Ru(bpy)_2(caip\text{-}COOH)]^{2+}$. This structure contains a caip ligand which has three pK_a values. The absorption spectrum reveals the presence of an MLCT band at ~ 460 nm which contains contributions from both the Ru-bpy and Ru-caip MLCT transitions. Excitation into this band results in emission at 610 nm. The absorption and emission properties can change as a function of pH, and the complex can also form amide bonds via the carboxylic acid group.

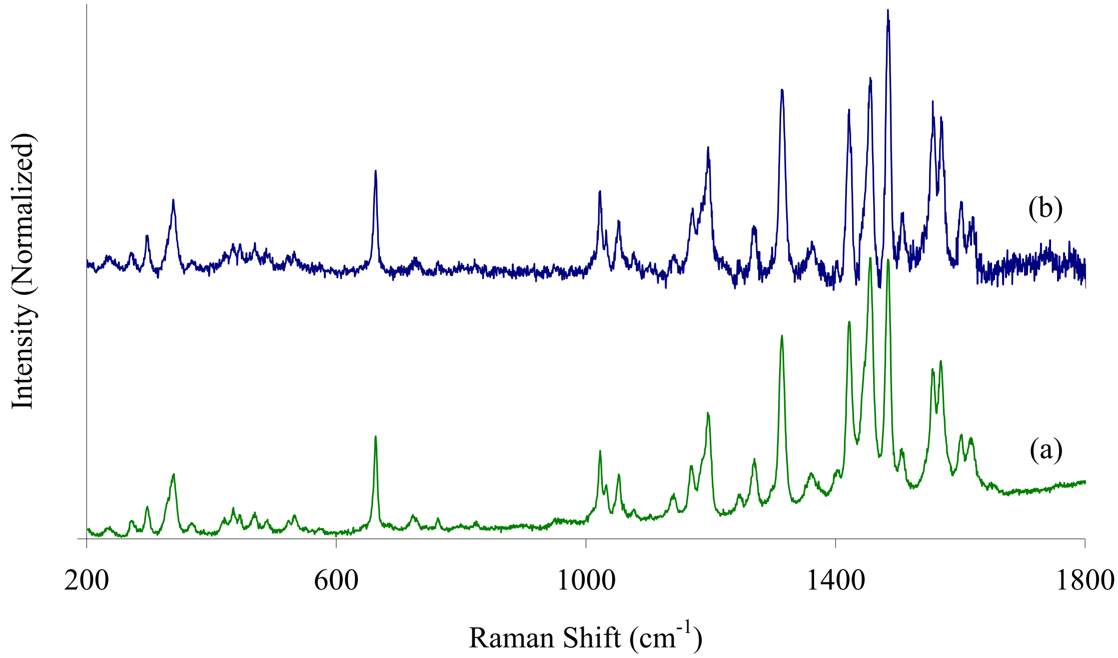

Fig 6.3.7: Resonance Raman spectra of (a) [Ru(bpy)$_2$(caip-COOH)](ClO$_4$)$_2$ and (b) [Ru(bpy)$_2$(caip-COOH)]$_2$α-[Mo$_{18}$O$_{54}$(SO$_4$)$_2$] in KBr discs (~ 5 % w/w) under 488 nm irradiation.

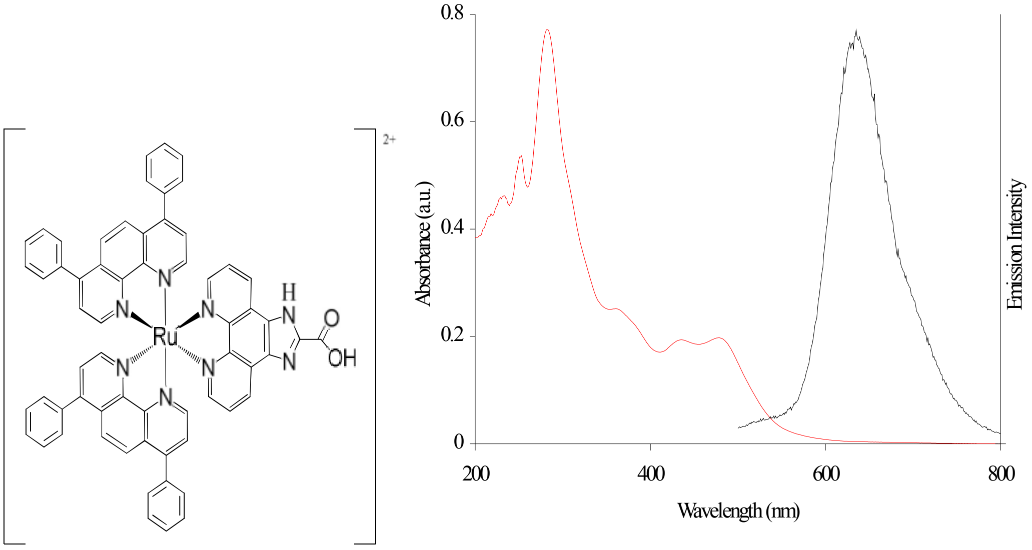

Fig 6.3.8: Structure of [Ru(dpp)$_2$(caip-COOH)]$^{2+}$ (left) and UV/Vis and emission spectroscopy of [Ru(dpp)$_2$(caip-COOH)]$^{2+}$ in DMSO (right). Excitation wavelength was 480 nm.

Fig 6.3.8 shows the structure and spectra of $[Ru(dpp)_2(caip\text{-}COOH)]^{2+}$. The MLCT of the complex clearly consists of two peaks, and excitation at 480 nm gave emission at approximately 635 nm. This complex also exhibits pH dependent spectroscopy.

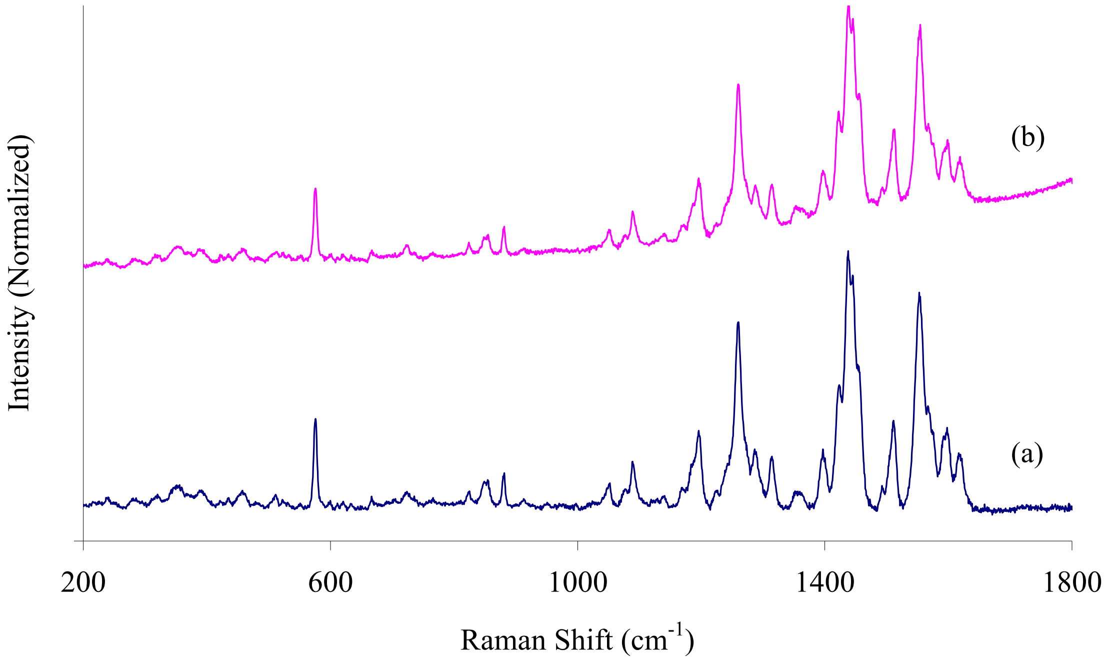

Fig 6.3.9: Resonance Raman spectra of (a) $[Ru(dpp)_2(caip\text{-}COOH)](ClO_4)_2$ and (b) $[Ru(dpp)_2(caip\text{-}COOH)]_2\alpha\text{-}[Mo_{18}O_{54}(SO_4)_2]$ in KBr discs (~ 5 % w/w) under 488 nm irradiation.

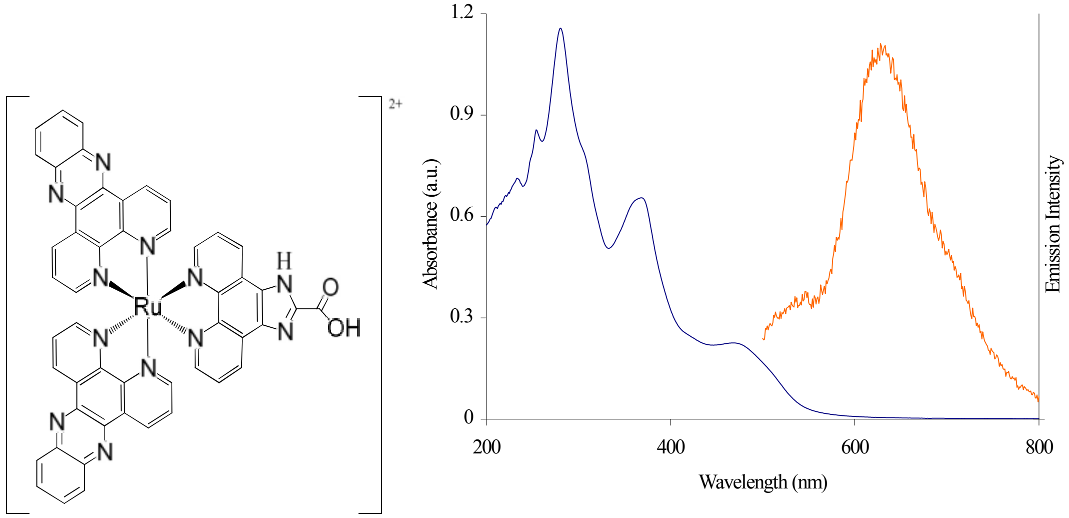

Fig 6.3.10: Structure of $[Ru(dppz)_2(caip\text{-}COOH)]^{2+}$ (left) and UV/Vis and emission spectroscopy of $[Ru(dppz)_2(caip\text{-}COOH)]^{2+}$ in DMSO (right). Excitation wavelength was 460 nm.

Fig 6.3.10 shows the structure and spectra of $[Ru(dppz)_2(caip\text{-}COOH)]^{2+}$. The peak at ~ 470 nm in the UV/Vis spectrum is the MLCT, and again contains contributions from the Ru-dppz and Ru-bpy transitions. The dppz $\pi \rightarrow \pi^*$ transition at 365 nm is very pronounced in this case. This molecule also exhibits pH dependent electronic spectroscopy.

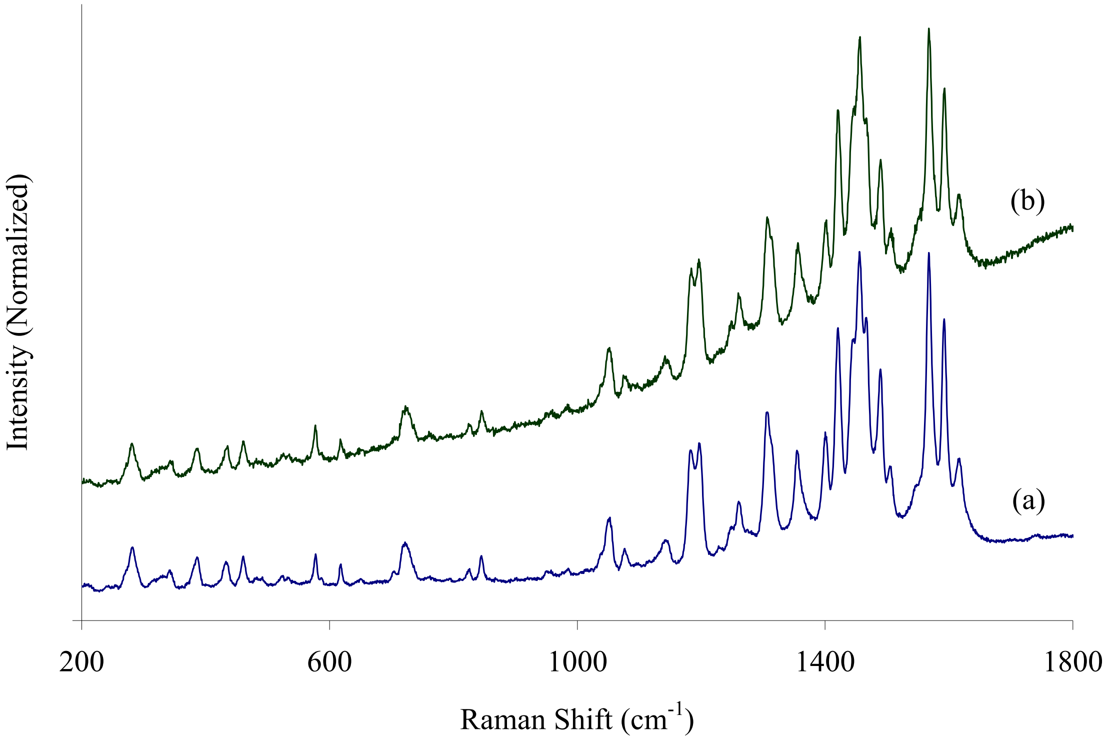

Fig 6.3.11: Resonance Raman spectra of (a) [Ru(dppz)$_2$(caip-COOH)](ClO$_4$)$_2$ and (b) [Ru(dppz)$_2$(caip-COOH)]$_2$α-[Mo$_{18}$O$_{54}$(SO$_4$)$_2$] in KBr discs (~ 5 % w/w) under 488 nm irradiation.

Figs 6.3.1.7 – 6.3.1.11 contain the spectra of a series of similar Ru complexes, all based on the caip ligand, and their electrostatic adducts with α-[Mo$_{18}$O$_{54}$(SO$_4$)$_2$]$^{4-}$. It is clear that in all three cases there is little or no change to the Ru Raman modes as a consequence of binding to the polyoxomolybdate. The degree of donor/acceptor energy level overlap should be extremely similar for all three complexes and for [Ru(bpy)$_3$]$^{2+}$, however these three complexes contain either one (caip-COOH) or three (caip-COOH and dpp or dppz) bulky ligands and hence molecular shape likely plays a crucial role. It is worth noting that the terminal COOH group in each case has no effect on the interaction with the molybdate, which is in contrast to the free pyridyl N atoms in Fig 6.3.4. It is therefore likely that an optimized sensitizer/polyoxometalate system would consist of a complex with relatively small ligands, facilitating close packing in the electrostatic adduct and possibly H-bonding, to accommodate charge-transfer.

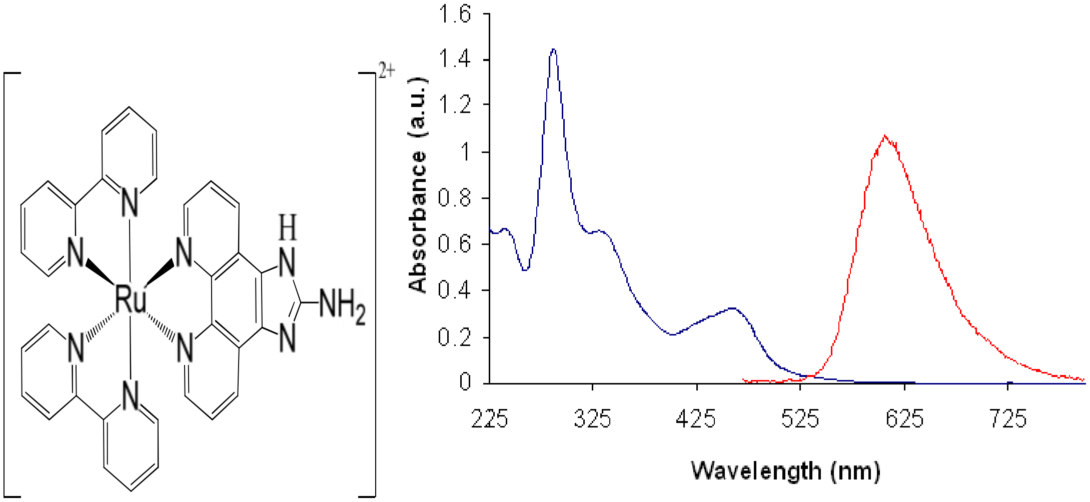

Fig 6.3.12: Structure of [Ru(bpy)$_2$(caip-NH$_2$)]$^{2+}$ (left) and UV/Vis and emission spectroscopy of [Ru(dppz)$_2$(caip-NH$_2$)]$^{2+}$ in MeCN (right). Excitation wavelength was 460 nm.

Fig 6.3.12 shows the spectra and structure of [Ru(bpy)$_2$(caip-NH$_2$)]$^{2+}$. The complex exhibits an MLCT with two contributions, Ru-bpy and Ru-caip, at approximately 460 nm. Excitation at 460 nm resulted in emission at approximately 615 nm in MeCN. The complex is spectroscopically and electrochemically similar to [Ru(bpy)$_2$(caip-COOH)]$^{2+}$, shown in Fig 6.3.6. However the free NH$_2$ group is basic and will undergo different chemical reactions than the acidic COOH terminated analogue.

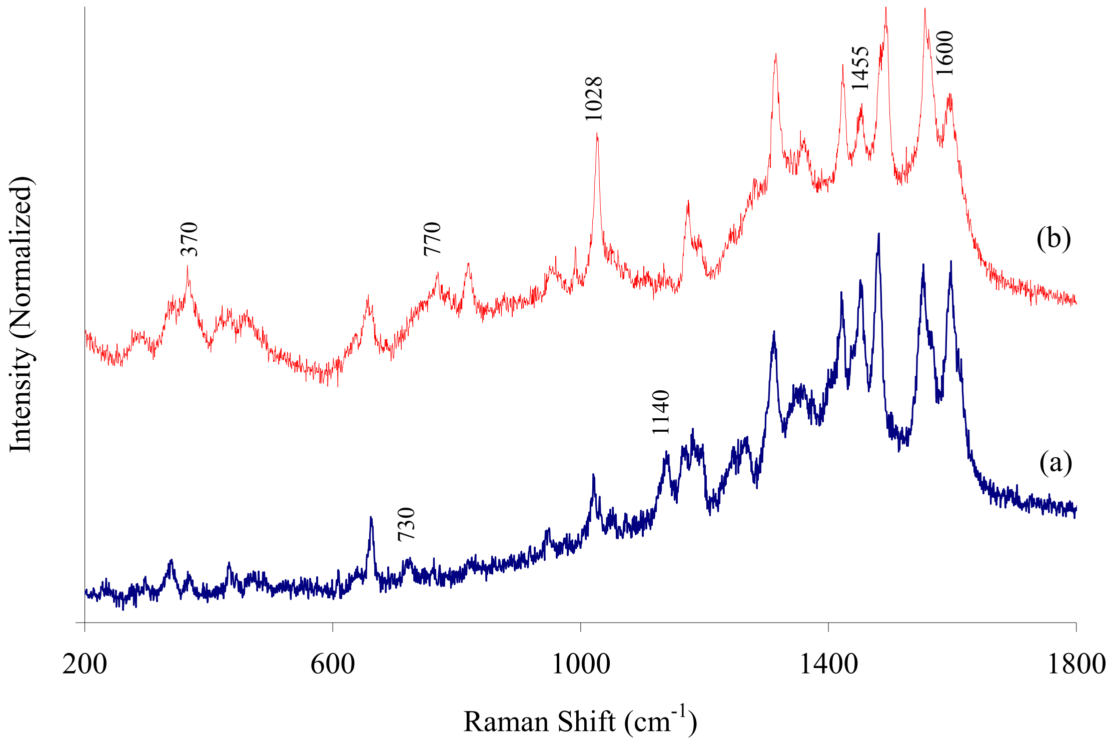

Fig 6.3.13: Resonance Raman spectra of (a) [Ru(bpy)$_2$(caip-NH$_2$)](ClO$_4$)$_2$ and (b) [Ru(bpy)$_2$(caip-NH$_2$)]$_2$α-[Mo$_{18}$O$_{54}$(SO$_4$)$_2$] 488 nm.

Fig 6.3.13 shows the resonance Raman spectra of the [Ru(bpy)$_2$(caip-NH$_2$)]$^{2+}$. Clearly several spectral changes occur upon association with the polyoxomolybdate. Notably, the band at 1140 cm^{-1} disappears when the POM is present. Other bands at 1600 and 1455 cm^{-1} are decreased in intensity whereas bands at 1028 and 370 cm^{-1} are increased in intensity, relative to the complex alone. The band at 730 cm^{-1} also increases in intensity and shifts to 770 cm^{-1}. The reason for these spectral changes is unclear but they are tentatively attribtuted to interaction between the terminal NH$_2$ group and the polyoxometalate structure, either due to a change in local elevtron density and/or H-bonding to the polyoxometalate.

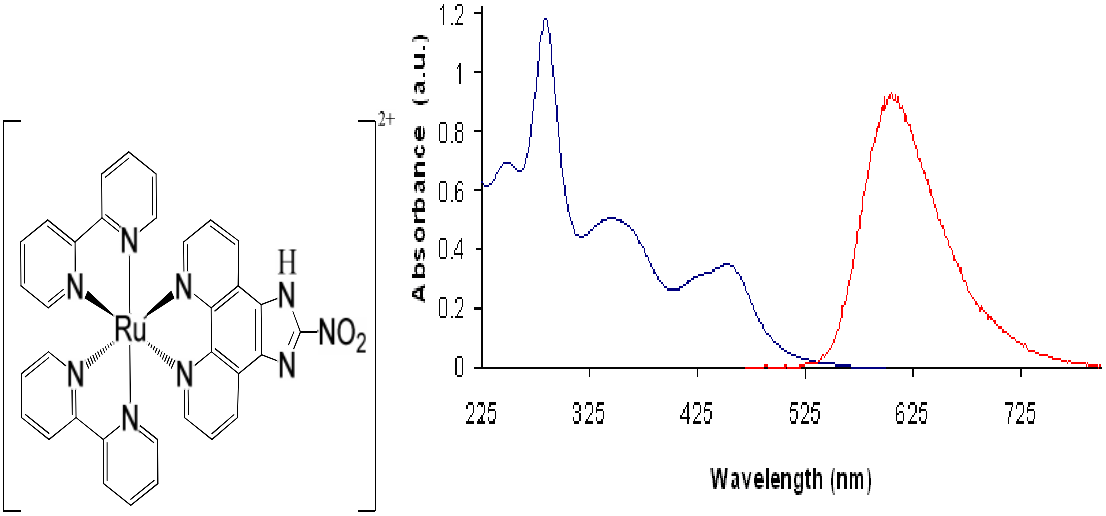

Fig 6.3.14: Structure of [Ru(bpy)$_2$(caip-NO$_2$)]$^{2+}$ (left) and UV/Vis and emission spectroscopy of [Ru(dppz)$_2$(caip-NO$_2$)]$^{2+}$ in MeCN (right). Excitation wavelength was 460 nm.

Fig 6.3.14 shows the structure and optical spectra of [Ru(bpy)$_2$(caip-NO$_2$)]$^{2+}$. The two contributions from the overlapping Ru-bpy and Ru-caip MLCT transitions are visible at ~ 460 nm. Excitation at this wavelength gave luminescence at ~ 615 nm. The spectra are very similar to that [Ru(bpy)$_2$(caip-COOH)]$^{2+}$ and [Ru(bpy)$_2$(caip-NH$_2$)]$^{2+}$ shown in Fig 6.3.6 and Fig 6.3.12 respectively.

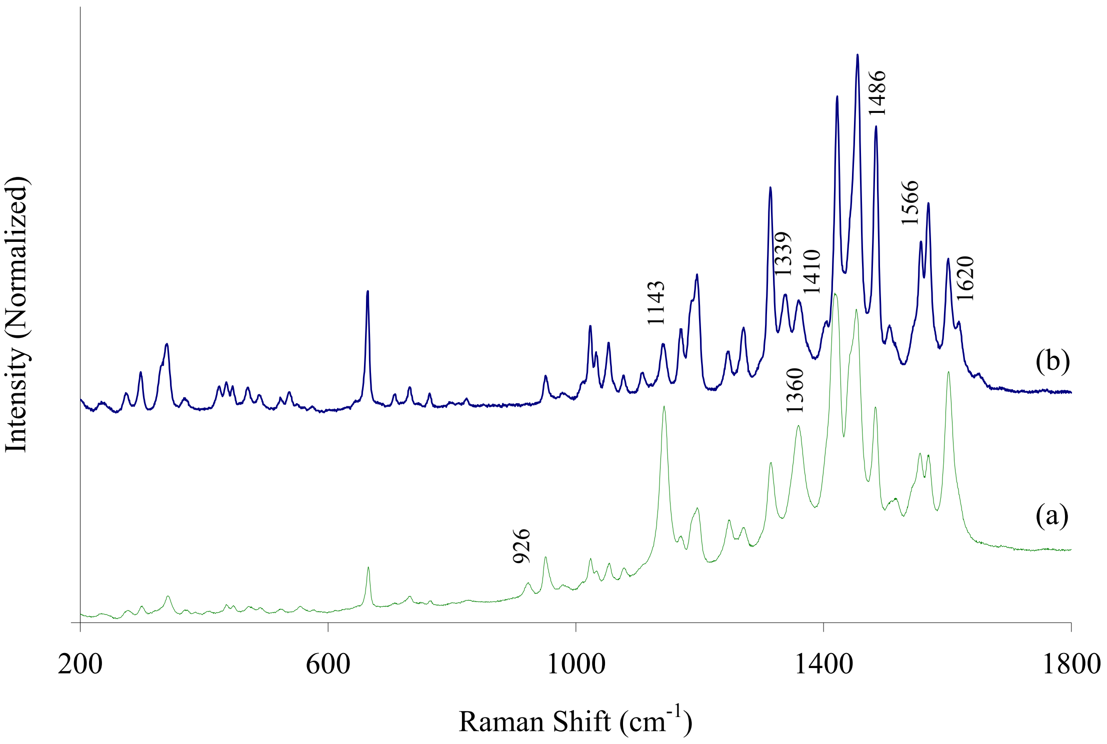

Fig 6.3.15: Resonance Raman spectra of (a) $[Ru(bpy)_2(caip\text{-}NO_2)](ClO_4)_2$ and (b) $[Ru(bpy)_2(caip\text{-}NO_2)]_2\alpha\text{-}[Mo_{18}O_{54}(SO_4)_2]$ dispersed in KBr (~ 5 % w/w) excitation wavelength 488 nm.

Fig 6.3.15 shows the resonance Raman of the Dawson polyoxomolybdate $\alpha\text{-}[Mo_{18}O_{54}(SO_4)_2]^{4-}$ and $[Ru(bpy)_2(caip\text{-}NO_2)]^{2+}$, which is very similar to the $[Ru(bpy)_2(caip\text{-}NH_2)]^{2+}$ complex used in Fig 6.3.13. Several features in the adduct spectrum appear enhanced relative to the spectrum of $[Ru(bpy)_2(caip\text{-}NO_2)]^{2+}$ alone. Pyridine and caip ring stretch modes at 1620, 1556 and 1486 cm^{-1} appear more intense, relative to the bpy modes, whereas the peak at 1360 cm^{-1} splits into two features of approximately equal intensity at 1339 and 1410 cm^{-1}. Interestingly the mode at 926 cm^{-1} disappears upon association. Many low frequency modes below 800 cm^{-1} also appear significantly enhanced. The mode at 1143 cm^{-1} decreases in intensity and the mode at 1028 cm^{-1} increases in intensity, which reflects the similar changes in Fig 6.3.13, and hence is likely to changes in the electronic distribution across the imidazole-based caip ligand. However it is clear that no polyoxometalate modes appear resonant in the adduct spectrum under 488 nm irradiation. The differences in the two spectra in this case likely arise from the change in electron density experienced by the Ru complex upon changing counterion. In particular the terminal NO_2 group appears to be sensitive to changes in its localized electronic environment, as when the corresponding COOH terminated ligand was employed the spectrum was virtually unchanged in the presence of the same polyoxomolybdate (see Fig 6.3.6). All of the spectral changes may suggest that the resonance of the complex itself is changing upon association, which could reflect an underlying shift in the Ru-caip transition.

Most of the complexes employed in this study exhibited negligible or no spectral changes upon electrostatic association with the Dawson polyoxometalates. Some of these data are quite surprising given the similarities between the complexes and $[Ru(bpy)_3]^{2+}$ which did appear to exhibit significant electronic communication with the Dawson polyoxometalates.

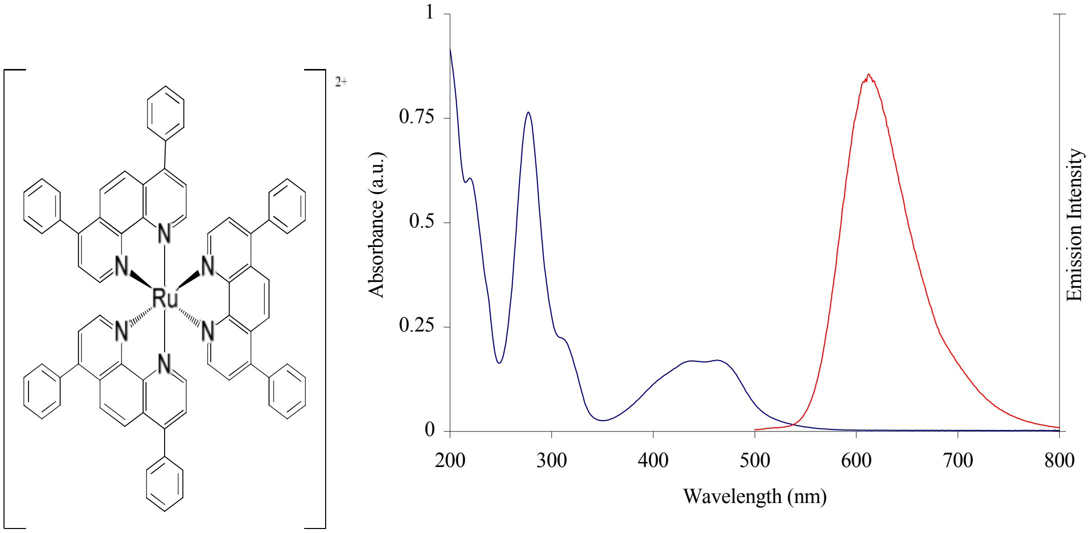

Fig 6.3.16: Structure of $[Ru(dpp)_3]^{2+}$ (left) and UV/Vis and emission spectroscopy of $[Ru(dpp)_3]^{2+}$ in MeCN (right). Excitation wavelength was 460 nm.

One complex in particular ($[Ru(dpp)_3]^{2+}$, which is shown in Fig 6.3.16) is analogous to $[Ru(bpy)_3]^{2+}$. As shown its MLCT absorbance occurs around 460 nm and excitation at this wavelength results in emission at ~ 610 nm. The spectroscopic and electrochemical energy levels of $[Ru(dpp)_3]^{2+}$ are almost identical to those of $[Ru(bpy)_3]^{2+}$.

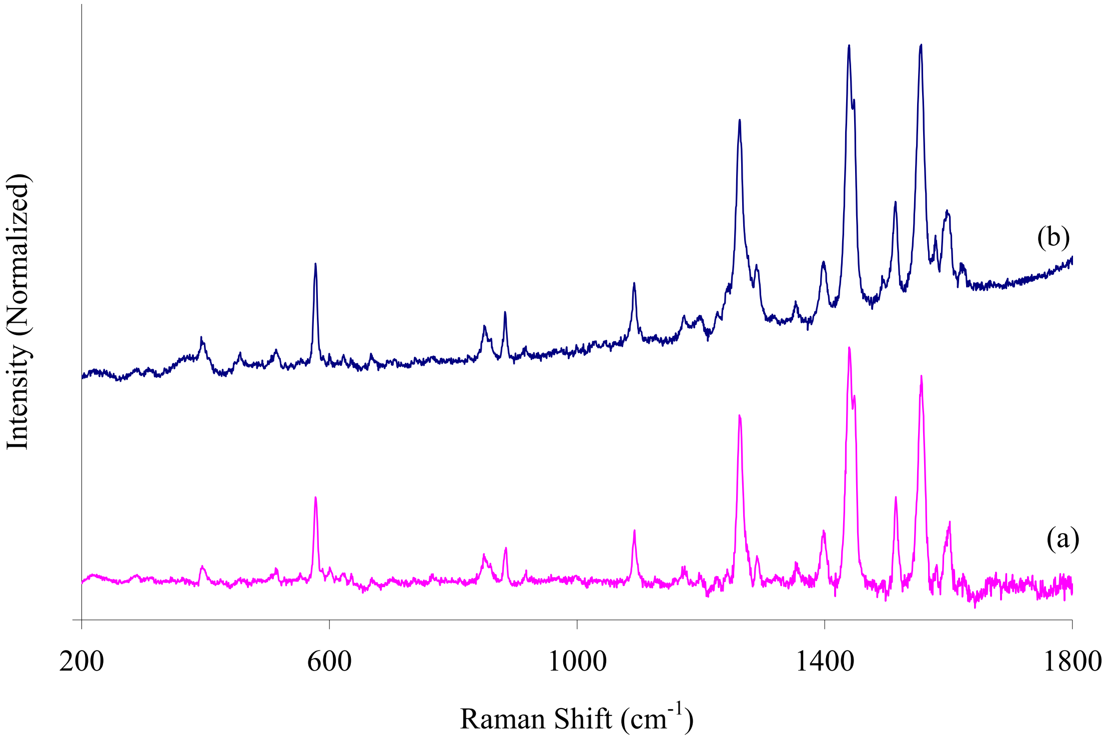

Fig 6.3.17: Resonance Raman spectra of (a) $[Ru(dpp)_3](PF_6)_2$ and (b) $[Ru(dpp)_3]_2\alpha$-$[Mo_{18}O_{54}(SO_4)_2]$ in KBr discs (~ 5 % w/w) under 488 nm laser excitation.

However, Fig 6.3.17 reveals that anion exchange from $[Ru(dpp)_3](PF_6)_2$ to $[Ru(dpp)_3]_2\alpha$-$[Mo_{18}O_{54}(SO_4)_2]$ resulted in very minor spectral changes. This is somewhat surprising, given the previously published data in Fig 6.1.1, as $[Ru(dpp)_3]^{2+}$ and $[Ru(bpy)_3]^{2+}$ have almost indistinguishable absorption, emission and electrochemical characteristics. The only significant difference between the two complexes lies in the bulky character of the diphenylphenanthroline ligands, relative to the much smaller bpy. Several literature examples of electrostatic donor/polyoxometalate systems cite the extent of charge-transfer to be strongly dependant on the distance between the two moieties.[15] Despite this it has also been shown in Chapter 4 that effective charge-transfer can occur in the case of $[Ru(bpy)_2(PVP)_{10}]_{4.5}\alpha$-$[Mo_{18}O_{54}(SO_4)_2]$, which is obviously very bulky. However bonding would almost certainly be favoured on the bipyridine side of the Ru centers and hence charge-transfer character is observed in the resonance Raman spectra (Fig 6.3.2). It must therefore be concluded that complexes where all three ligands are bulky are bad candidates for sensitizing the Dawson polyoxometalates. It is likely that H-bond bridging from the excited state (ie: LUMO containing) ligand to the terminal polyoxometalate oxygen ligand is necessary for charge-transfer and photosensitization. The H-bond here will probably be to the terminal phenyl groups, which is poorly coupled to the phenanthroline moieties.

6.4 – Resonance Raman spectroscopy of novel ion-clusters with Os complexes:

In many of the ion clusters studied there were significant changes to the metal complex resonance Raman upon association with polyoxometalates. These new features were difficult to identify as discrete polyoxometalate modes, as no polyoxometalate modes appear in the vicinity of these features. In addition, some bipyridine based modes actually disappear upon association with the polyoxometalates. An example of this kind of spectral behaviour is given in Fig 6.4.2.

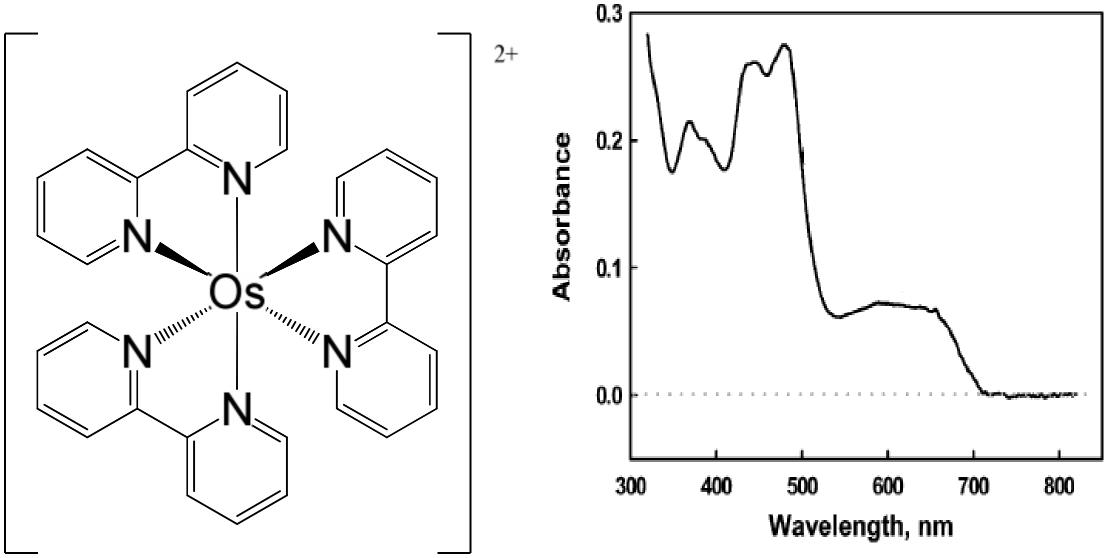

Fig 6.4.1: Structure of $[Os(bpy)_3]^{2+}$ (left) and UV/Vis spectrum of $[Os(bpy)_3]^{2+}$ in MeCN; spectrum was reproduced from [16]. Excitation at 480 nm gives rise to emission at 740 nm.

The structure and UV/Vis spectrum of $[Os(bpy)_3]^{2+}$ are presented in Fig 6.4.1. Os (II) polypyridyl complexes have very different properties than the corresponding Ru (II) complexes, due to the different relative energy levels of the metal bonding and antibonding orbitals. In the UV/Vis spectrum of $[Os(bpy)_3]^{2+}$ there are two important MLCT absorption bands in the visible region: an intense singlet absorption band centered at 450 nm and a weaker triplet absorption extending from 520 to 700 nm. Excitation into the ^{1}MLCT state is followed by rapid and efficient intersystem crossing to the ^{3}MLCT manifold, and long lived phosphorescence can occur from this state. In addition, unlike Ru complexes, the ^{3}MLCT can be excited directly, at lower wavelengths. The band at ultraviolet wavelengths (not shown) corresponds to the bpy $\pi \rightarrow \pi^*$ transition. In addition to the different spectroscopic properties, Os (II) complexes also exhibit lower oxidation potentials than their Ru (II) counterparts. The effects of these altered properties on the interaction with Dawson polyoxometalates is shown in Fig 6.4.2.

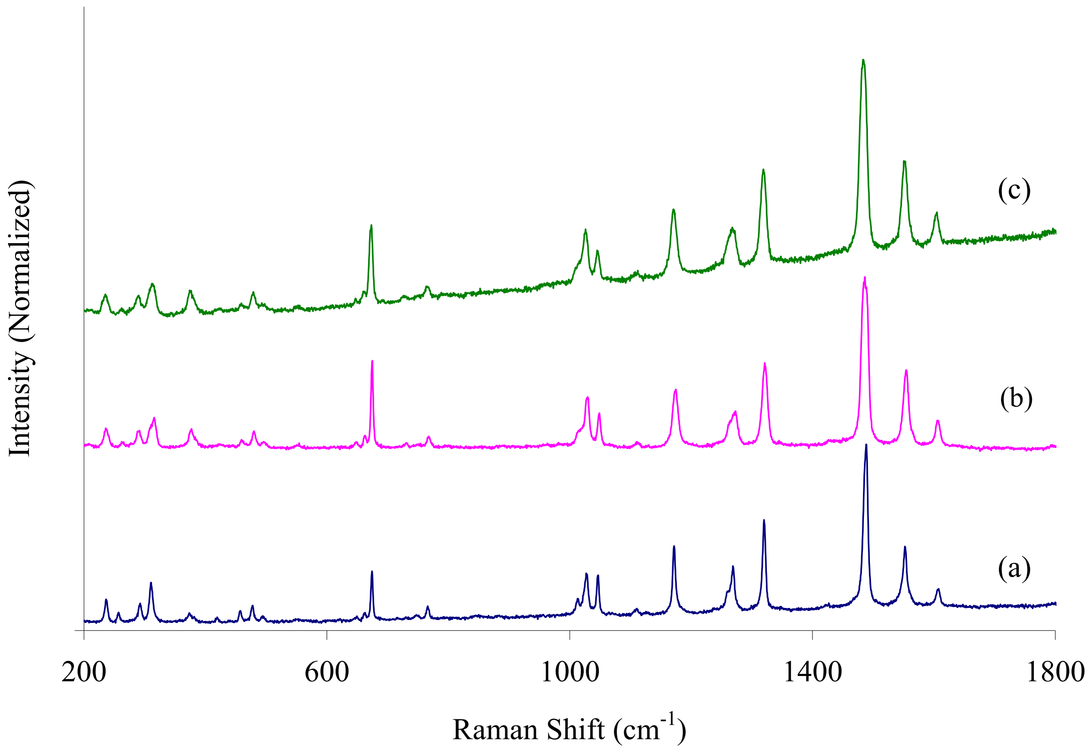

Fig 6.4.2 Resonance Raman spectra of (a) $[Os(bpy)_3]^{2+}$, (b) $[Os(bpy)_3]_2\gamma^*$-$[W_{18}O_{54}(SO_4)_2]$ and (c) $[Os(bpy)_3]_2\alpha$-$[Mo_{18}O_{54}(SO_4)_2]$in oven-dried KBr (~ 5 % w/w) under 514 nm excitation.

The spectra in Fig 6.4.2 reveal that coupling of $[Os(bpy)_3]^{2+}$ to the Dawson polyoxometalates results in very weak electronic interaction, as negligible spectral changes to the $[Os(bpy)_3]^{2+}$ bands are seen upon association. This is in stark contrast with $[Ru(bpy)_3]^{2+}$, as shown in Fig 6.1.1. Since the sterics of electrostatic association are expected to be identical in this case, it may be possible that the thermodynamics of charge-transfer are not favoured when Os is used. In addition, if H-bonding between bpy and the terminal polyoxometalate oxygen ligands is involved, the acidity of the bpy protons will be affected by the greater π-backbonding ability of Os, relative to Ru.

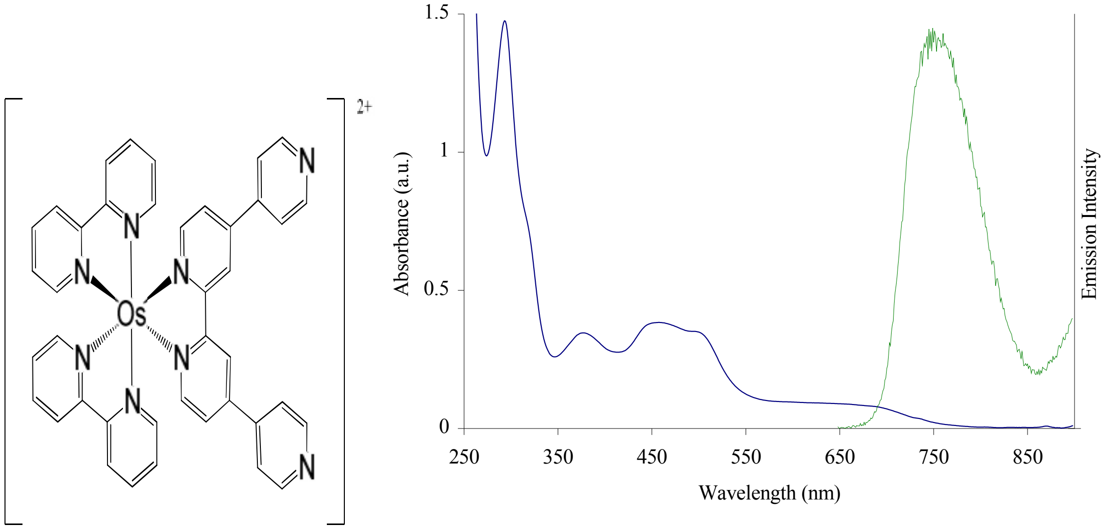

Fig 6.4.3: Structure of $[Os(bpy)_2(qpy)]^{2+}$ (left) and UV/Vis and emission spectra of $[Os(bpy)_2(qpy)]^{2+}$ in DMSO excited at 485 nm.

The structure and spectra of $[Os(bpy)_2(qpy)]^{2+}$ are shown in Fig 6.4.3. The ^{1}MLCT band at approximately 500 nm is weaker in this case, relative to the spectrum of $[Os(bpy)_3]^{2+}$. The emission maximum is also red-shifted by approximately 20 nm to ~ 760 nm. As in the case of $[Ru(bpy)_2(qpy)]^{2+}$, the free pyridyl nitrogen atoms can form coordination bonds with electron acceptors.

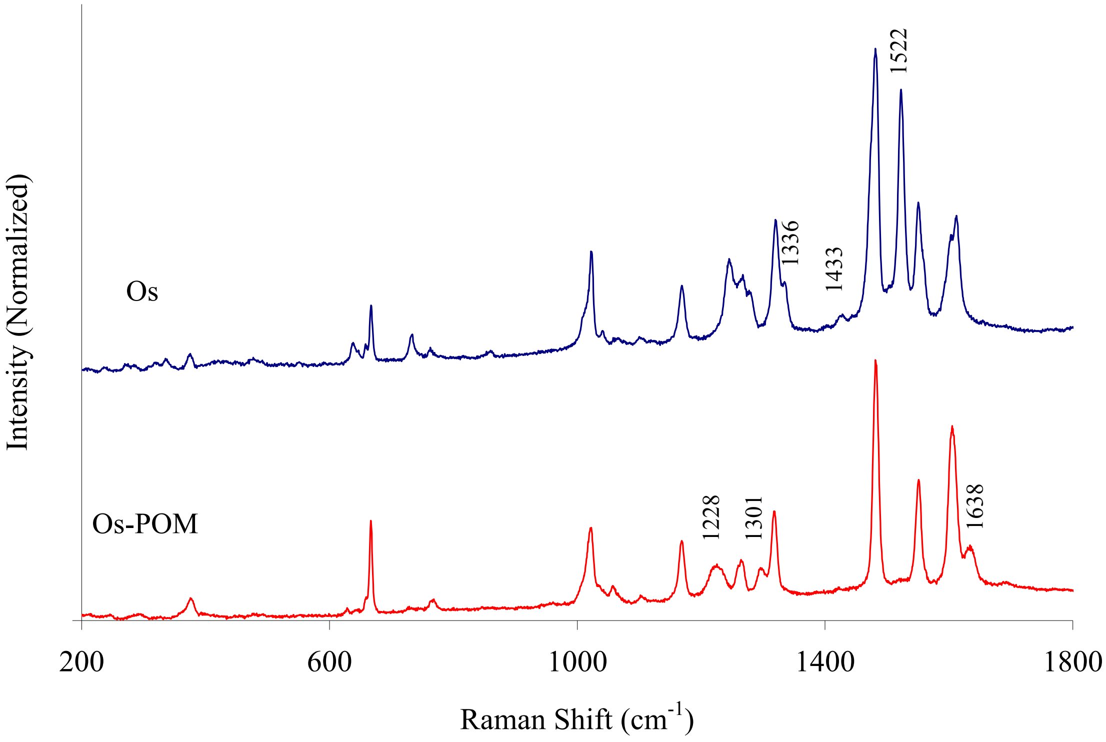

Fig 6.4.4: Resonance Raman spectra of $[Os(bpy)_2(qpy)]^{2+}$ and $[Os(bpy)_2(qpy)]_2[Mo_{18}O_{54}(SO_4)_2]$ in oven dried KBr discs (~ 5 % w/w) under 488 nm irradiation.

The spectra in Fig 6.4.4 show that the addition of the polyoxomolybdate to Os induces spectral changes in the Os resonance Raman. Strikingly the modes at 1522, 1433 and 1336 cm^{-1} disappear completely upon association, while new bands appear at 1638, 1301 and 1228 cm^{-1}. The main polyoxometalate band, the Mo-O terminal stretch, is very intense and usually appears between 800 and 900 cm^{-1}; however in this case there is no trace of this mode being resonant at 488 nm. There are several possible explanations for these spectral changes. Firstly the association of the Os to POM results in a significant change in the electronic environment experienced by the Os ligands, relative to the original ClO_4^- counterions. In the case of $[Ru(bpy)_2(qpy)]_2[Mo_{18}O_{54}(SO_4)_2]$ new modes grew-in at 1634 and 1335 cm^{-1}, relative to the spectrum of $[Ru(bpy)_2(qpy)]^{2+}$ alone, and a similar pattern is observed here with these modes appearing at 1638 and 1301 cm^{-1}. The mode that disappears at 1560 cm^{-1} in the Ru/molybdate adduct species disappears at 1522 cm^{-1} in the case of Os. It is therefore likely that both the Ru and Os complexes are interacting with $[Mo_{18}O_{54}(SO_4)_2]^{4-}$ in the same way, and this is likely to occur via the free pyridyl nitrogens on the qpy ligand. This data may indicate that binding of TM complexes to polyoxometalates through free pyridyl nitrogen atoms does not depend strongly on the identity of the cation metal. Mo is known to form coordination bonds with N but this is unlikely to be the binding mode in this case as it would almost certainly involve partial degradation of the robust POM structure.[17]

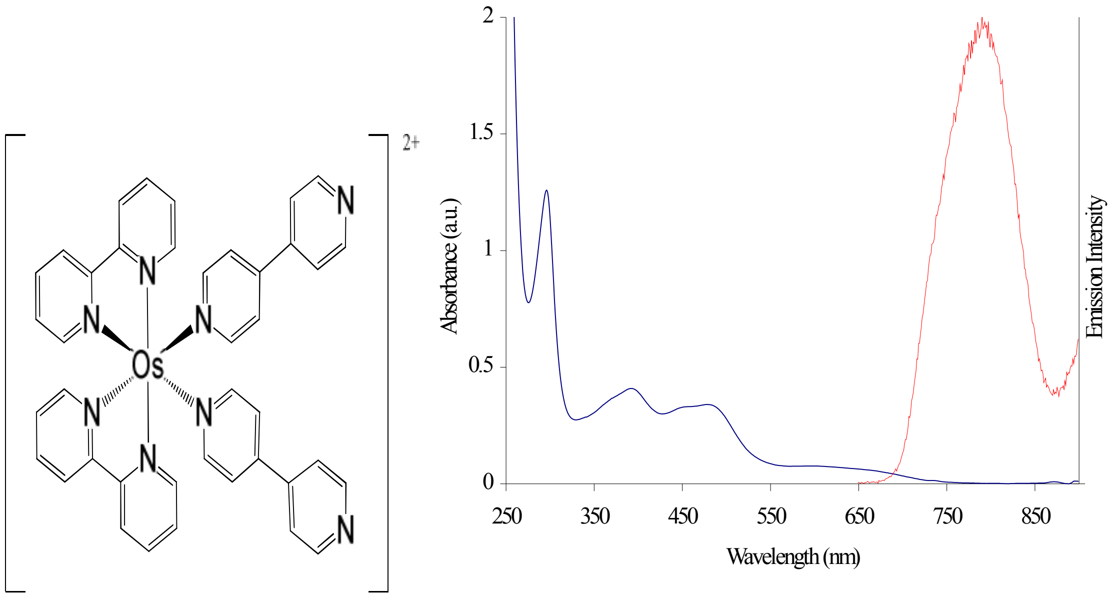

Fig 6.4.5: Structure of $[Os(bpy)_2(p0p)_2]^{2+}$ (left) and UV/Vis and emission spectra of $[Os(bpy)_2(p0p)_2]^{2+}$ in DMSO (~ 3 x 10^{-5} M) excited at 483 nm.

Fig 6.4.5 shows the structure and optical spectra of $[Os(bpy)_2(p0p)_2]^{2+}$ (sometimes called $[Os(2,2'\text{-}bpy)_2(4,4'\text{-}bpy)_2]^{2+}$). This complex is structurally similar to $[Os(bpy)_2(qpy)]^{2+}$ and hence has similar absorption and emission properties. The emission is red-shifted with respect to $[Os(bpy)_3]^{2+}$ and excitation at 483 nm yields an emission at ~ 795 nm. Like $[Os(bpy)_2(qpy)]^{2+}$, the free pyridyl nitrogen atoms can form dative covalent bonds.

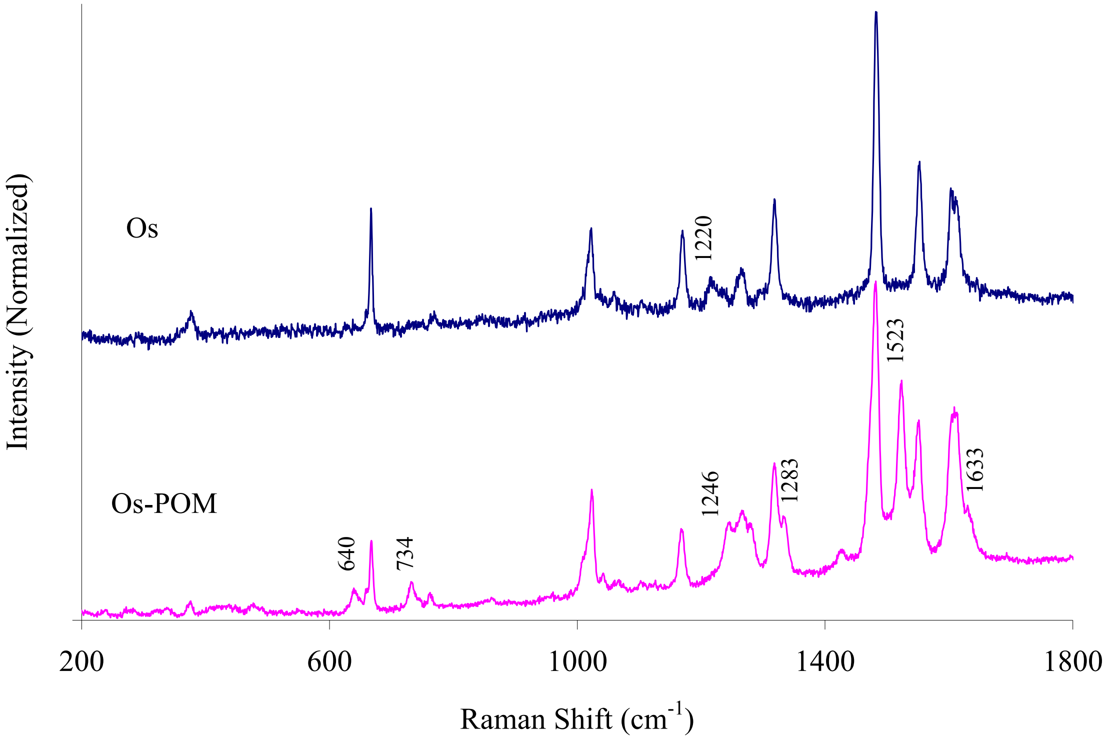

Fig 6.4.6: Resonance Raman spectra of $[Os(bpy)_2(p0p)_2]^{2+}$ and $[Os(bpy)_2(p0p)_2]_2$-$[Mo_{18}O_{54}(SO_4)_2]$ in oven-dried KBr (~ 5 % w/w) under 488 nm excitation.

The spectra of $[Os(bpy)_2(p0p)_2]^{2+}$ and its associated molybdate cluster are presented in Fig 6.4.6. The spectra show large similarities to those in Fig 6.4.4, where an almost isostructural Os complex was employed. New features grew in at 1633, 1283, 734 and 640 cm^{-1}. The changes in the spectra are again attributed to the free nitrogen groups coordinating to the polyoxomolybdate. However the band that appeared in the spectrum of $[Os(bpy)_2(qpy)]^{2+}$ at 1522 cm^{-1} and consequently disappeared upon Os/POM association is in this case only visible in the adduct spectrum. The reason for this difference in behaviour is unknown, but it may be that the qpy and p0p ligands move into resonance as a function of ion-association.

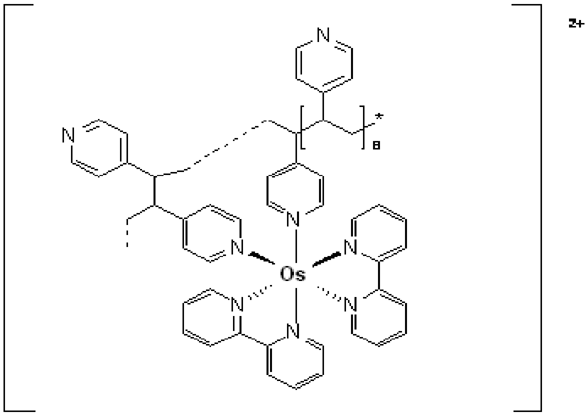

Fig 6.4.7: Structure of $[Os(bpy)_2(PVP)_{10}]^{2+}$.

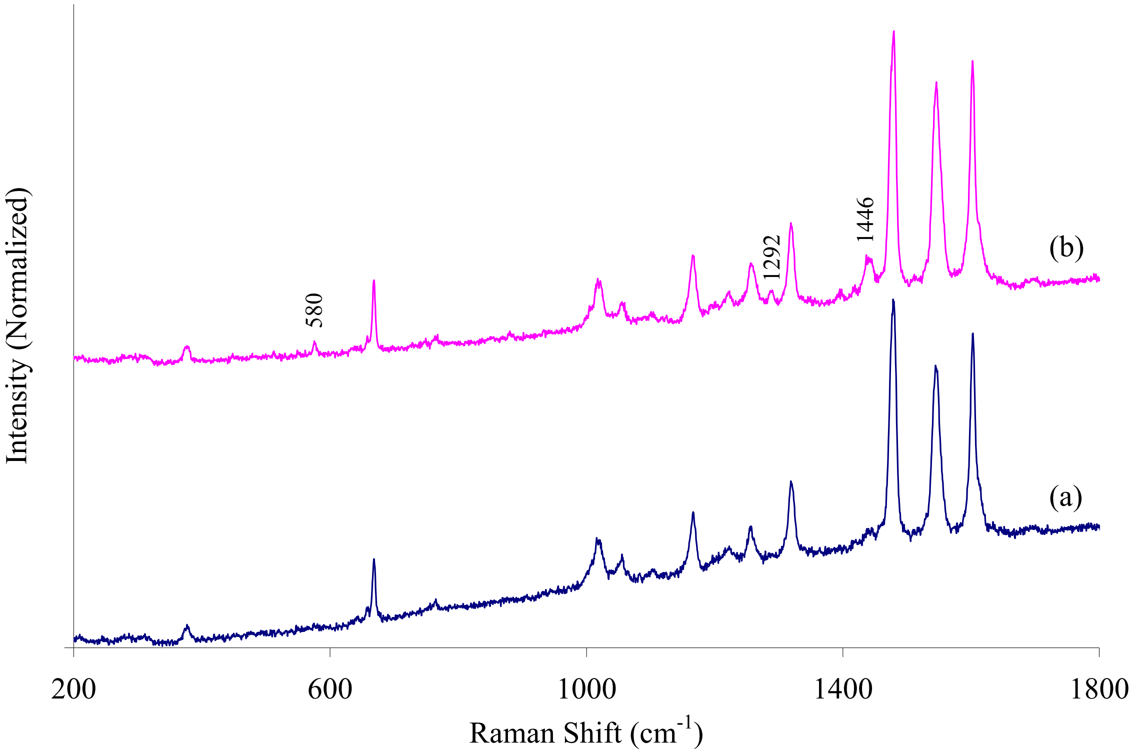

Fig 6.4.8: Resonance Raman spectra of (a) $[Os(bpy)_2(PVP)_{10}]^{2+}$ and (b) $[Os(bpy)_2(PVP)_{10}]_{4.5}\alpha$-$[Mo_{18}O_{54}(SO_4)_2]$in oven-dried KBr (~ 5 % w/w) under 514 nm excitation.

In direct comparison to the case of $[Ru(bpy)_2(PVP)_{10}]_{4.5}\alpha$-$[Mo_{18}O_{54}(SO_4)_2]$ discussed previously, Fig 6.4.8 shows the spectra obtained when the corresponding Os metallopolymer is employed. Some metallopolymer features are enhanced slightly in the adduct spectrum at 1446, 1292 and 580 cm^{-1} but no polyoxomolybdate modes appear resonant at this wavelength. In this case the structure and sterics of $[Os(bpy)_2(PVP)_{10}]_n\alpha$-$[Mo_{18}O_{54}(SO_4)_2]$ ion-cluster formation are identical to those in the case of $[Ru(bpy)_2(PVP)_{10}]_{4.5}\alpha$-$[Mo_{18}O_{54}(SO_4)_2]$. This trend mirrors the differences between $[Ru(bpy)_3]^{2+}$ and $[Os(bpy)_3]^{2+}$ and appears to confirm that the thermodynamics of charge-transfer from Os (II) polypyridyl complexes to polyoxometalates appear to be unfavourable for sensitisation.

6.5 – Resonance Raman spectroscopy of novel ion-clusters with Fe complexes:

In addition to the Os (II) and Ru (II) complexes some Fe (II) complexes were also investigated in this study. Iron (II) polypyridyl complexes are very different from both their corresponding Ru and Os analogues due to dramatic differences in their excited state potential energy surfaces. The biggest difference is manifested in the presence of several low lying Fe ligand-field states which promote extremely efficient thermal excited state decay, and hence iron polypyridyl complexes are non-luminescent. This deactivation pathway is highlighted in Fig 6.5.1.

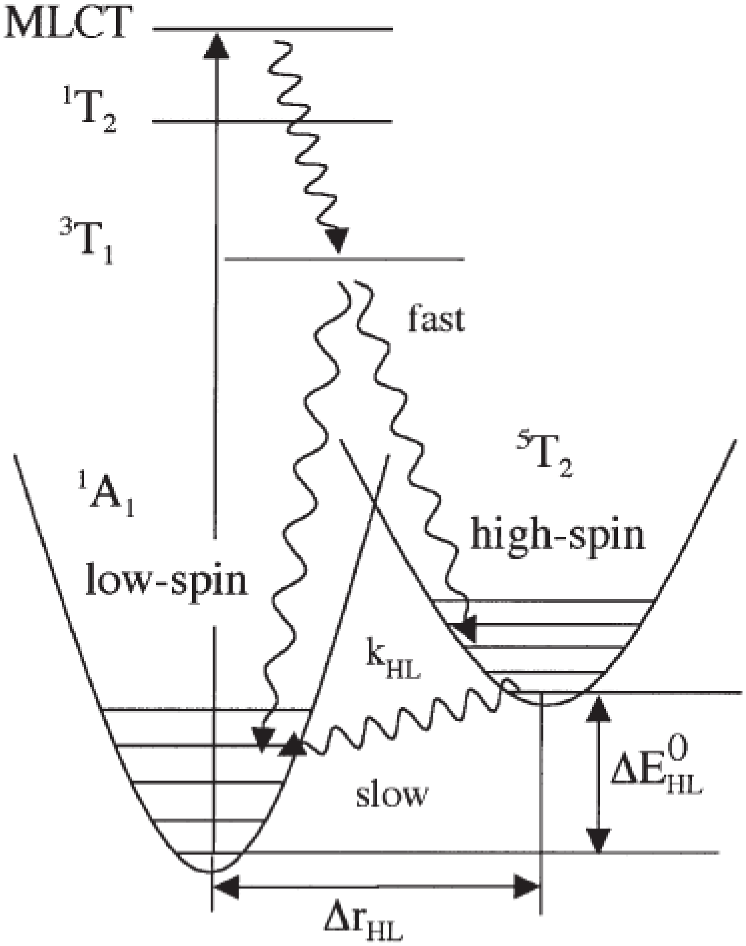

Fig 6.5.1: The electronic structure of $[Fe(bpy)_3]^{2+}$ including the low-spin $^1A_1$ ground state, excited ligand field states $^1T_2$ and $^3T_1$, and the low-lying MLCT state. Reproduced from [18].

The d-d transitions are not visible in the absorption spectrum of $[Fe(bpy)_3]^{2+}$ as their intensities are low relative to the adjacent intense MLCT band. However their presence is indirectly seen in their mediation of non-radiative decay. The double intersystem crossing ($^1T_2 \rightarrow {}^3T_1 \rightarrow {}^5T_2$) occurs through these states on a subpicoscond level, and the spin crossover back to the ground state is relatively long lived in comparison (nanosecond timescale, depending on the temperature).[18] As shown in Fig 6.5.1 this spin crossover is non-radiative and hence $[Fe(bpy)_3]^{2+}$ is non-emissive.

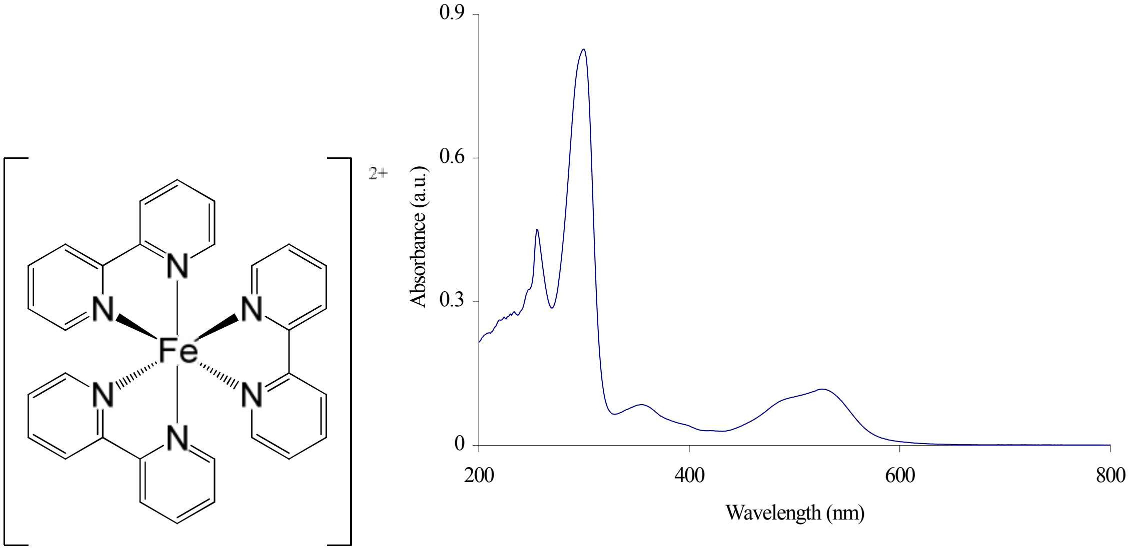

Fig 6.5.2: Structure of $[Fe(bpy)_3]^{2+}$ (left) and UV/Vis spectrum of $[Fe(bpy)_3](PF_6)_2$ in DMSO.

Fig 6.5.2 shows the structure and UV/Vis spectrum of $[Fe(bpy)_3]^{2+}$. The broad MLCT band is seen at approximately 530 nm, and the low intensity Laporte forbidden d-d transitions are underneath this peak.

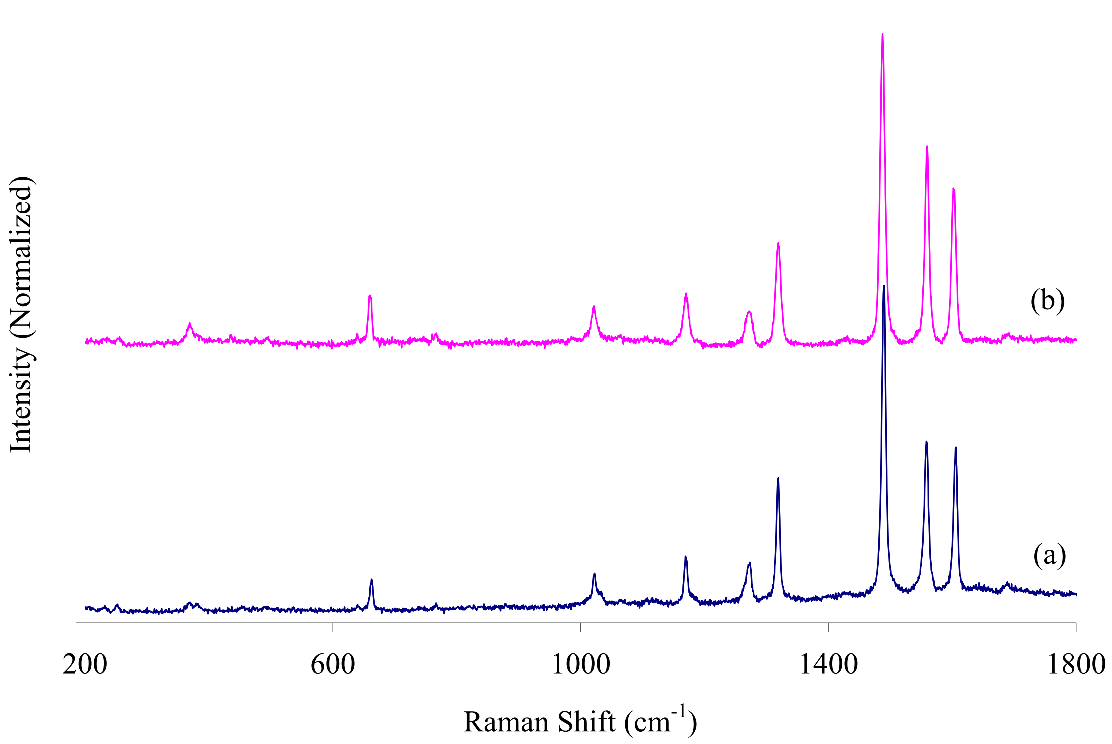

Fig 6.5.3: Resonance Raman spectra of (a) $[Fe(bpy)_3](PF_6)_2$ and (b) $[Fe(bpy)_3]_2\alpha$-$[Mo_{18}O_{54}(SO_4)_2]$ in KBr discs (~ 5 % w/w) under 488 nm laser excitation.

Fig 6.5.3 shows the Raman spectra of composites of $[Fe(bpy)_3]^{2+}$ with the Dawson polyoxometalates. In both cases no significant spectral changes are observed upon ionic association. In comparison with the spectrum of $[Ru(bpy)_3]_2\alpha$-$[Mo_{18}O_{54}(SO_4)_2]$ shown in Fig 6.1.1 it is again evident that the strong electronic communication observed in that case is not seen here. Like in the case of $[Ru(bpy)_3]^{2+}$, the ability of the complex to bind closely and strongly to the polyoxomolybdate should be high in this case as no bulky ligands are present to interfere with the bonding. The lack of polyoxomolybdate modes present in the spectrum of $[Fe(bpy)_3]_2\alpha$-$[Mo_{18}O_{54}(SO_4)_2]$ must therefore be attributed to poor orbital overlap or otherwise unfavourable thermodynamics.

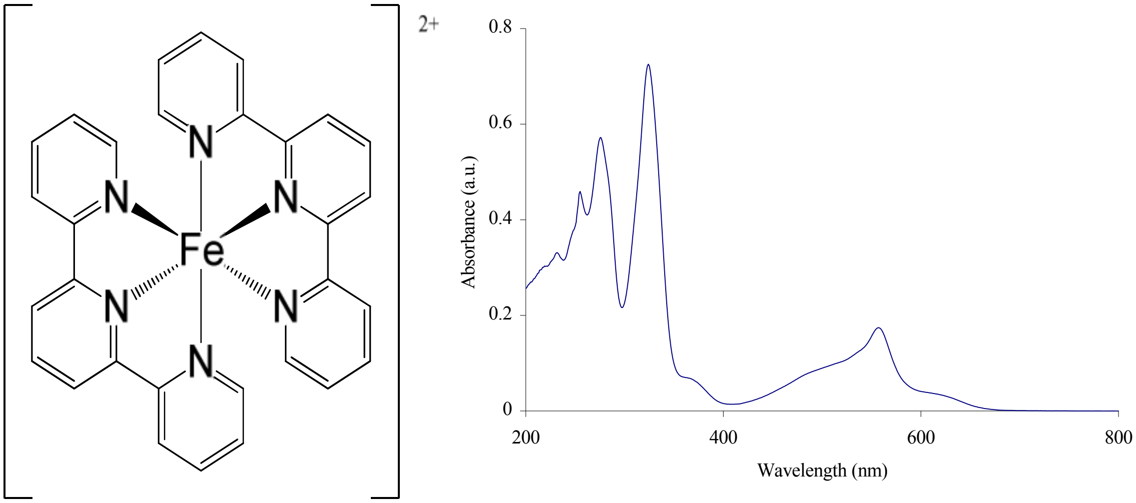

Fig 6.5.4: Structure of $[Fe(tpy)_2]^{2+}$ (left) and UV/Vis spectrum of $[Fe(tpy)_2](PF_6)_2$ in DMSO.

The structure and UV/Vis spectrum of $[Fe(tpy)_2]^{2+}$ is shown in Fig 6.5.4. The two tridentate terpyridine ligands give rise to an intense MLCT absorbance at approximately 570 nm. Like $[Fe(bpy)_3]^{2+}$, $[Fe(tpy)_2]^{2+}$ is also non-luminescent.

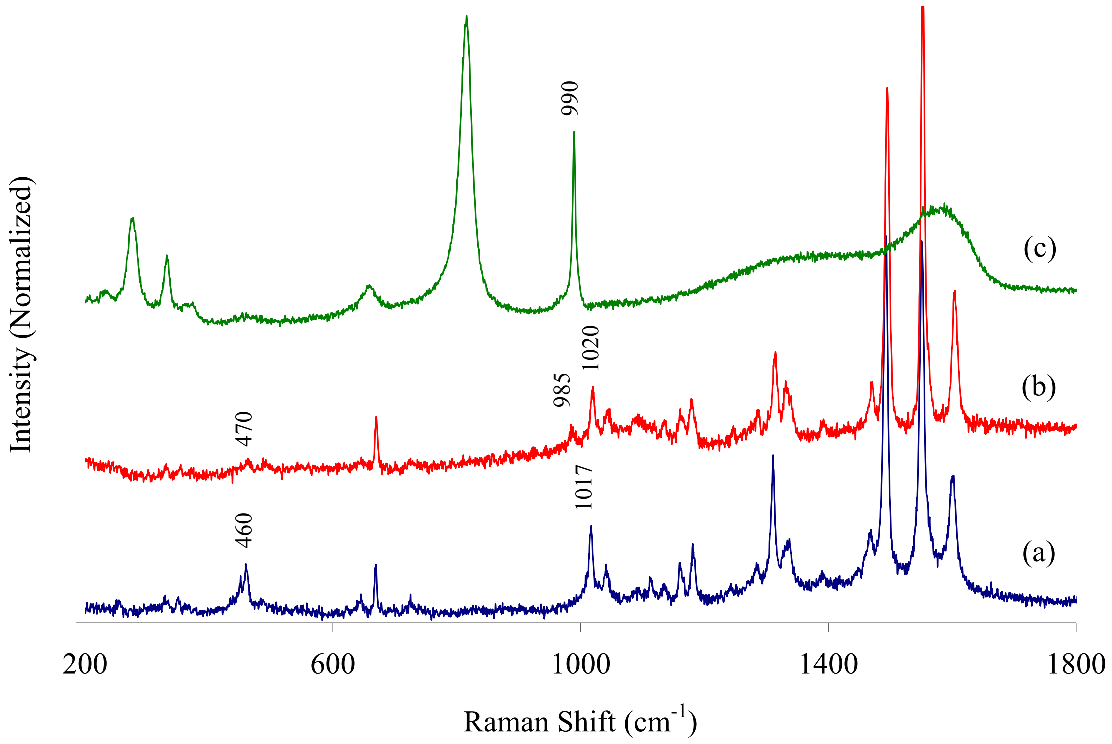

Fig 6.5.5: Resonance Raman spectra of (a) $[Fe(tpy)_2](PF_6)_2$, (b) $[Fe(tpy)_2]_2\alpha\text{-}[Mo_{18}O_{54}(SO_4)_2]$ and (c) $[(But)_4N]_4\alpha\text{-}[Mo_{18}O_{54}(SO_4)_2]$ in oven-dried KBr (~ 5 % w/w) under 488 nm excitation.

Fig 6.5.5 shows the change in the Raman spectroscopy upon binding of $\alpha\text{-}[Mo_{18}O_{54}(SO_4)_2]^{4-}$ to $[Fe(tpy)_2]^{2+}$. It appears as though the polyoxomolybdate mode at 990 cm^{-1} appears in the adduct spectrum at 985 cm^{-1}, possibly indicating a Fe-molybdate charge transfer transition is present at this wavelength. The Fe-terpy mode at 460 cm^{-1} is also affected upon binding to the POM, as it is shifted to 470 cm^{-1} and significantly reduced in intensity. Charge-transfer composites of Fe compounds and polyoxometalates have been observed previously. In the case of the Lindqvist polyoxometalates $[M_6O_{19}]^{2-}$ (where M = Mo, W) electrostatically bound to the cationic ferrocenyl $cpFecpCH_2N^+(CH_3)_3$ charge transfer bands were seen in the difference electronic spectra and the transient absorption spectra.[19] However the charge transfer character disappeared when the salt was dissolved in DMF and hence was attributed to close ion proximity via strong H-bonding in the solid state only. It may be that, in this case, close electrostatic packing of the two ions makes charge-transfer feasible. Therefore, it appears on the basis of electronic communication that the Fe complexes here are candidates for photosensitization, however, given the short-lived nature of the

Fe excited state it will be interesting to see whether they are capable in practice of sensitizing polyoxometalate photochemistry.

6.6 - Control spectra:

It is informative to compare the numerous spectra in sections 6.3 – 6.5 with a variety of controls to ensure that no false positive data is accidentally acquired. The basis of this chapter is that polyoxometalates alone are non-resonant under visible excitation and hence give extremely weak non-resonant Raman spectra under irradiation of 458, 488 or 514 nm. This knowledge, coupled with UV/Vis data indicating that intramolecular charge-transfer occurs upon Ru-polyoxometalate association, means we may be able to unambiguously assign which new optical transitions actually involve the polyoxoanions. Any polyoxoanion modes resonant under visible irradiation were concluded to be due to the presence of optical charge-transfer characteristics due to effective electronic coupling between ruthenium donor and polyoxometalate acceptor. Previous evidence points strongly to the fact that for the photochemistry to be sensitized this CT transition must be present. We believe it is likely that sensitization occurs through this transition. Therefore, we rationalized that resonance Raman could be used as a swift marker of likely sensitization as it can be readily used to confirm the presence of this transition. This argument is based on the assumption that the oxidized polyoxometalates used in this study are non-resonant in the visible region; however trace amounts of a resonantly absorbing impurity could lead to resonantly misidentification of resonantly enhanced Raman modes. The reduced polyoxometalates are well-known for their ability to absorb in the far-visible/near-infrared region, and it is possible that trace amounts of these reduced polyoxoanions could lead to the appearance of resonantly enhanced polyoxometalate modes under visible irradiation. Therefore control spectra of the reduced polyoxometalates were examined to identify what contribution, if any, they would make to resonance Raman spectra if present.

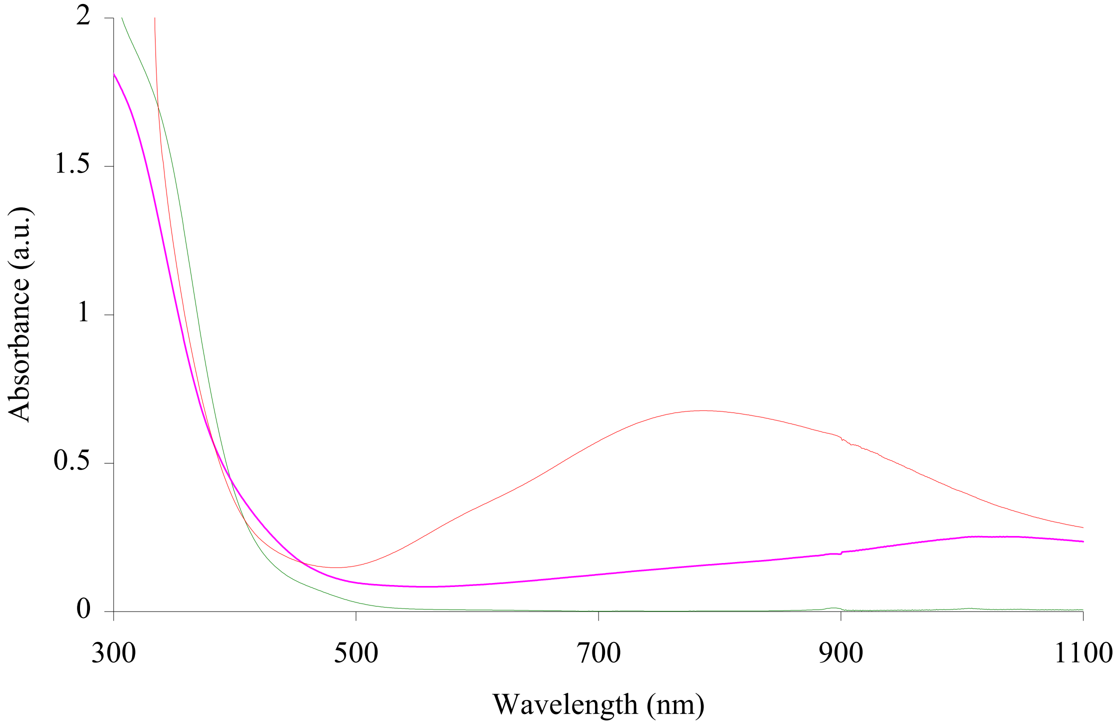

Fig 6.6.1: UV/Vis/NIR spectroelectrochemistry of ~ 2.9 x 10^{-4} M α-$[Mo^{VI}_{18}O_{54}(SO_4)_2]^{4-}$ (green), α-$[Mo^{VI}_{17}Mo^{V}O_{54}(SO_4)_2]^{5-}$ (pink) and α-$[Mo^{VI}_{16}Mo^{V}_{2}O_{54}(SO_4)_2]^{6-}$ (red) in MeCN containing 0.1 M $(But)_4NBr$.

The spectra of the reduced polyoxoanion species in Fig 6.6.1 were generated electrochemically by exhaustive one-electron reduction at 0.08 V and -0.4 V respectively in MeCN containing 0.1 M $(But)_4NBr$. These spectra have been reported previously and are typical of reduced polyoxomolybdates.[20] The new bands that grow in at low energy are due to intervalence charge-transfer transitions (IVCT) of the nature $Mo^{VI} \rightarrow Mo^{V}$. There are multiple sequential electrochemical reductions possible, some of which are proton-coupled in acidic media. These bands were probed using resonance Raman spectroscopy, and these spectra are shown in Fig 6.6.2.

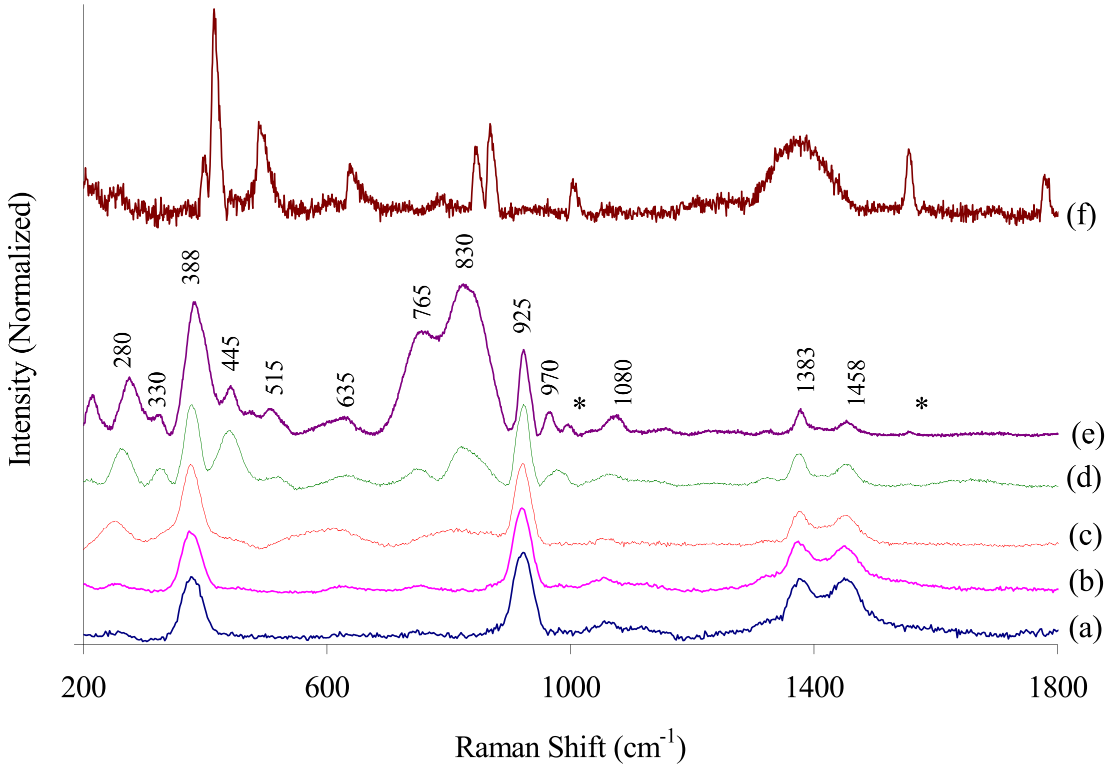

Fig 6.6.2: Resonance Raman spectroelectrochemistry of α-$[Mo^{VI}_{16}Mo^{V}_{2}O_{54}(SO_4)_2]^{6-}$ at (a) 458, (b) 488, (c) 514, (d) 633 and (e) 785 nm. The top trace (e) is the Raman spectrum (785 nm) of the MeCN/$(But)_4$NBr electrolyte used, and modes from this mixture are marked *.

Reduction of the polyoxometalate has a profound effect on its Raman spectrum. This is because as shown in Fig 6.6.1 the new optical transition is very broad, and is resonant with most of the excitation wavelengths explored here. However, as Fig 6.6.2 demonstrates none of the new modes are coincident with those identified as polyoxometalate modes seen in the adduct spectra throughout section 6.3 – 6.5. Thus the data in Fig 6.6.2 verify that the polyoxometalate modes identified in the adduct spectra in section 6.3 – 6.5 are not due to resonant enhancement of trace quantities of reduced product.

Another important control was required to ensure that any apparent new features do not appear to come into resonance as a function of increasing wavelength. This is because non-resonant Raman spectra of all modes in a system can be obtained at wavelengths where no chromophore absorbs and hence no resonance enhancement occurs, which would otherwise obscure all other modes. In Fig 6.6.3 the Ru to polyoxometalate charge-transfer transition of $[Ru(bpy)_2(PVP)_{10}]_{4.5}\alpha$-$[W_{18}O_{54}(PO_4)_2]$ is examined as a function of wavelength.

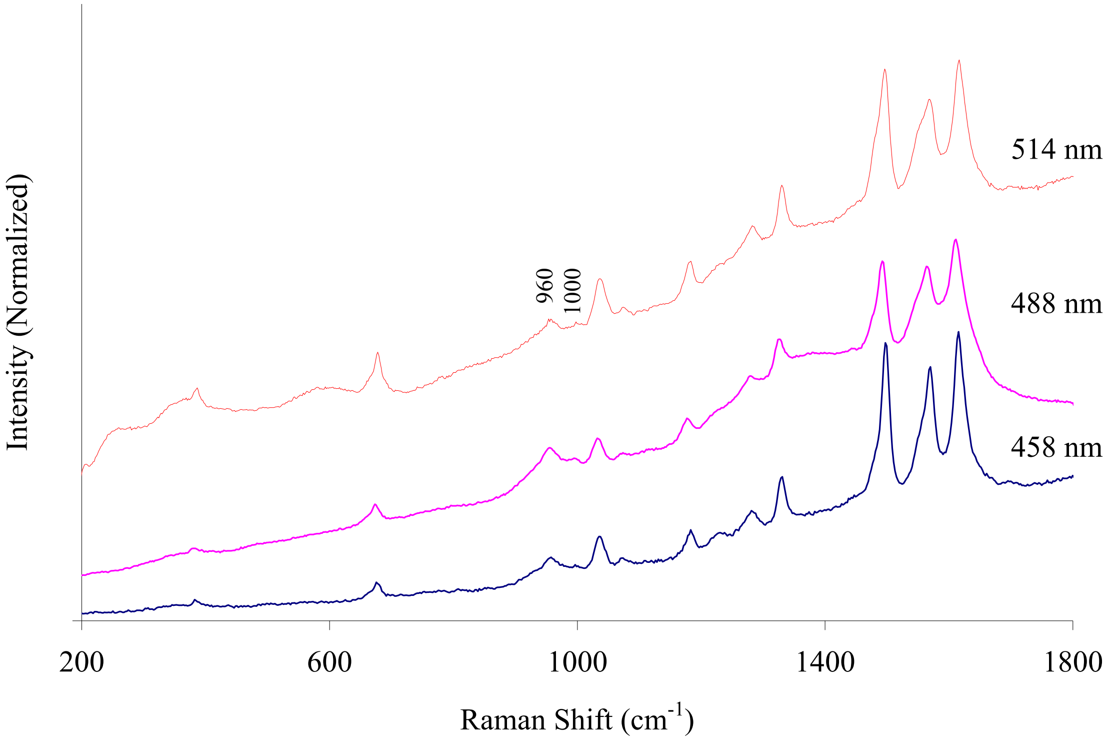

Fig 6.6.3: Resonance Raman spectra of $[Ru(bpy)_2(PVP)_{10}]_{4.5}\alpha$-$[W_{18}O_{54}(PO_4)_2]$ in a KBr disc (~ 5 % w/w) under 458, 488 or 514 nm irradiation.

Fig 6.6.3 demonstrates that the polyoxometalate mode seen at 960 cm^{-1} (488 nm spectrum is reproduced from Fig 6.3.1.2) appear resonantly enhanced under all three wavelengths. This is expected given the broad nature of the new optical transition. However it is clear that the modes are enhanced the most strongly under 488 nm excitation. The polyoxometalate mode has a higher intensity relative to the bpy peaks under 488 nm irradiation relative to when the cluster is excited at 458 or 514 nm. This strongly suggests that the new optical transition comes into resonance most strongly around the 488 nm laser line, and that the transition intensity drops before reaching 514 nm. Interestingly, this was not seen in the case of $[Ru(bpy)_2(PVP)_{10}]_{4.5}\alpha$-$[Mo_{18}O_{54}(SO_4)_2]$ (see

Chapter 4) when the new transition was demonstrated by resonance Raman and difference spectroscopy to tail strongly into the red. This difference in optical behaviour between the new transition involving the molybdate and the tungstate is not unexpected as molybdates are well known to absorb at higher wavelengths than their corresponding tungstates.[21]

The final control experiments performed were to ensure that any spectral changes observed upon complex electrostatic association was due to a true chemical interaction between the two species. In this experiment $[Os(bpy)_2(qpy)]_2\alpha\text{-}[Mo_{18}O_{54}(SO_4)_2]$ was synthesized and isolated according to standard methods. The sample was washed repeatedly, dried and ground into KBr for analysis. For comparison, two equivalents of $[Os(bpy)_2(qpy)](ClO_4)_2$ and one equivalent of $[(But)_4N]_4\alpha\text{-}[Mo_{18}O_{54}(SO_4)_2]$ were added to a mortar and pestle and simply ground together into a KBr disc. The Raman spectra demonstrate that no polyoxomolybdate modes are visible at this wavelength and that the Os complex undergoes negligible spectral change. The spectra are shown in Fig 6.6.4.

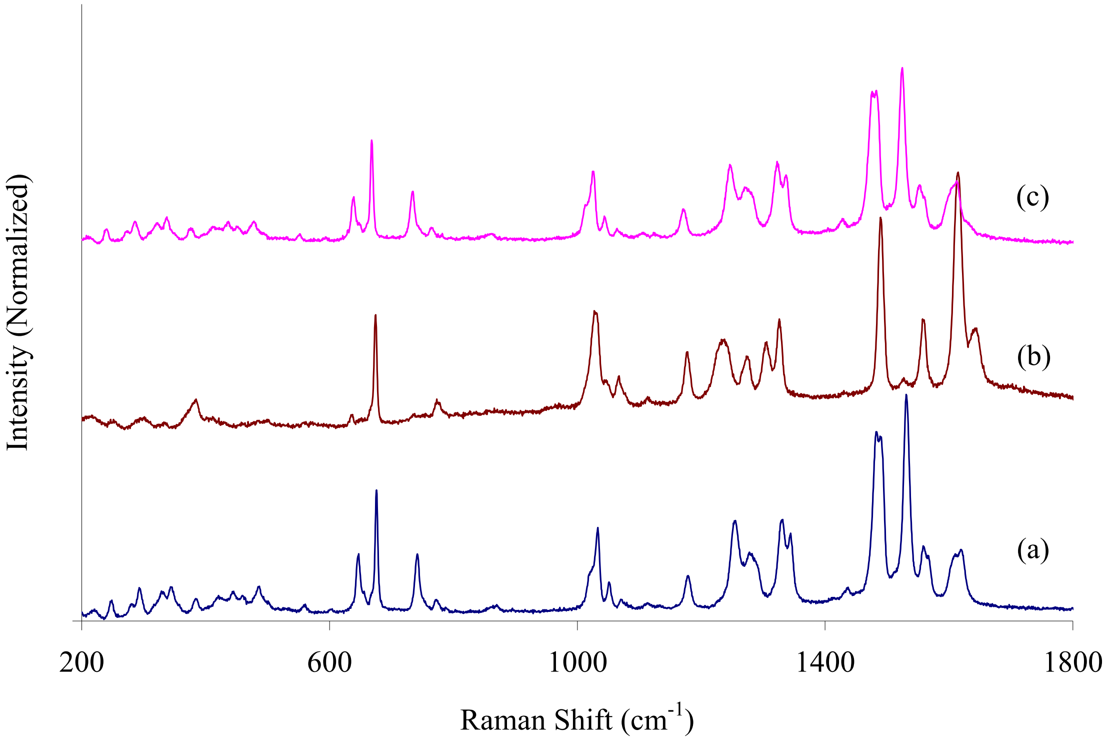

Fig 6.6.4: Resonance Raman spectra of (a) $[Os(bpy)_2(qpy)](ClO_4)_2$, (b) $[Os(bpy)_2(qpy)]_2\alpha$-$[Mo_{18}O_{54}(SO_4)_2]$ and (c) a solid mixture of unreacted $[Os(bpy)_2(qpy)](ClO_4)_2$ and $[(But)_4N]_4\alpha$-$[Mo_{18}O_{54}(SO_4)_2]$ in oven dried KBr discs (~ 5 % w/w) under 514 nm irradiation.

In these spectra it is demonstrated that the spectral changes upon addition of polyoxometalate to Os complex only occur when the two ions are paired together chemically in solution, and not through a trivial interaction with adjacent molecules. This demonstrates unambiguously that the changes in the Raman spectra arise out of electrostatic association only. It also demonstrates that residual $[(But)_4N]^+$ and $(Br)^-$ ions have no effect on the spectroscopy.

6.7 – Conclusions:

Evidence from this and previous work strongly indicates that an optical charge transfer transition between metal cation and anion is both necessary and indicative of visible sensitization of the polyoxometalate photochemistry by the metal cation. The most facile way of identifying this transition is to use resonance Raman spectroscopy as M-O vibrations become apparent when the charge transfer is operative at excitation wavelengths at which the polyoxometalate alone is not resonant. In this chapter we exploit this observation to take a broad combinatorial approach to identifying cation and anion pairs that are likely to lead to photosensitized photoelectrochemistry.

A total of 14 metal cations comprising Fe, Os and Ru (II) polypyridyl complexes were combined with the Dawson polyoxometalates to form electrostatic clusters, and their resonance Raman spectroscopy were examined under visible irradiation. Several of the systems analyzed showed the presence of both metal complex and polyoxometalate under visible irradiation and were successfully investigated in photoelectrochemical systems (see Chapters 4 and 5). Some other complexes have also been earmarked as potential sensitizers in future photoelectrochemical systems, in particular $[Fe(tpy)_2]^{2+}$ showed signs of effective electronic communication with α-$[Mo_{18}O_{54}(SO_4)_2]^{4-}$; however most of the complexes examined showed little or no signs of strong electronic communication between the two ions. In particular metal complexes with several bulky ligands, such as $[Ru(dpp)_3]^{2+}$, $[Ru(dpp)_2(caip\text{-}COOH)]^{2+}$ and $[Ru(dppz)_2(caip\text{-}COOH)]^{2+}$ showed no signs of electronic interaction with the polyoxoanions. This was attributed to the remoteness of any intramolecular H-bonding from the Ru centre which is likely to promote intramolecular charge-transfer. In other cases where the sterics of ion-pairing were favourable no polyoxometalate modes were observed. Poor electronic communication was observed when $[Fe(bpy)_3]^{2+}$ and $[Os(bpy)_3]^{2+}$ were employed, which are isostructural with $[Ru(bpy)_3]^{2+}$, and the differences in behaviour here were attributed to either poor donor/acceptor orbital overlap or unfavourable thermodynamics. Unfortunately relatively few donor-acceptor complex systems were successfully identified. In order to postulate an empirical relationship between ion-selection and potential sensitization photoelectrochemistry will be performed in future work on the pairs exhibiting the new optical transition. Sterics are extremely likely to play a role, and has been mentioned as an important factor in previous charge-transfer electrostatic polyoxometalate clusters.[15, 22] Future work will focus on further exploiting this method for rapidly identifying sensitized ion-clusters and will also focus on conducting detailed photoelectrochemistry of these ionic composites.

6.8 - References:

---

[1] T. E. Keyes, E. Gicquel, L. Guerin, R. J. Forster, V. M. Hultgren, A. M. Bond, and A. G. Wedd, *Inorg. Chem.*, 2003, **42**, 7897 - 7905.

[2] J. J. Walsh, D-L. Long, L. Cronin, A. M. Bond, R. J. Forster and T. E. Keyes, *Dalton Trans.*, 2011, **40**, 2038 - 2045.

[3] N. Fay, V. M. Hultgren, A. G. Wedd, T. E. Keyes, R. J. Forster, D. Leane and A. M. Bond, *Dalton Trans.*, 2006, 4218 - 4227.

[4] J. B. Cooper, D. M. Way, A. M. Bond and A. G. Wedd, *Inorg. Chem.,* 1993, **32**, 2416.

[5] P. J. S. Richardt, R. W. Gable, A. M. Bond and A. G. Wedd, *Inorg. Chem*., 2001, **40**, 703 - 709.

[6] I-M. Mbomekalle, Y. Wei Lu, B. Keita and L. Nadjo, *Inorg. Chem. Commun.*, 2004, **7**, 86 - 90.

[7] V. M. Hultgren, A. M. Bond and A. G. Wedd, *J. Chem. Soc., Dalton Trans*., 2001, 1076 - 1082.

[8] J. R. Ferraro, *Introduction to Raman Spectroscopy*, Academic Press, New York, 1994.

[9] R. Ballardini, M. T. Gandolfi and V. Balzani, *Inorg. Chem*., 1987, **26**, 862 - 867.

[10] "Photophysics of unusual electrostatic adducts of the metallopolymers $[Ru(bpy)_2(CAIP)CoP_7]^{2+}$ and $[Ru(bpy)_2(PVP)_{10}]^{2+}$ with the Dawson type α-$[Mo_{18}O_{54}(SO_4)_2]^{4-}$." Manuscript in preparation.

[11] M. K. Seery, L. Guerin, R. J. Forster, E. Gicquel, V. M. Hultgren, A. M. Bond, A. G. Wedd, and T. E. Keyes, *J. Phys. Chem. A*, 2004, **108**, 7399 - 7405.

[12] J. Song, Z. Luo, H. Zhu, Z. Huang, T. Lian, A. L. Kaledin, D. G. Musaev, S. Lense, K. I. Hardcastle and C. L. Hill, *Inorg. Chim. Acta*, 2010, **363**, 4381 - 4386.

[13] J. Zhu, Q. Zeng, S. O'Carroll, T. E. Keyes and R. J. Forster, *Electrochem. Commun.,* 2011, 13, 899 - 902.

---

[14] R. J. Forster, Y. Pellegrin, D. Leane, J. L. Brennan and T. E. Keyes, *J. Phys. Chem. C*, 2007, **111**, 2063 - 2068.

[15] L. Ruhlmann, C. Costa-Coquelard, J. Hao, S. Jiang, C. He, L. Sun and I. Lampre, *Can. J. Chem.*, 2008, **86**, 1034 -1043.

[16] G. B. Shaw, D. J. Styers-Barnett, E. Z. Gannon, J. C. Granger and J. M. Papanikolas, *J. Phys. Chem. A*, 2004, **108**, 4998 - 5006.

[17] C. Cornioley-Deuschel and A. von Zelewsky, *Inorg. Chem.*, 1987, **26**, 963 - 965.

[18] A. Hauser, N. Amstutz, S. Delahaye, A. Sadki, S. Schenker. R. Sieber and M. Zerara, *Struct. Bond.*, 2004, **106**, 81 - 96.

[19] P. L. Veya and J. K. Kochi, *J. Organomet. Chem.*, 1995, **488**, C4 - C8.

[20] D. M. Way, J. B. Cooper, M. Sadek, T. Vu, P. J. Mahon, A. M. Bond, R. T. C. Brownlee and A. G. Wedd, *Inorg. Chem.,* 1997, **36***,* 4227 - 4233.

[21] E. Papaconstantinou, *Chem. Soc. Rev.*, 1989, **18**, 1 - 31.

[22] P. Le Maguere, S. M. Hubig, S. V. Lindeman, P. Veya, and J. K. Kochi, *J. Am. Chem. Soc*., 2000, **122**, 10073 - 10082.

Chapter 7:

Conclusions and future work

The key goals of this thesis were twofold. Firstly, to investigate the photophysics of a variety of polyoxometalate/transition metal complex ion-clusters in order to provide some insight into what materials are capable of visible light sensitization of polyoxometalate photocatalysis; and secondly to use this knowledge to produce an optimized interfacial photoelectrochemical system. Chapter 3 explored the photophysics and photochemistry of $[Ru(bpy)_3]_2[Mo_{18}O_{54}(SO_3)_2]$, where bpy is 2, 2'-bipyridyl and $[Mo_{18}O_{54}(SO_3)_2]^{4-}$ is either the α or β-sulfite containing polyoxomolybdate. It was found that the sulfite anions form complex adducts with $[Ru(bpy)_3]^{2+}$ whose properties are considerably different from those formed with the analogous sulfate anion $[Mo_{18}O_{54}(SO_4)_2]^{4-}$, despite strong structural analogy. The K_a values inferred for the cluster complexes were 5.9×10^6 and 1.0×10^7 for the α and β-based clusters respectively. Although these new sulfite-containing clusters exhibit intramolecular charge-transfer transitions they were significantly weaker than in the case of the sulfate anion. This was reflected in the fact that no resonance Raman for these transitions were recorded and no visible-light sensitized POM photochemistry of benzyl alcohol substrate was observed when a film of the composite material was drop-cast onto an ITO electrode.

Ultimately, for photoelectrochemical applications, interfacial assemblies of polyoxometalate and sensitizing cations would be the best format for application. Therefore we explored the spectroscopy and photophysics of hydrogel metallopolymers incorporating $[Ru(bpy)_3]^{2+}$ analogues. In Chapter 4 the photophysics of a novel family of metallopolymers $[Ru(bpy)_2(\text{caip co-poly})_n]^{2+}$ (n = 5, 7, 9) were thoroughly investigated as a function of solvent pH and polarity and their properties compared with the parent cation. It was observed that increasing the chain length of the polymer had little impact on the electrochemistry and spectroscopy of the luminophore, as the excited state lies on the bipyridyl ligands and the metal centers are sufficiently separated so that inter-metal communication does not occur on a measurable scale, and this was also demonstrated by cyclic voltammetry which revealed that changing the metallopolymer loading had only a minor impact on the D_{CT} values of polymer thin films. Studies of the pH dependence of the polymers revealed the presence of three forms of the metallopolymers. At high pH values the imidazole moiety on the caip ligand was fully deprotonated and resonance Raman spectra revealed that the nature of the lowest energy optical transition was dependent on pH. The luminescent behaviour showed strong solvent dependence. In particular the polymers exhibited anomalous behaviour in DMSO, which tentatively was speculated to be due to interaction of the DMSO with the polymer backbone, and fluorescence anisotropy will be performed in future investigate this phenomenon.

The photophysics of $[Ru(bpy)_2(PVP)_{10}]^{2+}$ and the newly characterized $[Ru(bpy)_2(\text{caip co-poly})_7]^{+}$ were then investigated and compared in the presence of the sulfate Dawson polyoxomolybdate α-$[Mo_{18}O_{54}(SO_4)_2]^{4-}$. UV/Vis spectroscopy revealed the formation of electrostatic adducts of unexpected stoichiometries in solution, with the clusters $[Ru(bpy)_2(PVP)_{10}]_{4.5}$α-$[Mo_{18}O_{54}(SO_4)_2]$ and $[Ru(bpy)_2$(caip co-poly$)_7]_5$α-$[Mo_{18}O_{54}(SO_4)_2]$ appearing to be favoured. Difference spectroscopy revealed that the formation of $[Ru(bpy)_2(PVP)_{10}]_{4.5}$α-$[Mo_{18}O_{54}(SO_4)_2]$ in MeCN led to the appearance of a broad new intramolecular charge-transfer band stretching from 450 nm to 700 nm; however no such band was evident for $[Ru(bpy)_2$(caip co-poly$)_7]_5$α-$[Mo_{18}O_{54}(SO_4)_2]$. Stern-Volmer plots were used to estimate K_a values of 6.2×10^5 and 1.1×10^6 for the $[Ru(bpy)_2(PVP)_{10}]_{4.5}$α-$[Mo_{18}O_{54}(SO_4)_2]$ and $[Ru(bpy)_2$(caip co-poly$)_7]_5$α-$[Mo_{18}O_{54}(SO_4)_2]$ cluster ratios respectively. As the systems are polymeric the Perrin model was explored as a fit to the luminescent quenching data and was found to give good fits to the quenching data. From this model quenching sphere radii R_S were estimated to be 4.7 ± 0.1 and 5.7 ± 0.1 Å for $[Ru(bpy)_2(PVP)_{10}]_{4.5}$α-$[Mo_{18}O_{54}(SO_4)_2]$ and $[Ru(bpy)_2$(caip co-poly$)_7]_5$α-$[Mo_{18}O_{54}(SO_4)_2]$ respectively. These numbers are acceptable for a static charge-transfer quenching process; and energy transfer can been ruled out as a mechanism due to thermodynamic considerations (ie: poor donor-acceptor spectral overlap can rule out Forster energy transfer. In addition, Dexter energy transfer is collisional and we have demonstrated by TCSPC that the quenching mechanism is predominantly static). Surprisingly, lifetime data also indicated a weak dynamic quenching component to the behaviour of both polymers by α-$[Mo_{18}O_{54}(SO_4)_2]^{4-}$. Resonance Raman spectroscopy of the associated cluster complexes was undertaken in the solid state and confirmed that the new optical transition seen in the difference spectra was due to the formation of a new low-lying intramolecular charge-transfer state involving both metallopolymer and polyoxoanion. For both metallopolymer composites drop-cast onto ITO working electrodes and irradiated with visible light in the presence of benzyl alcohol substrate no enhanced photochemistry was observed in either case. Subsequent studies by Zhu *et al*. demonstrated that self-assembled interfacial films of the $[Ru(bpy)_2(PVP)_{10}]_{4.5}$α-$[Mo_{18}O_{54}(SO_4)_2]$ composite did result in sensitized photochemistry in the visible, but $[Ru(bpy)_2$(caip co-poly$)_7]_5$α-$[Mo_{18}O_{54}(SO_4)_2]$ did not. The differences in Zhu's results and the results obtained here are in the film formation process, and his data also suggested that film thickness is a defining factor in photocurrent generating efficiency and that drop-casting is not a viable method of thin film formation for photoelectrochemical studies. We therefore concluded that strong electronic interaction between polyoxometalate and sensitizer is necessary for the formation of the charge-transfer state if this state is to lead to visible light sensitized photochemistry.

In Chapter 5 the photophysical and photoelectrochemical properties of both ion-clusters and interfacial assemblies of $[Ru(bpy)_2(PVP)_{10}]^{2+}$ and α-$[P_2W_{18}O_{62}]^{6-}$ were compared, as the tungstates are known to have more negative reduction potentials which means a larger overpotential can be applied to reoxidise the reduced film after photocatalysis. UV/Vis and emission spectroscopy revealed the presence of 4.5:1 Ru:POW clusters in solution, with K_a values of 1.2 x 10^5 (from UV/Vis data) and 1 x 10^5 (from emission data) extrapolated from the Bourson-Valeur model for static association. The Perrin model for static association was also applied to the quenching data. The model fit the data well over a limited low concentration range, and yielded a quenching sphere radius R_S of 2.2 ± 0.1 Å; however over the full quenching range the model did not fit as two linear regions were observed which was tentatively attributed to formation of aggregates of the polymer forming upon addition of polyoxotungstate as a consequence of the greatly increased ionic strength of the mixture solution. When the Perrin equation was applied to the second linear region an R_S of 4.0 ± 0.1 Å; which is closer to the values obtained in Chapter 4 for $[Ru(bpy)_2(PVP)_{10}]_{4.5}\alpha$-$[Mo_{18}O_{54}(SO_4)_2]$ and $[Ru(bpy)_2(\text{caip co-poly})_7]_5\alpha$-$[Mo_{18}O_{54}(SO_4)_2]$. However both 2.2 and 4.0 Å are good estimates for charge-transfer quenching distance. The proposed aggregation will be addressed in the future with fluorescence anisotropy and DLS measurements.

Overall from these studies and previous literature we conclude that visible light sensitization of the Dawson polyoxomolybdate requires (a) strong electronic communication manifested by the appearance of a broad, low-energy charge-transfer band upon association; (b) appearance of polyoxometalate terminal oxygen modes in the resonance Raman spectra of the new transition, indicating H-bond bridging between the two ions which can facilitate CT; and (c) self-assembled composite material films on electrode surfaces instead of drop-cast films. So finally, Chapter 6 took a combinatorial approach to identifying pairs of cations and polyoxoanions which exhibited the new optical charge transfer using resonance Raman study of a range of TM complexes with a variety of Dawson polyoxometalates. Two of the composite material systems in which polyoxometalate modes were resonantly enhanced under visible irradiation were employed in photoelectrochemical studies ($[Ru(bpy)_2(PVP)_{10}]^{2+}$/α-$[S_2Mo_{18}O_{62}]^{4-}$ in Chapter 4 and $[Ru(bpy)_2(PVP)_{10}]^{2+}$/α-$[P_2W_{18}O_{62}]^{6-}$ in Chapter 5); the other complexes investigated by Raman were not employed in photoelectrochemical experiments. Future work will focus on the $[Fe(tpy)_2]^{2+}$/α-$[S_2Mo_{18}O_{62}]^{4-}$ system, which appeared to show the same resonantly enhanced polyoxomolybdate mode identified in the metallopolymer systems mentioned above, despite the very short excited state lifetime typical of Fe (II) polypyridyl complexes. Interestingly, $[Os(bpy)_2(PVP)_{10}]^{2+}$, $[Os(bpy)_3]^{2+}$ and $[Fe(bpy)_3]^{2+}$ showed little promise as sensitizers despite their structural analogies to $[Ru(bpy)_2(PVP)_{10}]^{2+}$ and $[Ru(bpy)_3]^{2+}$. In addition, $[Ru(dpp)_3]^{2+}$ which is isoelectronic with $[Ru(bpy)_3]^{2+}$, exhibited negligible spectral changes on association with α-$[S_2Mo_{18}O_{62}]^{4-}$, which strongly indicates that sterics play a role. We propose that the strength of the intramolecular charge-transfer transition in these cluster complexes is directly related to the visible sensitization of polyoxometalate photochemistry. We also believe that the strength of this transition is dependent on favorable thermodynamics, which are apparently imbued by Ru and possibly Fe but not Os; and on the ability of the donor/acceptor complex to bind closely. Literature studies of CT complexes involving polyoxometalates and donor molecules have demonstrated that the strength of CT transitions is distance dependent; hence we postulate that complexes with large ligands such as dpp and caip are unlikely candidates for sensitizers.

From the photophysical point of view, future work could focus on selecting the polyoxometalate/transition metal complex system with the largest possible gap between their initial redox processes, which would enable us to apply a large overpotential during photoelectrochemistry to reoxidise the films. This would very likely be achieved through the use of polyoxotungstates (which have more negative reduction potentials than molybdates) and iridium polypyridyl complexes. Iridium polypyridyl complexes exhibit extremely high metal oxidations and the large difference between this and the POW reduction could be used to apply very high overpotentials. Unfortunately Ir bpy complexes are usually yellow; hence a sensitizer complex with more extended absorption, while retaining the redox properties mentioned above, would need to be synthesized. From the photoelectrochemical point of view, studies by Zhu *et al* suggested that one of the limiting factors of photocurrent generation by interfacial thin films of $[Ru(bpy)_2(PVP)_{10}]_{4.5}\alpha$-$[Mo_{18}O_{54}(SO_4)_2]$ was due to the poor rate of charge transfer through the film. Therefore future work would focus on improving the conductivity of these assemblies by addition of nanoparticles. Recent studies performed by our group showed that the D_{CT} value of composite films of $([Ru(bpy)_2(PVP)_{10}]^{2+}$ immobilized on Au nanoparticles increased dramatically at a certain Ru/Au ratio (the percolation threshold), as this concentration of Au allowed electrons to hop between individual nanoparticles in close proximity to each other. Addition of gold nanoparticles to films of $[Ru(bpy)_2(PVP)_{10}]_{4.5}\alpha$-$[W_{18}O_{54}(PO_4)_2]$ and $[Ru(bpy)_2(PVP)_{10}]_{4.5}\alpha$-$[Mo_{18}O_{54}(SO_4)_2]$ will hence be explored.

Chapter 8:

Appendices

8.1 - Characterization of complexes:

8.1.1 - $[Os(bpy)_2(p0p)_2]^{2+}$:

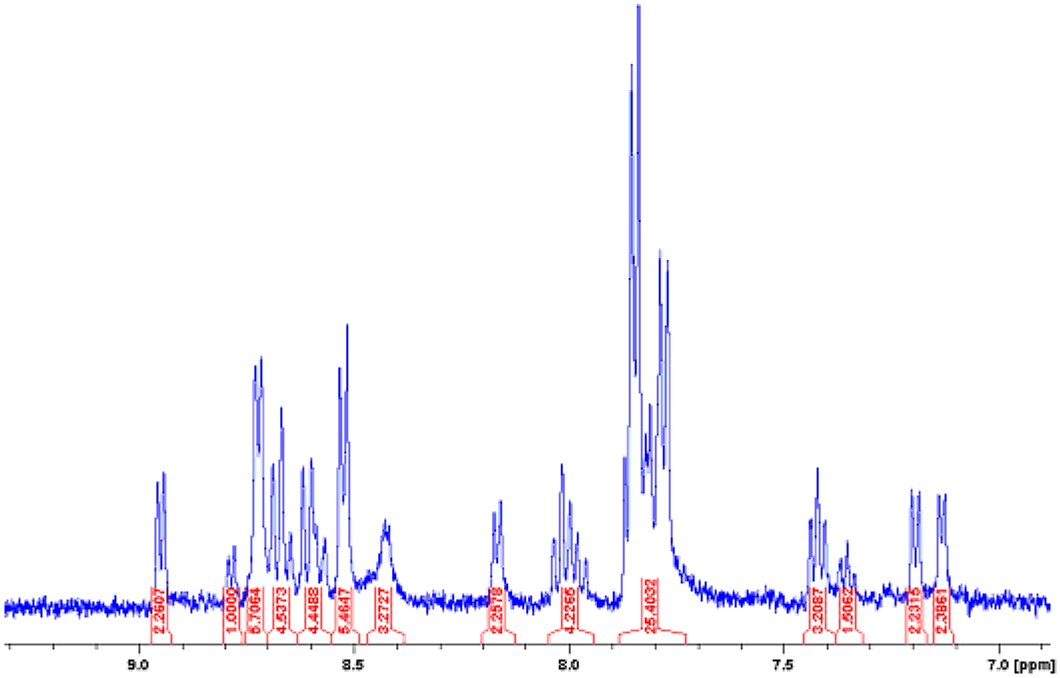

Fig 8.1.1: ^{1}H-NMR spectrum of $[Os(bpy)_2(p0p)_2]^{2+}$ in DMSO-d_6, recorded at 400 MHz. Total integration 32 protons.

Mass spectrometric data: Complex was dissolved in spec grade MeCN; spectrum acquired in negative mode. Molecular formula: $C_{40}OsN_8H_{32}$; molecular weight: 814.9 g.mol^{-1}. m/z = 407 observed.

8.1.2 - [Os(bpy)$_2$(qpy)]$^{2+}$:

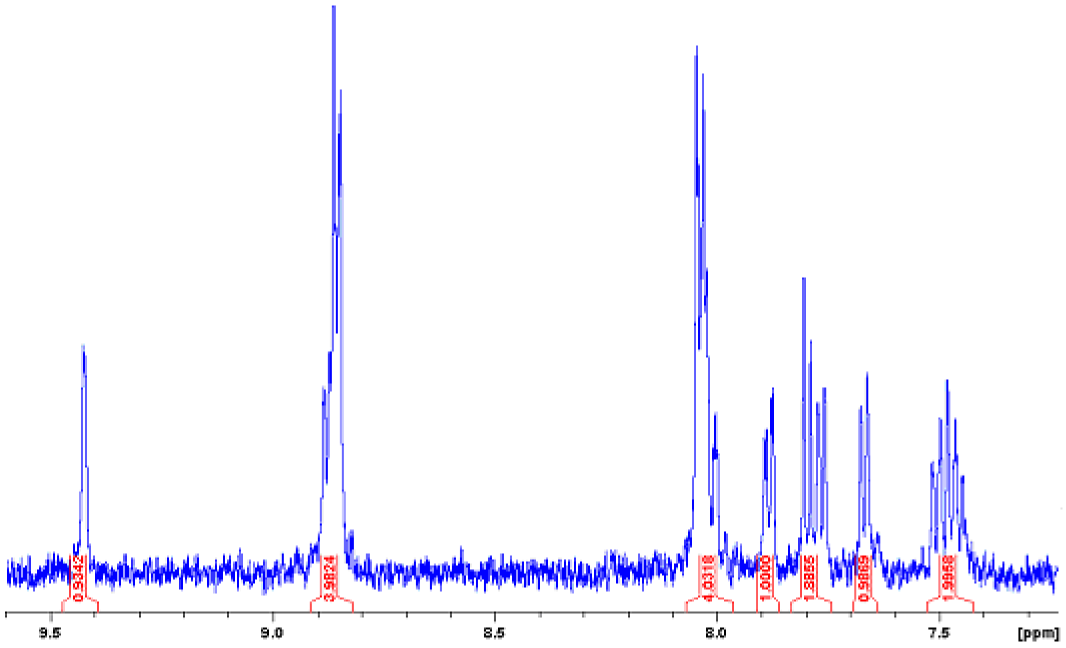

Fig 8.1.2: ^{1}H-NMR spectrum of [Os(bpy)$_2$(qpy)]$^{2+}$ in DMSO-d$_6$, recorded at 400 MHz. Total integration 30 protons.

Mass spectrometric data: Complex was dissolved in spec grade MeCN; spectrum acquired in negative mode. Molecular formula: $C_{40}OsN_8H_{30}$; molecular weight: 812.8 g.mol^{-1}. m/z = 406.5 observed.

8.1.3 - $[Ru(bpy)_2(qpy)]^{2+}$:

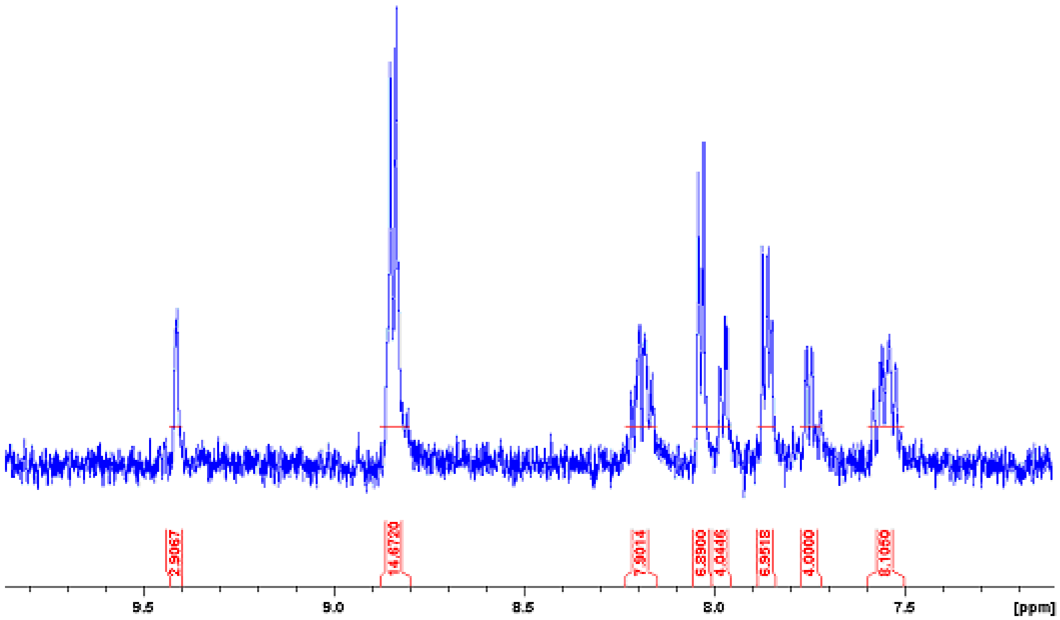

Fig 8.1.3: ^{1}H-NMR spectrum of $[Ru(bpy)_2(qpy)]^{2+}$ in DMSO-d_6, recorded at 400 MHz. Total integration 30 protons.

Mass spectrometric data: Complex was dissolved in spec grade MeCN; spectrum acquired in negative mode. Molecular formula: $C_{40}RuN_8H_{30}$; molecular weight: 724.6 g.mol^{-1}. m/z = 362 observed.

8.1.4 – [Ru(bpy)$_2$(caip-NH$_2$)]$^{2+}$:

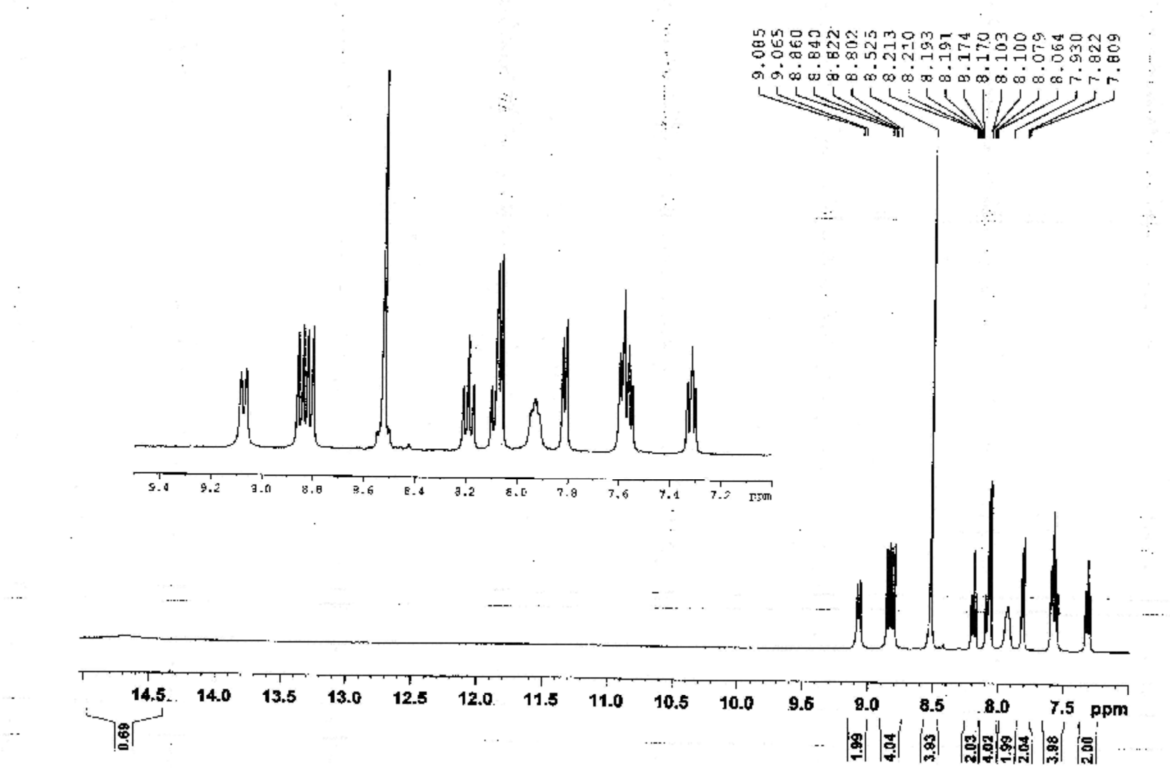

Fig 8.1.4: ^{1}H-NMR spectrum of [Ru(bpy)$_2$(caip-NH$_2$)]$^{2+}$ in DMSO-d$_6$, recorded at 400 MHz. Imidazolium and NH$_2$ protons appear only very weakly at ~ 14.7 ppm.

Mass spectrometric data: Complex was dissolved in spec grade MeCN; spectrum acquired in negative mode. Molecular formula: $C_{39}RuN_9H_{29}$; molecular weight: 725.6 g.mol^{-1}. m/z = 724 observed, corresponds to the deprotonated form [Ru(bpy)$_2$(caip-NH$_2$)]$^+$. NMR and MS courtesy of Mr. Ciarán Dolan.

8.1.5 – $[Ru(bpy)_2(caip\text{-}NO_2)]^{2+}$:

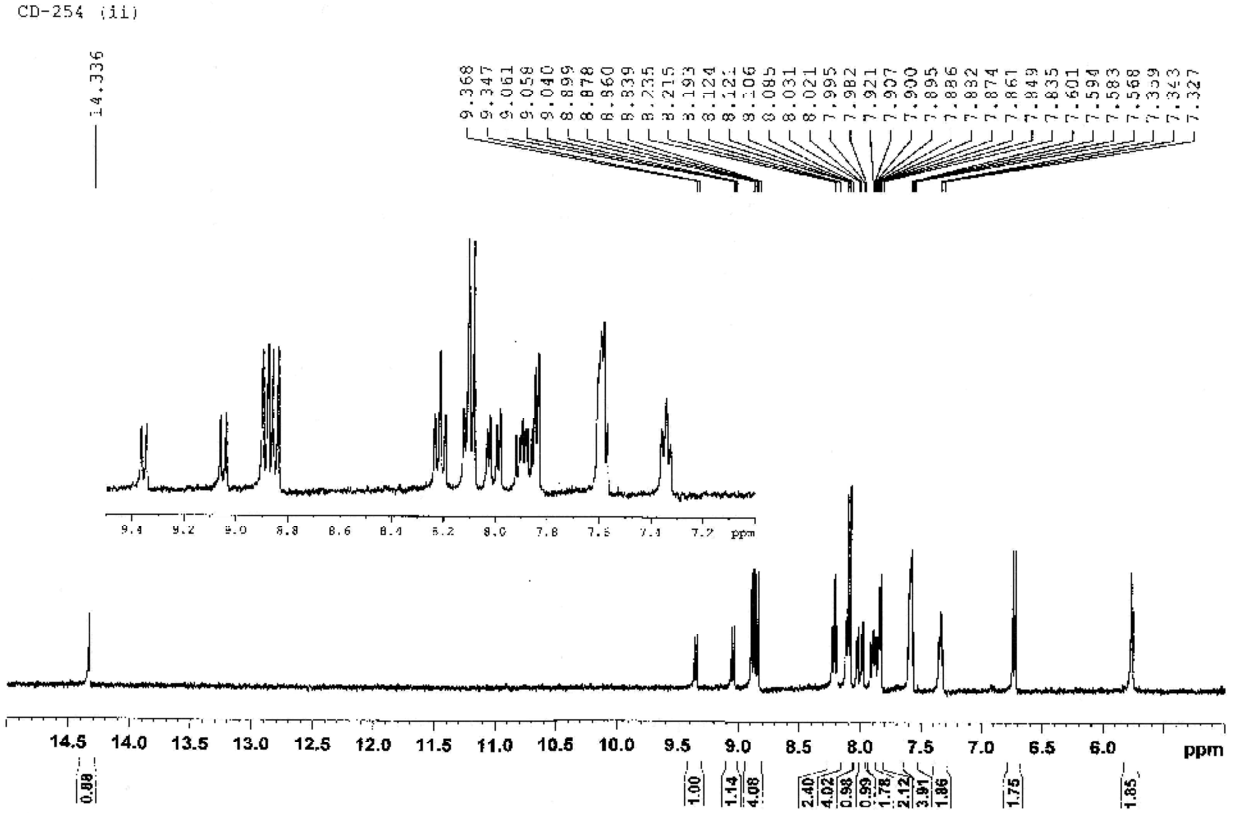

Fig 8.1.5: ^{1}H-NMR spectrum of $[Ru(bpy)_2(caip\text{-}NO_2)]^{2+}$ in DMSO-d_6, recorded at 400 MHz.

Mass spectrometric data: Complex was dissolved in spec grade MeCN; spectrum acquired in negative mode. Molecular formula: $C_{39}RuN_9H_{27}O_2$; molecular weight: 755.6 g.mol^{-1}. m/z = 754 observed, corresponds to the deprotonated form $[Ru(bpy)_2(caip\text{-}NO_2)]^+$. NMR and MS courtesy of Mr. Ciarán Dolan.

This text redacted due to 3rd party copyright
This text redacted due to 3rd party copyright
This text redacted due to 3rd party copyright
This text redacted due to 3rd party copyright
This text redacted due to 3rd party copyright
This text redacted due to 3rd party copyright
This text redacted due to 3rd party copyright
This text redacted due to 3rd party copyright
This text redacted due to 3rd party copyright
This text redacted due to 3rd party copyright
This text redacted due to 3rd party copyright
This text redacted due to 3rd party copyright
This text redacted due to 3rd party copyright
This text redacted due to 3rd party copyright
This text redacted due to 3rd party copyright
This text redacted due to 3rd party copyright
This text redacted due to 3rd party copyright
This text redacted due to 3rd party copyright
This text redacted due to 3rd party copyright
This text redacted due to 3rd party copyright
This text redacted due to 3rd party copyright
This text redacted due to 3rd party copyright
This text redacted due to 3rd party copyright
This text redacted due to 3rd party copyright
This text redacted due to 3rd party copyright

This text redacted due to 3rd party copyright
This text redacted due to 3rd party copyright
This text redacted due to 3rd party copyright
This text redacted due to 3rd party copyright
This text redacted due to 3rd party copyright
This text redacted due to 3rd party copyright
This text redacted due to 3rd party copyright
This text redacted due to 3rd party copyright
This text redacted due to 3rd party copyright
This text redacted due to 3rd party copyright
This text redacted due to 3rd party copyright
This text redacted due to 3rd party copyright
This text redacted due to 3rd party copyright
This text redacted due to 3rd party copyright
This text redacted due to 3rd party copyright
This text redacted due to 3rd party copyright
This text redacted due to 3rd party copyright
This text redacted due to 3rd party copyright
This text redacted due to 3rd party copyright
This text redacted due to 3rd party copyright
This text redacted due to 3rd party copyright
This text redacted due to 3rd party copyright
This text redacted due to 3rd party copyright
This text redacted due to 3rd party copyright
This text redacted due to 3rd party copyright

This text redacted due to 3rd party copyright
This text redacted due to 3rd party copyright
This text redacted due to 3rd party copyright
This text redacted due to 3rd party copyright
This text redacted due to 3rd party copyright
This text redacted due to 3rd party copyright
This text redacted due to 3rd party copyright
This text redacted due to 3rd party copyright
This text redacted due to 3rd party copyright
This text redacted due to 3rd party copyright
This text redacted due to 3rd party copyright
This text redacted due to 3rd party copyright
This text redacted due to 3rd party copyright
This text redacted due to 3rd party copyright
This text redacted due to 3rd party copyright
This text redacted due to 3rd party copyright
This text redacted due to 3rd party copyright
This text redacted due to 3rd party copyright
This text redacted due to 3rd party copyright
This text redacted due to 3rd party copyright
This text redacted due to 3rd party copyright
This text redacted due to 3rd party copyright
This text redacted due to 3rd party copyright
This text redacted due to 3rd party copyright
This text redacted due to 3rd party copyright